DESIGN AND FABRICATION OF INSTRUMENTS FOR BROADBAND SPECTROSCOPY OF COLD MOLECULES

Dissertation présentée en vue de l'obtention du grade de Docteur en Sciences

ALEXIS LIBERT

SUPERVISORS:

Clément Lauzin

Xavier Urbain

MEMBERS OF THE JURY:

Eric Gaigneaux (chairman)
Matthieu Génévriez (secretary)
Piotr Maslowski
Lucile Rutkowski
Jean Vander Auwera

UCLouvain
Institute of Condensed Matter and Nanosciences

January 2022

ABSTRACT

We report the first results concerning the in-house fabrication of an instrument to perform precise, broadband and sensitive measurements of cold species in the gaseous phase at high resolution. Ultimately, this instrument will consist of a frequency-stabilized frequency comb for the light source, of a buffer gas cooling setup for the cooling of the molecular species to cryogenic temperatures and of a high-resolution Fourier transform spectrometer as the spectrum analyzer. Measurements will be performed within a high-finesse optical cavity locked to the frequency comb, fulfilling the sensitivity requirement of the setup.

The spectrum analyzer is a homemade high-resolution Fourier transform spectrometer (FTS) working in the spectral range from 5880 cm^{-1} to 15380 cm^{-1}, with a spectral resolution down to 0.002 cm^{-1}. The FTS currently employs a supercontinuum as a broadband light source and a He:Ne laser with a homemade frequency-stabilization scheme as the spatial reference for the sampling of the interferogram on a constant optical path difference (OPD) grid. The sampling of the two lasers is performed at constant time intervals and the resampling process is performed at the software level. The resampling of the interferogram on a constant OPD grid relies on cubic approximations of the He:Ne interference pattern to determine its zero-crossings. The use of an invariant in the sampling process allows to perform on-the-fly data treatment. Both the hardware aspect and the data processing are described with, in each case, an original approach. The FTS is fully operational and we report the successful coupling of the FTS with a high-finesse optical cavity with effective mirror reflectivities of 99.76%, allowing to reach sensitivities down to $\alpha_{min} = 6.5 \times 10^{-8}$ cm^{-1} with a RMS accuracy of 0.0017 cm^{-1} on the position of the Doppler-broadened transitions with a mean transition width of 0.046 cm^{-1} for spectra recorded at a spectral resolution of 0.015 cm^{-1}. The sensitivity of the instrument per spectral element, once normalized, represents the best sensitivity reported in the literature for Fourier-transform incoherent broadband cavity-enhanced absorption spectroscopy with a supercontinuum light source.

We also report the design and fabrication of a buffer gas cooling setup that allows to cool down molecules to about 20 K while keeping them in the gaseous phase. All the key points concerning the design of the apparatus are made explicit in the manuscript: the mechanical design of the cold cell, the temperature measurement and control, the design of the gas injection lines, etc. In order to validate our design, we probed the methanol $2\nu_1$ overtone band lying between 7180 cm^{-1} and 7220 cm^{-1}, using the cavity ring-down spectroscopy technique. The translational and rotational temperatures of this spectrum are respectively equal to 21.8 ± 1.3 K and 20.3 ± 7.0 K. They were estimated using a two-temperature analysis on a series of assigned transitions.

First results concerning the design and fabrication from scratch of a frequency comb are given. In particular, we present the design of a femtosecond resonator with a 2 m long optical cavity and a 2 mm-thick Ti:sapphire crystal that is optically pumped by a frequency-doubled Nd:YAG laser from Coherent (Verdi V10). Calculations for the evaluation of the group-delay dispersion compensation and simulations for the determination of the setpoint are detailed. The procedure we followed to modelock the laser is made explicit. In parallel, we describe first attempts to stabilize mode-locked lasers using the $1f - 2f$ self-referencing technique.

Finally, we report our preliminary results concerning the locking of an optical cavity on a frequency-stabilized laser using the Pound-Drever-Hall stabilization scheme and the coupling of femtosecond lasers with optical cavities.

ACKNOWLEDGMENTS

En plus d'avoir été une aventure scientifique, ma thèse fut une aventure extraordinaire du point de vue humain. En effet, j'ai eu le plaisir de travailler au sein d'une équipe bienveillante, qui m'aura fait grandir tant comme individu que comme citoyen. Pour cela, je leur en suis reconnaissant.

Mes premiers remerciements vont vers Clément qui a rempli son rôle de promoteur à merveille en se montrant présent, à l'écoute, (parfois très) patient vis-à-vis de mon fort caractère et confiant en mes capacités. Merci d'avoir cru en moi et de m'avoir laissé prendre autant d'initiatives, de m'avoir mis à disposition tous les moyens nécessaires au bon déroulement du projet et de m'avoir soutenu dans mes idées même si tu n'y croyais pas toujours. Merci également pour ton intégrité et ta rigueur scientifiques à toute épreuve. Et finalement, merci pour ton amitié. Cela aura été un plaisir et un honneur de travailler à tes côtés.

Je souhaiterais également remercier vivement mon co-promoteur, Xavier, pour son encadrement, son écoute et ses conseils judicieux. Vous solliciter m'aura plus d'une fois sorti de situations qui semblaient, de prime abord, inextricables. Je voulais également vous remercier pour toutes les fois où vous m'avez dépanné en me prêtant du matériel et des instruments et pour nos discussions enrichissantes lors des pauses-café.

Merci à toi, Baptiste, d'avoir effectué six séjours d'un mois en Belgique pour m'aider sur ma thèse. Chacun de tes séjours, je les ai attendus avec impatience. Tu es la preuve vivante que l'on peut être à la fois incroyablement compétent et cool, jeune et vieux, et que l'on peut se nourrir uniquement de pâtes et être en bonne santé, que dormir ne sert à rien, etc. Même si tu prétendras le contraire, cette thèse, et en particulier le chapitre sur les peignes de fréquence, n'aurait pas été ce qu'elle est sans ton aide. Merci également de m'avoir fait découvrir Lestiac.

Je suis reconnaissant envers Eric Gaigneaux, Matthieu Génévriez, Piotr Maslowski, Lucile Rutkowski et Jean Vander Auwera d'avoir accepté

de faire partie de mon jury et pour le temps qu'ils vont consacrer à mon évaluation. J'espère que vous apprécierez la lecture autant que j'ai apprécié travailler sur le sujet.

Je remercie également Benoît Hackens , Simon-Pierre Gorza et Jean Vander Auwera pour leur présence dans mon comité d'accompagnement. Merci également à Benoît pour les échanges concernant la partie cryogénie de l'instrument ainsi que pour le prêt de l'ADC du spectromètre à transformée de Fourier et à Jean pour le prêt de sa séparatrice.

Je remercie aussi toutes les personnes ayant fait/faisant partie de l'équipe de Clément. Merci plus particulièrement à[1] :

- Anthony pour m'avoir partagé ta passion des toupies asymétriques, pour ta patience concernant mon désordre et pour toutes tes histoires dignes des *Feux de l'amour*;
- Raghed pour les moments de franche camaraderie partagés dans notre bureau et pour m'avoir fait faire un tour du Liban que je ne suis pas prêt d'oublier;
- Robin, pour m'avoir passé ta cavité en ULE, ta bonne humeur permanente et pour m'avoir fait découvrir ta passion pour l'aquariophilie;
- Séverine d'assurer la pérennité du projet sur le refroidissement par gaz tampon et de me rappeler où je range mes outils au labo. Merci aussi pour ce cours particulier sur la spectroscopie durant le premier confinement.

Sans un staff technique et administratif digne de ce nom, le bon déroulement de ce projet aurait été impossible. Merci à[1] :

- Daniel d'avoir veillé à ma bon intégration dès mon arrivée en t'assurant que je ne manque aucune pause café, d'avoir servi d'intermédiaire avec l'atelier de mécanique à mes débuts, etc.
- aux deux Fabienne pour l'efficacité dans le traitement des nombreuses commandes passées tout au long de ces 5 années et pour la résolution des divers problèmes informatiques que j'ai pu rencontrer;

1 Pour éviter tout incident diplomatique, les remerciements sont effectués suivant l'ordre alphabétique.

- Guilhem pour tous les câbles que tu m'as soudé, d'avoir réparé les circuits que je cramais, les programmes Labview, mais aussi pour toutes les discussions de couloir.
- Hervé d'avoir répondu si rapidement à mes nombreuses demandes de pièces, d'avoir consacré énormément de temps à me partager ta passion pour la mécanique et pour toutes nos autres discussions plus informelles.
- Laurence d'avoir fait en sorte que je ne manque jamais ni de stylos-billes ni de biscuits;
- Luca pour ton aide précieuse au labo, pour les pauses café et les bonnes tranches de rire;
- Marc d'avoir répondu à mes nombreuses demandes en électronique, d'avoir toujours veillé à mon épanouissement personnel et d'avoir prêté à maintes reprises ton propre matériel pour me dépanner mais également pour les restos/verres que tu m'as offert et ta gentillesse à mon égard;
- Thomas, pour ton efficacité et le suivi de tes dossiers, mais aussi de t'assurer que je ne laisse pas passer l'heure du repas en venant me chercher tous les midis dans mon bureau/labo.
- à tous les tourneurs/fraiseurs qui ont travaillé sur mes pièces (David, Lucas, Matheus, Michaël, Thomas, etc.). Merci de m'avoir expliqué certains aspects de votre métier, pour votre réactivité quand j'avais besoin de retoucher une pièce, etc.

Je tenais à vous remercier, tous mes copaings, pour les cafés, les voyages, les bières, les moulins, les tours à vélo, les restos U, etc. Merci pour tout en fait, vous êtes sympathiques. Vous lister serait me risquer à d'éventuels oublis, mais vous vous reconnaitrez.

Merci à ma famille de croire en moi et de me soutenir dans mes projets, mais aussi de m'avoir logé, nourri et blanchi tout au long de mon existence.

Merci Charlotte pour ton soutien indéfectible, ta confiance chaque fois que je te dis que je n'en ai que pour cinq minutes avant de rentrer... (ou pour lancer une simulation un samedi matin...) et ta patience/ton pardon quand il s'avérait que j'en avais en fait pour trois heures.

Et finalement, merci à toi, le contribuable belge, d'avoir financé mes recherches par le biais de tes impôts. Sans toi, rien de tout cela n'aurait été possible.

PUBLICATIONS

All the publications authored during this PhD thesis are listed below, ordered by publication date.

- Articles:
  - Libert, A., Urbain, X., Fabre, B., Daman, M., Lauzin, C. (2020). Design and characteristics of a cavity-enhanced Fourier-transform spectrometer based on a supercontinuum source. Review of Scientific Instruments, 91(11), 113104.
- Conferences:
  - Libert A. (2021). Cavity-enhanced and high-resolution Fourier-transform spectroscopy. Ph.D. Students'Day of the IMCN, Louvain-la-Neuve, Belgium;
  - Libert A., Roucou A., Fabre B., Urbain X., Lauzin C. (2019). Cavity-enhanced and high resolution Fourier-transform spectroscopy. HRMS, 26th colloquium, Dijon, France. Speaker: A. Libert;
  - Libert A., Urbain X., Lauzin C. (2018). Design and fabrication of a high-resolution Fourier-transform spectrometer with a supercontinuum laser source. HRMS, 25th colloquium, Bilbao, Spain. Speaker: C. Lauzin;
  - Libert, A. Schmutz, H., MERKT, F., Lauzin, C. (2018). Spectromètres à transformée de Fourier. Journées de spectroscopie moléculaire, Lyon, France. Speaker: C. Lauzin;
  - Libert A., Urbain X., Lauzin C. (2017). Design of a Fourier transform spectrometer for high-resolution spectroscopy. GDR Specmo, Lille, France. Speaker : A. Libert.
- Posters:
  - Libert A. (2019). Cavity-enhanced and high-resolution Fourier-transform spectroscopy. Ph.D. Students'Day of the IMCN, Louvain-la-Neuve, Belgium;

– Libert A., Urbain X., Lauzin C. (2019). Cavity-enhanced and high-resolution Fourier-transform spectroscopy. Journées de spectroscopie moléculaire, Créteil, France;

– Libert A. (2018). Novel approach in high-resolution Fourier-transform spectroscopy. Ph.D. Students'Day of the IMCN, Louvain-la-Neuve, Belgium.

CONTENTS

1 INTRODUCTION 1

2 FOURIER TRANSFORM SPECTROSCOPY 7
- 2.1 Introduction . . . 7
- 2.2 Working principle . . . 10
- 2.3 Design of the interferometer . . . 11
  - 2.3.1 Frequency-stabilized He:Ne reference laser . . . 11
  - 2.3.2 Translation stage . . . 16
  - 2.3.3 Auto-balanced detection scheme . . . 17
  - 2.3.4 Optical cavity . . . 19
- 2.4 Data processing . . . 20
  - 2.4.1 Data processing pipeline . . . 22
  - 2.4.2 Constant OPD grid generation . . . 25
- 2.5 Performances . . . 33
  - 2.5.1 Instrumental lineshape function . . . 35
  - 2.5.2 Wavenumber axis accuracy . . . 37
  - 2.5.3 Instrument sensitivity . . . 38
  - 2.5.4 Comparison with another FT-IBBCEAS setup . . . 41
- 2.6 Conclusion . . . 42

3 FREQUENCY COMBS 45
- 3.1 Introduction . . . 45
- 3.2 Propagation of ultrashort pulses in dispersive media . . . 46
  - 3.2.1 Temporal description of ultrashort pulses . . . 46
  - 3.2.2 Linear propagation . . . 47
- 3.3 Femtosecond lasers: introduction to mode-locking . . . 51
  - 3.3.1 Simple treatment of mode-locking . . . 52
  - 3.3.2 Passive mode-locking based on the Kerr effect . . . 55
- 3.4 Time and spectral representations of a train of ultrashort pulses emitted by a femtosecond laser . . . 57
- 3.5 The frequency comb: a source for spectroscopic applications . . . 61
- 3.6 Design and fabrication of a homemade frequency comb 62
  - 3.6.1 The femtosecond laser resonator . . . 63
  - 3.6.2 Stabilization of the femtosecond laser resonator . 86
- 3.7 Conclusion . . . 98

4 BUFFER GAS COOLING OF MOLECULES 99

4.1 Introduction . . . 99
4.2 Buffer gas cooling principle . . . 102
4.2.1 Cooling by colliding . . . 102
4.2.2 Distance traveled before thermalization . . . 105
4.3 Mechanical design . . . 106
4.3.1 Cold head description and specifications . . . 109
4.3.2 Cold cell design . . . 112
4.3.3 Thermal shield design . . . 114
4.3.4 Vacuum and gas injection management . . . 115
4.3.5 Optical cavity . . . 122
4.4 Dimensioning of the pumping capacity of the setup . . . 124
4.5 Cavity ring down spectroscopy . . . 126
4.6 First results . . . 129
4.6.1 Obtaining the first signal . . . 129
4.6.2 The J_{K_a,K_c}: $1_{01} \leftarrow 1_{10}$ transition in the $2\nu_1$ overtone band of water: characterization of the translational temperature . . . 133
4.7 The $2\nu_1$ overtone band of methanol: characterization of the rotational temperature . . . 135
4.8 Conclusion . . . 140
5 PERSPECTIVES: TOWARDS BROADBAND METROLOGICAL MEASUREMENTS 145
5.1 Introduction . . . 145
5.2 Surpassing the maximum resolution of the FTS . . . 145
5.3 Locking of the frequency comb on an optical cavity . . . 146
5.4 Conclusion . . . 153
6 CONCLUSION 155
A FOURIER TRANSFORM SPECTROMETER: SUPPLEMENTARY MATERIALS 159
A.1 Generation of an interferogram in a Michelson interferometer . . . 159
A.1.1 The Michelson interferometer . . . 160
A.1.2 Generation of an interferogram . . . 162
A.2 Instrumental lineshape function . . . 170
A.2.1 Effect of maximum path difference . . . 170
A.2.2 Effect of beam divergence . . . 172
A.3 Sampling . . . 178
A.3.1 Reference Laser . . . 178
A.3.2 Sampling frequency and aliasing . . . 180

A.3.3 Uniform time sampling versus uniform space sampling . . . 182
A.3.4 ADC resolution . . . 183
A.4 Stabilization of the He:Ne laser . . . 185
A.4.1 Theoretical background . . . 186
A.4.2 Implementation . . . 189
A.5 Time-domain filtering of the two channels . . . 191
A.6 Zero-crossings determination . . . 193
A.7 Ideal reconstruction of a sampled signal: the sinc interpolation . . . 196
A.8 Instrument sensitivity . . . 198
A.8.1 absorption coefficient in absence of an optical cavity 199
A.8.2 Cavity-enhancement of absorption . . . 201
B FREQUENCY COMBS: SUPPLEMENTARY MATERIALS 205
B.1 Measuring the duration of the pulses . . . 205
B.1.1 Working principle . . . 206
B.1.2 Design of our interferometric autocorrelator . . . 207
B.2 Optics of the homemade femtosecond resonator . . . 210
C BUFFER GAS COOLING SETUP: SUPPLEMENTARY MATERIALS 217
C.1 Vacuum and gas injection management - Detailed . . . 217
C.2 Temperature measurement and control . . . 221
C.2.1 Choice of cryogenic temperature sensors . . . 221
C.2.2 Choice of the heaters . . . 223
C.2.3 Temperature control . . . 224
C.3 Safety aspects of the buffer gas cooling setup . . . 224
D PERSPECTIVES: SUPPLEMENTARY MATERIALS 227
D.1 Pound-Drever-Hall (PDH) stabilization scheme: theoretical background . . . 227
D.1.1 General expression at the input of the cavity . . . 228
D.1.2 Slow modulation . . . 230
D.1.3 Fast modulation . . . 232
D.1.4 Electro-optic modulator and the generation of sidebands in practice . . . 233
D.2 Length drift of the optical cavity . . . 234
D.3 Characterization of the frequency response of the optical mounts . . . 236
E PEAK DETECTION ALGORITHM AND BASELINE DETERMINATION 241
E.1 Peak detection . . . 241

E.2 Weighted penalized least squares for the baseline evaluation . . . 244
F STUDY OF A HIGH-FINESSE CAVITY 249
F.1 Introduction . . . 249
F.2 Experimental setup . . . 250
F.2.1 Conditions of stability and mode matching . . . 252
F.2.2 Transverse modes . . . 253
F.2.3 Scanning the cavity . . . 253
F.3 Experiments and observations . . . 254
G PHOTOMETRY AND IMAGING TO INFER THE NUMBER, THE SIZE AND THE DYNAMICS OF EXHALED DROPLETS. 257
G.1 Abstract . . . 257
G.2 Introduction . . . 258
G.3 Application of Mie scattering to droplet size determination 259
G.4 Description of the experimental setup and procedure . . . 263
G.5 Data analysis . . . 265
G.5.1 Principles and general overview . . . 265
G.5.2 Energy map retrieval . . . 268
G.5.3 Tilt angle correction . . . 270
G.5.4 Determination of particles trajectories . . . 273
G.6 Results and discussion . . . 278
G.6.1 Validation of the size determination procedure . . . 278
G.6.2 Application to the dynamics of produced aerosols while yelling . . . 281
G.6.3 Characterization of aerosols lifetimes . . . 282
G.7 Conclusion and perspectives . . . 287
G.8 Acknowledgments . . . 288
G.9 Data availability . . . 288
Bibliography 289

LIST OF FIGURES

Figure 2.1 Layout of the Fourier transform spectrometer. . 12
Figure 2.2 Experimental setup for the characterization of the frequency stability of the He:Ne reference laser. 14
Figure 2.3 Carriage with the two retroreflectors placed back-to-back. 17
Figure 2.4 Comparison between a single-detector detection scheme and the auto-balanced detector scheme. 19
Figure 2.5 Piezo-actuated vacuum-tight optical mounts for the high-reflectivity mirrors of the optical cavity. 21
Figure 2.6 Data processing pipeline of the Fourier transform spectrometer. 23
Figure 2.7 Removal of the fringing effect from both the interferogram and spectrum perspectives. 26
Figure 2.8 Estimation of the zero-crossings of the He:Ne interference pattern. 27
Figure 2.9 Illustration of the filling process of the resampling kernel. 30
Figure 2.10 Brault resampling method. 31
Figure 2.11 Velocity fluctuations and their consequences on the fringe visibility and the resampling in the spatial domain. 33
Figure 2.12 Cavity-enhanced spectrum of H_2O desorbing from a 88 cm long cell at a resolution of 0.015 cm^{-1}. 34
Figure 2.13 Instrumental lineshape function of the FTS at 12849.56 cm^{-1} (778.24 nm). 36
Figure 2.14 Spectral analysis of the impact of the velocity fluctuations on the contrast of the He:Ne laser interference pattern and on the ILS. 37
Figure 2.15 Deviation of the central wavenumber of the experimental H_2O lines from the Hitran database. 38
Figure 2.16 Absorbance with respect to the wavenumber. . . 40
Figure 2.17 Zoom between 11920 cm^{-1} and 11930 cm^{-1} of the absorbance with respect to the wavenumber. 41

Figure 3.1 Consequences of dispersion on a pulse as it propagates in a dispersive medium. 50
Figure 3.2 Intensity at the output of a laser emitting simultaneously on $N = 61$ modes of equal amplitude and (a) random phases; (b) identical phases. . . 55
Figure 3.3 Time and spectral representations of light at the output of a ML femtosecond oscillator. 60
Figure 3.4 Optical layout of the femtosecond laser. 64
Figure 3.5 Linear representation of the resonator. 71
Figure 3.6 Contour map of the tangential small spot size variation δ in the plane of the mirror M_1. 73
Figure 3.7 Schematic and photograph of the first version of the homemade femtosecond resonator. 79
Figure 3.8 Schematic and photograph of the second version of the homemade femtosecond resonator. 82
Figure 3.9 Intensity with respect to time at the output of the second version of the femtosecond resonator. 83
Figure 3.10 Spectrum at the output of the second version of the femtosecond resonator. 83
Figure 3.11 Measurement of the pulse duration with the interferometric autocorrelator. 84
Figure 3.12 Contour map of the tangential small spot size variation δ in the plane of mirror M_1 of the second version of the femtosecond resonator. . . 85
Figure 3.13 Sequence of elements for the measurement and stabilization of the repetition and offset frequencies. 87
Figure 3.14 Layout of the $1f - 2f$ interferometer. 90
Figure 3.15 Photograph of our $1f - 2f$ interferometer. . . . 91
Figure 3.16 Photograph of the optical layout for the offset frequency adjustment. 94
Figure 3.17 Pictures of the supercontinuum generated at the output of the 8 cm long NL-PM-750 photonic-crystal fiber from NKT with the MIRA900 and of the setup for beam injection into the fiber. . . 96
Figure 3.18 Spectrum at the output of the photonic-crystal fiber. 97
Figure 4.1 Working principle of the buffer gas cooling technique. 101

Figure 4.2 Temperature of the molecule under study with respect to the number of collisions with helium at 10K. 105
Figure 4.3 Cut view of the buffer gas cooling setup. 107
Figure 4.4 Photographs of the complete buffer gas cooling setup. 111
Figure 4.5 CH208L cold head capacity map at 50 Hz. From Sumitomo. 112
Figure 4.6 Photographs of our cold cell 113
Figure 4.7 Photographs of the thermal shield. 116
Figure 4.8 Quick re-alignment system of the optical cavity. 117
Figure 4.9 xyz translation system for the injection pipe of the target gas line. 120
Figure 4.10 Photograph of the vacuum chamber, where the buffer gas line from the vacuum chamber wall to the cold cell is installed. 121
Figure 4.11 Photograph of the mirror mount at the output of the optical cavity. 123
Figure 4.12 Determination of the location of the turbopump. 126
Figure 4.13 Working principle of our CRDS setup. 128
Figure 4.14 Schematic of the cavity ring-down spectroscopy setup implemented on the buffer gas cooling setup.130
Figure 4.15 Interference pattern at the output of the 75 mm long ULE etalon with respect to the temperature of the DFB laser head. 134
Figure 4.16 First signal obtained with the CRDS. 135
Figure 4.17 Absorption coefficient of the J_{K_a,K_c}: $1_{01} \leftarrow 1_{10}$ transition in the $\nu_1 = 2$ stretching region of the water molecule recorded using our CRDS setup. 136
Figure 4.18 Absorption coefficient of the J_{K_a,K_c}: $1_{01} \leftarrow 1_{10}$ transition in the $\nu_1 = 2$ stretching region of the water molecule: fit with two Gaussian curves. . 137
Figure 4.19 Absorption spectrum of methanol between 7180 cm^{-1} and 7208 cm^{-1} recorded with the buffer gas cooling setup. 141
Figure 4.20 Comparison between the spectra of methanol between 7200.6 cm^{-1} and 7200.9 cm^{-1} measured at 23 K by Svoboda *et al.* and ours. 143
Figure 4.21 Comparison between the spectra of methanol measured at 20 K and 270 K. 144

Figure 5.1 Trace of the oscilloscope displaying the observation of the magic point. 148
Figure 5.2 Feedback loop for the locking of an optical cavity on a femtosecond laser. 148
Figure 5.3 Experimental setup of the PDH stabilization scheme. 149
Figure 5.4 Error signal obtained experimentally for a slow modulation 150
Figure 5.5 Error signal obtained experimentally for a fast modulation 152
Figure A.1 (a) schematic of a Michelson interferometer. (b) Intensity at the photodetector with respect to retardation δ of a purely monochromatic source. 161
Figure A.2 Schematic of a Michelson interferometer using retroreflectors. 162
Figure A.3 Expression of the electric field of a monochromatic source of angular frequency ω_0 at several positions in the interferometer. 163
Figure A.4 Intensity with respect to retardation for a purely monochromatic source. 166
Figure A.5 Interferogram of a blackbody source and its associated spectrum. 169
Figure A.6 Interferogram of two monochromatic waves with slightly different wavenumbers and its associated spectrum. 171
Figure A.7 Influence of finite path length on a monochromatic source of wavenumber $\tilde{\nu_0}$. 172
Figure A.8 Spectra of two single lines of equal intensity modified by the finite length of the translation stage. 172
Figure A.9 Schematic of the interferometer entrance aperture.173
Figure A.10 Ray tracing of a point source away from the centre of the optical axis and injected in a Michelson interferometer. 174
Figure A.11 Schematic of an off-axis ray striking the mobile mirror at different mirror displacements. 174
Figure A.12 Interferogram of a coherent monochromatic source for three maximum divergence angles. 177
Figure A.13 Haidinger Fringe pattern. 178
Figure A.14 Illustration of the resampling process. 179

Figure A.15 Sampled squared sinc function and its associated spectrum. 181
Figure A.16 Consequences of aliasing on the spectrum of a squared sinc function. 182
Figure A.17 Same interferogram measured with the same FTS and sampled with (a) a 6-bits ADC (b) a 16-bits ADC. 184
Figure A.18 Partial energy level diagram of the helium and neon atoms relevant for the He:Ne laser emission at 632.8 nm. 187
Figure A.19 Factors determining the emission wavelength of the He:Ne laser. 188
Figure A.20 Error signal generation for the stabilization of the reference He:Ne laser. 191
Figure A.21 He:Ne laser stabilization scheme. 192
Figure A.22 Frequency response of the FIR filters of the reference and the target channels. 193
Figure A.23 Intensity at the output of an optical cavity consisting of two mirrors separated by a distance d. 203
Figure B.1 Layout of an interferometric autocorrelator based on a Michelson interferometer. 208
Figure B.2 Layout of a background-free interferometric autocorrelator. 208
Figure B.3 Picture of our experimental setup. 211
Figure B.4 Butterfly pattern at the output of the properly aligned autocorrelator. 212
Figure B.5 Data processing pipeline of the second order optical autocorrelator. 212
Figure B.6 Background-free aucorrelation pattern at the output of the MIRA900. 213
Figure B.7 Calculated GDD of the folding chirped mirrors pair employed in our cavity at 0° angle of incidence. 214
Figure B.8 Calculated GDD of the output coupler employed in our cavity at 0° angle of incidence. 214
Figure B.9 Calculated GDD of the chirped end-mirror employed in our cavity at 0° angle of incidence. . . 215
Figure C.1 Layout for the vacuum and gas injection management of the buffer gas cooling setup. 218

Figure C.2 Gas flow curve of the 21124-KE0X-000 dosing valve of VAT. 220
Figure C.3 Photographs of the gas injection panel. 220
Figure C.4 Standard temperature-voltage curve of the DT670 temperature diode of Lake Shore for a forward current of 10 μA. 223
Figure C.5 Schematic of the temperature control layout. . . 225
Figure D.1 Exerimental setup of the PDH stabilization scheme. 228
Figure D.2 Magnitude and phase of the reflection coefficient of a Fabry-Perot cavity. 231
Figure D.3 Error signal for a slow modulation frequency. . 232
Figure D.4 Error signal for a fast modulation frequency. . . 233
Figure D.5 Procedure for the characterization of the optical cavity length drift. 235
Figure D.6 Length drift of a 150 mm long optical cavity in an unconditioned laboratory. 236
Figure D.7 Layout for the characterization of the mirror mounts. 238
Figure D.8 Calibration procedure for the determination of the displacement from the knowledge of the intensity at the output of the Michelson interferometer. 239
Figure D.9 Transfer functions of the piezo-mount when installed in a KM200 optical mount from Thorlabs or a Polaris K2T1 from Thorlabs. 239
Figure E.1 Mexican hat wavelet. 242
Figure E.2 Generation of the 2D map of CWT coefficients $C(a, b)$. 244
Figure E.3 Illustration of the peak detection algorithm. . . . 245
Figure E.4 Illustration of the peak detection algorithm on the spectrum of Methanol between 7175 cm^{-1} and 7190 cm^{-1} measured with the buffer gas cooling setup. 248
Figure F.1 Normalized reflected and transmitted light intensities by a Fabry-Perot cavity. 251
Figure F.2 Schematic of the experimental setup. 252
Figure F.3 TEM$_{mn}$ modes labelled with m, n of beams with (left) a planar symmetry (right) a cylindrical symmetry. 253

Figure G.1 Geometry of the scattering process from the emission to the detection through the entrance pupil. 260
Figure G.2 Scattering particle equivalent diameter with respect to the number of scattered photons for isopronanol droplets and a laser power of 0.25 mW. 262
Figure G.3 Experimental setup. 264
Figure G.4 Illustration of the tilt-and-shift photography and the Scheimpflug principle. 265
Figure G.5 Data processing pipeline applied to each image of the video. 266
Figure G.6 Image of the laser sheet, 30 seconds after someone yelled the word "particle" during 30 seconds in front of the box hole. 267
Figure G.7 Several photographs of an outdoor wall, taken at 9 exposure times from 1/8 seconds to 1/1250 seconds. 269
Figure G.8 g-curve of the Nikon D800 green channel obtained with a sensitivity of 1250 ISO. 270
Figure G.9 Illustration of the tilt-angle correction. 272
Figure G.10 Flowchart for the determination of the particle trajectories. 274
Figure G.11 Schematic illustrating the algorithm for the determination of the particle trajectories. 275
Figure G.12 Trajectories followed by particles in this study (a) on a 0.5 second interval starting 7 seconds after yelling (b) on a 5-second interval starting 110 seconds after yelling. 277
Figure G.13 Validation of our method on droplets generated with the liquid controller dropper. 279
Figure G.14 Geometrical method for the determination of the droplet diameter. 280
Figure G.15 Size distribution of droplets of the measurement without any fan. 282
Figure G.16 Comparison between Stadnytskyi *et al.* and this work. 283
Figure G.17 Trajectories followed by particles in the study of Stadnytskyi *et al.* (a) on a 20-second interval starting 50 seconds after yelling and b) on a 50-second interval starting 400 seconds after yelling. 286

Figure G.18 Evolution of the size distribution of droplets with respect to time. 287

ADC	analog-to-digital converter	ILS	instrumental lineshape function
AOM	acousto-optic modulator	IIR	infinite impulse response
AR	anti-reflection	KML	Kerr mode-locking
CEAS	cavity-enhanced absorption spectroscopy	LMS	low misalignment sensitivity
CEO	carrier-envelope offset	ML	mode-locked/mode locking
CRDS	cavity ring-down spectroscopy	OPD	optical path difference
CW	continuous wave	PBS	polarizing beamsplitter
ECDL	external cavity diode laser	PDH	Pound-Drever-Hall
EOM	electro-optic modulator	PID	proportional-integral-derivative
GDD	group delay dispersion	PWM	pulse width modulation
FFT	fast Fourier transform	RF	radio-frequency
FIR	finite impulse response	rms	root-mean-square
FSR	free spectral range	SAM	self-amplitude modulation
FT-IBBCEAS	Fourier-transform incoherent broadband cavity-enhanced absorption spectroscopy	SC	supercontinuum
FTS	Fourier-transform spectrometer	SHG	second harmonic generation
FSR	free spectral range	SNR	signal-to-noise ratio
HMS	High misalignment sensitivity	SPM	self-phase modulation
HRM	high-reflectivity mirror	TOD	third-order dispersion
		ZPD	zero path difference

1 INTRODUCTION

Optical spectroscopy, which is the study of matter by its interaction with light as a function of its frequency, has a long history in modern physics: it is at the origin of the discovery of quantum physics with the measurement and the understanding of the black body radiation spectrum and of the absorption spectrum of the hydrogen atom at the beginning of the 20^{th} century [1]. However, this research field is still very active with the advent of new techniques and technologies. Nowadays, spectroscopists routinely use the frequency distribution of light to determine the energy level structure within an atom or a molecule. This structure governs the unique interaction between radiation and emitting/absorbing matter, allowing to retrieve tremendous information about the sample. In the case of a gaseous sample, the spectroscopic information permits to evaluate the abundances of the molecules being studied, their temperatures, pressures and velocities [2]. Optical spectroscopy is therefore an invaluable tool for a myriad of applications, from fundamental physics [3] to environmental monitoring [4], healthcare and the semi-conductor industry. For example, in the latter, trace detection of some impurities in the process give considerable information about the quality of the end products [5]. A typical medical application of optical spectroscopy is the study of metabolic processes and the diagnosis of some diseases through breath analysis [6, 7].

In molecular physics, information brought by optical spectroscopy allows for the characterization of the molecular Hamiltonian. This governs the intramolecular dynamics and its eigenstates, ultimately leading to a determination of complex molecular structures and of exquisite details on the interatomic dynamics [8]. However, the spectroscopic data of molecules made of more than three atoms and their associated understanding is relatively poor or absent in the near-infrared (NIR) and the visible (VIS). This is illustrated in Table 1.1 presenting the current knowledge of the energy level spectrum of different molecules as a function of the number of atoms, using the Hitran database as

reference [9]. The current low level of knowledge in this frequency range (NIR-VIS) for molecules as important as CH_3OH is due to unfavorable parameters from the experimental and the theoretical point of view, as, a high density of states, increasing with energy, large partition functions, large amplitude motions, for certain vibrational excitations large intramolecular energy redistribution (IVR) and a decrease of the line strengths with increasing energy. The in-depth spectroscopic study of such systems is thus challenging both theoretically and experimentally. The advent of new light sources, optics, detectors, more efficient computers, better data acquisition systems, etc. but also the apparition of new techniques that permit, amongst others, to cool down atoms and molecules to cryogenic temperatures open the door to go beyond the state of the art in terms of molecular complexity with the study of large and heavy molecules at relatively high frequencies (NIR,VIS). Good examples being the recent measurements of the rovibrationally resolved spectra of fullerene in the far-infrared measured by Bryan Changala and co-workers [8] and of methane in the NIR by Foltynowicz and co-workers [10].

An ideal instrument employed for the study of large molecules by molecular spectroscopy should have a series of features. (i) It should have the ability to cool down molecules to a few Kelvin in order to decongest the dense spectra of complex molecules, making their analysis feasible, while increasing the precision on the location of the transitions by mitigating the Doppler broadening effect. In addition, this cooling goes along with a slowing of the molecules and favor saturation effects, increasing even more the precision on the line position [11]. (ii) It should be broadband, meaning it can cover a large region of the spectrum in a single measurement. (iii) It should be precise, that is the location of the peaks on the wavenumber axis, but also their intensities, lineshapes and widths present a better determination. (iv) Ideally, such an instrument should also be sensitive, meaning it can detect minute quantities of a gaseous sample [12] and to probe weak molecular transitions. All of this with (v) sufficient resolution to clearly distinguish the many transitions observable in typical molecular spectra.

The objective of this PhD thesis is to present the design, the fabrication and the characterization of an instrument that will ultimately embody all these features, allowing for the study of large molecules in the gaseous phase in the near-infrared and visible regions of the light spectrum. In its final form, it will consist of a frequency comb as a light source, a Fourier

Table 1.1: Current status of the Hitran database knowledge of the absorption spectrum for the most abundant isotopologue of different molecules as a function of the number of atoms [9].

Molecule formula	Number of atoms	Spectral coverage Hitran 2020
H_2O	3	$0 - 42000$ cm^{-1}
N_2O	3	$0 - 7797$ cm^{-1}
N_2H_3	4	$0 - 10349$ cm^{-1}
C_2H_4	6	$620 - 3243$ cm^{-1}
CH_3OH	6	$0 - 1408$ cm^{-1}
C_2H_6	8	$225 - 3070$ cm^{-1}

transform spectrometer (FTS) as a spectrum analyzer and a buffer gas cooling setup in order to perform the spectroscopy of cold molecules, the required sensitivity being achieved by making the measurements within an optical cavity. Motivations for building in-house and from scratch such an instrument are multiple. First, building an instrument makes it highly customizable and gives us a complete understanding of its assets and limitations. Secondly, even if individual commercial solutions exist for the light source and the spectrum analyzer, they are expensive and they do not offer the possibility to easily implement the new paradigms relying on the use of frequency-stabilized frequency combs in Fourier transform spectroscopy that appeared in the last few years and presented in detail in Ref. [13, 14]. This new paradigm allows to extend the range of applications of Fourier-transform spectroscopy to broadband metrological applications [15] by increasing the precision on the location of the transitions while suppressing the instrumental lineshape function due to the finite length of the translation stage that induces the optical path difference in the instrument and even to surpass the maximum resolution of conventional FTS [13, 14]. Moreover, no commercial solution is available at all concerning the buffer gas cooling setup.

This manuscript is divided into four chapters. An appendix is associated with each chapter, providing details that would make the manuscript more cumbersome if they were present in the main text. The first three chapters present in each case one particular element of the setup while the fourth chapter develops some perspectives for the instrument.

Following this introduction, chapter 2 details the FTS we built in-house, its calibration and its characterization. The FTS is the part of the instrument responsible for the broadband (ii) and high-resolution (v) (0.002 cm^{-1}) aspects, covering the range of wavelengths from 650 nm to 1.7 μm (or equivalently the range of wavenumbers from 5880 cm^{-1} to 15380 cm^{-1}). By coupling the FTS to an optical cavity with high-reflectivity mirrors in which the gaseous sample is placed, the sensitivity of the instrument (iv) is considerably improved. Its characterization was made on the cavity-enhanced spectrum of water in the range of wavenumbers from 10500 cm^{-1} to 14300 cm^{-1} measured in an auto-balanced detection scheme with a supercontinuum light source, allowing for the determination of its sensitivity and its benchmarking against the most sensitive incoherent broadband cavity-enhanced spectrometer reported in the literature <hich used a Vertex 80 FTS, commercialized by Bruker [16].

In chapter 3, we present the first results concerning the development of a frequency-stabilized frequency comb that will serve as a broadband light source (ii) for the FTS. As mentioned above, when properly combined with a FTS, these light sources boost the precision of the measurement (iii), opening the door to broadband metrological applications. In particular, the design and fabrication from scratch of a femtosecond laser are presented. First results concerning its stabilization are also given.

Chapter 4 is dedicated to the buffer gas cooling setup. It details its working principle and it deeply describes its design. It also presents the cavity-ring down spectroscopy setup we used to seek the first signals of cold molecules. The spectrum of the methanol $2\nu_1$ overtone band lying between 7180 cm^{-1} and 7220 cm^{-1} was recorded and used to characterize the ability of our setup to cool down molecules to cryogenic temperatures. This spectrum illustrates our ability to study large and complex molecules in the near-infrared.

Chapter 5 is dedicated to perspectives concerning the coupling of frequency combs with optical cavities and the FTS. This chapter also presents the first results regarding the stabilization of optical cavities on frequency combs, a mandatory step to simultaneously combine the frequency comb with an optical cavity and the FTS.

Finally, three more appendices were added to the manuscript. The fifth appendix is dedicated to the description of an algorithm that dis-

criminates the peaks against the baseline of a signal. This algorithm is useful in molecular spectroscopy in situations where it is impossible to perform sample-free measurements. The sixth appendix is a laboratory protocol that illustrates several concepts of high-finesse optical cavities. It was inspired from the research work realized in the laboratory and it is given to students who follow the course of optics and laser physics. In the present manuscript, this appendix serves as a support for chapters 2, 3, 4 and 5, optical cavities being somehow involved in all of them. The seventh appendix details a setup to characterize the size distribution and the dynamics of aerosols and droplets in suspension in air based on the use of a camera, a tilt-and-shift objective, and an appropriate data processing pipeline. This setup is not related to the main manuscript but its development was guided by the specific context of the COVID-19 pandemic.

2

FOURIER TRANSFORM SPECTROSCOPY

Most of this chapter was directly taken from the published paper [17].

2.1 INTRODUCTION

To perform optical spectroscopy with a broadband light source, one needs an instrument to disperse the light in terms of its frequency content. However, due to the limited bandwidth of optical detectors and electronics, recording the light intensity as a function of time and applying a Fourier transform does not provide the spectrum of this light source. Indeed, optical frequencies (about several hundreds of THz) are about 5 orders of magnitude higher than the fastest detectors[1] [2]. There are three common approaches to overcome this difficulty and resolve the light source with regard to its frequency, (1) only the light intensity in the spectral range of interest is measured thanks to the use of optical filters, (2) the spectral components of the light source are spatially separated with the help of dispersive instruments like gratings or prisms and their intensities are measured individually, (3) the interference signal at the output of a Michelson interferometer is recorded at specific values of optical path difference (OPD) induced in one of the arms of the interferometer. This signal is known as the interferogram. The spectrum is retrieved from the interferogram by means of the mathematical Fourier transform. This last approach is at the basis of Fourier-transform spectroscopy.

Fourier transform spectrometers (FTS) present three main advantages over the dispersive- and filter-based approaches. First, all the frequencies are recorded at the same time on a single photodetector. The contribution of each of these frequencies to the signal is then determined by taking the Fourier transform of this signal. This is known as the multiplex advantage or Felgett's advantage [19]. Secondly, light throughput for a given resolution is superior to the two other aforementioned

1 The temporal evolution of ultrashort laser pulses was recently directly measured by Korobenko *et al.* [18] by detecting transient currents in air plasma.

techniques, allowing for higher signal-to-noise ratio measurements in a given amount of time compared to dispersive- and filter-based approaches. This is known as Jacquinot's advantage [20]. Finally, the frequency scale of the spectrum is obtained via a reference laser in Fourier transform spectrometers, leading to self-calibrated spectra. This feature is Connes'advantage of FTS [21].

Since the apparition of the first commercial rapid scanning FTS in 1969 [22], a lot of progress was made in the design and the development of these instruments. They are now a mature technology and commercial FTS with resolution down to 0.0009 cm^{-1} are commercially available and used in laboratories all over the world, making them one of the workhorses of high-resolution molecular spectroscopy. They usually rely on conventional thermal sources to perform spectroscopy. In order to improve their sensitivity, the optical path through the sample must be increased. This is usually accomplished by using multi-pass cells but this approach suffers from the requirement of large sample volumes to reach interaction lengths of several hundreds of meters and an ill-defined interaction region. Another approach relies on the use of optical cavities instead of multi-pass cells, reducing by more than two orders of magnitude the volume required for a similar interaction length. The use of an optical cavity, along with an incoherent broadband light source and a FTS allows a considerable improvement in the sensitivity of the measurement while preserving the high resolution and the broadband characteristics of FTS. This combination was first reported by Ruth *et al.* [23] where a 75 W Xe arc lamp was successfully coupled to a cavity and a commercial FTS. This technique was named *Fourier-transform incoherent broadband cavity-enhanced absorption spectroscopy* or FT-IBBCEAS. Unfortunately, optical cavities exclude the use of thermal light sources because of the very poor coupling throughput due to their spatial divergence and low spectral brightness [24]. Alternative light sources for FT-IBBCEAS are light emitting diodes and supercontinuum light sources. Supercontinuum light sources have the ability to produce several watts of pulsed radiation on a very broad spectral range in the visible and infrared domains. Furthermore, the emitted light is already collimated, facilitating its coupling with optical cavities. Two groups made use of these light sources in FT-IBBCEAS setups [16, 25].

While there is a renewed interest in building or refurbishing in-house FTS for either economical or customization purposes [26–28] and even if numerous articles discuss specific parts of the design of FTS, we did

not find any article in the literature describing the complete design and development of such an instrument, including both the software and hardware aspects. Also, with the progress concerning, amongst others, computational power and data acquisition, alternative approaches compared to commercial instruments were considered in this work. These approaches make feasible the fabrication of high resolution FTS with limited material and human resources. The goal of this chapter is to fill the gap in the literature by precisely describing our instrument, presenting the advantages and limitations of our design and discussing some aspects and choices that were made during the development process for other groups to build their own high resolution FTS and gain a significant amount of time.

This chapter thus presents the design and fabrication of a Fourier transform spectrometer for high resolution spectroscopy, with resolution down to 0.002 cm^{-1}. Measurements are performed in an auto-balanced detection scheme and acquisition is performed at constant time intervals. Resampling of the interferograms on an OPD grid is performed at the software level. The instrument is capable of covering the spectral range from 5900 cm^{-1} to 14300 cm^{-1} by employing a supercontinuum laser source as the broadband source.

In this chapter, we will assume that the reader is familiar with Fourier transform spectrometers and the principles behind these instruments. A detailed description of their working principle can be found, amongst others, in Ref. [2, 29, 30] and in Appendix A that reminds several sections from Ref. [31]. To facilitate the discussion, some of these concepts are briefly reintroduced in section 2.2.

Section 2.3 describes the hardware of the instrument in its current form. Section 2.4 concerns the data processing pipeline which is at the heart of the instrument. Section 2.5 describes the performances of our instrument in terms of its instrumental lineshape function, its wavenumber accuracy and sensitivity. Furthermore, the instrument is benchmarked against the setup of O'Leary *et al.* [16]. Indeed these authors performed FT-IBBCEAS while having many features in common but they rely on a commercial Bruker FTS.

Fourier transform spectrometers rely on the use of a Michelson interferometer to measure the light spectrum. When injecting a monochromatic light source in this kind of interferometer, light undergoes constructive or destructive interference depending on the relative distance traveled by the beam in the two arms of the interferometer, resulting in a sine interference pattern at its output with respect to the OPD. Since the light source employed for spectroscopy covers a large spectral range, its spectral components will undergo constructive or destructive interference for different OPDs. Intensity $I(\delta)$ at the detector for a given OPD δ is the sum of the interference patterns of all the spectral components, that is:

$$I(\delta) = \int_0^{+\infty} B(\tilde{\nu}) \cos(2\pi\tilde{\nu}\delta)\, \mathrm{d}\tilde{\nu}, \tag{2.1}$$

where $\tilde{\nu}$ is the wavenumber and $B(\tilde{\nu})$ is the spectral irradiance which is the quantity of interest. $I(\delta)$ is the measured quantity and it is named interferogram. The spectral irradiance is obtained by taking its cosine transform:

$$B(\tilde{\nu}) = \int_0^{+\infty} I(\delta) \cos(2\pi\tilde{\nu}\delta)\, \mathrm{d}\delta. \tag{2.2}$$

In this expression, only the positive OPDs are considered. The interferogram is said to be single-sided. Theoretically, the interferogram is an even function of the OPD, *i.e.* $I(\delta) = I(-\delta)$, and taking double-sided interferograms, that is interferograms measured on a symmetrical range of retardation around the zero path difference (ZPD), *i.e.* $\delta = 0$, is unnecessary. However, the measurement of single-sided interferograms makes the instrument sensitive to phase errors, as detailed in section 2.4. Information about the phase is retrieved by replacing the cosine transform by a Fourier transform in equation (2.2), leading to:

$$B(\tilde{\nu}) = \frac{1}{2} \int_{-\infty}^{+\infty} I(\delta) \mathrm{e}^{2\pi \mathrm{j}\tilde{\nu}\delta} \mathrm{d}\delta. \tag{2.3}$$

with j the imaginary number. This equation means that the irradiance spectrum can be retrieved from the knowledge of the double-sided interferogram using a Fourier transform, the two conjugate variables being the OPD (in cm) and the wavenumbers (in cm^{-1}). The Fourier transform is evaluated using the fast Fourier transform (FFT) algorithm, implying to know the interferogram on a uniform OPD grid. This uniform OPD grid is determined using the interference pattern of a

frequency-stabilized laser as the spatial reference, the zero of the grid being the ZPD.

A complete derivation of equation (2.3), starting from the expression of the electric field of a monochromatic wave at the input of a Michelson interferometer can be found in Appendix A.1.

2.3 DESIGN OF THE INTERFEROMETER

A schematic of the optical bench in its current configuration is presented in Figure 2.1. The layout with both retroreflectors placed back-to-back on the moving carriage is adapted from Ref. [26, 27, 32, 33]. Such a layout presents the advantages of compactness and of a higher opto-mechanical gain, *i.e.* the OPD induced by the carriage displacement is multiplied by four with respect to the distance traveled by the carriage instead of two as in most FTS. Also, the ZPD is located at the centre of the translation stage, allowing the measurement of double-sided interferograms. The translation stage is 1.5 meters long (limited to 1.35 meters for practical purpose), leading to an ultimate spectral resolution of 0.002 cm^{-1} for the FTS. All the optics, except the high-reflectivity mirrors of the optical cavity and the beamsplitter, are standard optics from the Thorlabs catalog. The beamsplitter is the only optical element especially designed for the application and consists in a VIS/Q IT501/2 beamsplitter of Bruker. This component is indeed particular. It contains a beamsplitter and a compensator. The compensator ensures that light encounters the same optical path in the beamsplitter's material for both arms of the interferometer [34]. For the moment, the instrument is exposed to ambient air, restricting the spectral range of the instrument to regions where neither water, oxygen nor carbon dioxide present strong absorption. This represents one of the limitations of the current design.

2.3.1 *Frequency-stabilized He:Ne reference laser*

The purpose of the reference laser in the FTS is twofold: it serves as a spatial reference for the resampling of the broadband source and it is utilized for the proper alignment of the instrument. The use of a laser as a spatial reference implies that its wavelength should remain constant during the whole measurement session.

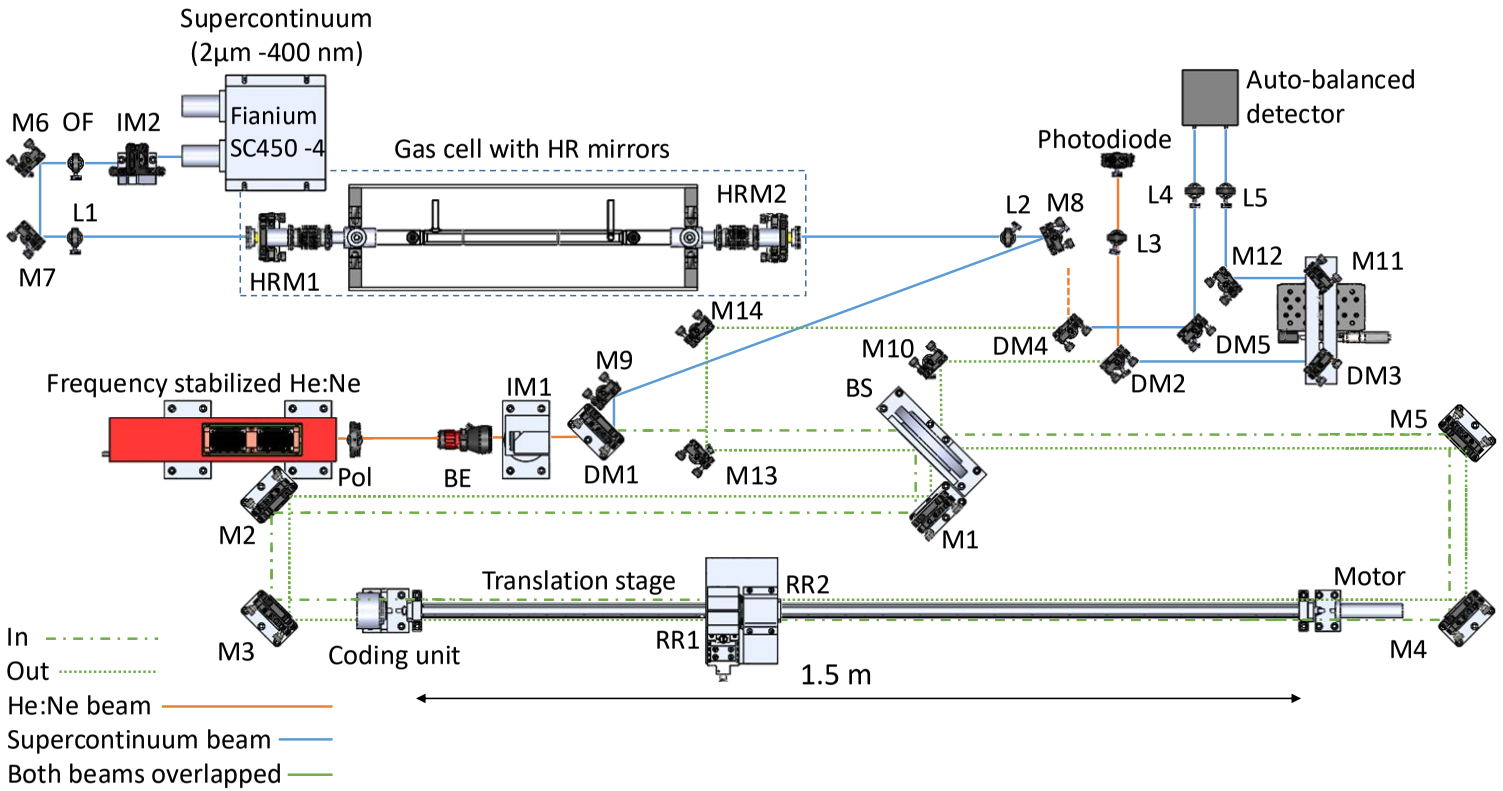


Figure 2.1: Layout of the Fourier transform spectrometer with the illustration of the path of the different light beams. BE: beam expander, DM: dichroic mirror, HRM: high reflectivity mirror, IM: injection mirror, L: lens, M: mirror, OF: optical filter, RR: retroreflector. Mirrors M1, M2, M3, M4 and M5 are 2-inches silver mirrors (Ref. PF20-03-P01 from Thorlabs). The other mirrors are 1-inch silver mirrors (Ref. PF10-03-P01 from Thorlabs). The retroreflectors are 2-inches corner cubes that rely on total internal reflection (Ref. PS976M from Thorlabs). The 2-inches dichroic mirror DM1 (Ref. DMLP650L from Thorlabs) and the 1-inch dichroic mirrors DM3 and DM5 (Ref. DMLP650 from Thorlabs) are transparent for wavelengths smaller than 650 nm and reflective for wavelengths from 650 nm to 1600 nm. The 1-inch dichroic mirrors DM2 and DM4 (Ref. DMSP650 from Thorlabs) are reflective for wavelengths smaller than 650 nm and transparent for wavelengths from 650 nm to 1600 nm.

The reference laser is an unpolarized He:Ne laser (model GLG5002 of NEC, manufactured in 1981). It was frequency-stabilized in-house by stabilizing its cavity length. The error signal is obtained by measuring the difference in intensity of the two orthogonally polarized modes that can be sustained in the gain curve of the laser. We impose this difference to be equal to zero. These two modes are spatially separated by means of a polarizing beamsplitter and their intensity measured with two photodiodes. This approach is described, amongst others, in Ref. [35, 36]. The cavity length is then adjusted by heating up or cooling down a piece of copper surrounding the discharge tube using thermoelectric coolers. This approach was also chosen by Shirvani *et al.* [37]. The controller used to fulfil the task is the PID controller Max 1978 from Maxim. More details concerning the implementation of the stabilization scheme are given in Appendix A.4. Frequency stability of the laser was determined by injecting two identical stabilized He:Ne lasers in a temperature-stabilized Fabry-Perot interferometer, with a free spectral range (FSR) of 1GHz (FPI100 of Toptica) and by monitoring the fluctuations in relative positions x and y of the two He:Ne lasers during the length sweep of the Fabry-Perot interferometer, as shown in Figure 2.2 using the following formula:

$$\Delta\nu = \frac{y - x}{z} * 1 \text{ GHz} \tag{2.4}$$

where $\Delta\nu$ is the frequency difference between the two lasers. Conversion in units of frequency relies on the knowledge of the FSR of the Fabry-Perot interferometer. Variations of $\Delta\nu$ with respect to time indicate a frequency drift of one laser with respect to the other. Fluctuations inferior to 3 MHz over a 45-minute period of time were observed with this method, meaning that the wavelength varied by less than 4 fm during this period. Similar results were obtained by observing the beating of the two frequency-stabilized He:Ne lasers.

In order to use the He:Ne laser as a reference for the retrieval of the constant OPD grid, it is also important to have a constant contrast over the complete travel of the translation stage. Requirements on (1) the polarization of the He:Ne laser, (2) its divergence and (3) its frequency stability should be fulfilled to ensure the constant contrast. For (1), a linear polarizer is directly placed at the output of the He:Ne laser to suppress one of the two orthogonal modes emitted by the laser. Otherwise, a beating pattern modulates the envelope of the He:Ne interference pattern. For (2), a beam expander is employed to enlarge

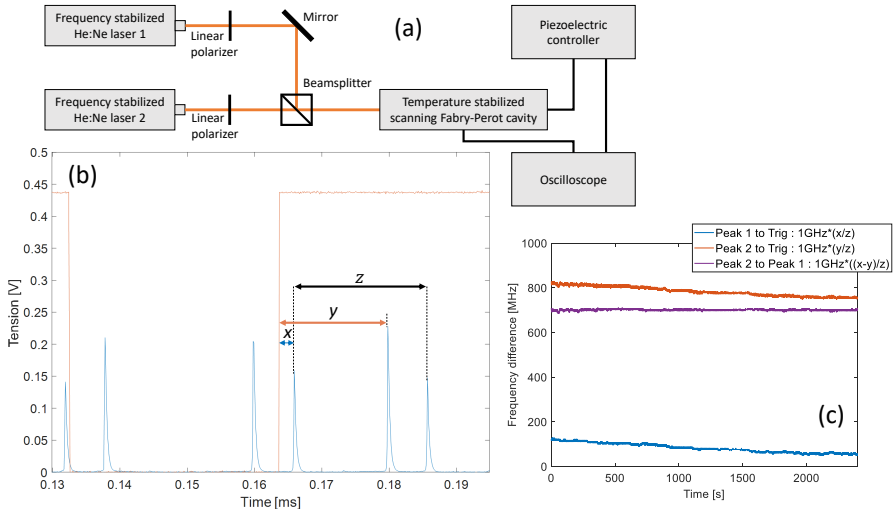


Figure 2.2: (a) Experimental setup for the characterization of the frequency stability of the He:Ne reference laser. Two stabilized He:Ne lasers are injected in a temperature-stabilized Fabry-Perot cavity (FSR = 1 GHz). The cavity length is swept over more than a FSR by means of a piezoelectric actuator. (b) Zoom on a small portion of the data recorded with the oscilloscope. The relative positions x and y are measured with respect to the trigger signal associated with a specific position of the piezo ceramic sweep. (c) Plots of $x/z * 1\text{GHz}$ in blue, $y/z * 1\text{GHz}$ in red and $(x-y)/z * 1\text{GHz}$ in yellow. RMS fluctuations of 3 MHz are observed on the purple curve on the 2500-second measurement time.

the spot size in order to reduce the beam divergence and to ensure a constant spot size at the output of the interferometer. The beam expander is tuned by imposing the spots issuing from the two arms of the interferometer to have the same diameter when the carriage is in the vicinity of the optical contact. Finally, for (3), the reference laser should have a coherence length longer than the maximum OPD that can be induced by the translation stage. In our case, considering fluctuations in frequency of 3 MHz for the laser light source, we have a coherence length of about 100 meters, more than 30 times the maximum OPD.

As already mentioned, the He:Ne laser is also employed for alignment purposes. A correct alignment of the instrument is mandatory to obtain good quality spectra at high resolution in a modest amount of time. Indeed, the beams coming from the two arms of the interferometer should perfectly overlap at the detector for any position of the translation stage described in a following section. The He:Ne laser beam is first injected parallel to the translation stage by imposing it to pass through two iris diaphragms located between the beamsplitter BS and mirror M5. Two other diaphragms located between mirrors M1 and M2 allow for the alignment of the beamsplitter BS and mirror M1. The four mirrors M2, M3, M4 and M5 are aligned thanks to a circular aperture placed instead of the two retroreflectors on the carriage. Two mirrors, one on each side of the translation stage, are aligned when the carriage is at one extreme position, near the coding unit, while the two others are aligned when the carriage is at the other extreme position, near the DC motor. Alignment is considered to be fine when light is retro-injected into the laser. This can be checked by looking at the error signal of the He:Ne laser which becomes erratic when it is the case. The retroreflectors are then placed on the carriage and the He:Ne laser beam is horizontally shifted using the injection optics IM1 in order to pass through two apertures placed between the BS and mirror M5. One of the retroreflectors is translated with respect to the other to maximize the contrast of the He:Ne interference pattern that is observed at the output of the interferometer. After proper alignment, the fringe visibility smoothly varies between 0.85 and 0.91 on the complete course of the carriage, with a mean value of 0.88. This represents a maximum decrease of 7 % relative to the maximum fringe visibility.

Once the FTS is aligned for the reference laser, injection of the broadband light source in the instrument is straightforward. Its beam is overlapped to the He:Ne laser beam using the dichroic mirror DM1. It

has to pass through the same two iris diaphragms located between the beamsplitter BS and mirror M5. The two beams are separated at the output using dichroic mirrors as well.

2.3.2 *Translation stage*

The OPD necessary to generate the interferograms is induced by a carriage moving along a 1.5 m translation stage. The carriage moves thanks to a screw shaft coupled to a DC motor and it is guided by a dovetail slide. A coding unit allows to measure the carriage velocity and a feedback loop ensures that the carriage velocity remains near its setpoint. Two stop sensors are symmetrically placed on both sides of the optical contact position. The distance separating the optical contact position from the stop sensors determines the resolution of the measurement. A Labview routine forces the carriage to travel back-and-forth between the two sensors. For each trip, acquisition at constant time intervals is triggered 1 second after the carriage starts moving. When designing the carriage, it is crucial to include alignment degrees of freedom on one of the two retroreflectors in order to maximize the overlap of the two beams at the output of the interferometer. In our case, two translation stages with micrometer screws were employed, as shown in Figure 2.3.

We currently limit the carriage velocity to 0.6 cm/s because of some mechanical concerns. At higher velocities, the screw shaft starts vibrating with a relatively high amplitude. There are several flaws on the current mechanical design: the screw diameter (1 cm) is too small for its length (150 cm) leading to bending of the shaft under its own weight, ultimately resulting in a poor mechanical loading of the drive nut placed on the carriage. Also, the screw shaft thread of 2 mm is too small for a continuous scan interferometer because it imposes a significant rotating speed before the carriage reaches a decent linear speed. Finally, the DC motor is directly coupled to the screw shaft so that the motor does not work at its nominal speed and the small fluctuations in its angular speed are directly transmitted to the shaft. However, even with these shortcomings, we show in section 2.4.2 that it has limited impact on the resampling process of the interferogram and in section 2.5.1 that there are minor consequences on the instrumental lineshape function (ILS). Obviously, upgrading the translation stage will improve the signal-to-noise ratio of each scan but it will also

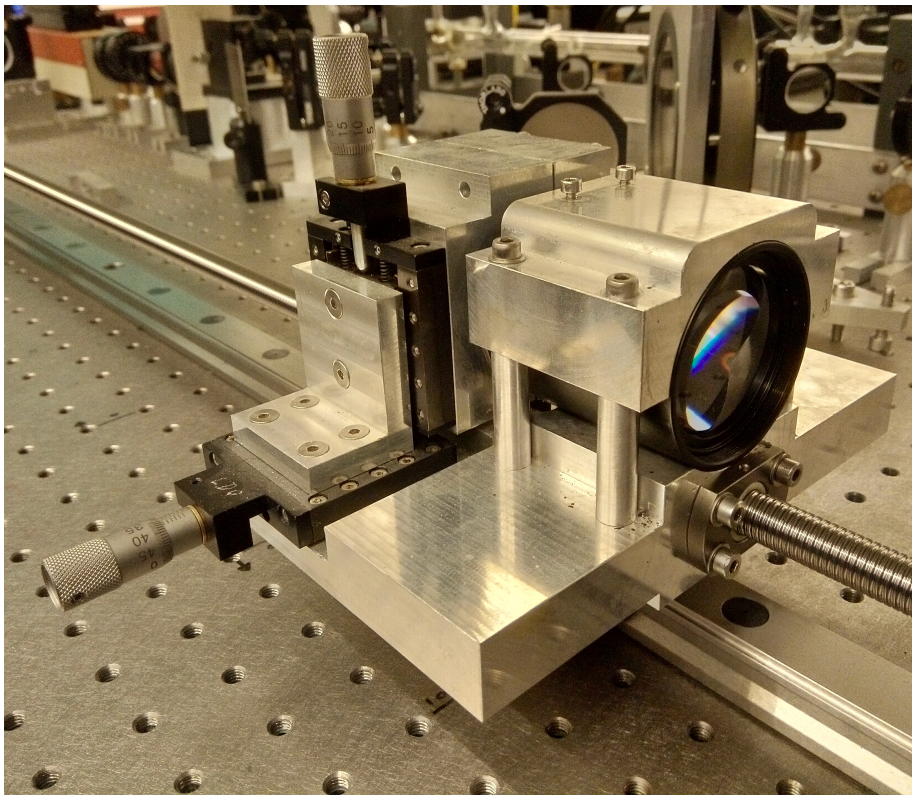


Figure 2.3: Carriage with the two retroreflectors placed back-to-back. One of the retroreflectors is mounted on two translation stages with micrometers screws to maximize the overlap of the two beams at the outputs of the interferometer.

considerably decrease the time needed to acquire them since higher carriage velocities will be possible.

Finally, when adjusting the carriage velocity, one has to be careful regarding the bandwidth of the detectors employed in the instrument. Indeed the temporal frequency content of the broadband light source interferogram and that of the He:Ne interference pattern depend on the carriage speed, imposing an upper limit independent of that imposed by faulty mechanics.

2.3.3 *Auto-balanced detection scheme*

Since retroreflectors are used instead of mirrors, it is possible to measure both outputs of the interferometer simultaneously and hence to

measure the interferograms in an auto-balanced scheme. Auto-balanced detection allows to double the measured signal since the interference patterns of the two outputs are out of phase by 180 degrees (see Ref. [38] and Appendix A.1.2 for more details), while removing fluctuations in intensity of the broadband source which are common to the two outputs. These fluctuations in intensity can be induced either by frequency-to-amplitude noise when coupling a frequency comb to an optical cavity [26, 27] or by the use of the supercontinuum as the broadband light source. Figure 2.4 compares the signal-to-noise ratio (SNR) of a spectrum measured with a single detector with the same spectrum measured with an auto-balanced detector. The spectrum presented in this figure was obtained by placing a 10 nm wide bandpass filter centred at 1.4 μm in the path of the SC beam. Absorption transitions are due to water present in ambient air. Four interferograms were coadded in both cases. The SNR was defined as the ratio of the height parameter of the gaussian fit of a randomly chosen water absorption transition (frame 1 in Figure 2.4) against the root-mean squared (rms) noise of frame 2 of Figure 2.4. The SNR was 2.6 times better in the case of the auto-balanced detection scheme.

The auto-balanced detector was inspired from the circuitry presented in Ref. [39] and fabricated in-house. The detector photocurrents are subtracted, and the difference of the DC currents is kept to zero by means of a feedback loop, leading to an adjustment of the gain. The signal common to both channels is suppressed when taking the difference between the two channels while the interferometric signals which are out of phase by 180 degrees are reinforced [26, 38].

Two dichroic mirrors are placed at each output arm of the interferometer. The dichroic mirror DM2 permits to separate the SC and the He:Ne beams in order to detect the He:Ne beam alone on a Si photodiode. Since there was still some light of the He:Ne laser reaching the right-hand-side photodiode of the auto-balanced detector, a second dichroic mirror DM3 was placed and simply serves as an optical filter. The two dichroic mirrors DM4 and DM5 in the second output arm guarantee that the two photodiodes of the auto-balanced photodetector observe a similar scene. A delay line ensures that the beams in the two output arms of the instrument travel the same distance before reaching the photodiodes.

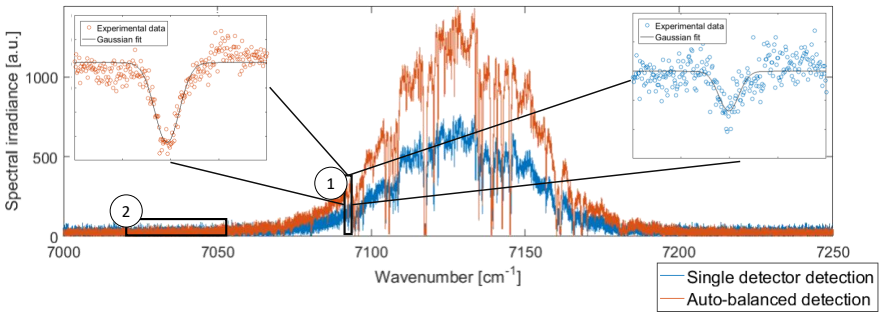


Figure 2.4: Comparison between a single-detector detection scheme and the auto-balanced detector scheme.

Optimization of the alignment and of the relative intensities on the two photodiodes is obtained by chopping the SC light source and by displaying the output of the detector on an oscilloscope. Alignment is optimized by maximizing the amplitude of the square-like pattern displayed on the oscilloscope for each photodiode while the second one is screened. Subtraction of the two signals gives a flat line on the oscilloscope at the exception of transient spikes at the times of rising and falling edges of the square-like patterns. In order to adjust the relative beam intensities reaching the two photodiodes to obtain this signal, a variable neutral density filter was placed in one of the two arms.

2.3.4 *Optical cavity*

The gaseous sample is placed in a glass cell on which high-reflectivity mirrors (HRM) can be mounted. The two HRMs are placed in optical mounts with o-rings to seal the cell. Annular piezo-actuators permit to displace the two mirrors over a distance of a few microns(PZT HPSt150/14-10/12 from Piezomechanik). Tightness of the cell is guaranteed by fixing the actuator to the other parts of the mount with low vapor pressure epoxy (Torr Seal). Figure 2.5 shows a picture of the optical mounts. This design presents the advantage of simplicity but it suffers from a poor bandwidth when used in a feedback loop. Indeed, the first mechanical resonance of these mounts at 130 Hz limits the frequency of the feedback loop when locking the cavity to either the frequency comb or another frequency-stabilized laser [40]. Currently, no length stabilization of the cell is implemented. Instead, a triangle

waveform at 100 Hz is applied on the mount to blur away the eventual frequency drift of the optical cavity due to fluctuations in its length. The two plano-concave HRM have a radius of curvature of 1 m and a reflectivity higher than 99.85% on the range of wavelengths extending from 630 nm to 1140 nm (Chirped mirrors 103521 from the Layertec catalog). They are placed 88 cm apart, on both sides of the cell tube containing the gas sample. In order to mechanically decouple the two mirrors from the cell and to allow for the alignment of the optical cell, the mirror mounts are connected to the cell via bellows. The mirror mounts are placed in Thorlabs Polaris holders which present the advantage of clamping the mirror mounts in the axial direction, leading to a better damping of the vibrations. Coupling of the SC inside the cavity was achieved by focusing the beam at the centre of the symmetrical optical cavity using a lens. Another lens was placed at the output of the cavity. Its focus coincided with the waist of the optical cavity in order to inject a well-collimated beam in the FTS. Two apertures on both sides of the cavity allow to overlap the supercontinuum laser with a He:Ne laser. Alignment is performed with the He:Ne laser and a CCD camera at the output of the cavity to observe the spatial distribution of the output modes in order to optimize the alignment on the TEM_{00} mode. The cavity is supposed to be aligned for the supercontinuum as well since the He:Ne and supercontinuum beams are overlapped. The display of the TEM_{00} on a screen is useful when placing the sample cell under vacuum. Indeed, the pumping down of the cell leads to a misalignment of the cell which can be compensated by performing a differential pumping with a needle valve while maintaining the mode displayed unchanged by continuously readjusting the mirror alignment. This method inspired a laboratory session for a master course in optics and laser physics. The laboratory protocol, along with the url link to a video where we observe the different transverse modes scrolling on the CCD camera as the cavity length is swept with the piezoelectric transducer, are given in Appendix F

2.4 DATA PROCESSING

A peculiar feature of FTS is that the observations are made in a conjugate space and that the measurements can only be interpreted after applying a mathematical operation: the Fourier transform. It means that the measured data need to be properly processed in order to retrieve the recognizable information, *i.e.* the irradiance spectrum. The

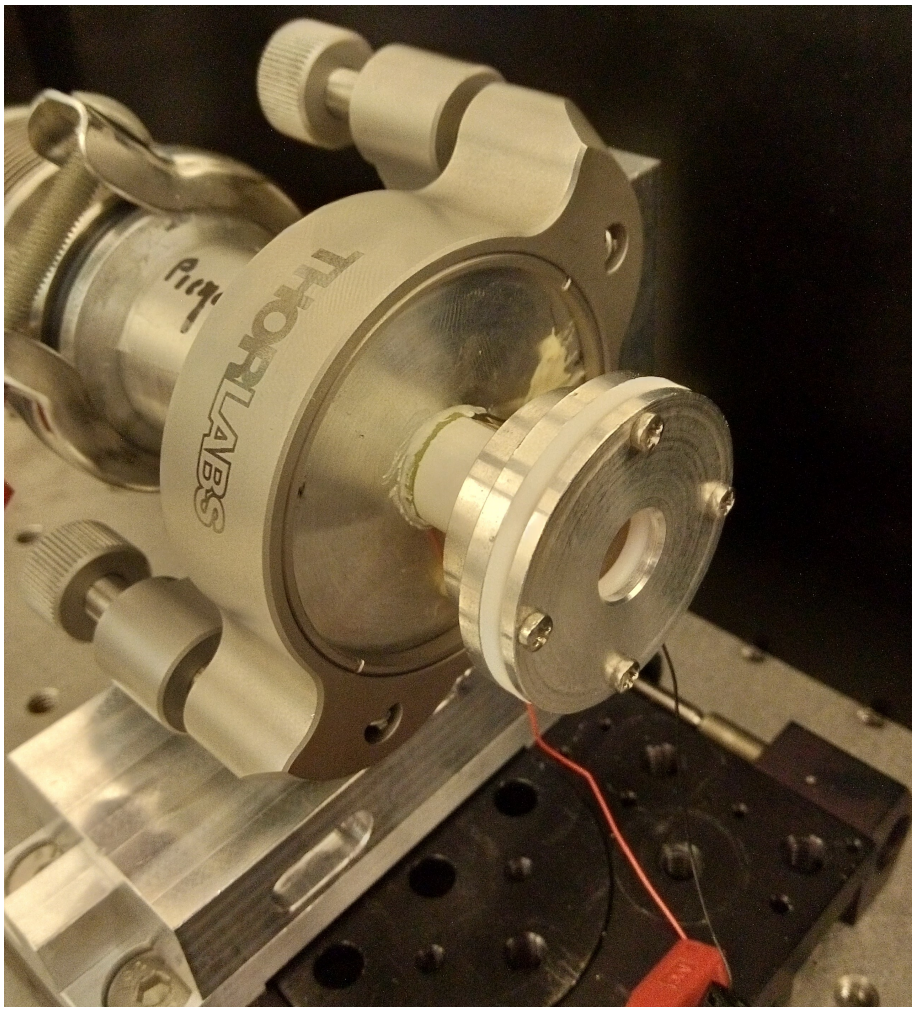


Figure 2.5: Piezo-actuated vacuum-tight optical mounts for the high-reflectivity mirrors of the optical cavity.

data processing implies a series of operations that have to be applied in a precise order. This is the topic of section 2.4.1. The conjugate variables in the Fourier transform of a FTS are the OPD and the wavenumbers. The sampling is performed at constant time intervals and since there are fluctuations in the carriage velocity, the interferogram needs to be resampled on a constant OPD grid. When processed at the software level, this is usually the bottleneck of the data processing pipeline because of the huge number of interpolations that have to be performed. We found an astute way to overcome this difficulty, allowing on-the-fly interferogram resampling. Section 2.4.2 details the resampling algorithm.

2.4.1 *Data processing pipeline*

The data processing pipeline of the FTS is presented in Figure 2.6. The order in which the different steps are performed relies on Ref. [41–43]. Data from both the He:Ne and the SC channels are simultaneously sampled at constant time intervals with a 24 bit Analog-to-digital converter (PXI-5922 ADC from National Instruments) and saved in two different binary files. Both data acquisition and carriage displacement are controlled within the same Labview program. About 4 points per period of the He:Ne interference pattern are recorded. The sampling frequency is therefore imposed by the carriage velocity. For example, when the carriage moves at 0.6 cm/s, the sampling frequency is equal to 150 kHz. The data processing pipeline was implemented in such a way that it does not depend on the sampling frequency, allowing for a great flexibility in the choice of the carriage velocity.

The first step of the data-processing pipeline consists in filtering the two channels with finite-impulse response (FIR) bandpass filters in order to remove both high-frequency and low-frequency components. A prior knowledge of the spectral range of the light sources allows to estimate the two cutoff frequencies. Moreover, if about 4 points per period of the He:Ne laser are effectively measured, the passband of the two signals does not change when they are expressed in terms of normalized frequency (*i.e.* frequency divided by the Nyquist frequency), meaning that the coefficients of the FIR filters do not have to be modified when changing the carriage velocity. Appendix A.5 gives further information concerning the design of FIR filters.

In order to retrieve the spectrum from the interferogram, a fast Fourier transform (FFT) is applied. It requires the knowledge of the inter-

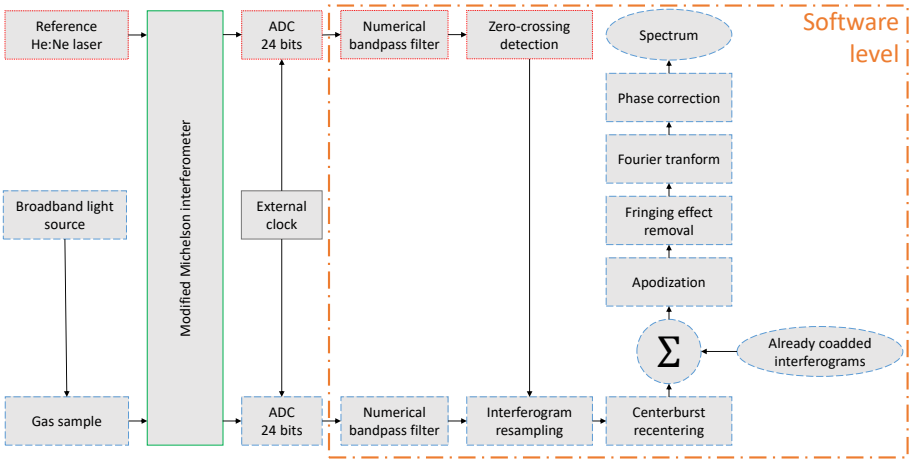


Figure 2.6: Data processing pipeline of the Fourier transform spectrometer. The blue dashed frames represent the interferogram channel, the red dotted frames are for the He:Ne reference channel and the green plain frame are common to both channels. The orange frame with an alternation of dashed lines and dots indicates the part of the process that is performed at the software level. Rectangular frames are stages in the data-processing pipeline. The oval frame labelled *Already coadded interferograms* is a vector containing all the previously recorded interferograms that were already treated up to the *centerburst recentering* stage included.

ferogram on a constant OPD grid since the conjugate variables in the Fourier transform are the OPD and the wavenumbers (cf. section 2.2). This constant OPD grid can be obtained by determining the exact times of the zero-crossings of the sine-like interference pattern of the He:Ne reference laser. The interferogram is then interpolated at these specific times. Description of the algorithms for zero-crossing determination and interferogram resampling are given in section 2.4.2.

The centerburst of the double-sided resampled interferogram is placed at the centre of the vector containing the samples. Interferograms are truncated on both extremities to ensure that all the datasets contain the same number of samples, permitting interferogram co-addition. In practice, we take the highest power of 2 for better performances of the FFT algorithm. The truncation on both extremities also ensures that no data is taken during starting/ending phases of the carriage translation. Since interferograms are measured for back-and-forth displacements of the carriage, one vector out of two is flipped right-to-left to ensure that every entry of the different vectors containing the interferograms always corresponds to a same OPD value.

Once all the interferograms are coadded, the resulting interferogram is apodized in order to reduce the ringing due to the instrumental lineshape function. The apodizing function employed is the one described by Naylor *et al.* [44]. The last step before applying the Fourier transform consists in removing the parasitic centerbursts due to multiple reflections in the optics (no wedged optics are employed), as depicted in Figure 2.7(a). If they are not removed, a fringing effect is present in the resulting spectrum, blurring away spectral lines (see Figure 2.7(c)). Setting these parasitic centerbursts to zero somehow corresponds to applying a notch filter in the constant OPD domain, leading to the suppression of the fringing effect on the spectrum while revealing spectroscopic information[2], as shown in Figure 2.7(f). Further details are given in Ref. [43]. As expected, the more the light source is coherent, the more the fringing effect is important. Indeed, much stronger parasitic centerbursts are observed when using the femtosecond laser (MIRA900 from Coherent), compared to the supercontinuum light source (SC450-4 from Fianium).

2 The removal of centerbursts suppresses small portion of the molecules signal in the OPD domain and might thus impact the transition lineshapes.

The last step of the data processing pipeline consists in applying the phase correction to the spectrum. The phase error is mainly caused by three factors: (1) there is no chance that the actual ZPD point is actually sampled, (2) there is some unbalanced dispersion in one arm of the interferometer, leading to non-symmetrical interferograms and finally (3) electronics employed for digitalizing the interferogram is frequency-dependent, ultimately resulting in frequency-dependent time delays [45]. This last point is also one of the main motivations to have a translation stage with a velocity as constant as possible. Information concerning the phase is obtained from the Fourier transform of a double-sided interferogram. However, most of the commercial FTS record single-sided interferograms. They usually measure a small portion of negative OPD and extrapolate the phase on the high-resolution interferogram in order to correct it. Commonly used phase-correction algorithms are described in Ref. [46, 47]. The measurement of single-sided interferograms presents the advantage of reducing by almost a factor two the translation stage length and the amount of data recorded for a single dataset, but this is done at the expense of an assumption on the phase. In our instrument, the interferograms that are recorded are double-sided, allowing a straightforward correction of the phase without any assumption on it. The extra number of data per dataset contains redundant information, increasing the SNR by $\sqrt{2}$ while doubling the measurement time[29]. From that perspective, it is thus a free operation because it reduces by a factor 2 the number of single-sided interferograms we would have coadded to obtain the same SNR.

2.4.2 *Constant OPD grid generation*

Both the reference and the SC signals are sampled at the same times, meaning that to a given index in the two vectors corresponds an identical sampling time. In order to evaluate the interferogram on a constant OPD grid, the precise times, or equivalently the fractional indices, of the zero-crossings of the He:Ne interference pattern must be determined. Indeed, they are half a wavelength apart. The interferogram is then resampled at these times. Choice was made to use fractional indices instead of time in order to make the data-processing pipeline independent of the sampling frequency and the carriage velocity. The only condition to fulfil is to record about 4 samples per period of the He:Ne interference pattern. The method suggested by Yang *et al.* [41] to retrieve the uniform OPD grid from the data sampled at constant

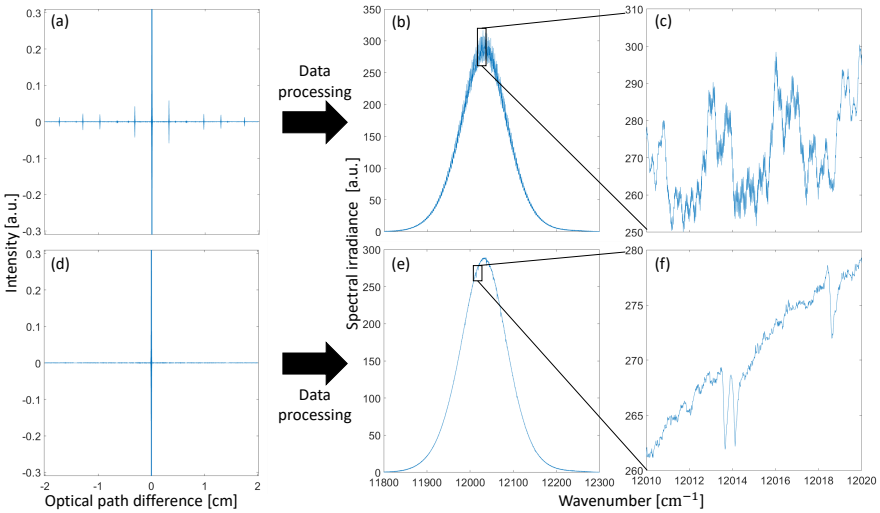


Figure 2.7: Fringing effect from both the interferogram (a) and spectrum perspectives (b). Removal of the parasitic centerbursts in the OPD domain (d) strongly attenuates the modulations in the frequency domain (e). Water absorption lines that could not be distinguished in (c) are now clearly visible in (f). The spectra correspond to the FFT of 12 coadded interferograms taken with the MIRA900 femtosecond laser emitting between 815 and 845 nm and traveling approximately 10 m in free air. Figures (a) and (d) are a zoom of the complete interferogram (about 32 cm of OPD) in the vicinity of the centerburst. The spectrum was taken at a resolution of 0.015 cm^{-1}.

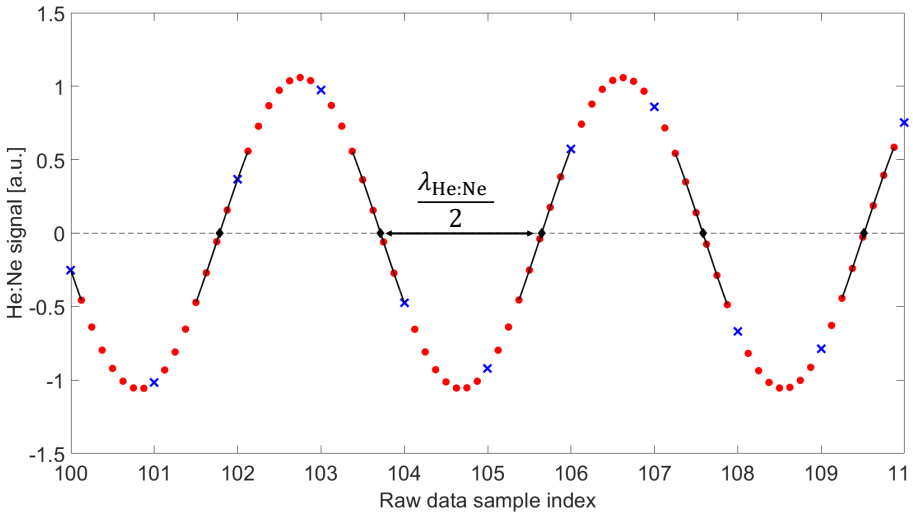


Figure 2.8: Estimation of the zero-crossings of the He:Ne interference pattern. Blue cross: experimental data, red dots: interpolated data (zero-padding), black curves: cubic approximation, black diamond: estimated zero-crossings.

time intervals consists in interpolating between the data to determine the zero-crossings fractional indices. To do so, the He:Ne signal is first zero-padded to increase the sampling grid by a factor 8. Location of the zero-crossings is then roughly estimated by finding changes in sign between adjacent samples of this denser grid. The 3 samples before and the 3 samples after the zero-crossings are approximated by a cubic function and the root of this cubic function located in the vicinity of the two middle samples is evaluated. The root is the fractional index at which the interferogram should be interpolated. This is illustrated in Figure 2.8. When spectra are recorded at full resolution of the FTS, more than 17 million interpolations should be performed, meaning that more than 17 million systems of equations have to be solved, which is computationally expensive. Fortunately, it is possible to take advantage of the fact that the abscissa are evenly spaced since they correspond to successive indices.

Finding the polynomial that best approximates the set of data involves solving the following system of linear equations:

$$\begin{bmatrix} (k-2)^3 & (k-2)^2 & (k-2) & 1 \\ (k-1)^3 & (k-1)^2 & (k-1) & 1 \\ k^3 & k^2 & k & 1 \\ (k+1)^3 & (k+1)^2 & (k+1) & 1 \\ (k+2)^3 & (k+2)^2 & (k+2) & 1 \\ (k+3)^3 & (k+3)^2 & (k+3) & 1 \end{bmatrix} \begin{bmatrix} p_1 \\ p_2 \\ p_3 \\ p_4 \end{bmatrix} = \begin{bmatrix} y_{k-2} \\ y_{k-1} \\ y_k \\ y_{k+1} \\ y_{k+2} \\ y_{k+3} \end{bmatrix}. \tag{2.5}$$

where $k-2$, $k-1$ and k are the indices of the samples y_{k-2}, y_{k-1} and y_k just before the zero-crossing, $k+1$, $k+2$ and $k+3$ are the indices of the samples y_{k+1}, y_{k+2} and y_{k+3} just after it and p_1, p_2, p_3 and p_4 are the coefficients of the third degree polynomial $y = p_1x^3 + p_2x^2 + p_3x + p_4$ that best fits the 6 samples. The first matrix in this problem is the so-called Vandermonde matrix. Finding the four coefficients of the polynomial implies to find the the pseudo-inverse of the Vandermonde matrix for each of the millions of zero-crossings that need to be found, which is time-consuming. Fortunately, in our case, this matrix has a similar form for all the polynomials that have to be evaluated, at the exception of the value of k. The problem can be shifted around zero by setting $k = 0$. A single pseudo-inverse has to be found for all the zero-crossings, reducing considerably the execution time. The value of the determined zero-crossing is then simply shifted back by k after having being determined around zero. Finding the p coefficients now simply requires evaluating 4 products. The root corresponding to the index of the zero-crossing is then found using the Newton-Raphson method. The 17 millions zero-crossings are evaluated in less than the time needed for the carriage to travel its full travel with Matlab on a typical laptop (Intel i5-644HQ CPU working at 2.6 GHz), allowing on-the-fly data processing. A more detailed description of the algorithm can be found in Appendix A.6.

Once the fractional indices i of the zero-crossings are determined, the interferogram needs to be ressampled at these specific times. This has to be done numerically. At first, an approach using simple cubic interpolations was chosen but it led to poor results. Thanks to the prior use of the two FIR filters (see Figure 2.4.1), the problem is properly band-limited. Moreover, samples are evenly spaced in the time domain. A better approach thus consists in using sinc interpolation. It can be

shown (see section A.7) that the exact value of a signal $y(t)$ at any time t can be estimated from the knowledge of this signal sampled at uniform time intervals using the following relationship:

$$y(t) = \sum_{n=-\infty}^{+\infty} y[n] * \text{sinc}\left(\frac{\omega_s(t - nT_s)}{2\pi}\right), \tag{2.6}$$

where $y[n]$ is the signal sampled at time n, ω_s the sampling frequency and $T_s = \frac{2\pi}{\omega_s}$ the sampling time. For convenience, equation (2.6) is re-expressed in terms of the fractional index i rather than the time t.

$$y(i) = \sum_{n=-\infty}^{+\infty} y[n] * \text{sinc}\,(i - n)\,. \tag{2.7}$$

Theoretically, finding the exact value at the zero crossing, $y(i)$, implies to use an infinite sum. In practice, the sinc function rapidly tends to zero, allowing for the use of a finite summation. Evaluating the sinc function for each term of the sum of equation (2.6) and for a large number of values (up to 17 million times for interferograms at full resolution) is too time demanding. In order to tackle this challenge, the interval between two measured points is discretized m times. Brault [48] introduced the idea to store vectors equidistant in times including one of the m interpolating points and gathering $n/2$ values of the sinc function on each side of the considered point. Those vectors are rows stored in a matrix named kernel resulting in an array of $m \times n$ values (see equation (2.9)). Those values are evaluated only once for the millions of points which need to be interpolated. Estimating the interferogram at a specific fractional index i now consists in choosing the index l (with $1 \leq l \leq m$) which is the closest to $(i - k)/m$, in this array and to perform an element-by-element product with the $n/2$ values before the zero-crossing fractional index and the $n/2$ values after it and to add together the n obtained values. The construction of this $m \times n$ matrix follows the principle illustrated in Figure 2.9 for $m = 6$ and $n = 12$. In this illustration, the upper curve is a sinc function evaluated at $6 \times 12 = 72$ discrete and equidistant values. These 72 values are parsed in 6 row vectors of 12 equidistant (in time) values that built up the kernel. The first row vector contains the 1^{st}, 7^{th}, 13^{th}, etc. values of the upper sinc function, the second row vector contains the 2^{nd}, 8^{th}, 14^{th}, etc. values, and so forth for the four remaining rows.

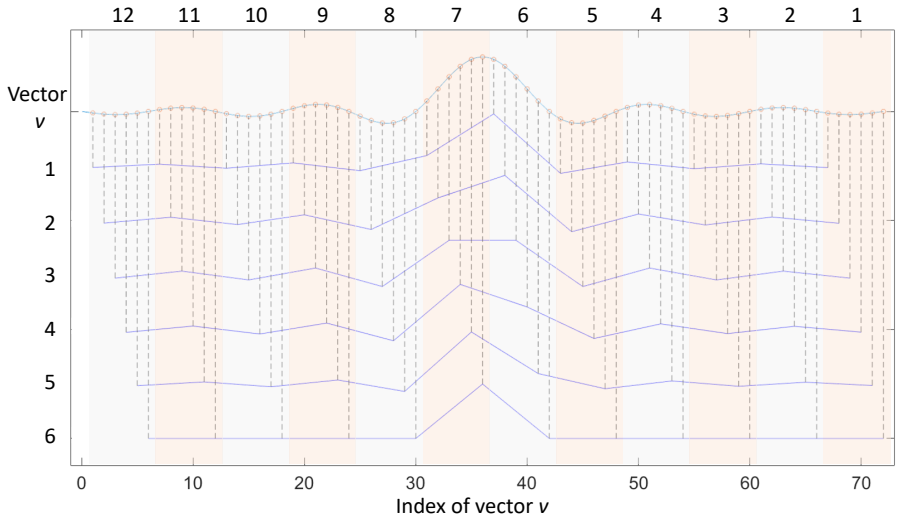


Figure 2.9: Illustration of the filling process of the matrix of equation (2.9) for $m = 6$ and $n = 12$. The sinc function is evaluated in 72 values which are then parsed in 6 rows of length 12.

The choice of the appropriate filter, *i.e.* the row l of the kernel, is made by evaluating the following expression:

$$l = 1 + \text{floor}(m * (i - k)), \tag{2.8}$$

where k is the index of the previous sample and i the fractional index at which we want to interpolate the signal. The term $+1$ comes from the fact that the first index of an array is 1 in Matlab. The function floor is a rounding function towards the lower integer.

$$\text{kernel} = \begin{bmatrix} v(m(n-1)+1) & \dots & \dots & v(m+1) & v(1) \\ \vdots & \vdots & \vdots & \vdots & v(2) \\ \vdots & \vdots & \vdots & \vdots & v(3) \\ \vdots & \vdots & \vdots & \vdots & \vdots \\ \vdots & \vdots & \vdots & \vdots & v(m-1) \\ v(mn) & v(m(n-1)) & \dots & v(2m) & v(m) \end{bmatrix}. \tag{2.9}$$

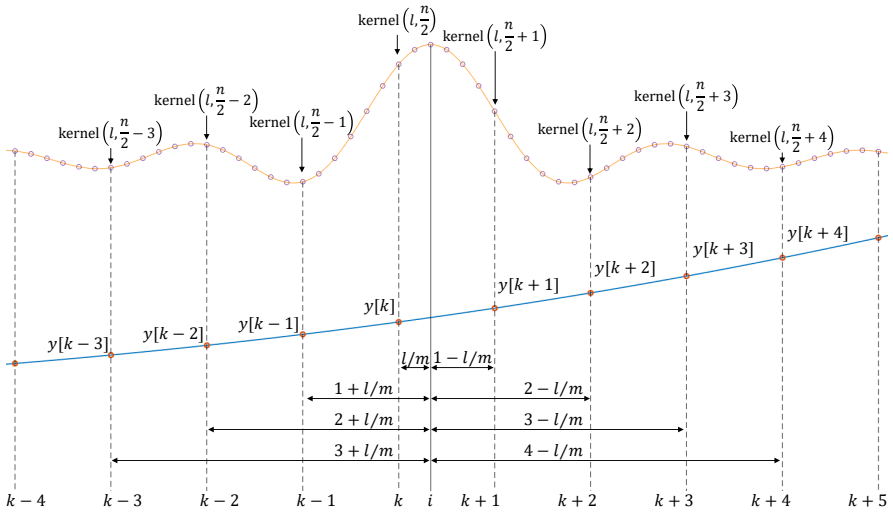


Figure 2.10: Brault resampling method. The blue curve corresponds to the signal, the red dots are the sampled values of the signal and the orange curve corresponds to the sinc function used to build the resampling kernel. The purple dots are the discrete values of the resampling kernel stored in the matrix of equation (2.9). Distance between the k^{th} sample and the fractionnal index i at which the signal is resampled is l/m.

The last step of the interpolation process is the evaluation of the following sum:

$$y(i) = y(k + \frac{l}{m}) = \sum_{j=1}^{n} y\left[k - \frac{n}{2} + j\right] * \text{kernel}(l, j). \tag{2.10}$$

This is illustrated in Figure 2.10. This figure depicts on the top the 72 points sinc function and the associated l^{th} row of the kernel is outlined using dashed lines. In practice, in our data processing pipeline, the values $n = 64$ and $m = 1024$ were chosen. They were determined by performing convergence studies on simulated interferograms. Moreover, in order to reduce eventual artefacts due to the finite number of terms in the summation of expression (2.6), the sinc function is multiplied by a Gaussian function, as suggested by Yang *et al.* [41].

Because of the fluctuations in the carriage velocity, the samples evenly spaced in the time domain are not evenly spaced in the OPD domain. But the values of the sampled interferogram only have a true meaning in the OPD domain. Brault suggested to adapt the digital filter to the instantaneous velocity of the carriage in order to correct the velocity

fluctuations. The method is better described in the article of Yang *et al.* [41]. We tried to implement this velocity correction and even if it generally gave better results on the resampling process, it ironically failed when velocity fluctuations were too severe. This velocity correction is therefore not used in the data analysis.

In order to verify the correct behavior of the whole interferogram resampling process and to study the consequences of the velocity fluctuations on the resampling, the He:Ne interference pattern was resampled at the times of its zero-crossings. If there was no error, the values obtained would be exactly equal to zero. Any deviation Δy from zero is therefore imputed to an error Δx on the position of the zero-crossing. To express Δx in terms of distance, a Taylor expansion of a sine wave around zero is performed as follows:

$$\Delta y = A \sin(\frac{2\pi}{\lambda}\Delta x) \approx A\frac{2\pi}{\lambda}\Delta x - \frac{A}{6}\left(\frac{2\pi}{\lambda}\Delta x\right)^3 + ... \tag{2.11}$$

Where λ is the wavelength of the He:Ne reference laser and A the amplitude of the interference fringes. Keeping only the first order term and isolating Δx leads to:

$$\Delta x = \frac{\lambda \Delta y}{2\pi A}. \tag{2.12}$$

A small trace of the resampling error with respect to the position, evaluated using equation (2.12), is shown on the bottom plot of Figure 2.11 while the two upper plots correspond to the velocity fluctuations and the fringe visibility with respect to the position. The instantaneous velocity was evaluated by using the knowledge of the times of the zero-crossings that are spatially equidistant of half a wavelength of the He:Ne laser. Both the fringe visibility and the instantaneous velocity seem to vary with a periodic pattern. This will be confirmed by a spectral analysis by means of their Fourier transforms in section 2.5.1. We can also observe that the error on the zero-crossing location tends to increase when the velocity fluctuations are large meaning that the mechanics actually impacts the resampling process. However, no structured pattern was observed on the Fourier transform of the resampling error with respect to the position. This is fortunate since a periodic error in the interval at which the interferogram is resampled would lead to the presence of a ghost line at a wavenumber $\sigma_g = \sigma_N - \sigma_l$, where σ_N is the Nyquist wavenumber and σ_l the wavenumber of the

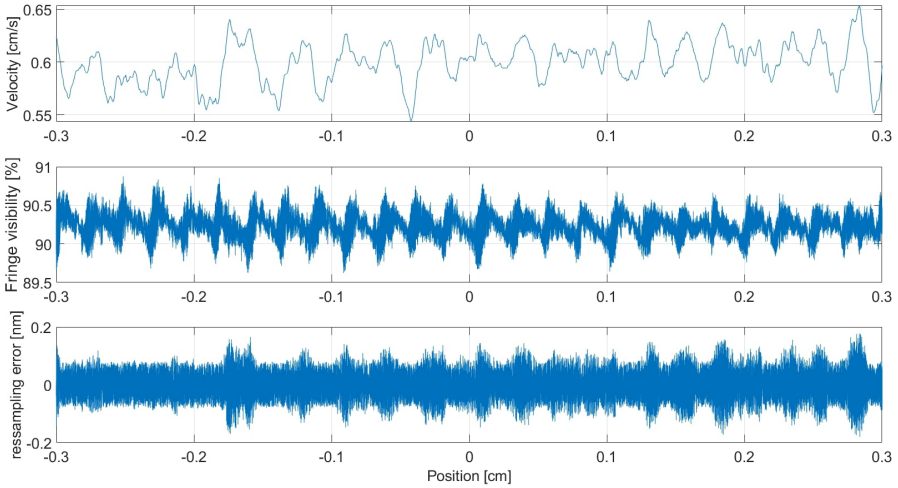


Figure 2.11: Velocity fluctuations and their consequences on the fringe visibility and the resampling in the spatial domain.

parent line [49]. Finally, even with the large fluctuations in the carriage velocity (*i.e.* about 10%), the zero-crossings locations are known with a precision better than 0.17 nm (3σ criterion), meaning that we are able to generate an OPD grid of 5.4 m long with ticks spaced by 316.4 nm with a precision better than 0.17 nm.

2.5 PERFORMANCES

We first characterize the instrumental lineshape function (ILS) of the instrument in section 2.5.1. It was experimentally measured by means of an external cavity diode laser (ECDL) at 778.2 nm. Consequences of velocity fluctuations on the ILS are underlined in the same section.

The characterizations of both the wavenumber axis accuracy and the sensitivity of the setup were performed on water desorbing from the cell walls. The wavenumbers associated with the transitions and their corresponding line intensities were retrieved from the 2008 Hitran database [50]. The spectrum is shown in Figure 2.12. It was measured at a resolution of 0.015 cm^{-1}. To obtain the spectrum, 1084 interferograms were coadded and the parasitic centerbursts were removed. The oscillations in the baseline are due to fluctuations in the reflectivity of the HRMs of the 88 cm long cavity. The strong cutoff at 14300 cm^{-1} is due to the use of an edgepass filter while the gentle cutoff at 10500 cm^{-1} is

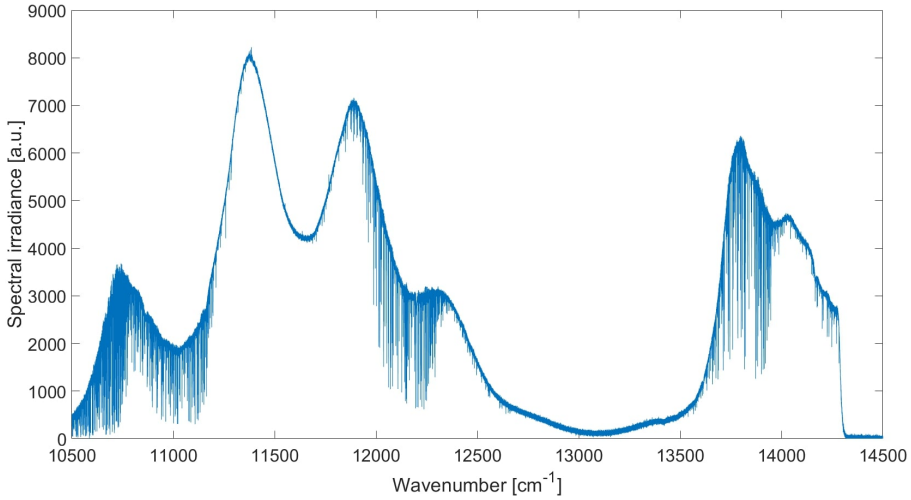


Figure 2.12: Cavity-enhanced spectrum of H_2O desorbing from a 88 cm long cell at a resolution of 0.015 cm^{-1}. The pressure varied between 2 and 4 Torr during the measurement. 1084 coadded interferograms.

caused by the filter splitter of the Fianium supercontinuum. The cell was pumped down with a rough-vacuum pump.

The wavenumber-axis accuracy, presented in section 2.5.2 requires the knowledge of the absorbance spectrum while the determination of the sensitivity of the instrument, detailed in section 2.5.3, necessitates to know the transmittance spectrum. The experimental measurement of these two physical quantities implies the measurement of a background spectrum, *i.e.* a spectrum in the absence of the sample. Since we measured the residual traces of water in the cavity, the background spectrum was unaccessible. To overcome this difficulty, a simulated transmittance spectrum from the Hitran database was utilized to generate a mask employed in a weighted penalized least squares fit of the spectrum. This fit is also known as the weighted Whittaker smoother algorithm [51]. The Whittaker algorithm is detailed in Appendix E.2. Since the peaks are hidden by the mask, the result of the fit is considered to be the background spectrum. The transmittance is then evaluated by dividing the spectrum by the estimated background. The absorbance is finally obtained by taking the opposite of the decimal logarithm of the transmittance.

Finally, we benchmarked our instrument with another recent setup performing FT-IBBCEAS with a FTS and a supercontinuum. This comparison is given in section 2.5.4.

2.5.1 *Instrumental lineshape function*

Ideally, the Fourier-transform of the interferogram recorded with the instrument should give access to the true spectrum. In practice, this is not the case because of the inherent practical and physical limitations of the instrument such as the finite length of the translation stage, the natural divergence of the light beams, the frequency-dependent response of the electronics, the imperfect mechanics, etc. All these non-idealities will modify the spectrum by convolving it with a function: the ILS that can be interpreted as the instrumental response to a monochromatic source [2]. Appendix A.2 details the consequences of the finite length of the translation stage and of the beam divergence on the ILS.

In order to characterize the ILS of the instrument, a temperature-stabilized external cavity diode laser (ECDL) working at 778.2 nm (DL100 ECDL from Toptica) was injected in the FTS and its spectrum was measured. It is plotted in Figure 2.13. A single interferogram was recorded at the resolution of 0.00322 cm^{-1}. No apodization was applied prior to evaluating the Fourier transform. The spectrum looks like a typical mode emitted from a laser but we can see a structured pattern of ghost lines symmetrically located on both sides of the ECLD emission line. However, the stronger ghost lines are about 3 orders of magnitude smaller than the emission line. They are caused by some modulation of the interferogram and they are offset from the parent line by the modulation frequency [52]. In our setup, these ghost lines are partly imputed to the mechanics, and more specifically to periodic misalignments due to the vibrations of the carriage, ultimately resulting in a modulation of the interferogram, leading to their apparition in the instrumental lineshape function [49]. In order to justify this statement, the right wing of the ECDL emission line was shifted around zero and it was compared to the Fourier transforms of the carriage velocity and the fringe visibility of the He:Ne interference pattern with respect to the position presented in Figure 2.11 of section 2.4.2. The three spectra are shown in Figure 2.14. We can see that most of the peaks present in the fringe visibility and velocity spectra are also present in the wings of the instrumental function, indicating an impact of the vibrations on

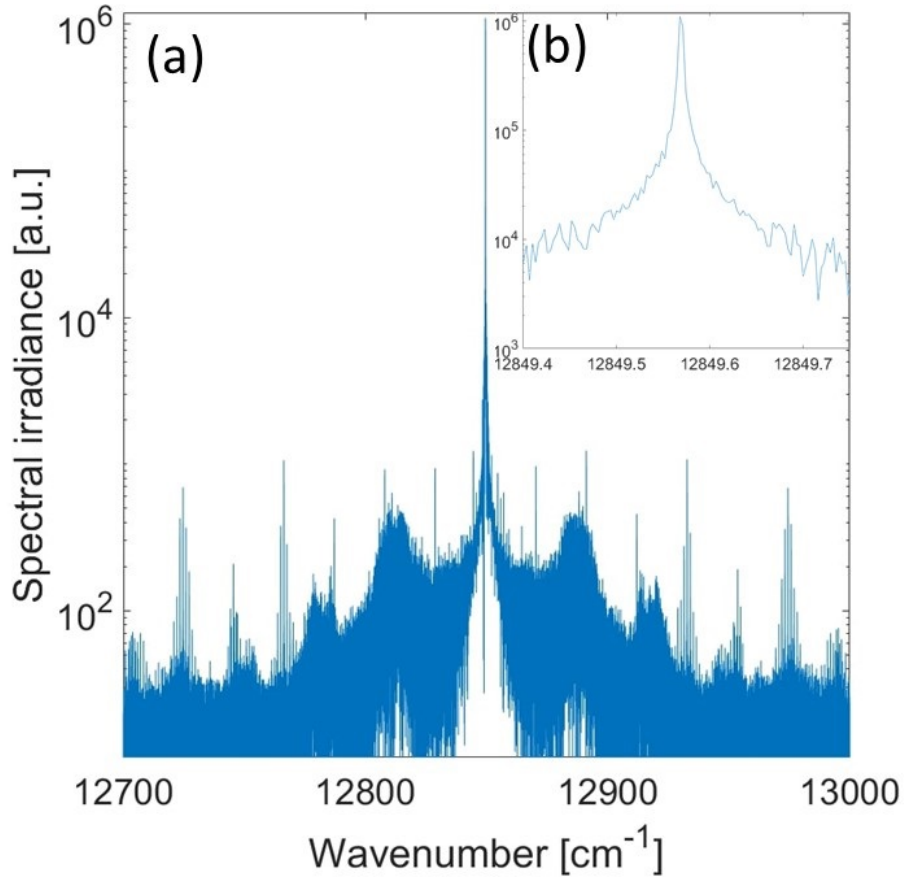


Figure 2.13: (a) Instrumental lineshape function of the FTS at 12849.56 cm^{-1} (778.24 nm).(b) Zoom on the laser emission line. A single interferogram was recorded at a resolution of 0.00322 cm^{-1}.

the measured spectra. Some peaks in the ILS are not present in neither the visibility spectrum nor the velocity spectrum. They correspond to higher harmonics of the fundamental modes present in both spectra. The structured patterns present in the velocity and fringe visibility spectra can be interpreted as "events" occurring a certain number of times per turn of the screw shaft. Such an analysis can help with the identification of the causes of these vibrations. Fortunately, the presence of these ghost lines in the ILS is auspicously mitigated in the case of absorption spectra by about two orders of magnitude when compared to emission lines because of the smaller signal-to-noise ratio [52].

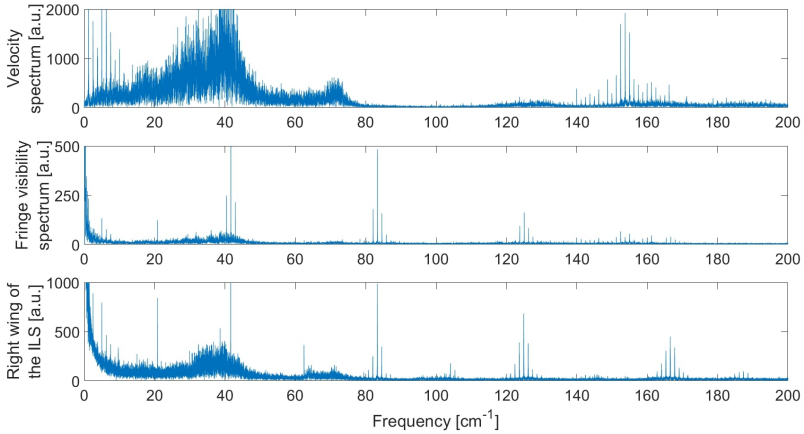


Figure 2.14: Spectral analysis of the impact of the velocity fluctuations on the contrast of the He:Ne laser interference pattern and on the ILS. Top: velocity spectrum. Middle: fringe visibility spectrum. Down: right wing of the ECDL emission line shifted around zero.

2.5.2 *Wavenumber axis accuracy*

Theoretically, a spectrum taken with a FTS is absolutely calibrated provided the wavelength of the reference laser is known. This is the so-called Connes' advantage of FTS over the other types of spectrometers. However, true FTS deviate from this ideal behaviour mainly for two reasons: (1) light of both the reference and the broadband light source are not perfectly collimated and (2) the He:Ne and the supercontinuum laser beams are not perfectly aligned [53, 54]. Therefore, as for dispersive spectrometers, it is necessary to apply the internal standard method which consists in recording a spectrum with both the unknown features and features whose positions have been independently measured. The wavenumber-axis is then calibrated by correcting it so that the central wavenumbers of the known transitions match with the wavenumber-axis [55]. The wavenumber-axis is corrected by considering known spectral features spanned on a large region of the spectrum and by imposing their position using a linear regression.

In our case, the spectrum was calibrated using H_2O desorbing from the cell walls. About half of the isolated peaks above a 0.05 absorbance threshold and resulting from a single transition were automatically fitted using Gaussian functions in order to determine their experimental central wavenumber. Gaussian profiles were chosen on the hypothesis

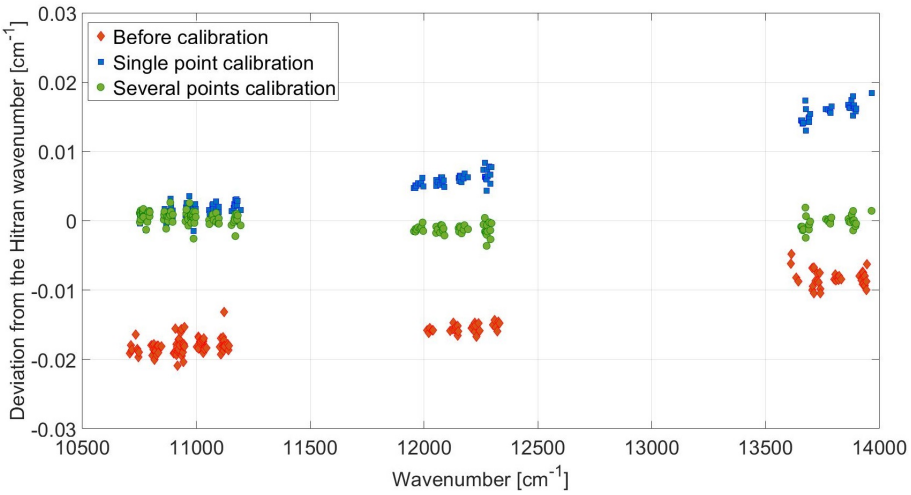


Figure 2.15: Deviation of the central wavenumber of the experimental H_2O lines from the Hitran database for the spectrum presented in Figure 2.12 recorded at a resolution of 0.015 cm^{-1}.

that pressure broadening can be neglected at 4 Torr, resulting in pure Doppler-broadened transitions. The wavenumber-axis was then corrected to impose that the experimental wavenumber of these lines matches the 2008 Hitran database [50]. The calibration process was validated by evaluating the deviation of the central wavenumber on the other half of the H_2O transitions from the ones of the Hitran database. For the sake of completeness, the deviation before calibration and for a single-line calibration are also plotted. As we can see, single-line calibration is only valid in the vicinity of the line. In the case of multiple-lines calibration, the root mean square deviation from the Hitran database was equal to 0.0017 cm^{-1} for a spectrum with a resolution of 0.015 cm^{-1} and a mean transition width of 0.046 cm^{-1} at half maximum. This value is in good accordance with Ref. [55].

2.5.3 *Instrument sensitivity*

Absorption spectroscopy relies on the measurement of the frequency-dependent attenuation of light after its interaction with the sample. Usually, the absorption is described using the Beer-Lambert's law which stipulates that the attenuation is proportional to the optical path through the sample:

$$\mathrm{d}I = -I(\tilde{\nu})\alpha(\tilde{\nu})\mathrm{d}l, \tag{2.13}$$

where $I(\tilde{\nu})$ is the intensity of light at wavenumber $\tilde{\nu}$, $\alpha(\tilde{\nu})$ is the wavenumber-dependent absorption coefficient which depends on the line intensity, the amount of the species under study and on their temperature. Finally, $\mathrm{d}I$ is the intensity reduction after interacting with the sample on a distance $\mathrm{d}l$. The sensitivity of the instrument is characterized by the smallest value of $\alpha(\tilde{\nu})$ the instrument can measure, denoted $\alpha_{\min}$. As mentioned in the introduction, the sensitivity can be improved by performing CEAS measurements. When working with optical cavities illuminated by a broadband light source, the retrieval of the absorption coefficient $\alpha(\tilde{\nu})$ from the transmittance spectrum is not as straightforward as in experimental setups with multi-pass cells since the transmission spectrum of the optical cavity must also be taken into account, leading to the following complicated expression[56]:

$$\alpha = \frac{1}{d}\left|\ln\left(\frac{1}{2R^2}\left(\sqrt{4R^2+\left(\frac{I_0}{I}(R^2-1)\right)^2}+\frac{I_0}{I}(R^2-1)\right)\right)\right|, \quad (2.14)$$

where R is the reflectivity of the HRM, d is the cavity length, I_0 the intensity at the output of the empty cavity and I the intensity at the output of the cavity in presence of the absorbing species. Comparison between single-pass measurements and cavity-enhanced measurements is presented in section A.8, along with the derivation of equation (2.14).

In order to determine the sensitivity of the instrument, it is therefore necessary to determine experimentally the reflectivity of the HRM. This is done by measuring the absorption of a known amount of H_2O in the cavity, whose line intensities i_H are known from the Hitran database and by employing the following formula:

$$R = 1 - \frac{Ndi_H}{\int\left(\frac{I_0(\tilde{\nu})}{I(\tilde{\nu})}-1\right)\mathrm{d}\tilde{\nu}}, \quad (2.15)$$

where N is the density (molecule $\times\mathrm{cm}^{-3}$) of water in the cavity. This equation is the one used by O'Leary *et al.* [16] and it is derived from equation (2.14) by imposing a high mirror reflectivity ($R \to 1$) and small losses due to absorption ($\frac{I}{I_0} \to 1$). The cavity length was equal to 88 cm, the density was obtained by supposing that the remaining residual pressure in the gas cell was only due to water desorbing from the cell walls, varying from 2 torr to 4 torr during the whole measurement time. The pressure was measured with a Pirani gauge. The

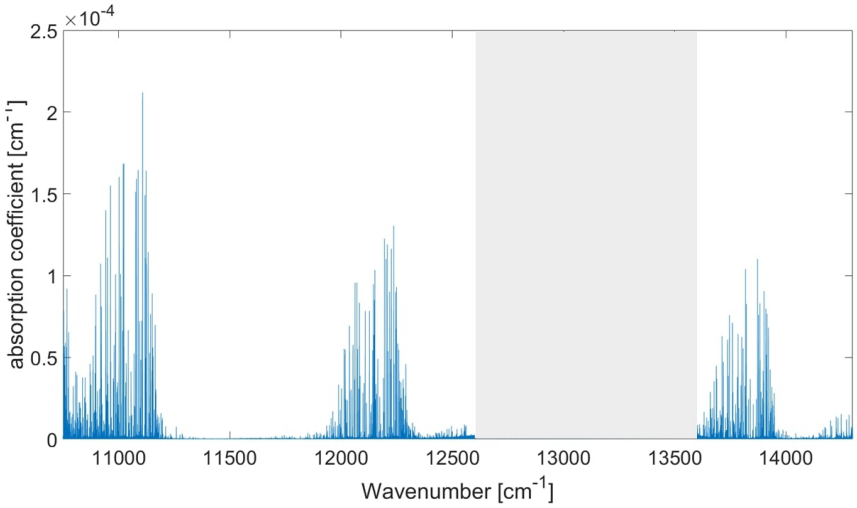


Figure 2.16: Absorbance with respect to the wavenumber, evaluated using equation (2.14) and with the mirror reflectivity found with equation (2.15). The grey zone was suppressed due to a lack of signal.

denominator in equation (2.15) is evaluated by fitting peaks corresponding to molecular transitions of water in the $\left(\frac{I_0(\tilde{\nu})}{I(\tilde{\nu})} - 1\right)$ spectrum with a Gaussian function and by using the resulting fitting coefficients in the analytical expression of the integral of the Gaussian function. To avoid poor fitting and to guarantee the validity of the formula, only peaks with transmission between 0.9 and 0.95 are considered for the determination of the mirrors reflectivity. A mean effective reflectivity $\overline{R}$ of 99.76% was estimated. Injecting this value in equation (2.14) allows to compute the absorption coefficient with respect to the wavenumber and therefore to estimate the sensitivity of the instrument, that is the lowest value of $\alpha(\tilde{\nu})$ that can be distinguished from the noise. A plot of the absorption coefficient with respect to the wavenumber is shown in Figure 2.16. A zoom of the absorption coefficient between 11920 cm^{-1} and 11930 cm^{-1} is given in Figure 2.17. The black dashed lines in this plot correspond to a $1\sigma = 6.5 \times 10^{-8}$ cm^{-1} noise in the value of the absorption coefficient. The red curve corresponds to the absorption coefficient of pure H_2O at 4 Torr and 293K simulated with the Hitran database.

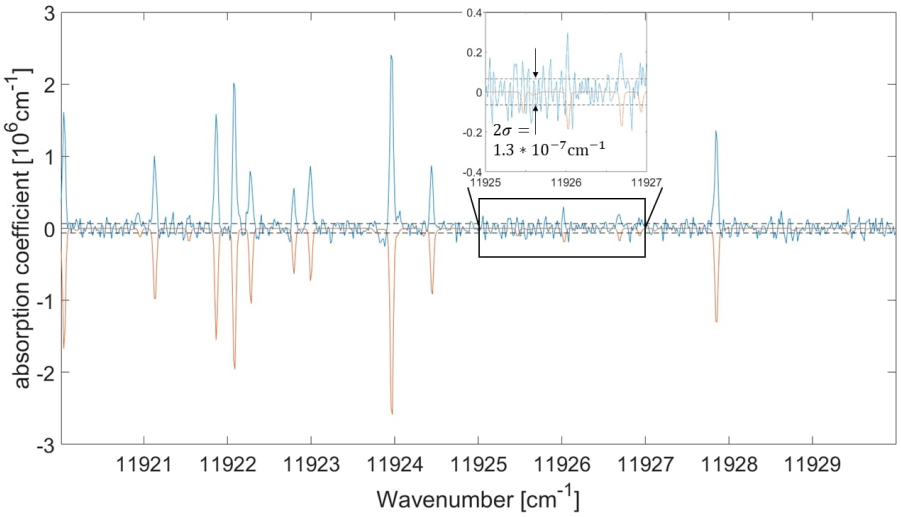


Figure 2.17: Zoom between 11920 cm^{-1} and 11930 cm^{-1} of the absorbance with respect to the wavenumber presented in Figure 2.16. A frame with a zoom between 11925 cm^{-1} and 11927 cm^{-1} is shown. Blue: experimental absorbance. Red: theoretical absorbance generated using the Hitran database ($T = 293$K, $P = 4$Torr). Black dashed lines: $\pm 1\sigma = 6.5 \times 10^{-8}$ cm^{-1} noise.

2.5.4 *Comparison with another FT-IBBCEAS setup*

In order to further characterize the performances of our setup, it is benchmarked against the setup of M. O'Leary *et al.* [16] where FT-IBBCEAS was performed with a Fianium SC450-6 supercontinuum laser source and a Vertex 80 FTS from Bruker. To our knowledge, their instrument is the setup that is closest to ours. Table 2.1 compares the specifications of the two setups, along with the relevant experimental parameters.

First, we can see that the light source they used in their instrument delivers 50% more optical power than ours, allowing for the use of mirrors with higher reflectivity and for more signal. The most relevant quantity is the minimum absorption coefficient since it is an indirect measurement of the SNR. Their minimal absorption coefficient is 6.5 times lower than ours. However, this value has to be manipulated cautiously. Indeed, from equation (2.14), we can see that optical cavities with mirrors of higher reflectivity ultimately lead to a higher sensitivity. Furthermore, they utilized an optical cavity with a length of 644 cm, against 88 cm for our optical cavity. From equation (2.14), we can

see that our minimal absorption coefficient would be improved by a factor 7.3 at equal cavity length. Furthermore, even if we remove the shaded area of Figure 2.16 due to poor signal, we still cover 2800 cm^{-1} of spectral range in the near infrared, against 2000 cm^{-1} for their measurement, and this at a resolution about 10 times better. The better resolution is counterbalanced by a much longer measurement time. The dead times due to the changes in direction of the carriage were set aside from the measurement duration specified in Table 2.1. In order to better compare the two setups, it is necessary to use a metric that incorporates all these features in a single scalar value. The absorption sensitivity per spectral element normalized to a 1-s acquisition time, denoted α'_{min}, found in Ref. [57], is given by:

$$\alpha'_{min} = \alpha_{min} \frac{\sqrt{T}}{\sqrt{M}} \left[cm^{-1} Hz^{-1/2} \right], \tag{2.16}$$

where T is the measurement time and M the number of spectral elements. This value was then multiplied by the respective cavity lengths of the two setups in order to have a single metric value that takes most of the experimental parameters into account. The values of this comparison metric and of α'_{min} are also given in Table 2.1. We can see that the two instruments have similar performances, assuring the proper working of our FTS when compared to the commercial instruments that lead the market[3].

2.6 CONCLUSION

In this chapter, we presented the FTS built in-house. We demonstrated the ability of this spectrum analyzer to perform broadband and sensitive measurements at high-resolution, three key-features for the study of large molecules, as outlined in Chapter 1. Concerning the sensitivity aspect of our instrument, it ranks among the best instruments presented in the literature when considering IBBCEAS.

3 For the sake of completeness, we mention here the work of Abbas *et al.* [58], published in 2021 with similar performances in the middle infrared in terms of sensitivity per spectral element.

Table 2.1: Comparison of the performances of our instrument with the experimental setup of M. O'Leary *et al.* [16]. The unfavorable comment indicated for the pressure highlights that the value should be considered as an upper bound.

	M. O'Leary *et al.* [16]	This work
Light source	Fianium SC450-6 [6W]	Fianium SC450-4 [4W]
Spectrometer	Bruker, Vertex 80	FTS built in-house
Detector	single	autobalanced
Effective reflectivity of the HRMs [%]	99.88	99.76
Pressure [mbar]	4	5.33 (unfavorable)
Resolution $\left[\mathrm{cm}^{-1}\right]$	0.12	0.015
Spectral range $\left[\mathrm{cm}^{-1}\right]$	6000-8000	10500-14300
Effective bandwidth $\left[\mathrm{cm}^{-1}\right]$	2000	2800
Cavity length d [cm]	644	88
Minimal absorption coefficient $\left[10^{-8}\mathrm{cm}^{-1}\right]$ (1σ noise)	1.0	6.5
Measurement time [min]	60	500
Minimal absorption coefficient per spectral element normalized to 1-s acquisition time α'_{min} $\left[10^{-8}\mathrm{cm}^{-1}\mathrm{Hz}^{-1/2}\right]$	0.465	2.241
$\alpha'_{\mathrm{min}} * d$, $\left[10^{-6}\mathrm{Hz}^{-1/2}\right]$	2.99	1.97

3

FREQUENCY COMBS

3.1 INTRODUCTION

In order to challenge the fundamental laws of physics further and to improve our understanding of internal dynamics and structure of molecules, considerable improvements in the sensitivity and precision of the measurements are needed. Thankfully, these requirements can be met on a broad wavenumber scale by using stabilized frequency combs to probe the molecules [59]. Frequency combs are bright, broadband and coherent light sources with a structured spectrum consisting in a comb of equidistant sharp lasers lines, each laser line optical frequency being given by: $\nu_m = m f_{\text{rep}} + f_{\text{CEO}}$, where m is an integer and f_{rep} and f_{CEO} are the two degrees of freedom of the frequency comb, with frequencies lying in the radio-frequency (RF) domain. The most common frequency-comb sources are mode-locked lasers, which generate trains of ultrashort pulses at a repetition rate f_{rep}. The offset frequency f_{CEO} is due to the pulse-to-pulse phase slip $\Delta\Phi_{\text{CEO}}$ of the carrier wave relative to the envelope of the pulses. These two degrees of freedom can be measured and stabilized with great accuracy, ultimately transferring their precision to the optical frequencies. Furthermore, these two frequencies lie in the RF domain, meaning that they may be compared directly with microwave frequency standards such as the caesium primary standard or the rubidium secondary standard, transferring their precision from the RF domain to the optical spectral region [60]. Several detection schemes exist to measure the spectrum of frequency combs and, regardless of the method, if they are able to resolve individual comb lines, the resolution and precision of the measurement are only limited by the precision on the comb repetition rate f_{rep} and offset frequency f_{CEO}. It is even possible to improve this limit by interleaving spectra with different repetition rates/offset frequencies [13, 14].

This chapter is divided in 5 parts. The key concepts of ultrashort pulses propagation in dispersive media are given in section 3.2.

Section 3.3 is dedicated to the mode-locking operation of laser resonators, which is at the heart of the frequency comb technology. This section also describes methods to favour the mode-locking (ML) operation over the continuous wave (CW) operation of laser resonators.

Section 3.4 relates the frequency structure to the temporal description of the light emitted by a femtosecond laser.

Applications and advantages of frequency-comb light sources in the field of optical spectroscopy are developed in section 3.5.

Finally, section 3.6 describes our first results concerning the development of such light sources in the laboratory.

3.2 PROPAGATION OF ULTRASHORT PULSES IN DISPERSIVE MEDIA

The goal of this section is to introduce key concepts of the propagation of ultrashort pulses in dispersive media. They are necessary for the understanding of the key parameters at play for the design of a frequency-comb light source. These concepts are described in two parts. First, the carrier wave and pulse envelope are introduced in section 3.2.1. Then, section 3.2.2 addresses the consequences of dispersion on ultrashort pulses propagation in a dispersive medium. The reader interested in having more details concerning the propagation of ultrashort pulses in dispersive media should refer to Chapter 17 of Ref [60] for example.

3.2.1 *Temporal description of ultrashort pulses*

This section mostly relies on Ref. [60].

In the time domain, the electric field $E(t)$ of an individual ultrashort pulse can be described as follows:

$$E(t) = A(t) \exp\left(-\mathrm{j}\omega_c t\right), \tag{3.1}$$

where $A(t)$ the pulse envelope and ω_c is the angular frequency of the carrier wave. Since short pulses contain a range of frequencies, the mean value of the pulse spectrum is usually employed for ω_c.

The electric field of equation (3.1) can be rewritten as a superposition of harmonic waves:

$$E(t) = \frac{1}{\sqrt{2\pi}} \int_{-\infty}^{+\infty} a(\omega) \exp(-\mathrm{j}\omega t) \mathrm{d}\omega, \tag{3.2}$$

where $a(\omega)$ is the amplitude per unit frequency interval, which can be evaluated by taking the inverse Fourier transform of equation (3.2):

$$a(\omega) = \frac{1}{\sqrt{2\pi}} \int_{-\infty}^{+\infty} [A(t) \exp(-\mathrm{j}\omega_c t)] \exp(\mathrm{j}\omega t) \mathrm{d}t. \tag{3.3}$$

Alternatively, using $\omega' = \omega - \omega_c$:

$$a(\omega_c + \omega') \equiv a'(\omega') = \frac{1}{\sqrt{2\pi}} \int_{-\infty}^{+\infty} A(t) \exp(\mathrm{j}\omega' t) \mathrm{d}t. \tag{3.4}$$

From equations (3.3) and (3.4), one can notice that the shape and width of the distribution over frequency are determined by the shape of the pulse envelope while the location of this distribution on the frequency axis is determined by the carrier angular frequency ω_c. For information, the passage from equation (3.3) to equation (3.4) is nothing but the proof of the frequency-shift property of Fourier transforms [61].

3.2.2 *Linear propagation*

This section relies on Ref. [60] and [62].

Let suppose that the electric field of a pulse propagating in a dispersive medium of refractive index $n(\omega)$ along the z-axis, towards positive z values, is described by the expression of equation (3.1), alternatively, by equation (3.2). In propagating through the medium, each frequency will accumulate a total phase shift of $\phi(\omega)$. The form of the optical pulse in the output plane of the optical system is then given by the superposition of the amplitudes of the phase-shifted frequencies, that is:

$$E_{\text{out}} = \frac{1}{\sqrt{2\pi}} \int_{-\infty}^{+\infty} [a(\omega) \exp(\mathrm{j}\phi(\omega)] \exp(-\mathrm{j}\omega t) \mathrm{d}\omega. \tag{3.5}$$

Or alternatively, using once again $\omega' = \omega - \omega_c$:

$$E_{\text{out}} = \exp(-\mathrm{j}\omega_c t) \frac{1}{\sqrt{2\pi}} \int_{-\infty}^{+\infty} \left[a'(\omega') \exp(\mathrm{j}\phi(\omega_c + \omega')\right] \times \exp(-\mathrm{j}\omega' t)\ \mathrm{d}\omega'. \tag{3.6}$$

The electric field at the output of the optical system remains the product of a wave at the carrier frequency and a pulse envelope which is in general modified from that of the input pulse.

When a pulse propagates through a dispersive medium with refractive index $n(\omega)$ located between the planes $z = 0$ and $z = l$, its Fourier components experience a phase shift given by:

$$\phi(\omega) = \int_0^l k(\omega, z)\mathrm{d}z = \int_0^l \frac{n(\omega, z)\omega}{c}\mathrm{d}z. \tag{3.7}$$

In the case of a uniform medium, the phase accumulated at each frequency component becomes:

$$\phi(\omega) = k(\omega)l = \frac{2\pi}{\lambda}l = \frac{\omega l}{v_p(\omega)} = \frac{\omega}{c}n(\omega)l, \tag{3.8}$$

where v_p is the phase velocity and $n(\omega)$ is the frequency-dependent index of refraction of the light. In the case of broadband mode-locked lasers, one has to take into account the frequency dependency of k, the wavenumber $k(\omega)$ present in equation (3.8) can then be expanded around the carrier angular frequency ω_c, leading to

$$\begin{aligned} k(\omega) &= k(\omega_c) + \left.\frac{\partial k}{\partial \omega}\right|_{\omega_c}(\omega - \omega_c) \\ &\quad + \frac{1}{2}\left.\frac{\partial^2 k}{\partial \omega^2}\right|_{\omega_c}(\omega - \omega_c)^2 + ... \\ &= k(\omega_c) + \left.\frac{\partial k}{\partial \omega}\right|_{\omega_c}\omega' + \frac{1}{2}\left.\frac{\partial^2 k}{\partial \omega^2}\right|_{\omega_c}\omega'^2 + ... \end{aligned} \tag{3.9}$$

where the definition $\omega' = \omega - \omega_c$ was used. In section 3.2.2, the impact of the first two terms on the propagation of the pulse is made explicit. Then, the consequences of higher order terms on the pulse propagation are developed in section 3.2.2. These concepts are important for the understanding of key concepts concerning the design of frequency comb light sources.

Phase and group velocity

In a dispersive medium, the pulse carrier and the envelope of the pulse will propagate at two different velocities: the phase velocity $v_p = \frac{\omega_c}{k(\omega_c)}$ and the group velocity $v_g = \left.\frac{\partial \omega}{\partial k}\right|_{\omega_c}$ respectively. This can be highlighted

by considering only the first two terms of equation (3.9), along with equations (3.6) and (3.8). This leads to:

$$\begin{aligned} E_{\text{out}} = &\exp(-\mathrm{j}\omega_c t)\frac{1}{\sqrt{2\pi}} \\ &\times \int_{-\infty}^{+\infty}\left[a'(\omega')\exp\left(\mathrm{j}\left(k(\omega_c)l + l\left.\frac{\partial k}{\partial \omega}\right|_{\omega_c}\omega'\right)\right)\right] \\ &\times \exp(-\mathrm{j}\omega' t)\mathrm{d}\omega'. \end{aligned} \tag{3.10}$$

By making use of the expressions of v_p and v_g, equation (3.10) can be rewritten as follows:

$$\begin{aligned} E_{\text{out}} = &\exp\left(-\mathrm{j}\omega_c\left(t - \frac{l}{v_p}\right)\right) \\ &\times \frac{1}{\sqrt{2\pi}}\int_{-\infty}^{+\infty} a'(\omega')\exp\left(-\mathrm{j}\omega'\left(t - \frac{l}{v_g}\right)\right)\mathrm{d}\omega'. \end{aligned} \tag{3.11}$$

From this equation, we see[1] that the pulse envelope maintains a constant shape that moves at the group velocity v_g while the carrier wave propagates at the phase velocity v_p. The fact that the carrier and the envelope do not propagate at the same velocity implies that the relative position of the carrier with the peak of the envelope will change as the pulse propagates in the medium. This change manifests itself as the carrier-envelope offset or carrier-envelope phase. This is illustrated in Figure 3.1(a). The mismatch between the phase velocity and the group velocity has consequences on the spectrum of femtosecond lasers, as it will be explained in section 3.4.

Higher-order terms

In the previous subsection, we noticed that the zeroth and first orders of the expansion of $k(\omega)$ around ω_c lead to the concepts of phase and group velocities. The carrier wave and the pulse envelope travel in the material at different velocities but the pulse envelope remains unchanged during its propagation. In this subsection, we will see that higher-order terms result in a distortion of the pulse envelope.

1 The two factors of the expression are functions of the form $f(t - z/v)$ which are solutions of the wave propagation differential equation.

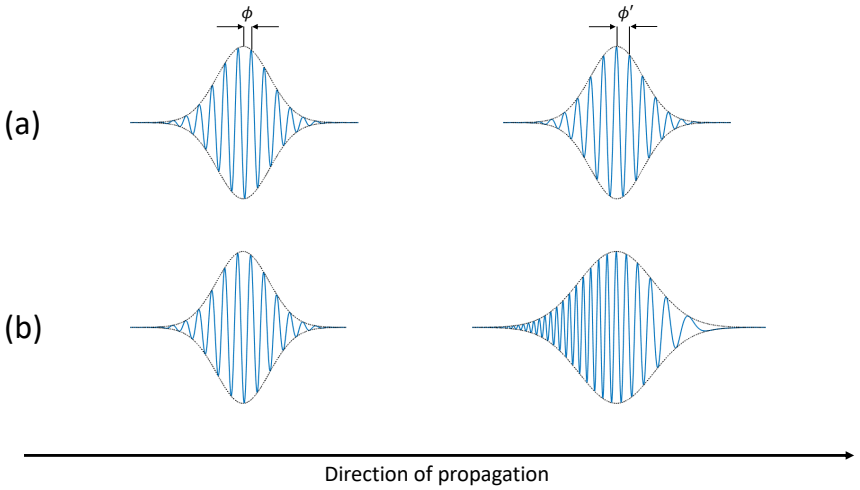


Figure 3.1: Consequences of dispersion on a pulse as it propagates in a dispersive medium. (a) Only the first two terms of equation (3.9) are considered. The pulse envelope propagates at the group velocity and the carrier at the phase velocity, leading to a change in the carrier-envelope phase ϕ. (b) Contribution of positive GDD is also considered, resulting in a separation of the frequency components and a broadening of the pulse envelope.

The total phase accumulated at each frequency of equation (3.8) can be expanded around the carrier frequency in a similar way to equation (3.9), leading to:

$$\begin{aligned}\phi(\omega) =& \phi_0 + \left.\frac{\partial \phi}{\partial \omega}\right|_{\omega_c} (\omega - \omega_c) + \frac{1}{2} \left.\frac{\partial^2 \phi}{\partial \omega^2}\right|_{\omega_c} (\omega - \omega_c)^2 \\ &+ \frac{1}{6} \left.\frac{\partial^3 \phi}{\partial \omega^3}\right|_{\omega_c} (\omega - \omega_c)^3 + ...\end{aligned} \tag{3.12}$$

Where $\phi_0 = \phi(\omega_c)$ is the total phase acquired by the carrier wave, $\left.\frac{\partial \phi}{\partial \omega}\right|_{\omega_c}$ is the group delay, $\left.\frac{\partial^2 \phi}{\partial \omega^2}\right|_{\omega_c}$ corresponds to the group delay dispersion (GDD) and $\left.\frac{\partial^3 \phi}{\partial \omega^3}\right|_{\omega_c}$ denotes the third-order dispersion (TOD). The group delay corresponds to the time T_g required for the pulse envelope to travel the distance l in the medium. Indeed, we have

$$T_g(\omega) = \frac{l}{v_g} = l \left.\frac{\partial k}{\partial \omega}\right|_{\omega_c} = \left.\frac{\partial \phi}{\partial \omega}\right|_{\omega_c}. \tag{3.13}$$

As explained in the previous subsection the total phase acquired by the carrier wave and the group delay do not modify the envelope of

the pulse, higher-order terms do result in its distortion. This can be shown by expanding equation (3.13) around the carrier wave angular frequency ω_c:

$$\begin{aligned} T_g(\omega) &= T_g(\omega_c) + \left.\frac{\partial T_g}{\partial \omega_c}\right|_{\omega_c} (\omega - \omega_c) \\ &\quad + \frac{1}{2} \left.\frac{\partial^2 T_g}{\partial \omega^2}\right|_{\omega_c} (\omega - \omega_c)^2 + ... \\ &= \left.\frac{\partial \phi}{\partial \omega}\right|_{\omega_c} + \left.\frac{\partial^2 \phi}{\partial \phi^2}\right|_{\omega_c} (\omega - \omega_c) + \frac{1}{2} \left.\frac{\partial^3 \phi}{\partial \omega^3}\right|_{\omega_c} (\omega - \omega_c)^2. \end{aligned} \tag{3.14}$$

From this equation, we see that dispersion, *i.e.* the dependence in frequency of the refractive index, manifests itself as a spectrally dependent propagation time of the wave in the material. Furthermore, we observe that the GDD represents a linear variation of the group delay, resulting in a separation or concentration of the frequency components in time, depending on the sign of the group dispersion. In the case of a positive GDD, the high-frequency components of the pulse will move to the rear of the pulse and the low-frequency components will lead, leading to a positive frequency chirp of the pulse and to a symmetrical broadening of the pulse envelope. This is illustrated in Figure 3.1(b). The TOD is the first order to asymmetrically distort the pulse envelope.

When dealing with pulses with a center wavelength around 800 nm, which is typically the case for pulses emitted by a Ti:Sapphire femtosecond laser, GDD starts to play a significant role for transform-limited pulses around 100 fs while TOD must be considered for pulses below 30 fs. Higher-order terms should be taken into account for pulses shorter than 10 fs [63].

3.3 FEMTOSECOND LASERS: INTRODUCTION TO MODE-LOCKING

This section aims at briefly explaining the concept of the ML operation of a laser resonator. Section 3.3.1 presents an intuitive way of understanding ML. Section 3.3.2 describes the technique employed in the MIRA900 from Coherent[2] and the homemade femtosecond resonator to favour the ML operation over the CW operation, which is based on the Kerr effect. These sections serve as a support for the discussion concerning the design and fabrication of our frequency comb light

2 This femtosecond resonator is available in our laboratory.

source. For the reader who wants a deeper understanding of the ML operation, there is abundant literature concerning this topic (see for example [60, 64–67]).

3.3.1 *Simple treatment of mode-locking*

This section relies on Ref. [60, 67, 68].

Neglecting dispersion in the laser cavity of length L, the longitudinal modes of the laser are spaced in angular frequency by an amount:

$$\Delta\omega = 2\pi\frac{c}{2L} = \frac{2\pi}{T_c}, \tag{3.15}$$

where T_c is the time taken for light to travel one cavity round-trip and c the velocity of light in vacuum. The frequencies of the cavity modes are then given by:

$$\omega_p = \omega_{\text{ceo}} + p\Delta\omega \tag{3.16}$$

where ω_{ceo} is known as the offset angular frequency and p is an integer indexing the mode of cavity. The right- and left-going waves of a cavity mode are given by:

$$E(z,t) = a_p e^{j\left(k_p z \mp \omega_p t + \phi_p\right)}, \tag{3.17}$$

with a_p the amplitude of the wave, ϕ_p its phase. The upper (lower) sign refers to waves propagating towards positive (negative) z. Information concerning the transverse profile of the waves was neglected in this expression.

If the laser oscillates simultaneously on N longitudinal modes $p = q_0, q_0+1, q_0+2, ...$, then the amplitude of the laser radiation emerging from the output coupler would have the form:

$$E(z,t) = \sum_{p=q_0}^{q_0+N-1} a_p e^{j\left(k_p z - \omega_p t + \phi_p\right)}. \tag{3.18}$$

Figure 3.2 is simulation of the intensity at the output of a laser emitting on several modes simultaneously over several longitudinal modes with either a random-but-constant phase relationship between the modes (Figure 3.2(a)) or with the same phase for all the modes (Figure 3.2(b)). In both cases, the pattern repeats itself on a period T_c. If there is no

phase relationship between the lasing modes, the output contains sharp fluctuations in intensity that are distributed randomly. On the other hand, when all the modes have the same phase, the output consists in a train of short pulses separated by the cavity round-trip time. Because of this phase relationship, the situation is known as mode-locking. The peak has a duration on the order of $2\pi/\Delta\omega_{\text{osc}}$, with $\Delta\omega_{\text{osc}} = (N-1)\Delta\omega$, the total bandwidth occupied by the oscillating modes. In other words, this phase relationship causes the lasing longitudinal modes to constructively interfere during a short period of time while destructively interfering at all other times, resulting in the formation of short optical pulses with a high peak intensity [65, 69].

It is possible to derive an analytical expression for the intensity with respect to time at the output of the femtosecond laser depicted in Figure 3.2(b) by supposing that all the modes have the same amplitude E_0. For convenience, we will consider the wave at $z = 0$ and with the same phase $\phi_p = 0$. The sum in equation (3.18) becomes:

$$\begin{aligned} E(0,t) &= E_0 \sum_{p=q_0}^{q_0+N-1} \mathrm{e}^{-\mathrm{j}(\omega_{\text{ceo}}+p\Delta\omega)t} \\ &= E_0 \mathrm{e}^{-\mathrm{j}\omega_{\text{ceo}}t} \mathrm{e}^{-\mathrm{j}q_0\Delta\omega t} \sum_{p=0}^{N-1} \mathrm{e}^{-\mathrm{j}p\Delta\omega t}. \end{aligned} \tag{3.19}$$

The last factor in the above expression is the partial sum of a geometric series of the form $ar^{(p-1)}$ where $r = \mathrm{e}^{-\mathrm{j}\Delta\omega t}$ is the common ratio and $a = 1$ is the first term. This sum can be evaluated using the following result of geometrical series[3]:

$$\sum_{p=0}^{N-1} ar^p = \frac{a\,(1-r^n)}{1-r}. \tag{3.20}$$

3 The N^{th} partial sum of a geometric series can be evaluated as follows:

$$\begin{array}{lcccccccc} \sum_{p=1}^{N} ar^{p-1} & = & a+ & ar+ & ar^2+ & ar^3 + \ldots + ar^{N-1} & \\ r\sum_{p=1}^{N} ar^{p} & = & & ar+ & ar^2+ & ar^3 + \ldots + ar^{N-1} & +ar^N \end{array}$$

The second line was obtained by multiplying the first one by r. Subtracting these two equations and supposing $r \neq 1$ allows one to obtain:

$$\sum_{p=1}^{N} ar^{p-1} = \frac{a\,(1-r^n)}{1-r}.$$

Equation (3.19) becomes:

$$E(0,t) = E_0 \mathrm{e}^{-\mathrm{j}\omega_{\mathrm{ceo}}t} \mathrm{e}^{-\mathrm{j}q_0\Delta\omega t} \frac{1-\mathrm{e}^{-\mathrm{j}N\Delta\omega t}}{1-\mathrm{e}^{-\mathrm{j}\Delta\omega t}}. \tag{3.21}$$

This expression can be rewritten as follows:

$$E(0,t) = E_0 \mathrm{e}^{-\mathrm{j}\omega_{\mathrm{ceo}}t} \mathrm{e}^{-\mathrm{j}\overline{p}\Delta\omega t} \frac{\sin\left(\frac{N}{2}\Delta\omega t\right)}{\sin\left(\frac{1}{2}\Delta\omega t\right)} \tag{3.22}$$

$$= \mathrm{e}^{-\mathrm{j}\overline{\omega}t} \frac{\sin\left(\frac{N}{2}\Delta\omega t\right)}{\sin\left(\frac{1}{2}\Delta\omega t\right)}, \tag{3.23}$$

where $\overline{p} = q_0 + \frac{N-1}{2}$ and $\overline{\omega} = \omega_{\mathrm{ceo}} + \overline{p}\Delta\omega$ are respectively the mean mode number and mean frequency of the oscillating modes. The electric field at the output of the laser takes the form of a carrier wave of frequency $\overline{\omega}$ multiplied by an envelope function $\frac{\sin\left(\frac{N}{2}\Delta\omega t\right)}{\sin\left(\frac{1}{2}\Delta\omega t\right)}$. The intensity at the output of the mode-locked laser, $I(t)$, is proportional to $|E(0,t)|^2$ and it is thus given by:

$$I(t) = E_0^2 \frac{\sin^2\left(\frac{N}{2}\Delta\omega t\right)}{\sin^2\left(\frac{1}{2}\Delta\omega t\right)}. \tag{3.24}$$

This last expression is the function plotted in Figure 3.2(b).

In order to force the resonator to work in a ML operation rather than in a CW operation, a periodic loss/gain modulation is applied to the intracavity radiation whose period matches with the cavity round trip time. In the frequency domain, the periodic modulation leads to the apparition of sidebands whose frequencies coincide with those of the adjacent longitudinal laser modes. In this way, energy is transferred from one mode to adjacent ones, and as a result, all longitudinal modes become finally locked in phase. In the time domain, the periodic modulation can be visualized as an intracavity shutter that is open once per round trip time, leading to higher net gain on each round trip for the light concentrated in that time window. Mode-locking requires a mechanism that results in higher net gain for short pulses compared to the CW operation. This can be done either by means of an active element or passively by means of a saturable absorption (real or effective) [70]. The active ML technique consists in the introduction of an external modulation inside the cavity that enforces pulsed operation. In the case of intracavity amplitude modulation, the modulator is used

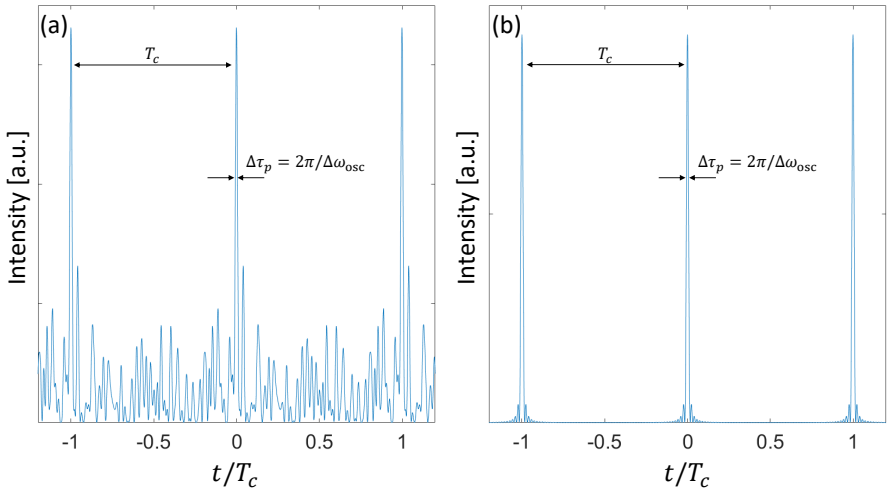


Figure 3.2: Intensity at the output of a laser emitting simultaneously on $N = 61$ modes of equal amplitude and (a) random phases; (b) identical phases. In both cases, the pattern repeats itself every cavity round-trip time T_c and the sharpest peak has approximately the same width $\Delta\tau_p$. The y scales are not the same on the two plots. The strongest peak of the mode-locked laser in (b) is approximately N times greater than the mean intensity in (a). Adapted from Ref. [60].

as a fast shutter in the cavity. It has to work at an exact multiple of the cavity repetition rate f_{rep} so that a pulse will always pass through the modulator when the shutter is open, cutting away the pulse edges and pushing it towards shorter periods [65]. In the case of passive mode-locking, the ML operation is usually achieved by introducing a saturable absorber into the cavity. The absorber will reduce the losses when the laser works in the pulsed operation due to the saturation of the absorbing medium. The saturable absorber acts as a shutter that the pulse itself activates with a much faster modulation rate than active shutters. This phenomenon is known as self-amplitude modulation (SAM) [65, 71]. In section 3.3.2, we will see how the Kerr effect can be utilized as an effective saturable absorbent.

3.3.2 *Passive mode-locking based on the Kerr effect*

When an optical pulse of high intensity travels through a dielectric material, the polarization inside the dielectric medium is no more directly proportional to the electric field (the proportionality factor

being the refractive index n_0). A term proportional to the time- and space-dependent intensity $I(t, \boldsymbol{r})$ has to be added to n_0 in order to take into account the nonlinearity:

$$n(t, \boldsymbol{r}) = n_0 + n_2 I(t, \boldsymbol{r}), \tag{3.25}$$

where $\boldsymbol{r}$ is the position transverse to the beam propagation and n_2 is the nonlinear refractive index. This effect is known as the optical Kerr effect [65, 71, 72]. It has consequences both in the spatial and in the temporal domains. In the transverse spatial domain, *i.e.* the $\boldsymbol{r}$ direction, due to the Gaussian-shaped beam profile, light intensity at the center of the beam is higher. It will thus experience a larger refractive index, leading to a retardation of the most intense part of the beam relative to its wings. The dielectric material therefore behaves as an effective converging lens for intense light pulses. In the time domain, the refractive index will vary with the pulse propagation. Indeed, the refractive index will increase with increasing intensity, that is on the leading part of the pulse envelope, causing an increase in the optical thickness (*i.e.* the product between the material thickness and the refractive index) with respect to time. This situation is analogous to a light source moving away from the propagation direction, resulting in a red shift of the leading part of the pulse. Similarly, the trailing part of the pulse will undergo a blue shift. The consequence of the Kerr effect in the time domain is known as self-phase modulation (SPM) [65, 71, 73].

The Kerr lensing effect can be employed as a saturable absorber to perform SAM and thus to favour the ML operation over the CW one in solid-state lasers. High intensity pulses are focused more strongly due to the Kerr effect taking place in the crystal of the gain medium. When combined with an intracavity aperture, the Kerr lensing effect increases the net gain for short pulses with high peak intensities compared to the low intensity modes of a continuous mode operation. The technique is known as Kerr mode-locking (KML). The intracavity aperture can be either a physical aperture placed in the resonator cavity or a better overlap between the pump beam and the pulse beam inside the gain medium. The first approach is known as hard aperture mode-locking and the second one as soft aperture. Hard-aperture KLM is usually reproducible and easier to specify. A stable ML regime strongly depends on a careful adjustment of the resonator. The resonator stability and the focusing conditions in the Kerr medium must be properly controlled [65, 66, 71, 74].

The pulse duration depends on the bandwidth of the gain medium. The broad fluorescence emission of Ti:Sapphire laser crystals can potentially support light pulses of a few fs in duration [66]. While SAM is necessary to favour ML operation over CW operation, it is not sufficient to generate pulses of a few fs alone [64, 66, 71]. Pulse shape and duration depend more on SPM and GDD than SAM. The duration is ultimately limited by the onset of instabilities, by the finite bandwidth of the gain medium and/or the frequency dependence of the cavity GDD. If the overall GDD is positive, pulse shortening induced by SAM will be limited to the picosecond level. On the other hand, an overall negative GDD, combined with SPM can efficiently support pulse shortening into the fs regime [65, 66, 75, 76].

3.4 Time and spectral representations of a train of ultrashort pulses emitted by a femtosecond laser

This section relies on Ref. [62, 77, 78].

A femtosecond laser emits a train of ultrashort pulses with a pulse repetition period T_R, each of these pulses being described by the expression of equation (3.1). The resulting electric field therefore consists in the convolution of the electric field of equation (3.1) with the delta comb function, leading to:

$$E_{\text{train}} = A(t)\exp\left(\mathrm{j}\omega_c t\right) * \sum_{m=-\infty}^{+\infty} \delta(t - mT_R). \tag{3.26}$$

From one pulse to another, the absolute phase $\phi_0(t)$ will vary of a quantity $\Delta\phi_{\text{GPO}}$, known as the group-phase offset phase because of the presence of dispersive elements inside the laser cavity, *i.e.* the Ti:Sapphire amplifier medium and the eventual prisms. Indeed, inside the cavity, the carrier will propagate at the phase velocity $v_p = \omega/k$ and the envelope at the group velocity $v_g = \mathrm{d}\omega/\mathrm{d}k$, resulting in a phase lag $\Delta\phi_{\text{GPO}}$ between the pulse envelope and carrier per round trip of the pulse in the laser cavity. The pulse train is illustrated in Figure 3.3(a), where the meaning of the group-phase offset phase is made explicit. The phase lag between the pulse envelope and the carrier

can be estimated by combining equation (3.7) with the fundamental definitions of the phase and group velocities:

$$\Delta\Phi_{GPO} = -\omega \int_0^L \left(\frac{1}{v_g} - \frac{1}{v_p}\right) \mathrm{d}x = \int_0^L \frac{\omega^2}{c} \frac{\mathrm{d}n(\omega, x)}{\mathrm{d}\omega} \mathrm{d}x. \tag{3.27}$$

It should be noted that the group-phase offset only arises from the first-order dispersion of all elements present in the laser cavity.

Since group-phase offsets of integer multiples of 2π do not change the electric field pattern of a laser pulse, the quantity of interest is:

$$\Delta\phi_{\mathrm{CEO}} = \Delta\phi_{\mathrm{GPO}} \bmod 2\pi \tag{3.28}$$

Equation (3.28) describes the changes of the carrier-envelope offset phase ϕ_{CEO} per round-trip. Since $\Delta\phi_{\mathrm{CEO}}$ depends on the intracavity materials properties, fluctuations in these properties will give rise to variations in $\Delta\phi_{\mathrm{CEO}}$. However, pulse-to-pulse fluctuations are extremely small since they correspond to changes in one round-trip time. Causes of these fluctuations, along with ways to suppress them are further developed in section 3.6.2.

The carrier-envelope offset frequency f_{CEO} is defined as:

$$2\pi f_{\mathrm{CEO}} = \omega_{\mathrm{CEO}} = \frac{\Delta\phi_{\mathrm{CEO}}}{T_R}. \tag{3.29}$$

Alternatively:

$$f_{\mathrm{CEO}} = \frac{\Delta\phi_{\mathrm{CEO}}}{2\pi} f_{\mathrm{rep}}. \tag{3.30}$$

It should be noted that the carrier-envelope offset frequency also depends on the repetition rate f_{rep} of the femtosecond laser which is a function of the laser cavity length. The two degrees of freedom of the frequency comb are thus coupled. However, the impact of the fluctuations of f_{rep} on f_{CEO} is small compared to the variations of the dispersion of the intracavity elements. Indeed, f_{rep} typically changes of about 100 Hz per second while f_{CEO} can sweep of several MHz per second in the absence of proper environmental shielding of the laser. The main cause of fluctuations in the offset frequency is therefore the dispersion variation of the intracavity elements [77].

Equation (3.29) allows to rewrite equation (3.26) as follows:

$$E_{\mathrm{train}} = A(t) \exp\left(\mathrm{j}\omega_c t + \mathrm{j}\omega_{\mathrm{CEO}} t\right) * \sum_{m=-\infty}^{+\infty} \delta(t - mT_R). \tag{3.31}$$

The spectrum $\tilde{E}(f)$ of the light emitted by a femtosecond laser is given by the Fourier transform of equation (3.31):

$$\tilde{E}(f) = \tilde{A}(f - f_c) \cdot \sum_{m=-\infty}^{+\infty} \delta(f - m f_{\text{rep}} - f_{\text{CEO}}), \tag{3.32}$$

with $f_c = \frac{\omega_c}{2\pi}$, the carrier frequency. The spectrum $\tilde{E}(f)$ thus consists in the spectrum of the envelope pulse, denoted $\tilde{A}(f - f_c)$, multiplied by a delta comb function or frequency comb. In other words, the laser only emits light at discrete frequencies ν_n given by:

$$\nu_n = n f_{\text{rep}} + f_{\text{CEO}}, \tag{3.33}$$

where n is a large integer on the order of 10^6 that indexes the comb line. The resulting spectrum is illustrated in Figure 3.3(b). Equation (3.33) implies that each optical frequency at the output of the light source can be unambiguously described by the use of only three parameters: f_{rep}, f_{CEO} and n. The first two parameters are frequencies lying in the RF domain. Their measurement and stabilization is the topic of section 3.6.2. Once stabilized, the frequency comb can be seen as a frequency ruler, leading to metrological measurements in optical spectroscopy if one is capable of measuring the comb line index n with either dispersive or interferometric methods, as discussed in section 3.5.

The frequency comb generated by a ML oscillator should not be confused with the longitudinal modes of the cavity, which are only equidistant in the absence of intracavity dispersion. From a glance at the relationship between equations (3.31) and (3.32), we see that the spacing between the teeth of the frequency comb generated by a mode-locked laser is imposed by the cavity round-trip time of the pulse propagating inside the cavity [77].

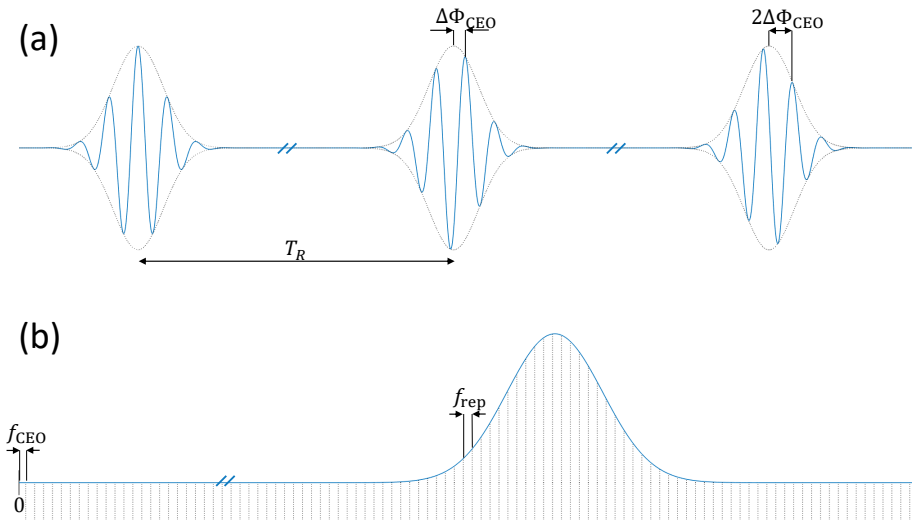


Figure 3.3: Time and spectral representations of light at the output of a ML femtosecond oscillator. (a) Electric field at the output of a femtosecond laser with respect to time. The different pulses are separated by the repetition period T_R. There is a phase lag $\Delta\phi_{\text{GPO}}$ per round trip between the envelope and the carrier. (b) Spectrum of the light at the output of a femtosecond laser. The teeth of the generated frequency comb are spaced by the repetition frequency f_{rep} of the laser and the whole comb is shifted by a value f_{CEO} because of intracavity dispersion phenomena.

3.5 THE FREQUENCY COMB: A SOURCE FOR SPECTROSCOPIC APPLICATIONS

The use of frequency combs for high-resolution molecular optical spectroscopy requires to precisely determine the molecular transition frequencies in order to ease the interpretation of their fingerprints. In section 3.4, we have seen that light emitted by a ML femtosecond laser was structured in the frequency domain, the structure being a frequency comb where each discrete frequency ν_n is described by three parameters: the offset frequency f_{CEO}, the repetition frequency f_{rep} and the comb line index n (see equation (3.33)). If f_{CEO} and f_{rep} are known and remain constant, a rough estimate of n permits absolute frequency measurements, opening the door to high precision metrological applications. Moreover, f_{CEO} and f_{rep} both lie in the radiofrequency domain, allowing for the transposition of RF standards such as the caesium atomic clock or the rubidium atomic clock in the optical domain [78]. Considerations about their measurement and stabilization are given in section 3.6.2. The rest of this section is devoted to techniques allowing for the measurement of n.

In the near-infrared spectral range, the comb lines can be resolved using dispersive or interferometric methods. Dispersive methods usually rely on the combination of a Virtually-Imaged Phased Array (VIPA) and of a grating in order to build a 2D map of the one-dimensional spectrum on a CCD camera [27, 79, 80]. While this method allows for very fast measurements, it suffers from a smaller resolving power compared to interferometric methods. Furthermore, dispersive methods are very sensitive to misalignment. Interferometric methods either rely on the use of a FTS [81] or on the use of a second frequency comb with a different repetition rate in order to perform multi-heterodyne detection of the comb spectrum by measuring the beating of the two combs. This second method is known as dual-comb spectroscopy [82]. Both approaches are similar in the sense that two comb pulse trains scan through one another in the time domain but dual comb spectroscopy does it much faster, since an entire scan is completed in a time period of $1/\Delta f_{\mathrm{rep}}$, where Δf_{rep} is the difference between the two repetition rates [59]. However, this technique requires the use of two stabilized frequency-combs, making the experimental setup complex and too expensive for the frame of this thesis.

On the other hand, combining the frequency comb with a FTS is straightforward and, by matching the repetition frequency of the comb with the maximum OPD induced by the translation stage, it is possible to overcome the intrinsic resolution imposed by the FTS [13, 14]. Indeed, in Fourier transform spectroscopy, the true interferogram is multiplied by a boxcar-like function associated with the finite length of the translation stage. The spectrum is therefore convolved with a sinc function. Because the spectrum without any instrumental lineshape is a frequency comb, the measured spectrum consists in a sum of sinc functions centered on the teeth of the frequency comb. If the maximum OPD is such that the zero-crossings of each sinc function match with the other teeth, no crosstalk between them is observed, resulting in the absence of instrumental lineshape. The sub-nominal resolution is reached by changing slightly f_{rep} or f_{CEO} in order to interleave new values between existing ones. Further details will be given in Chapter 5.

3.6 DESIGN AND FABRICATION OF A HOMEMADE FREQUENCY COMB

In sections 3.4 and 3.5, we have seen that the light spectrum at the output of a femtosecond resonator can only take discrete values ν_n that only depend on f_{CEO} and f_{rep}. If these two physical quantities are stable and known, we can use the structured spectrum as a frequency ruler. This section is divided in two parts. Section 3.6.1 first introduces the methodology followed for the design and fabrication of the femtosecond resonator which is at the heart of the frequency-comb setup. Then section 3.6.2 develops the method for the stabilization of f_{CEO} and f_{rep}, along with the first results.

From a chronological perspective, the design of the homemade femtosecond resonator came in a second time in the project. Its development was justified by our inability to stabilize the Mira 900 femtosecond resonator of Coherent that was already present in the laboratory due to intrinsic limitations concerning its pulse duration (see section 3.6.2). However, we have made the choice to first present the design of the new resonator because it seemed more relevant from the reader perspective to do it that way. The stabilization scheme presented in section 3.6.2 will be applied to the resonator presented in section 3.6.1.

3.6.1 *The femtosecond laser resonator*

In this section, we present the dimensioning of the resonator cavity for the homemade femtosecond laser we designed. It consists of 4 mirrors placed in a z-folded configuration and of a thin Ti:Sapphire crystal plate tilted at the Brewster's angle, as depicted in Figure 3.4(a). The two end mirrors are flat mirrors while the two others are concave mirrors used to focus the beam in the crystal and which ensure the resonator cavity stability. No prism was employed to compensate for the group-delay dispersion induced both by the crystal and air. Further considerations concerning the GDD compensation are given in subsection *Group-delay dispersion compensation*. The design makes use of Ref. [76] for several practical aspects. The method followed for the analysis of both resonator stability and the feasibility to mode-lock the laser depends on Ref. [74, 83]. This approach relies on the use of the ABCD law of Gaussian beam transformation in linear optical systems to model the cavity [84]. In this context, the Kerr medium is represented by a nonlinear ABCD matrix which is derived in the framework of aberrationless theory [85]. The derivation of the nonlinear ABCD matrix for the Kerr effect is presented in the subsection *Resonator cavity* along with the optimization of the dimensions of the resonator that ensure both self mode-locking and resonator stability. The dimensions of the resonator should also match with the dimensions of the cavity of the buffer gas cooling setup presented in chapter 4.

The reader who is unfamiliar with the ABCD formalism should refer to Ref. [84] for a good introduction of the key concepts.

Resonator cavity

This section relies on Ref. [84–86].

In this section, the ABCD representation of the Kerr medium is derived using the framework of aberrationless theory. To do so, analytical expressions for the modification of the beam spot size and for the radius of curvature of a Gaussian beam propagating in a Kerr medium are first obtained, starting from the scalar wave equation in the Kerr medium. In a second time, the ABCD matrix is estimated by looking at the evolution of the q parameter of the Gaussian beam between the input and the output of the Kerr medium.

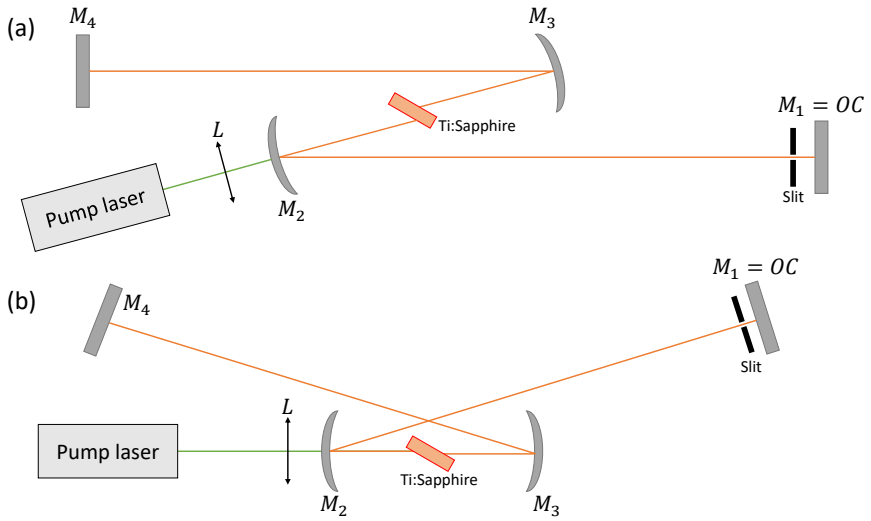


Figure 3.4: Optical layout of the femtosecond laser. The Ti:Sapphire crystal plate is placed at the Brewster angle for a wavelength of 800 nm and a polarization parallel to the optical bench. L stands for lens, M for mirror and OC for output coupler. The pump laser is a frequency-doubled Nd:YAG laser. (a) Z-shaped optical cavity. (b) γ-shaped cavity.

The electric field of a beam polarized in the $\hat{e}_x$ direction propagating along the z axis is given by:

$$\boldsymbol{E} = \frac{1}{2}\left[u\mathrm{e}^{\mathrm{j}(\omega t - kz)} + \text{c.c.}\right]\hat{e}_x, \tag{3.34}$$

with ω the angular frequency, $k = n_0\omega/c$, c being the velocity of light in vacuum, u the complex field amplitude which slowly varies with z and c.c. stands for complex conjugate. The beam profile is supposed to be Gaussian, meaning that the complex field amplitude u can be described by the following expression:

$$u(r,z) = \frac{U}{w}\exp\left(-\left(\frac{r}{w}\right)^2 - \mathrm{j}\frac{kr^2}{2R} + \mathrm{j}\Phi\right), \tag{3.35}$$

where r is the distanced from the z axis, U is a real constant amplitude factor, $w(z)$ is the spot size, $R(z)$ the radius of curvature and $\Phi(z)$ is the phase shift. The amplitude U is a constant value, considering the conservation of the beam power P, which is given by:

$$P = \frac{\pi c\varepsilon_0 n_0 U^2}{4}, \tag{3.36}$$

with $\varepsilon_0 = 8.854 \times 10^{-1}\text{F m}^{-1}$ the electric permittivity of free space.

We are interested in the propagation of this Gaussian beam in a Kerr medium which implies an intensity-dependent index of refraction given by:

$$n = n_0 + \frac{1}{2} n_2 |u|^2. \tag{3.37}$$

Within the paraxial approximation of the scalar diffraction theory, the propagation of the beam in this medium is described by the following scalar equation:

$$\nabla_T^2 u - 2\mathrm{j}k\frac{\partial u}{\partial z} + k^2 \frac{n_2}{n_0}|u|^2 u = 0, \tag{3.38}$$

where ∇_T^2 is the transverse Laplacian acting on the coordinates orthogonal to z.

Solving equation (3.38) requires the knowledge of the term $|u|^2$. In the framework of the aberrationless theory of diffraction, the beam maintains its Gaussian shape during its propagation in the Kerr medium [65]. The lenslike medium induces a Gouy phase shift which depends on the distance r from the z axis. To preserve the Gaussian shape, the phase shift and therefore the index of refraction n of equation (3.37) should vary in a quadratic manner with r [86]. This is accomplished by imposing $|u|^2$ to be a quadratic function of the form $c_1 + c_2 r^2$. The two coefficients c_1 and c_2 are determined by minimizing the Weighted Square Mean Error WSME:

$$\text{WSME} = \int_0^\infty \left(c_1 + c_2 r^2 - |u|^2\right)^2 |u|^2 2\pi r \mathrm{d}r, \tag{3.39}$$

leading to the following expression:

$$|u|^2 \simeq \frac{3}{4}\frac{U^2}{w^2}\left(1 - \frac{2r^2}{3w^2}\right). \tag{3.40}$$

Combining equations (3.35), (3.38) and (3.40) leads to a set of ordinary differential equations that, once solved, gives the expressions of $w(z)$, $R(z)$ and $\Phi(z)$:

$$w^2(z) = w_1^2\left[\left(1+\frac{z}{R_1}\right)^2+\left(\frac{\lambda z}{\pi n_0 w_1^2}\right)^2\left(1-\frac{P}{P_c}\right)\right] \tag{3.41}$$

$$\frac{1}{R(z)} = \left(\frac{w_1}{w(z)}\right)^2\left[\frac{1}{R_1}+\frac{z}{R_1^2}+z\left(\frac{\lambda}{\pi n_0 w_1^2}\right)^2\left(1-\frac{P}{P_c}\right)\right] \tag{3.42}$$

$$\begin{aligned}\Phi(z) = \Phi_1 + \frac{1-\frac{3P}{2P_c}}{\sqrt{1-\frac{P}{P_c}}}\Bigg[&\arctan\left(\frac{\pi n_0 w^2(z)}{\lambda R(z)\sqrt{1-\frac{P}{P_c}}}\right)\\ &-\arctan\left(\frac{\pi n_0 w_1^2}{\lambda R_1\sqrt{1-\frac{P}{P_c}}}\right)\Bigg],\end{aligned} \tag{3.43}$$

where w_1, R_1 and Φ_1 are the initial values for $z=0$ and λ is the vacuum wavelength. The parameter P_c is the critical power for self-focusing and it is given by:

$$P_c = \frac{c\varepsilon_0\lambda^2}{2\pi n_2}. \tag{3.44}$$

It is convenient to rewrite equations (3.41) and (3.42) using the ABCD formalism in order to use the resulting matrix for the simulation of the cavity and optimization of its dimensions. If q_1 represents the complex radius of curvature q in a plane just before the Kerr medium and q_2 the complex radius of curvature just after it, then, they are related by the following expression:

$$q_2 = \frac{Aq_1+B}{Cq_1+D}. \tag{3.45}$$

The optical system that is considered is made of a nonlinear material of length d with flat faces perpendicular to the z axis surrounded by a medium with refractive index 1. The refraction at the two interfaces is taken into account by multiplying the real radius of curvature by n_0 at the input and by dividing it by n_0 at the output. The resulting ray-transfer matrix is then given by:

$$\boldsymbol{M} = \sqrt{1-\gamma}\begin{pmatrix}1 & d_e\\ \frac{-\gamma}{(1-\gamma)d_e} & 1\end{pmatrix} \tag{3.46}$$

where $d_e = d/n_0$ is the effective length of the medium for $P = 0$ and

$$\gamma = \left[1 + \frac{1}{4}\left(\frac{2\pi w_c^2}{\lambda d_e} - \frac{\lambda d_e}{2\pi w_0^2}\right)^2\right]^{-1} \frac{P}{P_c}, \tag{3.47}$$

where w_c is the spot size at the center of the medium and w_0 is the spot size at the beam waist calculated as if $P/P_c = 0$. Since the elements of the matrix in equation (3.46) depend on the beam power and the complex radius, the matrix is therefore nonlinear. From equation (3.47), we can see that $\gamma \leq P/P_c$. Also, equation (3.46) is no longer valid for $\gamma > 1$.

In order to distinguish the linear propagation through a length d_e and the nonlinear part due the Kerr effect, the matrix $\boldsymbol{M}$ is re-expressed as follows:

$$\boldsymbol{M} = \begin{pmatrix} 1 & \frac{d_e}{2} \\ 0 & 1 \end{pmatrix} \boldsymbol{M_k} \begin{pmatrix} 1 & \frac{d_e}{2} \\ 0 & 1 \end{pmatrix}, \tag{3.48}$$

where

$$\boldsymbol{M_k} = \frac{1}{\sqrt{1-\gamma}} \begin{pmatrix} 1 - \frac{\gamma}{2} & -\frac{\gamma d_e}{4} \\ \frac{-\gamma}{d_e} & 1 - \frac{\gamma}{2} \end{pmatrix}. \tag{3.49}$$

The two matrices on the right and on the left of the matrix $\boldsymbol{M_k}$ in equation (3.48) correspond to a linear propagation through a medium of length $d_e/2$, the entire nonlinear effect is therefore lumped into the matrix $\boldsymbol{M_k}$. Finally, if $\gamma \ll 1$, $\boldsymbol{M_k}$ becomes:

$$\boldsymbol{M_k} \approx \begin{pmatrix} 1 & -\frac{\gamma d_e}{4} \\ -\frac{\gamma}{d_e} & 1 \end{pmatrix}. \tag{3.50}$$

This ray matrix is similar to the one obtained by combining the action of a lens of focal $f_k = d_e/\gamma$ with propagation through a negative distance $z_k = -\gamma d_e/4$ when neglecting the term in z/f [4]. The focal length f_k represents the self-focusing effect while the negative distance represents the self-shortening effect.

---

4 The ABCD matrix to model a lens is given by $\begin{pmatrix} 1 & 0 \\ -1/f & 1 \end{pmatrix}$ while the ABCD matrix associated with free propagation is given by $\begin{pmatrix} 1 & z \\ 0 & 1 \end{pmatrix}$. Combining the lens effect and the free propagation leads to $\begin{pmatrix} 1 & z \\ -\frac{1}{f} & 1 - \frac{z}{f} \end{pmatrix}$. If $z \ll f$, the term $\frac{z}{f}$ can be neglected.

The ABCD matrix given in equation (3.46) is not a true matrix operator but it can still be used like ABCD matrices associated with linear components, and combined with them by means of classical matrix multiplication, allowing for the estimation of the radius of curvature and the spot size in any position of the resonator as a function of the parameter γ. This formalism allows to derive a quantity of great importance for the design of an optical resonator for Kerr mode-locking: the small signal relative spot size variation, defined as follows:

$$\delta = \left(\frac{1}{w} \frac{\mathrm{d}w}{\mathrm{d}P} \right)_{P=0}, \tag{3.51}$$

where w is the spot size at a given plane inside the resonator. Self Kerr-lens mode-locking is possible when δ takes negative values since the spot size and the diffraction losses decrease when the power increases. It can be shown that for a given resonator, the value of $|\delta|$ reaches a maximum at the plane of one of the end mirrors and in the planes where the propagation from that mirror corresponds to a Fourier transform or to the formation of an image. These specific planes are the most relevant positions for placing an aperture that introduces nonlinear losses since the nonlinear effects are maximized. It is possible to derive an analytical expression for δ in the plane of mirror M_1:

$$\delta_1 = -\frac{1}{2} \frac{\alpha_1 + \alpha_2 S}{\alpha_1^2 + \alpha_2^2 + 2\alpha_1 \alpha_2 S}, \tag{3.52}$$

where α_1, α_2 and S are defined with respect to Figure 3.5 as follows:

$$\alpha_1 = \frac{2B_1 D_1}{d_e} - \frac{A_1 C_1 d_e}{2}, \tag{3.53}$$

$$\alpha_2 = \frac{2B_2 D_2}{d_e} - \frac{A_2 C_2 d_e}{2}, \tag{3.54}$$

$$S = A_0 D_0 + B_0 C_0, \tag{3.55}$$

where A_0, B_0, C_0 and D_0 are the elements of the one-way matrix relevant to the propagation from mirror M_1 to mirror M_2. The matrices associated with the linear optical elements at the left and the right of the Kerr nonlinear matrix must include the linear propagation from the center of the Kerr medium to the relevant end-faces of the crystal.

To achieve large sport size variations and, hence, strong nonlinear loss modulations, the resonator must be operated close to the stability limits. This is accomplished by placing two folding mirrors that strongly focus

the beam in the cavity, the stability of the resonator then deeply depends on the distance z between these two focusing elements. The behaviour of the resonator is also greatly affected by the location of the Kerr medium around this focus. This variable also controls the focusing condition without affecting the resonator stability. The distance between mirror M_2 and the closer face of the Ti:Sapphire rod is denoted by the variable x. A practical way to optimize the cavity consists in mapping the value of δ_1 as a function of x and z and to determine the regions in which the best trade-off between large values of δ_1 and acceptable tolerances can be achieved [74].

Derivation of the nonlinear ABCD matrix representing the Kerr medium relied on the hypothesis of a TEM_{00} Gaussian beam. In practice it is not the case because the folding mirrors and the Brewster angle of the Ti:Sapphire medium break the cylindrical symmetry of the beam [66]. If the resulting astigmatism is not very pronounced, the formalism can still be employed provided that the resonator is separated into two equivalent one-dimensional resonators corresponding to the tangential plane (in the cavity plane) and the sagittal plane (in the plane perpendicular to the cavity plane), with different equivalent lengths d_e of the Ti:Sapphire rod. In the case of the sagittal plane, d_e remains d/n while in the tangential plane, it becomes equal to d/n^3. The matrices associated with the folding mirrors also depend on the considered plane [74, 83]. For most of the resonators, the effect of astigmatism is to overestimate the value of δ_1 in the saggittal plane and to underestimate it in the tangential plane . However the formalism still describes reasonably well, apart from a scale factor, the mode behaviour in astigmatic resonators [74]. Another consequence of the break in symmetry of the cavity is that the Kerr-induced change in the beam diameter at the position of mirror M_1 is stronger in the tangential plane than in the saggittal plane. This Kerr-induced astigmatism is a consequence of the different self-focusing actions in the two transverse dimensions, which results from a difference in the corresponding confocal parameters of the cavity mode in the gain medium [74]. Because of the stronger effect in the tangential plane, a stronger SAM effect relative to the small signal loss can be achieved with a vertical slit than with a circular aperture [66].

In order to determine the dimensions of our setup, we estimated the relative spot size variation at the position of the mirror M_1, where the slit will be placed, as a function of x and z. We imposed the radii

of curvature of the two focusing mirrors to be equal to 100 mm for several reasons: (1) this radius of curvature is a standard value of the Layertec optics supplier and thus the mirrors were in stock, (2) it facilitates the design of the mount where the mirrors and the crystal are placed, smaller radii of curvature would lead to a much more congested layout in the vicinity of the crystal, (3) and finally, it allows to obtain a stable resonator with a cavity length of about 2 meters. The repetition frequency of such a resonator is approximately equal to 75 MHz, opening the door of dual comb spectroscopy when combined with the MIRA900 femtosecond laser already available in the laboratory.

An important factor, when designing the resonator is the cavity asymmetry factor ζ defined as:

$$\zeta = \frac{f_1^2}{f_2^2}\frac{L_2 - f_2}{L_1 - f_1}, \tag{3.56}$$

with f_1, f_2 the focal lengths of the two focusing mirrors and L_1, L_2 the lengths of the two arms of the resonator (see Figure 3.4). This factor will impact the stability range of the cavity but also the strength of SAM. An increase in the symmetry of the cavity, *i.e.* $\zeta \to 1$, will result in a higher SAM but the resonator will have to work closer to its stability limits, and it will therefore increase the constraints on the mechanics stability. A trade-off has to be found between these two considerations. A value $\zeta = 1.75$ is suggested by Spielmann *et al.* [66]. The slit is placed in the short arm of the cavity because it allows for broader regions with a negative value of δ as a function of x and z [74].

The dimensions of the Kerr mode-locked laser we designed are given in Figure 3.5, along with the matrices relevant for the estimation of the value of δ_1 given by equation (3.52). Their evaluation relies on the elementary matrices presented in Table 3.1. A plot of δ_1 as a function of x and z for the tangential plane is shown in Figure 3.6. The code for generating Figure 3.6 was validated by reproducing Figure 2 of Cerullo *et al.* in Ref. [74]. This contour plot only shows negative values of δ_1 since they represent the situations favourable to KML. We observe two stability regions that only depend on the distance z between the two mirrors. The lower zone is more sensitive to misalignments because the two mirrors are in a nearly confocal configuration. On the other hand, the upper region corresponds to the situation where the two end mirrors lie in nearly conjugated planes, meaning that the system is much less sensitive to misalignments. Cerullo *et al.* [74] respectively

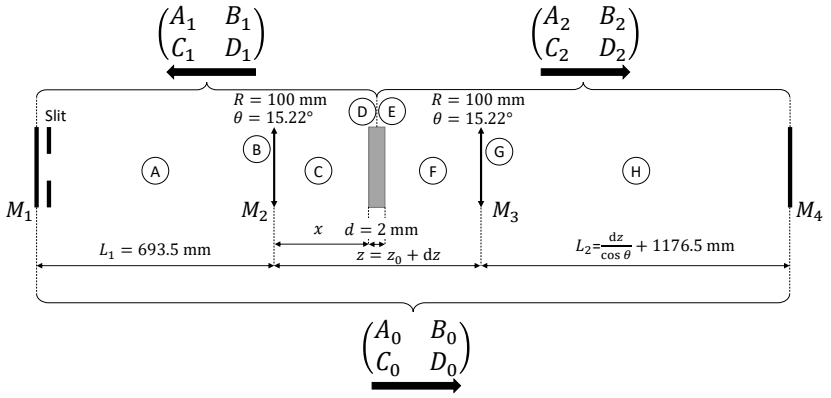


Figure 3.5: Linear representation of the resonator. The ABCD matrices with subscripts 1 and 2 represent the propagation from the Lumped Kerr medium to the two end mirrors. The ABCD matrix with the subscript 0 corresponds to the one-way matrix from mirror M_1 to mirror M_4. The slit is placed in front of M_1. The labels from A to H correspond to the linear matrices given in Table 3.1. The annotated dimensions are the ones employed for our laser resonator.

named these two regions the *high misalignment sensitivity* (HMS) region and *low misalignment sensitivity* (LMS) region. Cerullo *et al.* suggest to work in the LMS region at a distance $\Delta z = 0.5 - 1$ mm from the lower stability limit of this region since it represents the best trade-off in terms of output power, stability, and tolerance to the exact positions of the components of the resonator.

Table 3.1: Individual ABCD matrices associated with the linear optical system of Figure 3.5.

A: propagation from mirror M_1 to mirror M_2 $\begin{pmatrix} 1 & L_1 \\ 0 & 1 \end{pmatrix}$	B: reflection at the surface of mirror M_2 (tangential plane) $\begin{pmatrix} 1 & 0 \\ -\frac{2}{R\cos(\theta/2)} & 1 \end{pmatrix}$	C: propagation from mirror M_2 to the Ti:Sapphire plate $\begin{pmatrix} 1 & x \\ 0 & 1 \end{pmatrix}$	D: propagation from the surface of the Ti:Sapphire plate to the lumped nonlinearity plane (tangential plane) $\begin{pmatrix} 1 & \frac{d}{2n^3} \\ 0 & 1 \end{pmatrix}$
E: propagation from the lumped Kerr nonlinearity plane to the surface of the Ti:Sapphire plate (tangential plane) $\begin{pmatrix} 1 & \frac{d}{2n^3} \\ 0 & 1 \end{pmatrix}$	F: propagation from the Ti:Sapphire plate to mirror M_3 $\begin{pmatrix} 1 & (z_0 + \mathrm{d}z) - d - x \\ 0 & 1 \end{pmatrix}$	G: reflection at the surface of mirror M_3 (tangential plane) $\begin{pmatrix} 1 & 0 \\ -\frac{2}{R\cos(\theta/2)} & 1 \end{pmatrix}$	H: propagation from mirror M_3 to mirror M_4 $\begin{pmatrix} 1 & L_2 + \frac{\mathrm{d}z}{\cos(\theta)} \\ 0 & 1 \end{pmatrix}$

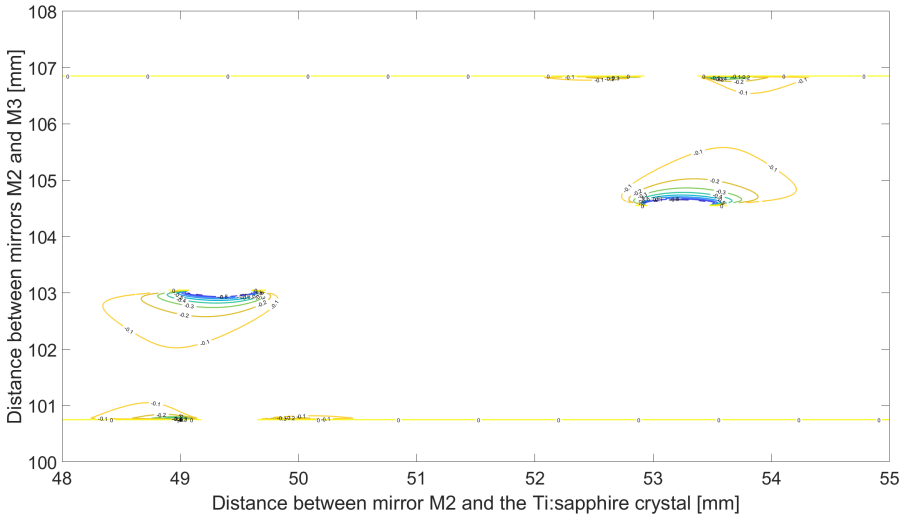


Figure 3.6: Contour map of the tangential small spot size variation δ in the plane of the mirror M_1 for $L_1 = 693.5$ mm, $L_2 + z = 1276.5$ mm, $\theta = 15.22°$, $R = 100$ mm and $d = 2$ mm.

Group-delay dispersion compensation

A stable resonator that favours the mode-locked behaviour over continuous emission is not enough to obtain pulses with duration lying in the femtosecond domain. It is necessary to add some compensation scheme for the positive GDD induced by the Ti:Sapphire amplification medium and ambient air. Indeed, as it was outlined in section 3.2.2, a net positive intracavity GDD leads a symmetrical temporal stretch of the pulse envelope, with the long wavelengths preceding the shorter ones. In a typical sub-10-fs Ti:Sapphire laser, the uncompensated round-trip GDD caused by the laser crystal alone amounts to more than 100 fs delay between the long and short wavelength components covered by the gain material [71]. To compensate for this positive GDD, a component with negative GDD should be inserted into the cavity. As mentioned in section 3.3.2, the overall GDD inside the cavity should be negative to reach pulses with duration in the fs domain [66].

Since no transparent material presents a negative GDD in the near infrared, we have to add optical components/layouts in the cavity that make use of the geometrical path length dependence of phase shift or multibeam interference effects to achieve effective negative GDD between the input and the output of such devices [63]. The first

category relies on the use of a combination of prisms or gratings in order to induce an angular dispersion in order to create the desired path length differences for the various frequency components of the pulse. While gratings are more efficient, they induce too-important losses for intracavity dispersion compensation. The prism compressor provides less GDD compensation for a similar footprint than a typical grating compressor but they introduce very little losses because the individual prisms that constitute the compressor are designed to be used at the Brewster incidence angle. However they are only capable of compensating GDD and not higher order dispersion terms, limiting their use in oscillators generating pulses longer than 10 fs. Furthermore, their use increases the design complexity and makes the alignment of the resonator more difficult [63].

The second category makes use of dielectric mirrors with an increasing thickness in the layers constituting the coating of the mirrors. The Bragg condition for maximum reflection efficiency becomes a function of penetration depth into the coating structure. The shorter wavelengths are therefore reflected earlier in the mirror structure while longer wavelengths deeper. Negative GDD results from the longer optical path lengths experienced by increasingly longer wavelengths [63]. As suggested by Tsermaa *et al.* [76], we will use a 2 mm-thin Ti:Sapphire crystal in the resonator that is highly doped (see Table B.2 of Appendix B.2 for its complete specifications). As a consequence, the positive GDD induced in the crystal can be compensated using only chirped mirrors. In the remaining of this section, we will first detail the estimation of the GDD in the cavity. In a second time, we will present the optics employed in the resonator and their GDD.

As already mentioned, in order to select the chirped mirrors for GDD compensation, we first have to estimate the intracavity GDD, which may be obtained using the following expression (see section 3.2.2):

$$\mathrm{GDD}(\omega_c) = \left.\frac{\partial^2 \phi}{\partial \omega}\right|_{\omega_c} = l \left.\frac{\partial^2 k(\omega)}{\partial \omega^2}\right|_{\omega_c} = \frac{l}{c} \left.\frac{\partial^2 (\omega n(\omega))}{\partial \omega^2}\right|_{\omega_c}, \qquad (3.57)$$

where l is the distance traveled by light in the medium characterized by a frequency-dependent refractive index $n(\omega)$ and c the velocity of light in vacuum.

From equation (3.57), we see that it is necessary to know the expression of $n(\omega)$ to evaluate the GDD. Empirical expressions of $n(\omega)$ were

found in the literature for both sapphire [87] and air [88] and the second derivative of the product $k(\omega) = n(\omega)\omega$ was computed by means of fourth order central finite differences:

$$\left.\frac{\partial^2 k}{\partial \omega^2}\right|_{\omega_c} = \frac{-k_{\omega_c+2\Delta\omega} + 16k_{\omega_c+\Delta\omega} - 30k_{\omega_c} + 16k_{\omega_c-\Delta\omega} - k_{\omega_c-2\Delta\omega}}{12\Delta\omega^2}, \tag{3.58}$$

where $\Delta\omega$ is the spacing between two adjacent equidistant values of $k(\omega)$ on which the function is evaluated.

The distance l traveled by light in these two media was obtained using the dimensions of the setup given in Figure 3.5.

In the case of sapphire, the empirical refractive index was obtained using the Sellmeier equation presented in Ref. [87] and given by:

$$n(\lambda) = \sqrt{\frac{A_1\lambda^2}{\lambda^2 - \lambda_1^2} + \frac{A_2\lambda^2}{\lambda^2 - \lambda_2^2} + \frac{A_3\lambda^2}{\lambda^2 - \lambda_3^2}}, \tag{3.59}$$

with

$$\begin{cases} A_1 = 1.023798, & \lambda_1 = 0.06144821 \\ A_2 = 1.058264, & \lambda_2 = 0.1106997 \\ A_3 = 5.280792, & \lambda_3 = 17.92656. \end{cases}$$

In equation (3.59), the wavelength λ is expressed in μm. Equation (3.59) can be rewritten in terms of ω rather than λ as follows:

$$n(\omega) = \sqrt{\frac{A_1}{1 - B_1^2\omega^2} + \frac{A_2}{1 - B_2^2\omega^2} + \frac{A_3}{1 - B_3\omega^2}}, \tag{3.60}$$

with $B_i = \frac{\lambda_i}{2\pi c_{\mu\text{m}}}$ and $c_{\mu\text{m}}$ the light velocity in μm s^{-1}.

Similarly, an expression of the refractive index for standard air at 15 degrees Celcius, 1 atm and 0% humidity with respect to the wavelength was found in Ref. [88] and is given by:

$$10^8(n_{\text{Air}} - 1) = \frac{k_1}{k_0 - \left(\frac{1}{\lambda}\right)^2} + \frac{k_3}{k_2 - \left(\frac{1}{\lambda}\right)^2}, \tag{3.61}$$

with

$$\begin{cases} k_0 = 238.0185 & k_2 = 57.362 \\ k_1 = 5792105 & k_3 = 167917. \end{cases}$$

Equation (3.61) can be rewritten as follows:

$$n_{\text{Air}}(\lambda) = 1 + \frac{10^{-8}\frac{k_1}{k_0}}{1 - \frac{1}{k_0}\left(\frac{1}{\lambda}\right)^2} + \frac{10^{-8}\frac{k_3}{k_2}}{1 - \frac{1}{k_2}\left(\frac{1}{\lambda}\right)^2}. \tag{3.62}$$

Finally, the refractive index of equation (3.62) is re-expressed as a function of ω, leading to:

$$n_{\text{Air}}(\omega) = 1 + \frac{A_1}{1 - B_1^2\omega^2} + \frac{A_2}{1 - B_2^2\omega^2}, \tag{3.63}$$

with

$$\begin{cases} A_1 = 10^{-8}\dfrac{k_1}{k_0} & B_1 = \dfrac{1}{2\pi c\sqrt{k_0}} \\ A_2 = 10^{-8}\dfrac{k_3}{k_2} & B_2 = \dfrac{1}{2\pi c\sqrt{k_2}}. \end{cases}$$

All the ingredients required to evaluate the GDD are now available. In order to validate our approach, we first reproduced the values given by Tsermaa *et al.* [76]. In a second time, we estimated the positive GDD induced by air and the crystal in our cavity and we obtained a value of 350 fs^2 per cavity round trip at 780 nm. In other words, the GDD compensating optical elements should induce a negative GDD of at least 350 fs^2 per cavity round trip to ensure an overall negative cavity GDD necessary for reaching pulses with duration in the fs range [66].

We will attempt to only rely on the use of chirped mirrors to compensate for the positive GDD induced by the crystal and air. A balanced distribution of the negative GDD in the two arms of the cavity allows the pulse to be short at each end of mirror and at the centre of the gain medium. It guarantees that the spatial and temporal foci of the pulse coincide in the crystal, allowing for higher peak intensity which enhances SAM [76]. The GDD is mainly compensated by the pair of focusing mirrors (Ref. 142348 from Layertec) placed on each side of the gain medium (their GDD curves are given in Figure B.7 of Appendix B.2. We observe oscillations in the group delay dispersion for each chirped mirror. They are due to unwanted interference from multiple reflections between the chirped mirror structure and the top layer of the coating [71]. Purchasing a pair of chirped mirrors avoids this problem since they possess shifted dispersion characteristics to alleviate these oscillations. The output coupler (Ref. 101907 from Layertec) and the cavity-end mirror (Ref. 104219 from Layertec) also both compensate for positive GDD. Their GDD curves are respectively given in Figure B.8 and in Figure B.9 of Appendix B.2. Taking into account the fact that there are two reflections on the two folding mirrors per cavity round trip, and one reflection per round trip for the two other optics, the

cumulated negative GDD is comparable to the positive GDD in the cavity at 780 nm.

First results

The two above sections described the main considerations that need to be taken into account for the design of a femtosecond resonator, *i.e.* the resonator (i) should be at the limit of stability but stable, (ii) should favor KML over CW operation, and (iii) should have a small but negative overall GDD. To satisfy (iii), we used a thin highly doped Ti:Sapphire crystal cut at Brewster angle and we relied on the GDD compensation induced by the cavity mirrors. The population inversion in the Ti:Sapphire crystal required for the laser effect is obtained by optical pumping using a frequency-doubled Nd:YAG laser (model Verdi V-10 from Coherent). To satisfy conditions (i) and (ii), we used the contour map given in Figure 3.6. The contour map serves as a guideline for the mechanical design of our resonator. A schematic obtained with Solidworks and a photograph of our setup are respectively presented in Figures 3.7(a) and 3.7(b). The crystal and mirror M3 are placed on translation stages to adjust their positions with respect to mirror M2. It permits to sweep the contour map shown in Figure 3.6. The crystal is fixed on a rotation stage to optimize its orientation in order to place it at the Brewster angle with respect to the laser beam sustained in the cavity. This condition is required for reducing intracavity losses. Furthermore, the crystal needs to be cooled to avoid thermo-optical distortion and lensing effects due to the pumping process [89]. This is accomplished by connecting the crystal mount to the chiller already in use for the cooling of the pump laser.

A lens with a focal length of 150 mm and an AR coating at 532 nm (LA1433-YAG from Thorlabs) is employed to focus the Verdi pump beam into the crystal, the position of the focus being adjusted thanks to a third translation stage. The beam emitted by the Verdi pump laser is $s-$polarized while a $p-$polarization is needed for having no reflection at the Brewster incidence angle at the Ti:Sapphire crystal interface. We thus placed a multi-order half-wave plate at 532 nm (WPMQ05M-532) before the lens to inject the pump beam with the right polarization. Two diagnosis tools are placed at the output of the laser: a powermeter and a fast photodiode with enough bandwidth, *i.e.* higher than the repetition frequency of the laser in the KML mode (see section 3.6.2).

Another glance at Figures 3.7(a) and 3.7(b) allows to notice that a slit was placed in the arm L_1 in order to perform hard-aperture KML. The slit is placed on a translation stage for proper positioning. A micrometer screw allows to precisely adjust its opening. A last translation stage was employed to translate mirror M4 when mirror M3 is displaced so that the beam is correctly centred.

We determined a procedure to align the resonator. Following this procedure, the resonator was able to work in the CW operation, but we were not able to have a stable KML operation. When sweeping the end mirror M4 back and forth to trigger the KML operation, as suggested by Ref. [66, 74], we saw oscillations on the oscilloscope connected to the fast photodiode, indicating that it was at the edge of working in the KML operation. Inability to sustain the KML mode may be due to several reasons that were identified with this first version. (i) The folding angles of the $z-$shaped cavity are slightly above the specifications of Layertec, so that the GDD curves are no more applicable, meaning we cannot guarantee to have an overall negative GDD. (ii) Orientation of the mechanical piece supporting the two folding mirrors and the crystal does not match the mesh of threaded holes of the optical bench. The incidence angle on the injection mirrors of the pump beam is not equal to 45°, generating astigmatism in the pump beam. Furthermore the adjusting screws of these are too sensitive, preventing any fine-tuning of the pump beam alignment in the crystal. (iii) The adjusting screws of the two end mirrors (M1 and M4) are too sensitive as well, preventing optimization of the cavity alignment. (iv) The angle of the crystal is currently adjusted using slotted holes, which is not precise enough for a fine adjustment of the crystal angular position. (v) Finally, the resonator is not protected from airflows by any means. These air flows can disturb the KML operation.

A second version has been developed, with improvements for every drawback listed above. Changing the cavity geometry from a $z-$shaped to a $\gamma-$shaped cavity allowed us to work with smaller folding angles since the crystal mount starts hindering the beam passage for smaller folding angles, *i.e.* 11°. The schematic and the photograph of this second version are given in Figures 3.8(a) and 3.8(b). For this resonator, the orientation of the mechanical piece supporting the crystal and the two folding mirrors matches the threading holes mesh of the optical bench. In order to improve the overall mechanical stability, we employed stainless steel for all the mechanical pieces. We replaced

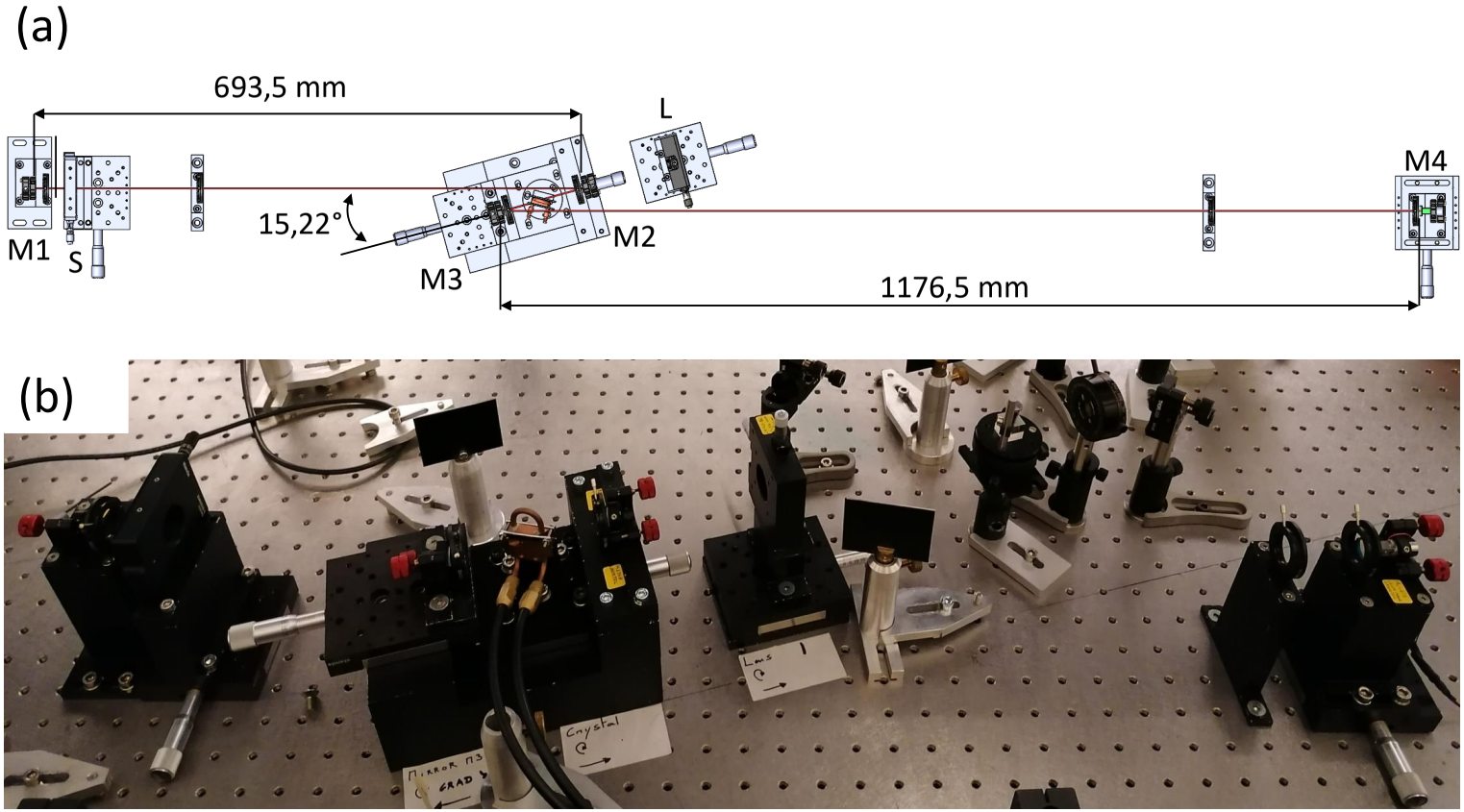


Figure 3.7: (a) Schematic of the homemade femtosecond resonator. L stands for lens, M for mirror and S for slit. The dimensions match with the ones shown in Figure 3.5.(b) Photograph of the resonator. The lengths $L_{1,2}$ of the two arms were equal to 230 mm and 400 mm on this photograph.

the KM05/M and the KM05T/M optical mounts from Thorlabs by the Polaris-K05S1 and the Polaris-K05T1 optical mounts from Thorlabs. These latter are more stable but they also have adjusters with a thinner thread, allowing to gain in tuning fineness of the cavity alignment. Furthermore, the crystal was placed on a commercial rotation stage (XRNR1/M reference from Thorlabs). To ensure that problem (i) is solved, we purchased another pair of chirped mirrors, (Ref. 141888 from Layertec) that compensates for 80 ± 40 fs^2 per bounce. When compared to prisms for the GDD compensation, the use of chirped mirrors presents the advantages of facilitating the cavity alignment and of avoiding that the pulse has to travel through extra materials. However, this is at the expense of the inability to fine-tune the GDD compensation. The latter could be overcome by placing the resonator inside a vacuum chamber since it would represent an elegant way to tune the contribution of air on the overall GDD.

In order to solve concern (v), we placed the femtosecond resonator in a box. We placed the lens and the crystal onto a same translation stage, avoiding to move the lens when the crystal is displaced. The focal length of the lens was changed to 100 mm (LA1509-YAG from Thorlabs). Changes in the distance between M2 and the crystal, and between M2 and M3 are measured using two digital indicators (ID-C112XB digimatic indicator from Mitutoyo). It simplifies the reading of these distances. They are complementary to the micrometer screws of the translation stages. Finally, we added to the aforementioned diagnosis tools a grating spectrometer (model S2000 from Ocean Optics). We were able to mode-lock this second resonator, as illustrated in Figures 3.9 and 3.10. Figure 3.9 shows a periodic signal with a frequency equal to 73.9 MHz measured with a fast photodiode (model 1801 from Newport) placed at the output of the resonator. The frequency of this signal matches with the expected repetition frequency, estimated using equation (3.15). Figure 3.10 depicts the spectrum measured with the grating spectrometer. We can see that the spectrum covers a large bandwidth, about 40 nm, indicating that the laser emits on a large number of modes. Supposing that the pulses emitted by the femtosecond laser are transform-limited, we can expect a duration of approximately 30 fs. The latter was used using the time-bandwidth product (see chapter 17 of Ref. [60]):

$$\Delta f_{\mathrm{FWHM}} \Delta t_{\mathrm{FWHM}} \geq 1.98. \tag{3.64}$$

Where Δf_{FWHM} and Δt_{FWHM} are the frequency bandwidth and the pulse duration at FWHM. The coefficient 1.98 supposes a sech^2 temporal profile. We employed the interferometric autocorrelator described in Appendix B.1 and we measured a pulse duration of 60 fs, the envelope of the autocorrelation pattern being depicted in Figure 3.11. The power at its output is about 200 mW for a pump power of 5 W.

Figure 3.12 depicts the contour map of the small spot size variation δ for the second version of our laser. The set points we were able to reach are displayed on the contour map in blue. There is some uncertainty in their absolute positioning because the digital indicators were adjusted using a digital caliper but we had to avoid touching the optics with it. We considered ± 0.5 mm of uncertainty in Figure 3.12. There are two arrows illustrating the path we followed to obtain the mode-locking operation. We first aligned it in order to optimize its power in the continuous wave operation. We then started sweeping back and forth mirror M4 using the PZT and we displaced mirror M3 towards mirror M2 until the power is reduced to about 30% of the maximum power (step 1 in Figure 3.12). We finally moved the crystal in order to broaden the emission spectrum of the laser (step 2 in Figure 3.12). At some point, the laser naturally switched from CW operation to ML operation, without requiring the use of the slit. The ML operation was sustained on time scales of about two hours. However, when the laser switched back from the ML operation to the CW operation, we had to re-align the cavity. We think it is due to changes in the pump beam pointing with time. However, even the alignment degrees of freedom of the new pump beam mirrors are too coarse to find back the ML operation using only them.

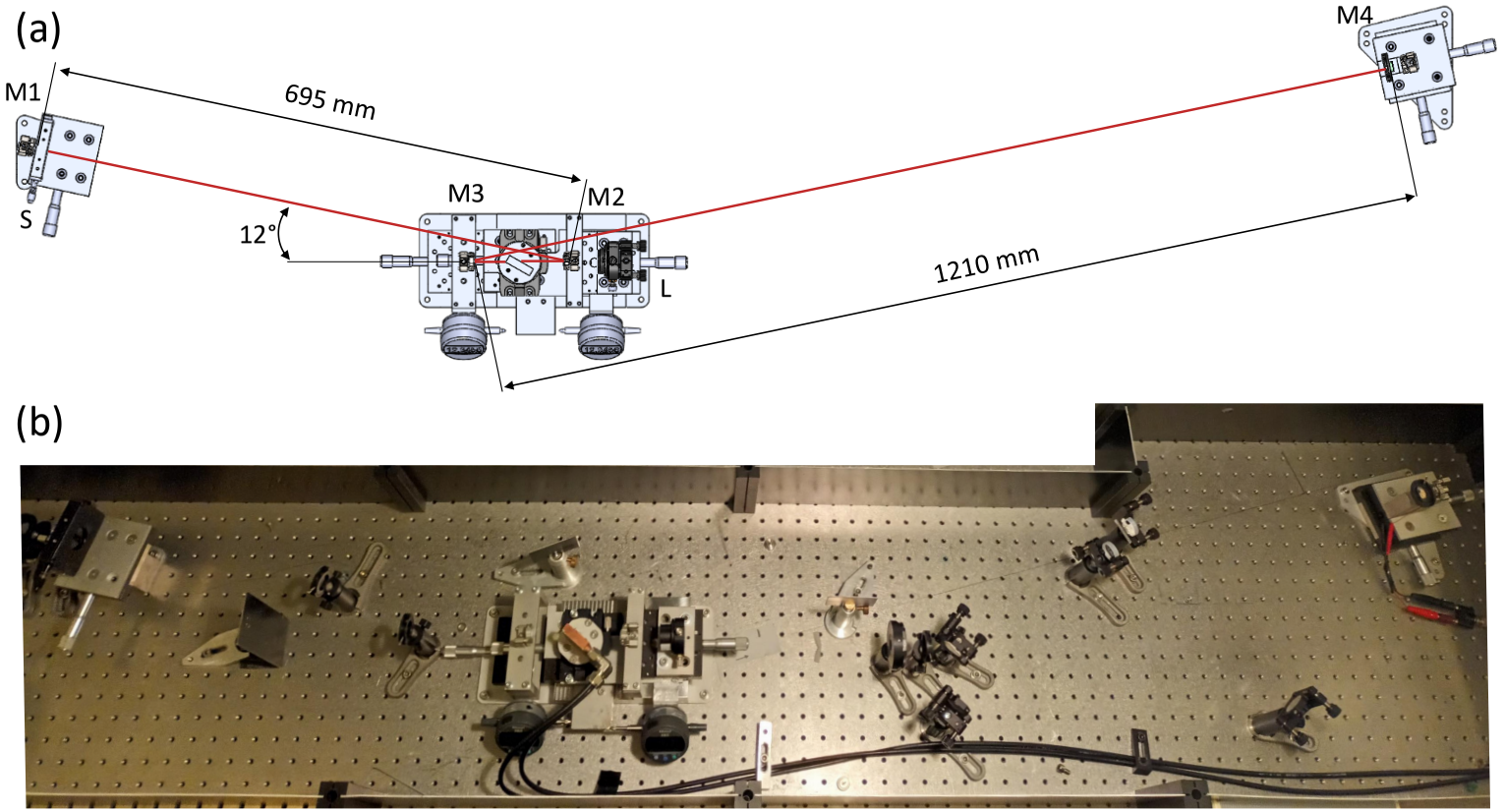


Figure 3.8: (a) Schematic of the second version of the homemade femtosecond resonator. L stands for lens, M for mirror and S for slit. The dimensions match with the ones shown in Figure 3.5, except for the folding angle, which is equal to 12°.(b) Photograph of the resonator. The lengths $L_{1,2}$ of the two arms were equal to 1210 mm and 695 mm. Two additional chirped mirrors are placed in the longer arm (not displayed in (a)).

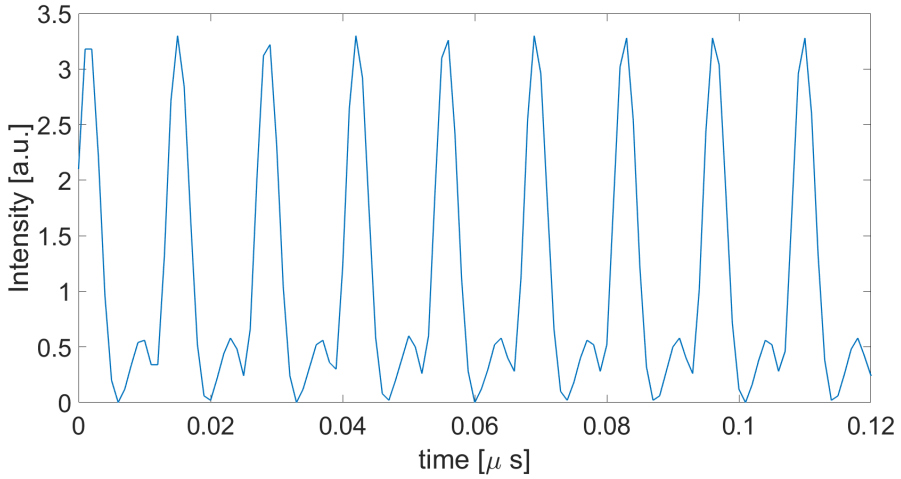


Figure 3.9: Intensity with respect to time at the output of the second version of the femtosecond resonator. The frequency of the signal is equal to 73.9 MHz.

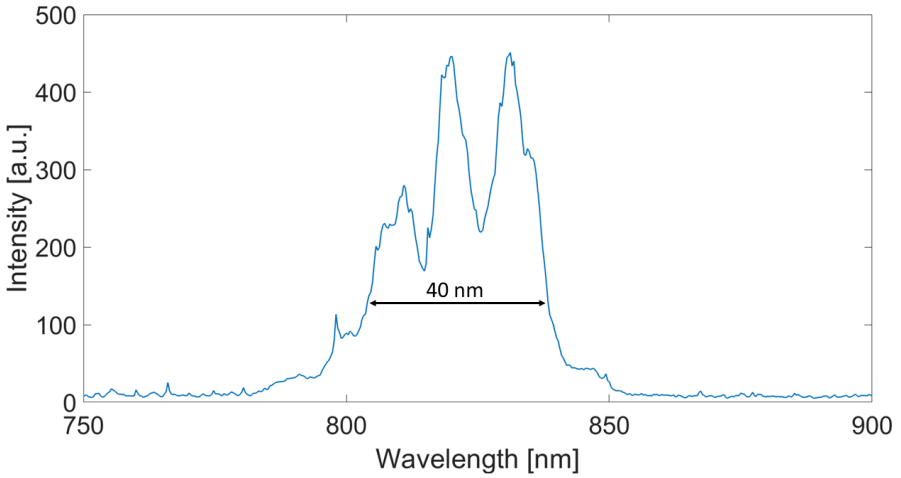


Figure 3.10: Spectrum at the output of the second version of the femtosecond resonator. It covers more than 40 nm around 820 nm.

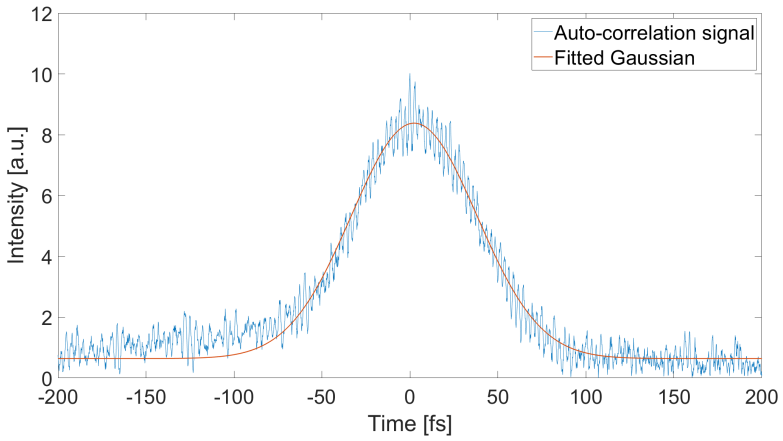


Figure 3.11: Measurement of the pulse duration with the interferometric autocorrelator. The FWHM of the Gaussian curve is equal to 84.17 fs, corresponding to a pulse duration of 59.51 fs using the deconvolution factor of Table B.1.

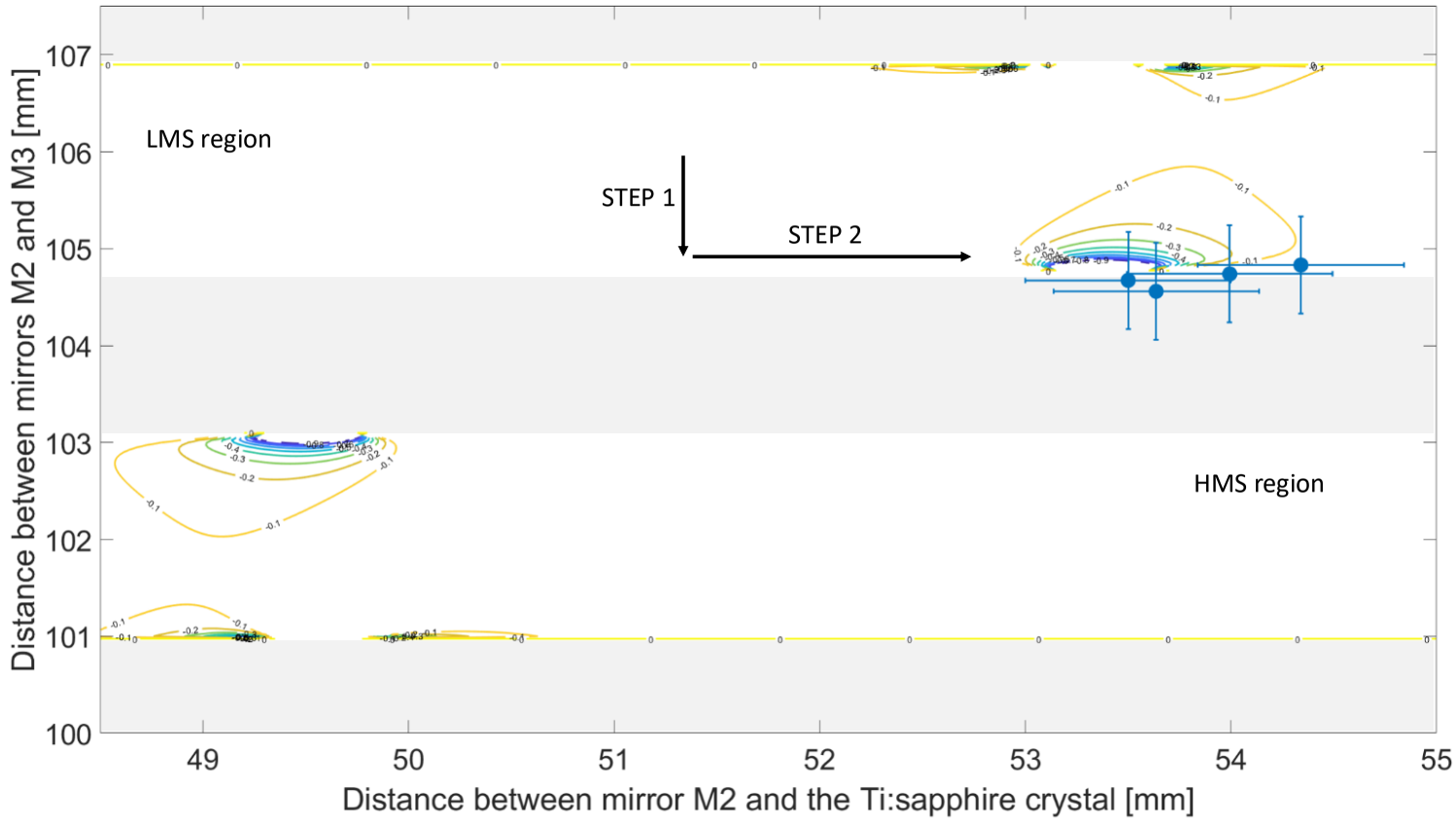


Figure 3.12: Contour map of the tangential small spot size variation δ in the plane of mirror M_1 of the second version of the femtosecond resonator. The 4 blue dots represent the set points for which the resonator worked in the pulsed mode. The gray areas are regions for which the CW operation is unstable. Dimensions of the resonator: $L_1 = 695$ mm, $\theta_{L_1} = 12°$, $L_2 = 1210$ mm, $\theta_{L_2} = 14°$, $\lambda = 825$ nm. The output power is reduced to about 30% of the maximum output power when in Step 1.

3.6.2 *Stabilization of the femtosecond laser resonator*

As already discussed in section 3.4, the spectrum of a ML laser consists of a comb of optical frequencies spaced by the repetition frequency and shifted by the offset frequency. These two frequencies lie in the RF domain, allowing for the transposition of the microwave caesium/rubidium frequency standard to the optical frequency domain [90]. This is accomplished by measuring the repetition and offset frequencies and locking them on an external clock. The sequence of elements is very similar for the two stabilization schemes. It is shown in Figure 3.13. They will differ in the method employed for the measurement of the physical value of interest, *i.e.* the repetition frequency or the offset frequency, and in the actuation used to actually provide the feedback to the system. As will see in the next two subsections, these physical values will be measured by observing a beating signal that is compared with a sine wave generated by a RF-synthesizer that plays the role of the external clock. The model employed for the two feedback loops is an A2255 arbitrary waveform generator from the Berkeley Nucleonics corp. company that has two independent outputs, one per feedback loop. It is provided with an input for an external frequency standard required for metrological applications. Comparison between the beat signal and the RF-synthesizer is performed by cascading a frequency mixer (ZRPD-1+ phase detector from MiniCircuits) and a lowpass filter.

The next two subsections are dedicated to specificities associated with either f_{rep} or f_{CEO}.

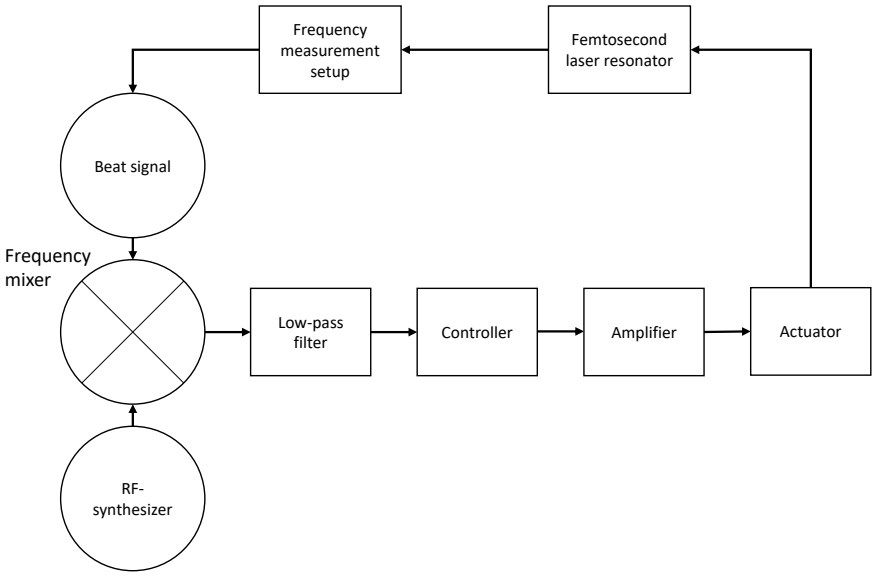


Figure 3.13: Sequence of elements for the measurement and stabilization of the repetition and offset frequencies. For the repetition frequency: the actuator is the end mirror mounted on a piezoelectric crystal and the frequency measurement setup is a fast photodiode placed at the output of the cavity. For the offset frequency: the actuator is an AOM placed between the pump laser and the femtosecond laser resonator and the frequency measurement setup is the 1f-2f interferometer detailed in the text.

Repetition frequency

We have seen in section 3.2.1 that the value of the repetition frequency depends on the cavity length L following (see equation (3.15)):

$$f_{\text{rep}} = \frac{c}{2L}, \tag{3.65}$$

with c the light velocity. Therefore, any fluctuation in the cavity length will lead to fluctuations in the repetition frequency, making some stabilization scheme mandatory for metrological applications.

Measurement of the repetition frequency is straightforward. It simply requires to inject a part of the KML laser output beam on a photodiode with enough bandwidth to measure the beating between two adjacent teeth of the frequency comb [90]. For our light source, the beating frequency is approximately equal to 75 MHz. The repetition frequency can be tuned, and thus corrected, by adjusting the cavity length using a piezoelectric transducer to translate the end mirror, as suggested in Ref. [91].

In the case of the repetition frequency, the signal shown in Figure 3.13 is directly available for the MIRA900 and it is measured by a photodiode with a bandwidth of 125 MHz (model 1801 photodiode from Newport) for the homemade resonator. The error signal is generated by mixing the signal at the output of the fast photodiode with the signal generated by a RF-synthesizer (reference frequency) and by lowpass filtering the resulting signal. The error signal is finally sent into a PID controller to generate the correction signal applied on a piezoelectric transducer. For the MIRA900, we replaced one of the mirrors by another one mounted on a preloaded piezoelectric transducer (commercial solution from Coherent). For the homemade femtosecond resonator, the end-mirror was simply glued on a low-voltage piezoelectric transducer (P-887.31 from PI).

Offset frequency

There is no coupling mechanism between the propagation speeds of the carrier and of the envelope inside a KML laser, meaning that the carrier-to-envelope phase, and thus the offset frequency, will exhibit irregular fluctuations in the absence of some locking scheme (see section 3.4). Intensity and beam pointing fluctuations in the laser may be at the origin of the carrier-envelope phase changes [62].

While the measurement of the repetition frequency is straightforward, measurement of the offset frequency is more complicated it cannot be measured directly. The measurement has to be performed in an indirect manner by performing some heterodyne detection [62]. A common way to accomplish this is to measure the beating between the second harmonic of the n^{th} tooth from the low-frequency wing of the comb with $2\nu_n$, obtained via second harmonic generation (SHG), with the $2n^{\text{th}}$ tooth from the high-frequency wing ν_{2n} [62, 77, 90, 92]:

$$2\nu_n - \nu_{2n} = 2\left(nf_{\text{rep}} + f_{\text{CEO}}\right) - \left(2nf_{\text{rep}} + f_{\text{CEO}}\right) = f_{\text{CEO}}, \tag{3.66}$$

where equation (3.33) was used to re-express ν_n and ν_{2n} in terms of f_{rep} and f_{CEO}. Since this technique does not require any external reference, it is known as a self-referencing method. The beating can be measured using a $1f - 2f$ interferometer that requires the spectrum to spread over an octave. A schematic and a photograph of the layout of the interferometer we implemented are respectively presented in Figures 3.14 and 3.15. A beamsplitter separates the horizontally polarized beams issuing from the photonic-crystal fiber in two parts. The low-frequency content of the transmitted beam is removed thanks to a short-pass edge filter (model FESH800 from Thorlabs) with a cut-off wavelength at 800 nm. In a similar way, the high-frequency content of the reflected beam is removed using a long-pass edge filter (model FELH600 from Thorlabs), with a cut-on wavelength at 600 nm. The BBO-type 1 crystal for SHG is placed in this arm of the interferometer. In this type of crystal, the SHG beam has a polarization orthogonal to the pump beam, meaning that the frequency-doubled content has a vertical polarization. The two beams of interest are overlapped using a polarizing beamsplitter (PBS). Indeed, as shown in Figure 3.14 frequency-doubled content beam issuing from the first arm of the interferometer is reflected while the beam propagating in the second arm, with a horizontal propagation, is transmitted. A linear polarizer then projects the polarizations of the two beams on a same axis in order to measure their beating. The frequency content at frequencies $2\nu_n$ and ν_{2n} are selected using a diffraction grating and sent onto a photomultiplier to perform the heterodyne detection. In this layout, we have chosen to use two optical filters and a beamsplitter rather than a dichroic mirror because we wanted to use a He:Ne laser for the proper alignment of the two arms of the interferometer and the femtosecond laser to tune the translation stage of Arm 1 as a means to find the ZPD location of the interferometer. In order to have enough power in the

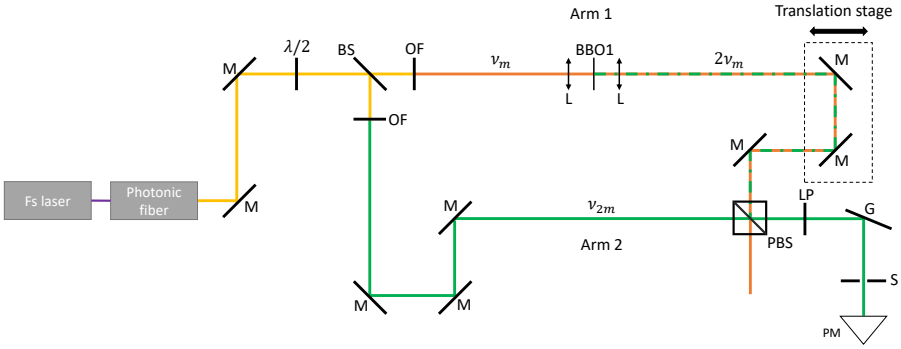


Figure 3.14: Layout of the $1f - 2f$ interferometer. BBO1: type 1 BBO crystal, BS: beamsplitter, G: gratings, M: mirror, OF: optical filter, L: lens, LP: linear polarizer, PBS: polarizing beamsplitter, PM: photomultiplier tube, S: slit, $\lambda/2$: half-wave plate.

arm where the nonlinear crystal is placed (arm 1), the beamsplitter is unbalanced: 90% of the light is transmitted while the remaining 10% is reflected (Ref. 111211 from Layertec).

As mentioned, this method requires an octave-spanning frequency comb to have light at a frequency ν_{2n} and to actually measure the beating note. Ti:Sapphire KML femtosecond lasers usually cover about 70 nm or 30 THz centred at about 800 nm or 375 THz, far less than a full octave. It is therefore necessary to stretch the frequency comb spectrum while preserving its comb structure. It can be accomplished by employing a photonic-crystal fiber in which the spectrum is broadened by SPM. The fiber needs to present zero dispersion near 800 nm in order to maintain the important peak power necessary for SPM and thus for spectral broadening [60, 62, 77]. The new frequencies are generated by sum- and difference-mixing of the frequencies present in the pulse before its injection in the fiber, so that the frequency spectrum of the supercontinnuum (SC) generated in the fiber is also a frequency comb [60]. However, other effects, such as Raman scattering, can have detrimental effects on the structure of the generated SC, blurring away the structure [77, 93]. When the pump beam wavelength lies in the anomalous (negative) GDD region, the injected pulse can propagate in the form of quasi-stable wave-packets known as solitons [27]. The ability to preserve the comb structure depends on the order N of the solitons propagating into the photonic fiber which is a function of the

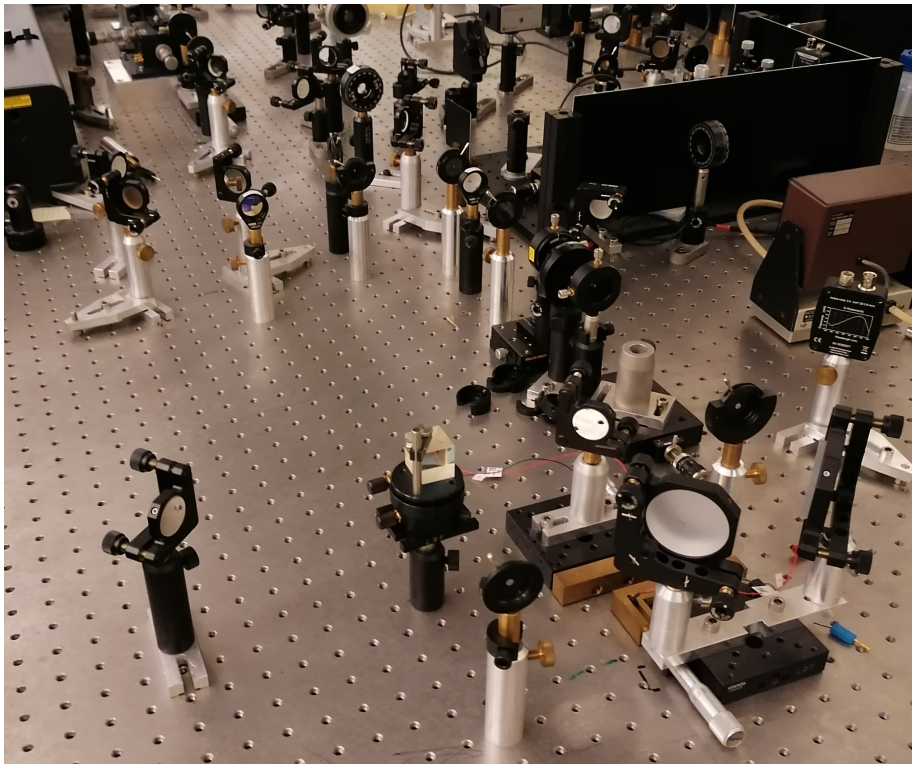


Figure 3.15: Photograph of our $1f - 2f$ interferometer.

pulse peak power P_{peak}, its duration T_0 and its wavelength λ but also on the photonic fiber characteristics [93]:

$$N^2 = \frac{T_0^2 \gamma P_{\text{peak}}}{|\beta_2(\lambda)|}, \tag{3.67}$$

where $\beta_2(\lambda)$ is the group-velocity dispersion coefficient of the fiber materials and $\gamma = \frac{n_2(\lambda)}{A_{\text{eff}}(\lambda)} \frac{2\pi}{\lambda}$ is the nonlinear coefficient, with $n_2(\lambda)$ the nonlinear Kerr index of the fiber and $A_{\text{eff}}(\lambda)$ the effective area of the mode propagating in the fiber. For a given fiber and wavelength, supposing that the pulse has a sech^2 shape and supposing that $A_{\text{eff}}(\lambda)$ is equal to the section of the fiber core, it is possible to find an expression of the soliton order which is a function of the femtosecond mean power P_{mean} and pulse duration:

$$N^2 = 1.76 \frac{T_0 P_{\text{mean}} n_2(\lambda)}{\lambda |\beta_2| r_{\text{fiber}}^2 f_{\text{rep}}}, \tag{3.68}$$

with r_{fiber} the radius of the fiber core and P_{mean} the mean power of the train of femtosecond pulses coupled the photonic-crystal fiber. The soliton order should be smaller than 16 to guarantee the generation of a coherent supercontinuum [93]. Reducing the power of the pulses injected in the photonic-crystal fiber will lower the order of the generated soliton. Unfortunately, this is done at the expense of the spectral broadening. Another possibility is to have pulses short enough to ensure the coherent broadening of the frequency comb.

Once we observe a beat signal at the photomultiplier, we can generate the error signal required for the stabilization of f_{CEO} (see Figure 3.13). We still need some actuation of the offset frequency in order to tune and thus stabilize it. One possibility is to make use of the dependence of the offset frequency on the intracavity peak power and adjust this quantity by regulating the pump power with an acousto-optic modulator (AOM) placed between between the pump laser and the Ti:Sapphire oscillator [77]. The AOM deflects a small portion of the pump power into the first diffraction order while the zeroth order of the AOM is used to pump the Ti:Sapphire laser. The AOM placed in our setup is an AOMO-3080-125 from Gooch & Housego. Criteria for its selection were a wavelength range matching with the Verdi emission wavelength, a damage threshold sufficient enough to inject the Verdi at full power without damaging the AOM crystal and an angular separation between the zeroth and first diffraction orders high enough to remove the first

order before its injection in the crystal. Unfortunately, we did not find any model with an active aperture sufficiently large to directly inject the Verdi beam without truncating it. We thus placed a combination of two beam reducers/expanders (GBE02-A from Thorlabs), a first one to reduce the beam diameter by a factor 2 for proper coupling with the AOM and a second one to then retrieve the original beam diameter for proper pumping of the Ti:Sapphire crystal. The optical layout is shown in Figure 3.16. We adjusted the two beam expanders using two CMOS cameras, one observing the VERDI beam in the near-field region, another in the far field region before and after placing the optics. Proper adjustment is obtained for an unmodified beam, except for its diameter. The method is not sensitive enough and required a fine adjustment when injecting the pump beam at full power into the MIRA900 in order to mode-lock it, which may be risky for the Ti:Sapphire crystal. A better approach would rely on the use of a shearing interferometer to ensure proper collimation of the laser pump beam after its travel through the two beam expanders.

Figure 3.17(a) shows the supercontinuum light generated at the output of a 8 cm-long NL-PM-750 photonic-crystal fiber from NKT using the MIRA900 femtosecond laser while Figure 3.17(b) is a photograph of the setup for beam injection into the fiber. The beam mean power just before the 45$\times$ objective used to focus the beam in the 2 μm fiber core was equal to 410 mW. The choice of the objective magnification was based on a series of trials-and-errors. This was the one available in the laboratory giving the best coupling efficiency. The objective presents no AR coating and it is not dedicated to ultrafast laser physics applications. The numerical aperture of the objective is equal to 0.65. In order to align the fiber, we placed the fiber on a tapered V-groove fiber holder fixed on a nanopositioning flexure stage (MAX312D/M from Thorlabs).

Figure 3.18 shows the associated spectrum measured with two commercial dispersive spectrometers covering the near-infrared and the visible parts of the light spectrum (models HR4000 and NIRQuest from Ocean Optics). As we can see, we satisfy the octave-spanning spectrum condition for the stabilization of the offset frequency. However, we were not able to measure any beating signal at the output of the $1f-2f$ interferometer (the two arms were perfectly equal in length). We associated the absence of beating to the lack of frequency-comb structure at the output of the optical fiber. This was confirmed by our inability to measure a beating between the supercontinuum and a

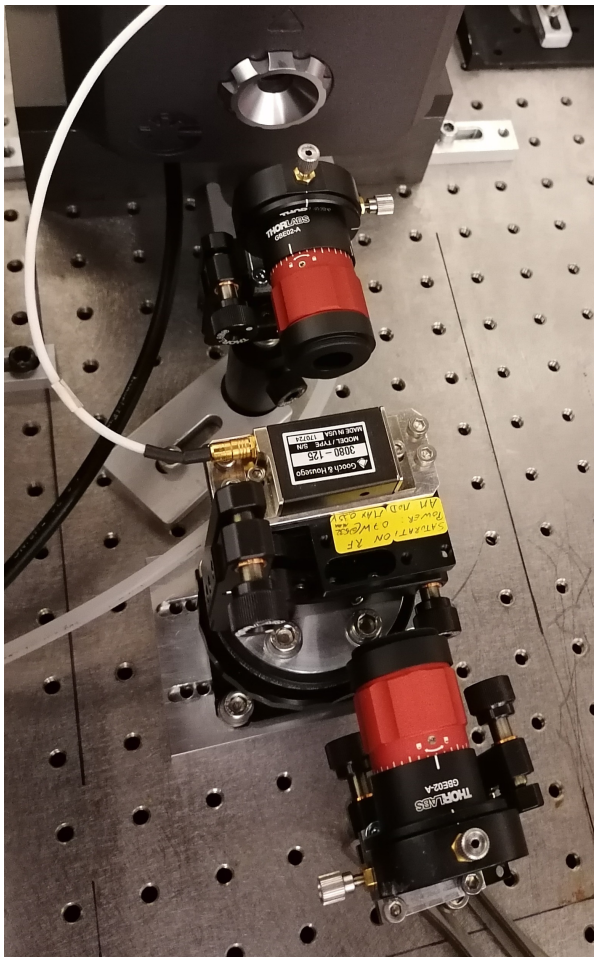


Figure 3.16: Photograph of the optical layout for the offset frequency adjustment.

frequency-stabilized He:Ne laser. Following Ref. [93], the generation of a coherent supercontinuum imposes stringent conditions on the pulse duration and on the pulse power for a given photonic-crystal fiber (see equation (3.68)). To check if the pulses were short enough for the generation of a coherent supercontinuum, we employed the second-order autocorrelator described in Appendix B.1 in order to characterize the pulse duration of pulses emitted by the MIRA900. We measured pulses with a duration of 373 fs for the Mira 900, far above the value of 25 fs evaluated using equation (3.68) with the characteristics of our fiber (fused silica, $|\beta(800\text{ nm})| = 36.163\text{ ps}^2/\text{km}$, $r_{\text{fiber}} = 1\ \mu\text{m}$, $n_2 = 30.9 \times 10^{-21}\text{ m}^2/\text{W}$). It is the reason why we decided to design the new femtosecond resonator presented in section 3.6.1. As we have seen in section 3.6.1, the new resonator is currently able to sustain pulses down to 30 fs if the pulses are transform-limited for an output power of 200 mW. Injecting these values in equation (3.68) leads to solitons of order 12, making possible its stabilization.

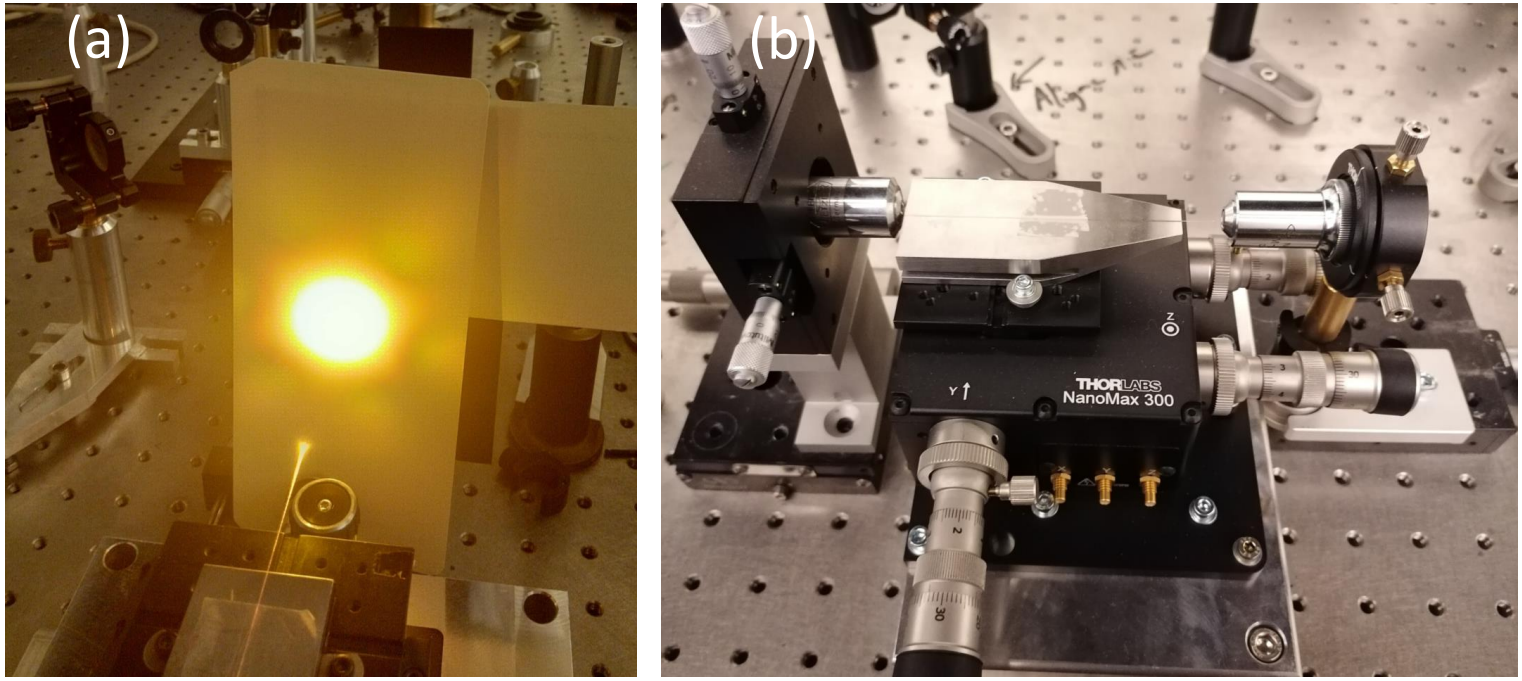


Figure 3.17: Pictures of (a) the supercontinuum generated at the output of the 8 cm long NL-PM-750 photonic-crystal fiber from NKT with the MIRA900 (mean power just before the fiber: 410 mW) and of (b) the setup for beam injection into the fiber.

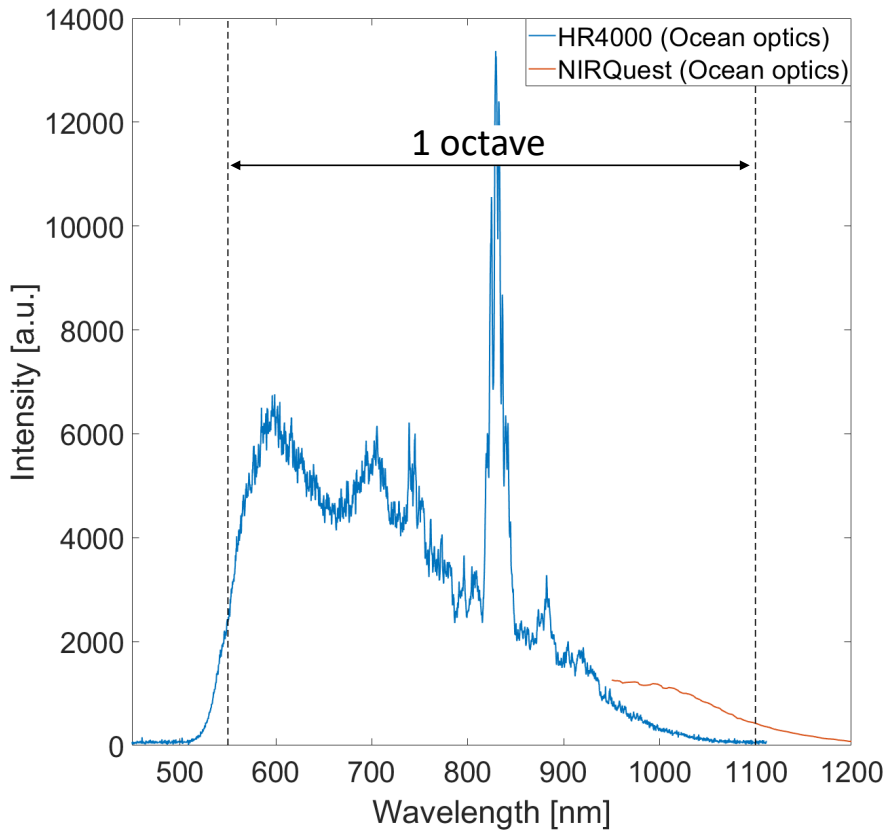


Figure 3.18: Spectrum at the output of the photonic-crystal fiber measured with two dispersive spectrometers (models HR4000 and NIRQuest from Ocean Optics). The spectrum spreads over more than 1 octave.

3.7 CONCLUSION

In this chapter, we presented the first results concerning the design and fabrication of a frequency-stabilized frequency comb light source. We were not able to combine all the necessary ingredients in time to have such a light source but we opened the way to future researchers that will join our group in the future, giving them guidelines and possible improvement to succeed at the task.

4

BUFFER GAS COOLING OF MOLECULES

4.1 INTRODUCTION

High-resolution infrared spectroscopy is an essential tool for studying the structure and dynamics of molecules. However, at room temperature, this technique is limited to simple molecules made of only a few atoms because of the large density of rotational and vibrational levels, leading to highly congested spectra which are almost impossible to analyze [94–96]. In order to overcome this problem, spectroscopy can be performed at cryogenic temperatures, at about a few Kelvin. Doing so presents two advantages: (1) only the states lying low in energy are populated, resulting in an important simplification of the measured spectra along with an amplification of the remaining spectral lines for an identical number of molecules and (2) a narrowing of the Doppler-broadened lines [94, 96].

Several methods exist for cooling down molecules from ambient temperature to cryogenic ones. These methods can be either direct or indirect depending on whether the molecules are directly cooled down or the cold molecules are formed starting from cold atoms. Indirect cooling methods are very complicated to employ and are restricted to a few favorable cases. Amongst the direct cooling methods, there are slow molecule filtering from an effusive source, supersonic expansion and buffer gas cooling [97, 98].

Supersonic cooling relies on the thermodynamic properties of the isentropic expansion of a fluid, which always leads to its cooling. In practice, cooling is accomplished by expanding the gas through an orifice from a stagnation reservoir at high pressure into a vacuum chamber, at lower residual pressure. The shape and the dimension of the orifice, or nozzle, influence the thermodynamic and kinetic properties of the downstream expansion. The cooling arises from a partial conversion of the thermal energy of the molecules contained in the stagnation reservoir into kinetic energy when expanding into the vacuum chamber. The flow of

cold molecules exiting the nozzle thus acquires an important forward velocity in the laboratory reference frame. While the method is effective for cooling down the translational, vibrational and rotational degrees of freedom of molecules, setups depending on supersonic expansions to cool down molecules require important pumping capabilities, even when working in pulsed operation [95, 99]. Furthermore, the pulsed operation is usually incompatible with the coupling of the supersonic jet expansion with a continuous scan Fourier transform spectrometer, such as the one developed in-house and presented in chapter 2 [100].

Buffer gas cooling relies on the thermalization of a buffer gas with a surface brought at cryogenic temperatures which in turn thermalizes the target molecules through collisions, as illustrated in Figure 4.1. Because this process does not rely on any particular energy pattern, any molecule can be brought to the temperature of the buffer gas. Advantages of buffer gas cooling are numerous: it is a continuous source of slow laboratory frame velocities, allowing for long observation times. Moreover, in contrast to supersonic expansion, it does not require important pumping infrastructure because it relies on small gas throughput and cryogenic pumping [94]. Finally, buffer gas cooling is applicable to nearly all molecules and it is very efficient in terms of produced sample density [101]. The concept behind buffer gas cooling is developed in section 4.2 and the experimental setup in section 4.3. The technique requires to continuously inject helium atoms and the species under study inside a vacuum chamber, imposing special attention concerning the dimensioning of the pumping capacity of the setup, as detailed in section 4.4. We developed a cavity ring-down spectroscopy setup to seek the first cold molecules obtained with our apparatus. The CRDS setup is described in section 4.5. The first results obtained with the buffer gas cooling setup are given in section 4.6. Finally, in section 4.7, we present the spectrum of methanol cooled down at cryogenic temperatures and we evaluate the rotational temperature of the molecules using a two-temperature analysis.

The gas injection system associated with the buffer gas cooling setup is described in Appendix C.1. Considerations about the temperature measurement and control are given in Appendix C.2. Because of the cryogenic temperatures, the use of large amounts of gas, the management of vacuum, etc., the setup is inherently dangerous. Safety aspects are presented and discussed in Appendix C.3.

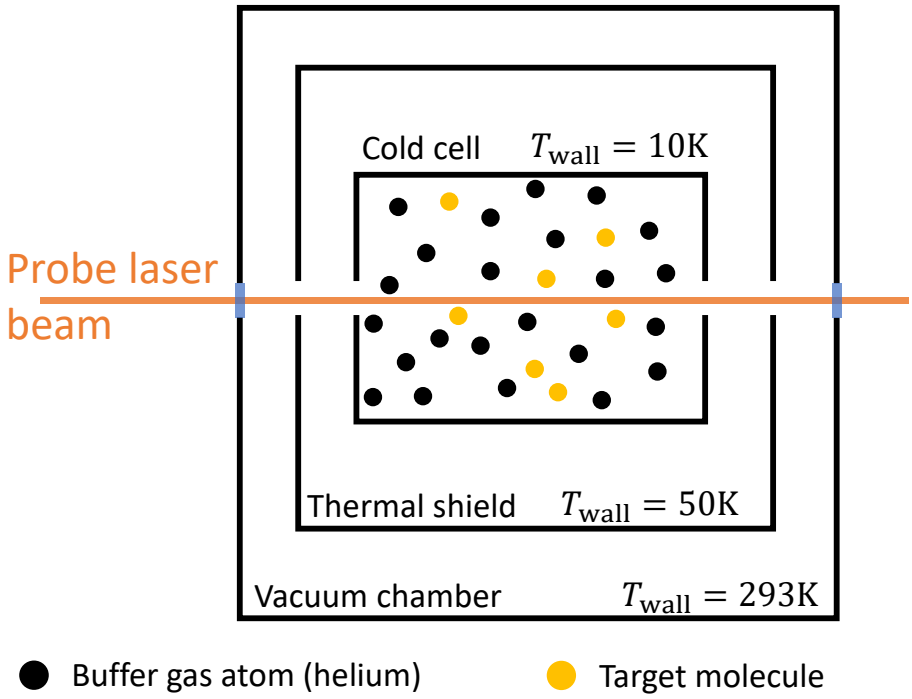


Figure 4.1: Working principle of the buffer gas cooling technique. A buffer gas, usually helium, is thermalized with the walls of a cold cell brought at cryogenic temperature. The target molecules are cooled through collisions with helium. They are then studied via their interaction with a laser beam. The cold cell is usually surrounded by a thermal shield and placed in a vacuum chamber to reduce the heat load on it.

This section is divided in three parts. In section 4.2.1, physics behind buffer gas cooling is briefly developed. The number of collisions necessary for the hot molecules of interest to reach the temperature of the buffer gas is evaluated in section 4.2.2. This information is of prime importance since it will determine the characteristic dimensions of the cold cell (cf. section 4.3.2).

4.2.1 *Cooling by colliding*

This section relies on Ref. [102, 103].

The principle behind buffer gas cooling is the cooling down of molecules at cryogenic temperatures, well below their freezing point, by means of collisions of these molecules with a cold buffer gas. This section details the physics behind thermalization of the molecules under study in the buffer gas environment by assuming the process only involves elastic collisions. This section is divided in two parts: (i) description of elastic collisions in the center of mass frame is first presented. Then (ii) the mean change of temperature during collisions is derived using results of part (i).

Elastic collisions in the center of mass frame

The center of mass (CM) location is defined as follows for a number n of particles:

$$\sum_{i=1}^{n} m_i \left(\mathbf{r}_i - \mathbf{r}_{\mathrm{CM}}\right) = 0, \tag{4.1}$$

where m_i denotes the mass of the particle i, $\mathbf{r_i}$ its position and $\mathbf{r}_{\mathrm{CM}}$ the position of the center of mass which can be expressed as follows:

$$\mathbf{r}_{\mathrm{CM}} = \frac{\sum_{i=1}^{n} m_i \mathbf{r}_i}{\sum_{i=1}^{n} m_i}. \tag{4.2}$$

The velocity of the centre of mass is obtained by deriving equation (4.2) with respect to time:

$$\mathbf{v}_{\mathrm{CM}} = \dot{\mathbf{r}}_{\mathrm{CM}} = \frac{\sum_{i=1}^{n} m_i \dot{\mathbf{r}}_i}{\sum_{i=1}^{n} m_i}. \tag{4.3}$$

The velocity, $\mathbf{v}'_i$, of a particle in the centre of mass frame relative to the laboratory frame is given by:

$$\mathbf{v}'_i = \mathbf{v}_i - \mathbf{v}_{\mathrm{CM}}, \tag{4.4}$$

with $\mathbf{v}_i = \dot{\mathbf{r}}_i$. The prime notation indicates that the velocity is expressed in the center of mass frame.
The total momentum in the CM can be derived using equation (4.4):

$$\mathbf{p}'_{Tot} = \sum_{i=1}^{n} \mathbf{p}'_i = \sum_{i=1}^{n} m_i \mathbf{v}'_i = \sum_{i=1}^{n} m_i \left(\mathbf{v}_i - \mathbf{v}_{\mathrm{CM}}\right) = 0 \tag{4.5}$$

In the case of a collision between two particles, equation (4.5) leads to:

$$m_1 \mathbf{v}'_{1i} + m_2 \mathbf{v}'_{2i} = 0 \tag{4.6}$$

$$m_1 \mathbf{v}'_{1f} + m_2 \mathbf{v}'_{2f} = 0, \tag{4.7}$$

where $\mathbf{v}'_1$ and $\mathbf{v}'_2$ are the velocities of the two particles. The subscripts i and f correspond to the situations before and after the collision.
Furthermore, if the collision is elastic, kinetic energy is conserved as well:

$$m_1 v'^2_{1i} + m_2 v'^2_{2i} = m_1 v'^2_{1f} + m_2 v'^2_{2f}, \tag{4.8}$$

with v_1 and v_2 the speed of the particles.

Change of temperature during the collision

In this section, the expression of the difference of temperatures of an atom or of a molecule before and after a collision with the buffer gas is derived. Knowledge of this expression allows to determine the number of collisions necessary thermalize the molecules with the buffer gas.

Solving for $\mathbf{v}'_{2f}$ and $\mathbf{v}'_{2i}$ in equations (4.6), (4.7) and (4.8) and using $\mathbf{v}_{\mathrm{CM}} = \frac{m_1 \mathbf{v}_{1i} + m_2 \mathbf{v}_{2i}}{m_1 + m_2}$ (see equation (4.3)) gives:

$$\begin{aligned} \mathbf{v}'^2_{1f} &= \mathbf{v}'^2_{1i} = \left(\mathbf{v}_{1i} - \mathbf{v}_{\mathrm{CM}}\right)^2 \\ &= \mathbf{v}^2_{1i} + {\mathbf{v}_{\mathrm{CM}}}^2 - 2\mathbf{v}_{\mathrm{CM}} \cdot \mathbf{v}_{1i} \\ &= \left(1 - \frac{2m_1}{m_1 + m_2}\right) \mathbf{v}^2_{1i} + {\mathbf{v}_{\mathrm{CM}}}^2 - \frac{2m_2}{m_1 + m_2} \mathbf{v}_{1i} \cdot \mathbf{v}_{2i} \end{aligned} \tag{4.9}$$

Because the initial particle velocities $\mathbf{v}_{1i}$ and $\mathbf{v}_{2i}$ are random with respect to one another, *i.e.* $\langle \mathbf{v}_{1i} \cdot \mathbf{v}_{2i} \rangle = 0$, the average collision yields:

$$\left\langle \mathbf{v}'^2_{1f} \right\rangle = \left(1 - \frac{2m_1}{m_1 + m_2}\right) \left\langle \mathbf{v}^2_{1i} \right\rangle + \left\langle {\mathbf{v}_{\mathrm{CM}}}^2 \right\rangle \tag{4.10}$$

Re-expressing the final velocity of particle 1 in the laboratory frame gives:

$$\mathbf{v}_{1f}^2 = \left(\mathbf{v}_{1f}'^2 + \mathbf{v}_{\mathrm{CM}}\right)^2 = \mathbf{v}_{1f}'^2 + \mathbf{v}_{\mathrm{CM}}{}^2 + 2\mathbf{v}_{1f}' \cdot \mathbf{v}_{\mathrm{CM}}. \tag{4.11}$$

Since $\mathbf{v}_{1f}'$ is randomly oriented with respect to $\mathbf{v}_{\mathrm{CM}}$, $\left\langle \mathbf{v}_{1f}' \cdot \mathbf{v}_{\mathbf{CM}} \right\rangle = 0$, equation (4.11) becomes:

$$\left\langle \mathbf{v}_{1f}^2 \right\rangle = \left\langle \mathbf{v}_{1f}'^2 \right\rangle + \left\langle \mathbf{v}_{\mathbf{CM}}{}^2 \right\rangle. \tag{4.12}$$

The average temperature change $\langle T_f - T_i \rangle$ during the collision can now be found for particle 1 using equations (4.10) and (4.12):

$$\begin{aligned}
\langle T_{1f} - T_{1i} \rangle &= \frac{2}{3k_b}\frac{m_1}{2}\left(\left\langle \mathbf{v}_{1f}^2 \right\rangle - \left\langle \mathbf{v}_{1i}^2 \right\rangle\right) && (4.13)\\
&= \frac{-2m_1m_2}{(m_1+m_2)^2}\left(\frac{2}{3k_b}\frac{m_1}{2}\left\langle \mathbf{v}_{1i}^2 \right\rangle - \frac{2}{3k_b}\frac{m_2}{2}\left\langle \mathbf{v}_{2i}^2 \right\rangle\right) && (4.14)\\
&= \frac{-2m_1m_2}{(m_1+m_2)^2}(T_{1i} - T_{2i}), && (4.15)
\end{aligned}$$

where T_{1i} and T_{2i} are the initial temperatures of the particles and k_B the Boltzmann constant. This single-collision temperature change can be used to model the case where thermalizing collisions occur between an initially hot molecule of temperature T_i and cold buffer gas atoms. The temperature T_N after N collisions of a molecule of mass M colliding with buffer gas of temperature T_B and mass m_B can thus be cast into differential form:

$$\frac{\mathrm{d}T_N}{\mathrm{d}T} = \frac{-2Mm_B}{(M+m_B)^2}(T_N - T_B); \tag{4.16}$$

Solving this differential equation leads to:

$$T_N = T_B + (T_i - T_B)\mathrm{e}^{\frac{-2Mm_B}{(M+m_B)^2}N}. \tag{4.17}$$

It is a simple exponential form. Figure 4.2 is a plot of equation (4.17) for the cooling down of a molecule of mass equal to 40 amu from 300 K to 10 K with helium as the buffer gas. After 39 collisions, the molecules are thermalized to 10 K (within 5% of the final temperature).

The discussion of this section concerned the cooling of translational temperature by means of collisions. However, the method is also effective at thermalizing the internal states of the molecules [98], and

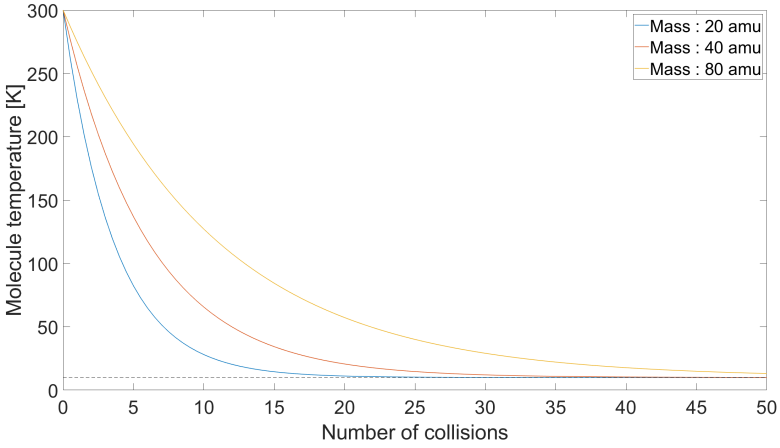


Figure 4.2: Temperature of the molecule under study with respect to the number of collisions with helium at 10K for a molecule at an initial temperature of 300K. The three curves correspond to three different molecule masses.

more specifically at cooling rotational internal degrees of freedom. The energy transfer cross-sections are similar for translational and rotational degrees of freedom, meaning that the expression of equation (4.17) gives a good estimate of the number of collisions required to thermalize this internal state as well, both occurring in tandem. Buffer gas cooling is not efficient at cooling the vibrational motion of the nuclei because vibrations are much faster than the duration of a cold helium atom collision, leading to a small energy transfer cross-section [104].

4.2.2 *Distance traveled before thermalization*

Molecules need to undergo about 40 collisions in order to thermalize with the buffer gas. The mean distance traveled between two consecutive collisions of the molecule with helium buffer gas, *i.e.* the mean free path of the molecule $\lambda_{s-b,0}$, is given by (see Ref. [98]):

$$\lambda_{s-b,0} = \frac{1}{\left(\sqrt{1+\frac{m_s}{m_b}}\right) n_{0,b}\sigma_{b-s}}; \tag{4.18}$$

where $\sigma_{b,s}$ is the molecule-helium collision cross-section, which takes typical values of 10^{-14} cm^2. The subscript 0 indicates in-cell, stagnation conditions. Considering a buffer gas density between 10^{15} cm^{-3} and 10^{16} cm^{-3}. This range of buffer gas density is typical of buffer gas

cooling setups, as further detailed in section 4.4. Typical distances before thermalization are between 0.1 cm and 1 cm.

As will be outlined in section 4.3.2, the knowledge of the distance traveled before thermalization is of prime importance. It will set constraints on the dimensioning of the cold cell as the molecules need to be thermalized before being probed or lost. Typical loss mechanisms of molecules in the cold cell are the formation of clusters due to collisions between the cold molecules being studied and the sticking of molecules on the walls of the cold cell [105].

4.3 MECHANICAL DESIGN

In its simplest form, the setup only consists of a cold cell, with walls at about 10 K. Helium thermalizes with the walls of the cold cell by means of collisions. Helium will in turn cool down the species under study also by means of collisions. However, this is only a conceptual picture. Indeed, this cold cell should be under vacuum and surrounded by a thermal shield. The need for vacuum is twofold: (1) buffer gas involves low gas densities, *i.e.* $10^{12} - 10^{17}\text{cm}^{-3}$, and (2) a good thermal insulation of the cold cell is needed. Otherwise, it would be impossible to reach such low temperatures. Indeed, vacuum allows for the suppression of gas thermal conduction and convection. The only remaining heat loads on the cold cell are the radiation and the cooling of the buffer gas. To further reduce the heat load on the cold cell in order to reach temperatures as low as possible, the cold cell is surrounded by a thermal shield. It consists in an aluminum shell at an intermediary temperature of about 50 K that protects the cold cell from radiation emitted by the vacuum chamber which is at room temperature. Gas lines with flow controllers, temperature sensors, vacuum gauges, vacuum pumps, etc. complete the setup. Figure 4.3 is a simplified cut view of the vacuum chamber. The cold cell is surrounded by the thermal shield, itself placed in a vacuum chamber, the three of them are fixed to the three flanges of the cold head responsible for the cooling of the cold cell and the thermal shield.

The vacuum chamber consists in a vertical cylinder vessel closed by two metallic plates, one at each of its extremities. The cylinder vessel was built by bending a steel sheet. All the elements and vacuum feedthroughs that are connected to the vessel are listed in Table 4.1. Because our application requires a high vacuum, with pressures below

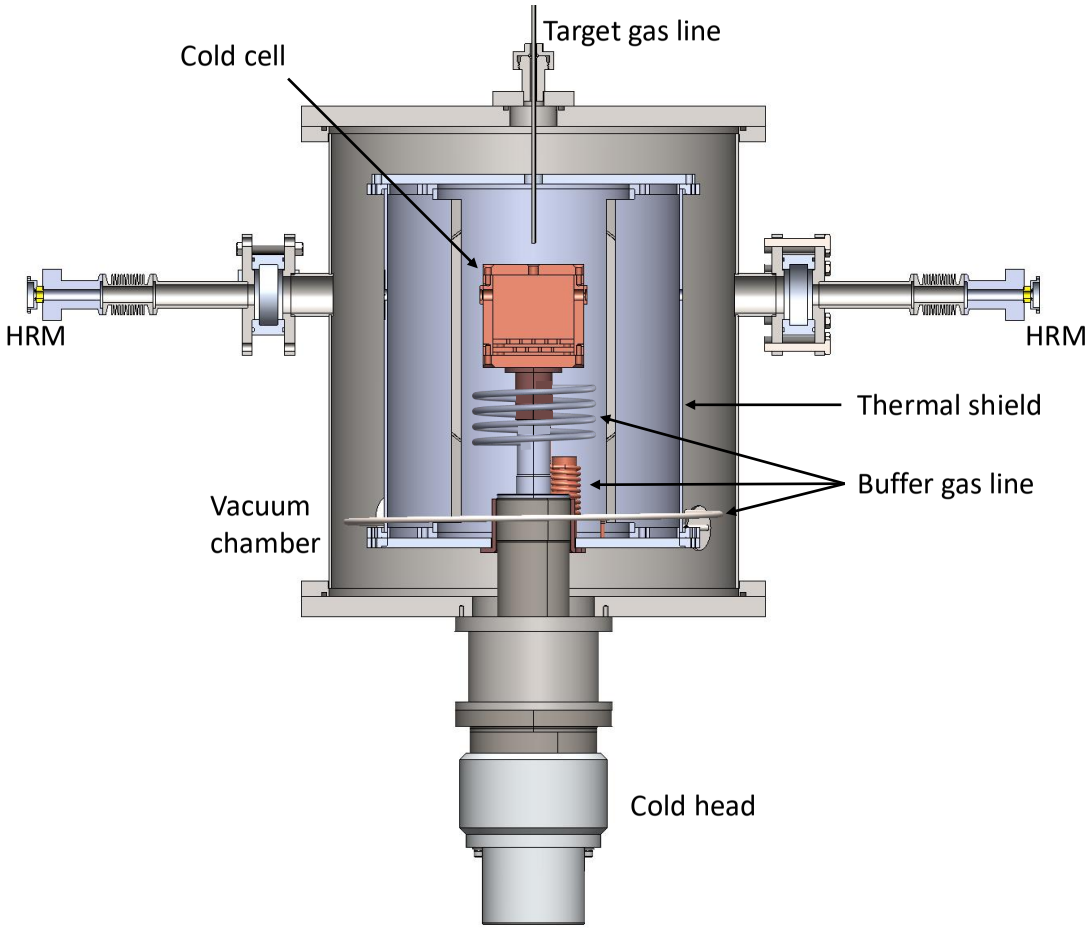


Figure 4.3: Cut view of the buffer gas cooling setup. Several mechanical pieces were hidden from the assembly to simplify the figure. HRM stands for High reflectivity mirror.

10^{-4} mbar, the type of flanges was only based on the ease of use and the availability of specific feedthroughs on the market. Photographs of the setup are given in Figure 4.4. The remaining of this section is devoted to giving more information concerning the list of Table 4.1. If a more detailed description/attention is required for a specific element, it is given in a dedicated subsection, and we will simply refer to it.

The cold head is the element responsible for the cooling of the thermal shield and of the cold cell. It is detailed in section 4.3.1. Considerations concerning the cold cell which is fixed on the second stage of the cold head are given in section 4.3.2 while the design of the thermal shield which is fixed on the first stage of the cold head is presented in section 4.3.3.

The pressure inside the vacuum chamber is measured using a full range gauge (PTR 90 N from Leybold).

Vacuum is obtained thanks to a turbomolecular pump backed by a multi-stage roots pump . Their dimensioning and the determination of the location of the turbomolecular pump on the vacuum chamber are developed in section 4.4.

The low gas densities involved in the buffer gas cooling method require to perform measurements within an optical cavity. Considerations about the cavity are given in section 4.3.5 where the imperious need for custom connections of the two mirror mounts and the use of two windows to re-align the cavity without breaking the vacuum are highlighted.

Details about the two gas lines are given in section 4.3.4 and in Appendix C.1.

A pressure relief valve and a venting valve are also connected to the vacuum chamber. The role of the venting valve is to put back to atmospheric pressure the vacuum vessel when required. The pressure relief valve is a security valve that opens when the pressure inside the vessel rises above 1.2 bar. This can occur if the temperature of the cold head rapidly increases, leading to the desorption of all the species that were adsorbed on it.

An electrical feedthrough with 2×25 D-plugs allows to connect all the temperature sensors and the heat cartridges to the temperature controller unit built in-house. Details are given in section C.2.

Three extra flanges were added for possible upgrades.

The vacuum chamber is installed on a metallic frame on which all the elements necessary to operate the setup are installed: vacuum gauge and turbomolecular pump drivers, the temperature measurement and control unit, the gas injection panel, optical breadboards, miscellaneous electronics required for the CRDS setup, etc. The metallic frame is made with aluminum profiles that can be assembled without welding or machining thanks to grooves and a specific screw system. It permits to easily add new modules/elements to the setup. Vibrations caused by the cold head are attenuated by installing the vacuum chamber on a series of shock mount absorbers along the same axis as the cold head.

4.3.1 *Cold head description and specifications*

The cold head is the part of the setup responsible for the cooling of the cold cell and of the thermal shield. The cooling effect is based on the Gifford-McMahon refrigeration cycle, in which high-pressure helium gas expands in the cold head to produce the refrigeration effect. A compressor unit is employed to compress helium, the compressor and the cold head being connected via flexible hoses [106]. From a mechanical perspective, the cold head consists of a long cylindrical piece putting together three flanges. The first flange serves to vacuum-tightly fix the cold head to the vacuum chamber. The two other flanges correspond to the first and second stages of the cold head, on which are anchored the thermal shield and the cold cell, respectively. Under steady-state conditions, the temperatures that can be reached by the cold cell and the thermal shield depend on the heat load they are subjected to, as indicated by the cold head capacity map. Figure 4.5 shows the capacity map of our cold head, the CH208L from Sumitomo. As we can see in this figure, temperatures of the cold head and of the thermal shield are interdependent, and in any case, we will not be able to reach temperatures below 10 K with the cold head. The CH208L cold head was the model with the best refrigeration performances in our budget. It was also the model which was best characterized in terms of the vibrations it generates when turned on, with vibrations below 0.1 mm (see Ref. [107]), meaning that the light beam passing through the optical cavity will not be intermittently truncated.

Table 4.1: List of the elements and feedthroughs connected to the vacuum chamber.

Element	Flange type	Number of flanges	Comments
Cold head	Custom	1	The cold head should be placed vertically
Vacuum gauge	KF40	1	N.A.
Turbo molecular pump	ISO-K DN 160	1	see section 4.4
Optical cavity mirrors	custom	2	Location constraint by the beam path. A decentering system is required to recenter the flange on the probe beam at cold temperature
Windows for cavity alignment	Custom	2	A cross pattern is engraved on the thermal shield for alignment purposes and it should be in the field of view of the two windows
Window for target gas line alignment	Custom	1	The extremity of the pipe and the lid of the cold cell should be in the field of view of the window
Gas feedthrough - He line	ISO-KF DN 40	1	N.A.
Gas feedthrough - target gas line	Custom	1	The target gas line should have translation degrees of freedom (x-y-z) to align the extremity of the pipe with the hole in the lid of the cold cell
Venting valve	ISO-KF DN 40	1	N.A.
Pressure relief valve	ISO-KF DN 40	1	N.A.
Electrical feedthrough - temperature and measurement control	ISO-CF 63	1	commercial feedthrough with 2×25 D-plugs
Extra flange	ISO-KF 40	1	for potential upgrades
Extra flange	ISO-CF 40	1	for potential upgrades
Extra flange	ISO-CF 250	1	Flange for an additional turbomolecular pump

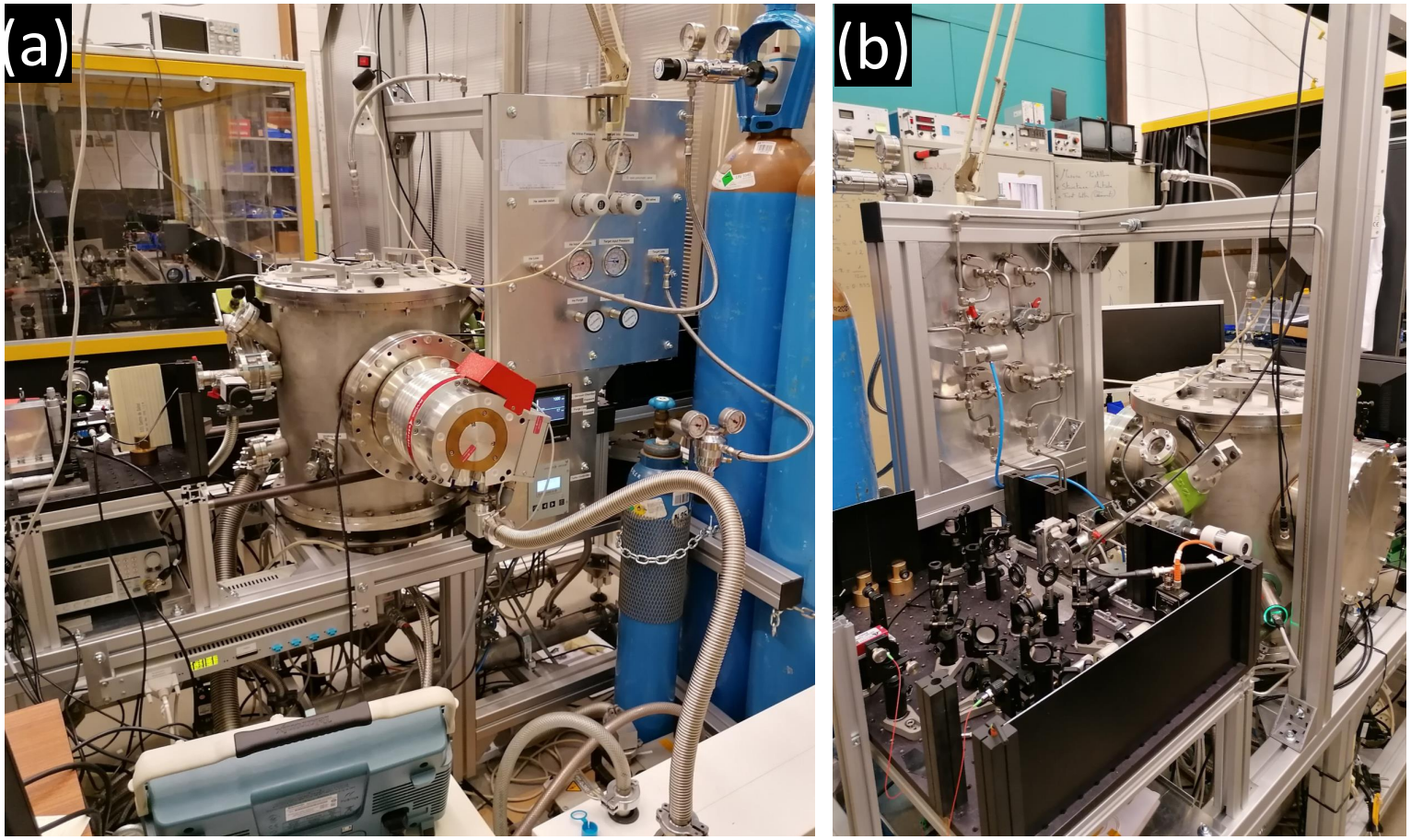


Figure 4.4: Photographs of the complete buffer gas cooling setup. (a) Front view. The bubbler is visible in the lower right part of the picture. (b) Rear view.

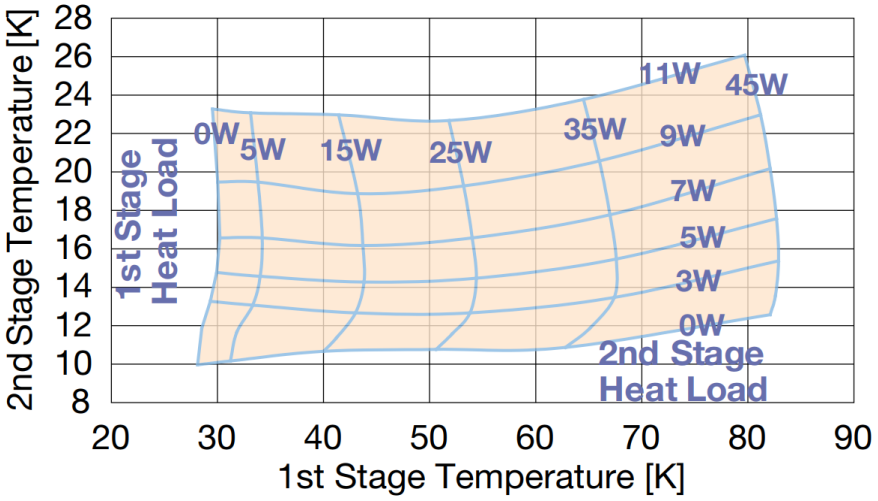


Figure 4.5: CH208L cold head capacity map at 50 Hz. From Sumitomo.

Special attention was given to reduce heat load on the two stages of the cold head, allowing us to currently reach temperatures of 13 K on the cold head and 49 K on the thermal shield.

4.3.2 *Cold cell design*

The cold cell is the central part of the setup. It consists in a copper box anchored on the first stage of the cold head. Considerations about the cell dimensions are multiple: (i) Molecules under study should undergo enough collisions to be cooled down before interacting with the probe beam, imposing a minimum cell height. (ii) Its length and width should be large enough for the molecules to be cooled down and probed before diffusing to the walls of the cell where they will freeze. (iii) The interaction length between the probe beam and the molecules should be sufficient to produce a signal given the sensitivity of the employed spectrometer. Finally, (iv) the dimensions of the cell should remain reasonable to ensure that the walls temperature remains homogeneous.

The minimum distance necessary to cool down the molecules was derived in section 4.2.2 and was estimated to be about a centimeter. Inner dimensions of the cell are 80(W) $\times$ 80(L) $\times$ 80(H) mm^3. These dimensions are in accordance with the literature [94–96, 108, 109]. The choice of the material for the cold cell was driven by the need of a

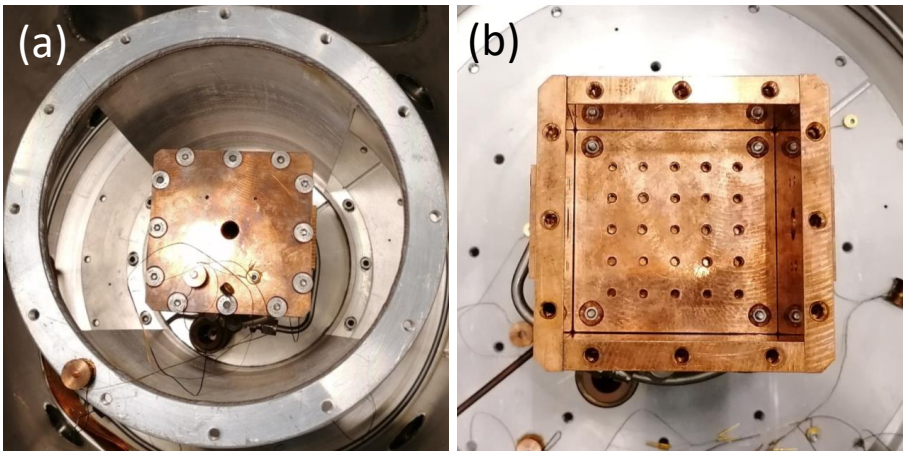


Figure 4.6: Cold cell of our apparatus. (a) Outside view. The 1 cm diameter hole at the center of the cold cell lid allows for the target gas injection inside the cell. (b) Inside view. The upper diffuser is visible on the photograph.

high thermal conductivity to avoid any thermal gradient in the cold cell. Some groups make use of aluminum as an alternative to copper [94, 96, 109].

Photographs of the inside and outside of the cell are given in Figure 4.6. Two holes, placed 2 cm below the top of the cold cell allow the laser beam to probe the molecules. In order to change the diameter of the holes and their height without having to change the complete cell, they are bored in plates screwed to the cold cell. The plates surrounding the holes are very thin (1 mm tick) in order to avoid the clogging of the holes due to molecules freezing. Helium is injected at the bottom of the cell via a pipe with an inner diameter of 4 mm. Two diffusers consisting in copper plates with a 5×5 grid of 3 mm wide holes force helium to undergo several collisions with the walls before entering the cell in order to quickly cool down the buffer gas. The upper diffuser is visible in Figure 4.6(b). Two temperature sensors are fixed to the cold cell, one at its bottom and the other one at its top. The sensor placed on the top of the cold cell is visible in Figure 4.6(a) (there is another sensor that is not fixed to the cold cell on the same photograph: it is for the lid of the thermal shield).

4.3.3 *Thermal shield design*

In the absence of convection and conduction, the only remaining heat load on the cell is radiation from its surroundings. If there were no thermal shield, the cell would be exposed to radiation from the vacuum chamber at ambient temperature. This heat load $\frac{\mathrm{d}Q_{\mathrm{rad}}}{\mathrm{d}t}$ can be estimated using the Stefan-Boltzmann law as follows:

$$\frac{\mathrm{d}Q_{\mathrm{rad}}}{\mathrm{d}t} = A\epsilon\sigma(T_1^4 - T_2^4) \tag{4.19}$$

With A the surface of the cold cell , T_1 and T_2 the temperatures of the vacuum chamber and the cold cell respectively, ϵ the emissivity of the cold cell, and σ the Stefan-Boltzmann constant ($\sigma = 5.67 \times 10^{-8}\mathrm{W\ m^{-2}K^{-4}}$) [110]. Considering $T_1 = 293$ K, (the vacuum chamber walls are at room temperature) $T_2 = 10$ K and $A = 600\ \mathrm{cm}^2$, $\epsilon = 0.2$ (typical value for roughened copper), the radiation power transmitted to the cold cell is equal to 5 W, which will prevent us from reaching temperatures down to the desired 10 K. Indeed, as shown in Figure 4.5, the power extracted from the cold cell rapidly decreases with the temperature. To take full benefits of the cold head, unnecessary heat loads on the coldest part of the setup must be avoided at all costs. Because of the strong temperature dependence of the radiant flux, placing a thermal shield at a temperature of about 50 K considerably reduces the heat load on the cold cell due to radiation. The first constraint for the design of the thermal shield is that it should screen any visual access to the cell from the vacuum chamber.

Measurements being performed in cavity, there are no windows on the cold cell to allow for the beam to pass but only holes. Also, as described in section 4.3.4, the target gas is injected ballistically inside the cold cell via a third hole. In order to have the desired target and helium gas densities inside the cold cell, we need to continuously inject the two gas species (target and buffer gases) inside the cold cell. Once they exit the cold cell, the two gas are in the thermal shield. While cryopumping of the two gases is usually retained as a solution [94, 108, 110, 111] to extract them, we could not afford this solution because the second stage of the cold head is limited to 10 K (see Figure 4.5), a temperature too high for the efficient cryopumping of helium [111]. Therefore, a second constraint for the design of the thermal shield is that it should exhibit a high molecular conductance to evacuate as quickly as possible the helium atoms to ensure a pressure low enough around the cold cell.

Finally, for practical purposes, the weight of the thermal shield should be reduced to a minimum in order to decrease the cooling time. Furthermore, it should exhibit a good thermal conductance to avoid any important temperature gradient between the top of the shield and its bottom, where it is actually anchored on the second stage of the cold head.

Because of cost, thermal conductance and weight concerns, the thermal shield is made of aluminum. The geometry of the shield will have consequences on these four features. We performed thermal and molecular conductance simulations using respectively the Solidworks and the *Molflow+* [112] softwares on several thermal shield geometries in order to select the best design for our application. We also kept in mind the ease of fabrication and installation during the selection process. A schematic and photographs of the design we retained are presented in Figure 4.7. It consists of two 1-cm thick circular plates with a diameter of 320 mm (one for the base and one for the lid) and of four walls fixed on two concentric flange pairs. The walls are 3-mm thick metallic plates bent and welded on the two flanges. The combination of the four walls allows for the thermal shielding, while efficiently guiding the molecules and atoms outside of the thermal shield. The two walls welded on the outer two flanges are bored so that the laser beam can pass. Two plates with an engraved cross pattern and a central hole are placed in front of these two holes. When combined with the two windows placed at 60° on the vacuum chamber, they allow to realign the optical cavity without breaking the vacuum, as detailed in section 4.3.5. One of the two windows is shown in Figure 4.8(a) while one of the two aforementioned plates seen through the window is shown in Figure 4.8(b).

4.3.4 *Vacuum and gas injection management*

As already mentioned at the beginning of section 4.3, the cold cell and the thermal shields are placed in a vacuum chamber in order to reduce the heat load on the cold cell and to reach the desired helium and target gas densities inside it. Therefore, we need a way to inject both gases inside the cold cell (and thus in the vacuum chamber) in a controllable manner. We also want to be able to re-align the optical cavity without breaking the vacuum. Finally, the setup needs to be safe for the user. A series of valves, gauges, vacuum pumps, etc. are placed on the setup

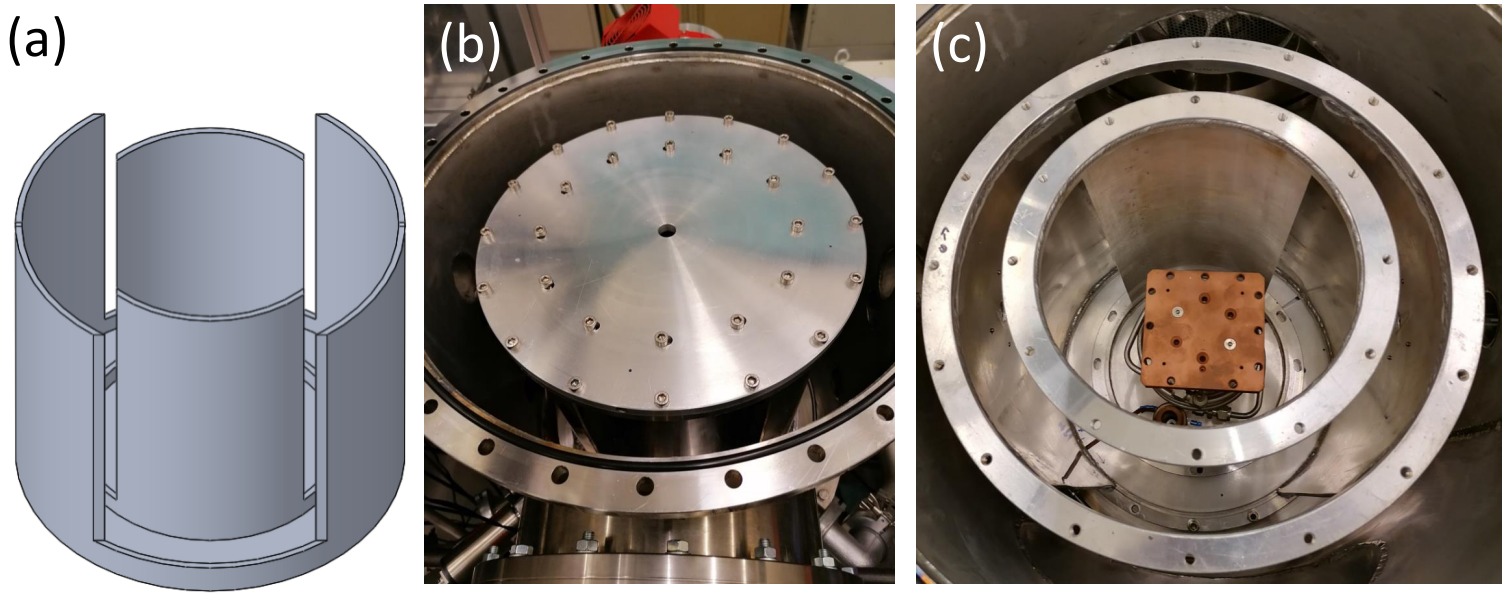


Figure 4.7: Thermal shield: (a) schematic (cut view) (b) outside view, (b) inside view. On this photograph, the cold cell was only partially assembled.

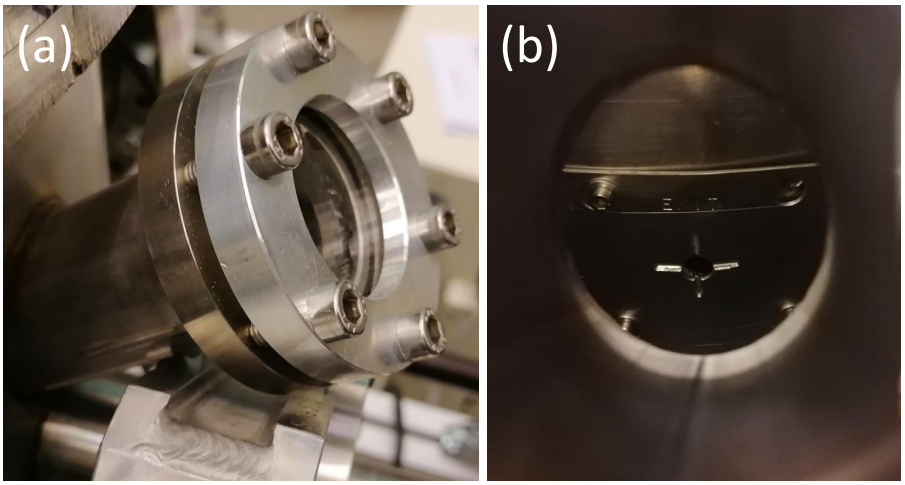


Figure 4.8: (a) One of the two windows placed on the vacuum chamber for the alignment of the optical cavity. (b) Plate with the engraved cross pattern fixed on the thermal shield for the alignment of the optical cavity.

in order to deal with the aforementioned requirements and features. Figure C.1 is a schematic of our setup from the perspective of vacuum and gas injection management. It is fully described in Appendix C.1. in this section, we will restrict the discussion to the techniques employed to inject the target gas and helium inside the cold cell. They are very different from one another. Indeed, while the helium pipe is directly connected to the cold cell, the target gas is injected ballistically by aligning its pipe extremity with a one-centimetre diameter hole on the top of the cold cell. This is due to a risk of clogging of the target gas line since the species of interest condense at such low temperatures. Other approaches than the ballistic one are possible for the target gas line. They are described in the subsection *Target gas injection* below. On the other hand, special care should be given concerning the connection of the helium gas line on the cold cell since it increases the heat load on it, as discussed in the subsection *Buffer gas injection* below.

Target gas injection

There are several ways to inject the species of interest in the buffer gas cell: laser ablation, laser-induced desorption, discharge etching, capillary filling and beam injection. They are all well described in Ref. [104]. Laser ablation, laser-induced desorption and discharge etching were excluded because they imply the use of powerful lasers such as

Nd:YAG lasers that are not available for this experiment. The two remaining ways to inject the molecules in the cold cell are capillary filling and beam injection. In the case of capillary filling, molecules are directly injected into the cell by means of a capillary. This technique adds heat load on the cold cell and can cause blockage of the capillary because the molecules under study can freeze into the tube. This last difficulty can be overcome by using a gas flow along with the species under study and by a tight control of the temperature of the tube. In the absence of this coflow, the technique is limited only to a small subset of atomic and molecular species.

The last technique to inject the molecules in the cold cell is the beam injection. It consists in injecting the molecules of interest through a hole in the lid of the cold cell. It is the method we chose. The hole has a diameter of 10 mm in our case. The molecules are brought in front of the hole via a pipe placed 1-2 cm away from the cell wall. Molecules then travel more or less ballistically from the pipe to the aperture. This technique also brings its share of difficulties: helium escaping the cold cell can build up density just outside it, knocking incoming molecules out of the molecular beam and preventing them from entering the cell. Also, even if molecules are able to enter the cell, there is a risk they are hydrodynamically pulled back out of it since helium is continuously escaping through the orifice. However, the advantage is that there is no restriction on the molecules that can be injected using this technique [104]. Choice was made to use beam injection because it seems to be the most accessible approach.

In our setup, molecules are injected by a hole located at the top of the cell, as shown in Figure 4.3. Since the pipe is in the vertical axis, it does not bend, avoiding the need to actually support it. In order to align the beam with respect to the hole in the cell, the injection system can be translated horizontally on a distance of 1 cm in two perpendicular directions. The injection system has a third degree of freedom for varying the distance between the cell and the pipe. A photograph of the alignment system is given in Figure 4.9. The plate maintaining the pipe slides on an o-ring lubricated with high-vacuum grease. The o-ring is responsible for the tightness of the vacuum chamber. The pipe can vertically slide in its tubular support, allowing for the third degree of freedom. Vacuum tightness is guaranteed by another greased o-ring, with an inner diameter equal to the outer diameter of the pipe, *i.e.* 6 mm. To do so, the o-ring is pressed in a chamfer at the top of the

support. From a glance at Figure 4.9, we can see that the pipe is made of copper and wrapped in a heater sheet. This was necessary to avoid the clogging of the pipe due to target molecules freezing in it. Copper was chosen for its excellent thermal conductivity.

A window on the lid of the vacuum chamber, visible in Figure 4.9, allows to pre-align the pipe. To do so, the lid of the thermal shield is removed. The top of the cold cell is now in the field of view of the window and the pipe can be displaced accordingly. The lid of the vacuum chamber is then removed in order to complete the assembly of the setup. This method allows only for a good first guess of the pipe positioning. Indeed, the cold cell is suspected to slightly move at low temperature and parallax effects can lead to erroneous positioning, the window being off centred. A fine alignment of the pipe positioning has to be performed at low temperature based on some spectroscopic signal. Another possibility to obtain a rough alignment relies on the use of a hollow conical PEEK piece centred on the hole of the cold cell lid. It permits to correlate the height with the two other coordinates in the absence of a direct visual.

Buffer gas injection

Whereas helium can be injected in the cold cell by directly connecting the helium pipe to the cold cell as there is no risk of clogging, a special attention has to be given to avoid thermal bridges between the different temperature stages of the setup. Santamaria *et al.* [108] suggested to divide the buffer gas line in four connected segments: two copper pipes fixed on the thermal shield and the cold cell are interleaved with two long stainless steel pipes. The role of the two copper sections is to progressively cool helium before it enters the cold cell. On the other hand, the two long stainless steel sections are used to reduce the heat load on the two cold stages. Indeed, the choice of stainless steel as the material constituting the pipes and increasing their length aim at reducing the heat conductance of these two sections.

A photograph of the inside of the vacuum chamber, where we can see the buffer gas line is given in Figure 4.10. The buffer gas line is also depicted in Figure 4.3.

One extremity of a 6-mm outer diameter stainless steel pipe is connected to a thermally insulated fluid feedthrough with Swagelok connections (Ref. 120XFN040-SS from Pfeiffer). The other extremity is connected

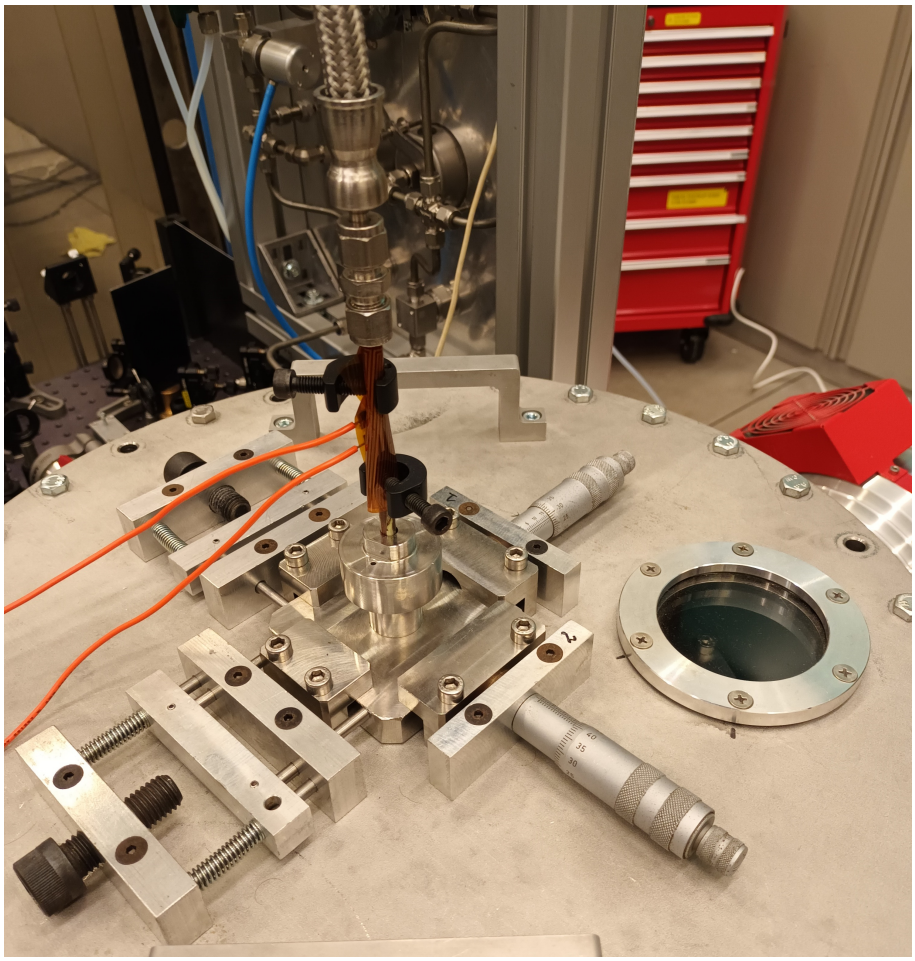


Figure 4.9: xyz translation system for the injection pipe of the target gas line. The copper pipe is wrapped in a heater sheet.

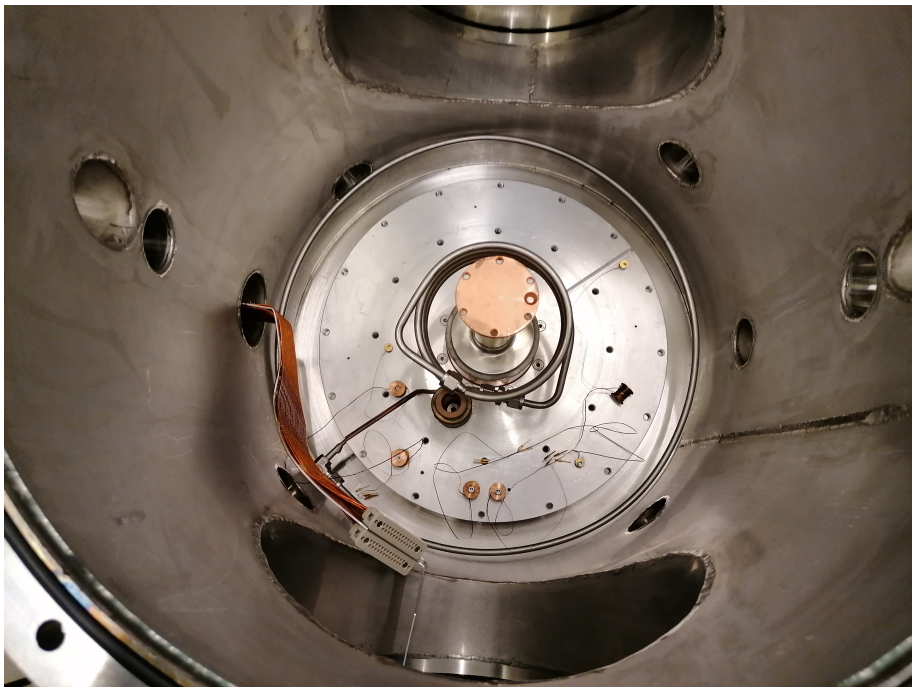


Figure 4.10: Photograph of the vacuum chamber, where the buffer gas line from the vacuum chamber wall to the cold cell is installed.

to a copper pipe section anchored on the bottom plate of the thermal shield. As we can see in Figure 4.10, the pipe is hoop-shaped in order to increase its length between the vacuum chamber and the thermal shield. It makes a full turn of the thermal shield, leading to a 1.2 meters length. The copper pipe section anchored on the thermal shield winds around a copper block, the two of them being welded together with silver. The goal of this segment is to pre-cool the helium atoms at the thermal shield temperature in order to reduce the heat load on the cold cell. In a similar manner, the pipe bridging the thermal shield and the cold cell makes several turns in order to reduce the pipe thermal conductance, increasing its length to 1.2 meters as well. The last segment, made of copper, passes through the bottom of the cold cell where it reaches the two diffusers described in section 4.3.2. All the aforementioned pipe segments are connected via Swagelok connectors.

4.3.5 *Optical cavity*

The low target gas density involved in buffer gas cooling necessitates to perform cavity-enhanced measurements, adding constraints to the design of the buffer gas cooling setup that are discussed in this section.

When performing cavity-enhanced absorption spectroscopy, intra-cavity losses should be avoided at all cost, meaning that no window can be placed inside it. The cavity mirrors are thus responsible for the vacuum tightness of the vacuum vessel. The mirror mounts detailed in section 2.3.4 are employed on the buffer gas cooling setup. They are fixed to the vacuum chamber by means of bellows in order to mechanically decouple them from the chamber, allowing for their proper alignment. Four degrees of freedom are available with our optical mount: the mirror can be tilted (yaw and pitch) and translated in a plane perpendicular to the optical axis.

We put in place a system permitting to change/clean the cavity mirrors and to align the optical cavity without venting the whole vacuum chamber. It makes use of the four valves (OC1, OC2, OC3 and OC4 of Figure C.1). The two gate valves OC1 and OC2 guarantee the vacuum tightness of the vacuum chamber when the mirrors mounts are disassembled. Valves OC3 and OC4 allow to pre-empty the death volume present in the mirror mount and in the bellows before reopening the gate valve by linking these dead volumes to the purge line. Figure 4.11 shows a picture of the mirror mount at the output of the optical cavity where the gate valve OC2 and the manual operation valve OC4 are visible. The window allowing to look for the back reflection beam from the high-reflectivity mirror is also present in Figure 4.11. Using the engraved cross pattern shown in Figure 4.8(b), we can quickly overlap the back-reflection from the end mirror with the incoming beam, allowing us to effectively align the optical cavity without breaking the vacuum.

This system is of great help since we observed a displacement of the two apertures for the passage of the beam in the cold cell depending on whether it is at cryogenic temperature or at room temperature. This displacement changed the beam pointing of about half a centimetre at the output of the cavity. The shift between the vacuum chamber flange and the optical mount induced by the beam pointing displacement was too important to be compensated with a single bellow. We thus built

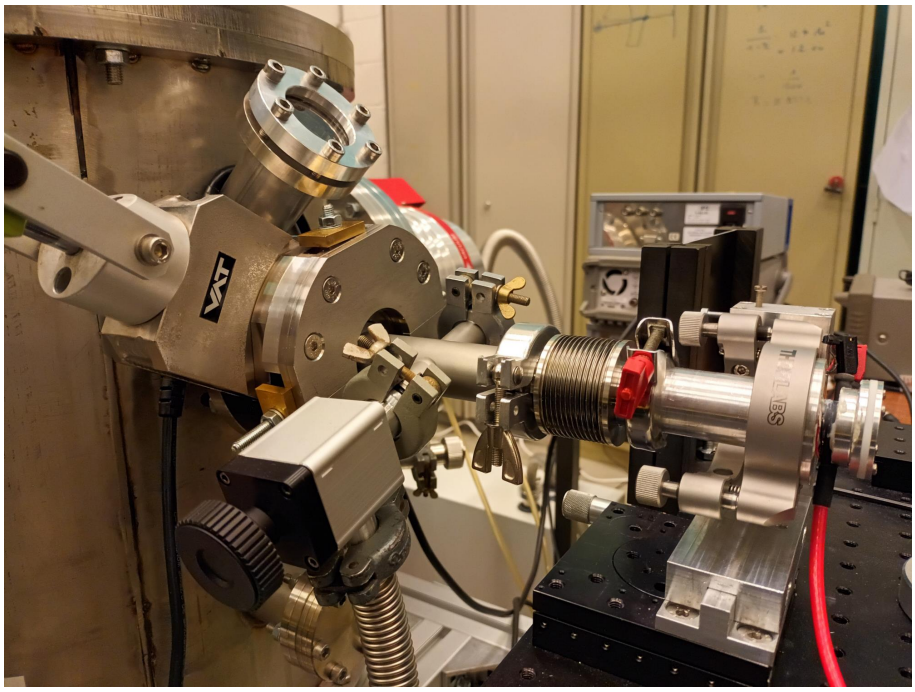


Figure 4.11: Photograph of the mirror mount at the output of the optical cavity.

a system for shifting the vacuum chamber flange so that it remains centred with the optical mount flange. It is visible in Figure 4.11.

Ultimately, we will perform frequency-comb enhanced absorption spectroscopy by coupling the femtosecond laser presented in chapter 3 with the FTS presented in chapter 2. This imposes a condition on the length of the optical cavity in order to match its FSR with the repetition frequency of the frequency comb so that the cavity FSR and the repetition frequency are in an integer ratio. When it is the case, the teeth of the frequency comb coincide with cavity transmission resonances, leading to a high coupling efficiency. This situation is known as the *magic point* [24]. More details are given in section 5.3. Since the repetition frequency of the MIRA900 is approximately equal to 76 MHz, the length of the cavity was set to 0.98 m. We placed the two mirror mounts on translation stages in order to fine-tune the cavity length to reach the magic point.

The pressure in the vacuum chamber should not exceed $p_{\max} = 10^{-4}$ mbar to avoid heat conduction by the residual gas [113]. Performing cavity-enhanced spectroscopy prevents the use of windows for the cold cell since they induce too much light loss, meaning that helium, which is continuously injected inside the cold cell has to be extracted. This puts stringent conditions on the pumping capacity of the vacuum pumping system.

Considering that the only gas load in the chamber is due to the injection of helium in the cold cell allows us to estimate the effective pumping speed, S_{eff}, using the following relationship:

$$S_{\text{eff}} = \frac{f_{0,b}}{p_{\max}}, \tag{4.20}$$

where $f_{0,b}$ is the helium throughput. Neglecting other gas loads such as the target gas injection throughput or outgassing is justified by the presence of cold walls at 12 K for the cold cell, and at 50 K for the shield, on which all atoms and molecules but helium will be adsorbed.

Evaluation of the required pumping speed, using equation (4.20), necessitates the knowledge of the helium throughput. It is imposed by the helium density inside the cold cell which is needed for buffer gas cooling. The higher the density, the more frequent are the collisions responsible for the cooling effect inside the cold cell, until reaching a maximum density of 10^{18} atoms per cubic centimeter, resulting in a high probability to form molecular complexes because of three-particle collisions [98]. The lower limit is imposed by the dimensions of the cell since there needs to be enough collisions to cool down the molecules before they reach the walls of the cell.

In steady-state conditions (denoted by a subscript "0" in the following expressions), the density of helium in the cold cells depends on the temperature of the cell, the size of the apertures for the laser beam which probes the cold molecules and the aperture through which the molecules under study are injected. Equation (4.21), which is derived in Ref. [98] , allows to evaluate this density:

$$n_{0,b} = \frac{4 f_{0,b}}{A_{\text{Apertures}} \bar{v}_{0,b}}, \tag{4.21}$$

where $n_{0,b}$ is the helium density in the cell, $f_{0,b}$ the helium throughput, $A_{\text{Apertures}}$ is the surface of the openings of the cold cell, and $\bar{v}_{0,b}$ is the mean thermal velocity of the buffer gas which is species- and temperature-dependent and given by:

$$\bar{v}_{0,b} = \sqrt{\frac{8RT_0}{\pi m_{0,b}}} \tag{4.22}$$

with R the ideal gas law constant ($R = 8.3145\,\text{J mol}^{-1}\text{K}^{-1}$), T_0 the temperature of the buffer gas and $m_{0,b}$ its molar mass, expressed in kg mol^{-1}. Supposing that the buffer gas will reach temperatures down to 15 K (pessimistic value), helium will have a mean thermal velocity of 282 m/s. In order to have a helium density of 10^{16} cm^{-3} in cold cell provided with two apertures with a diameter of 4 mm[1] for the passage of the laser light beam and an orifice of 10 mm of diameter for the target gas injection, we need to inject helium at a rate of 0.028 mbar$\cdot$l/s. Simulations with the *MolFlow+* software lead to a throughput of 0.079 mbar$\cdot$l/s. For comparison purposes, helium densities found in the literature lie between 5×10^{12} cm^{-3} and 10^{16} cm^{-3} with helium throughput ranging from 0.0169 mbar$\cdot$l/s to 0.169 mbar$\cdot$l/s [94–96, 108, 109].

Injecting the helium throughput found with the *Molflow+* software and the maximum acceptable pressure in the vacuum chamber, *i.e.* $p_{\text{max}} = 10^{-4}$ mbar, into equation (4.20), leads to an effective pumping speed of 790 l/s. Because of budget constraints, we purchased a single turbomolecular pump with a pumping speed of 655 l/s for helium. However, we prepared the ground for extending the pumping capacity by purchasing a foreline vacuum pump able to back a second 655 l/s turbomolecular pump and we placed a blank flange on the vacuum chamber in order to accommodate this second turbomolecular pump (see Figure 4.4). The turbomolecular pump(s) is(are) placed horizontally, lowering the risk to damage it(them) during successive assemblies/disassemblies of the setup.

A specificity of our thermal shield is that it actually guides the molecules in the direction of the turbomolecular pump inlet, as depicted in Figure 4.12(a) where *Moleflow+* simulations depict particle hits on the vacuum vessel walls. It guarantees us that the effective pumping speed of the system is not limited because of molecular conductance

1 It appeared to be too small and it limited ring-down times to about 80 μs

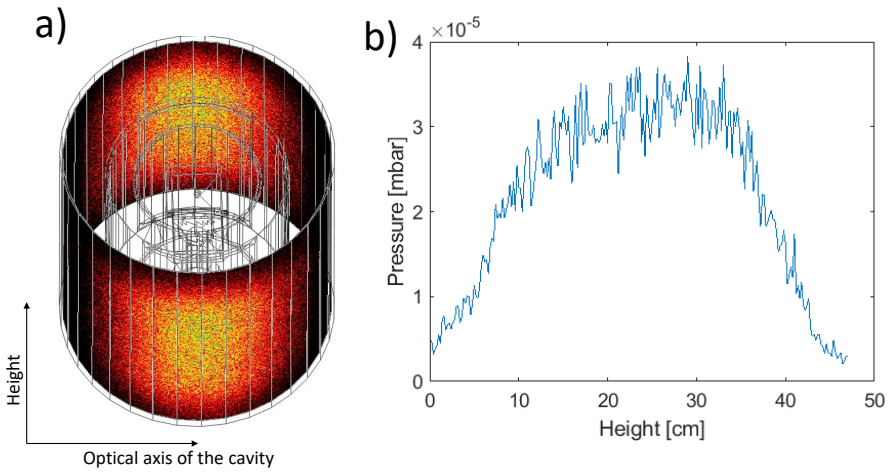


Figure 4.12: Determination of the location of the turbopump. a) Pressure mapping on the walls of the vacuum chamber. b) Pressure profile along the facet in front of the shield hole. Simulations are performed with the *Molflow+* software.

issues. The height of the turbomolecular pump was determined using the pressure profile of Figure 4.12(b). The pump is placed in the vicinity of the maximum of this curve, *i.e.* at 25 cm from the bottom of the chamber.

4.5 CAVITY RING DOWN SPECTROSCOPY

The buffer gas cooling setup requires the setting of several parameters in order to work properly, amongst which the tuning of the helium and target gas throughput and the positioning of the target gas line pipe. They require some signal that instantaneously reacts with their adjustment in order to determine the working setpoint of the setup. While the use of the FTS presented in chapter 2 presents the multiplex advantage, allowing to cover broad spectral regions in a single measurement, it lacks a real-time response which can be provided by the cavity ring-down spectroscopy (CRDS) technique. CRDS is an attractive technique for the buffer gas cooling setup since it possesses a high spectral resolution and a high sensitivity. Furthermore, this technique is insensitive to fluctuations in intensity of the laser employed for probing the gaseous sample. Figure 4.13 illustrates the working principle of CRDS. A laser with a very narrow linewidth is injected into an optical

cavity. Usually, the cavity's configuration consists in a stable two-mirror resonator [114]. When the laser and the cavity are in resonance[2], light intensity inside the cavity builds up. Since the cavity mirrors are not perfectly reflective, there is light leaking at the output of the cavity. A detector is placed at the cavity output and measures the leakage beam. Once light intensity at the detector exceeds a certain threshold value thanks to sufficient intensity build-up in the cavity, coupling of light inside the cavity is abruptly stopped. Light intensity at the detector then decreases exponentially. In the absence of absorbing species, the decay time mainly depends on the reflectivity of the cavity mirrors. Absorbing species will introduce extra-losses, leading to a decrease in the decay time at specific wavenumbers. This spectroscopic technique thus consists in measuring changes in a resonant cavity's decay time that are caused by light absorption in the cavity medium as the wavenumber of the laser is swept. The decay time is inversely proportional to the absorption coefficient, allowing to retrieve the molecular fingerprint from the measured ring-down times, as illustrated in Figures 4.13(b) and 4.13(c).

Figure 4.14 is a schematic of the CRDS setup we used to seek the first cold molecules obtained with the buffer gas cooling setup. A single-mode distributed feedback (DFB) laser[3] passes through an AOM (model MGAS80-A1 from AA opto-electronics). The first diffraction order of the AOM is injected into the optical cavity. The AOM is the element responsible for the rapid light coupling interruption. Indeed, since we aligned the optical cavity on the first diffraction order of the AOM, turning off the AOM RF source actually stops the light coupling with the cavity. A low-voltage piezoelectric transducer is employed to rapidly sweep back-and-forth the entire cavity FSR by applying a triangular ramp function using an arbitrary waveform generator (Model 4045B from BK Precision). The DFB laser is mounted on a universal 14-Pin butterfly laser diode mount (model LM14S2 from Thorlabs). The wavelength of the DFB laser is scanned by adjusting its temperature using the circuitry from the *Fantasio+* setup. The constant current laser driver is a circuitry made in-house by the electronical workshop. Ninety percent of the DFB light is coupled to the optical cavity, the ten remaining percent is equally shared between a reference cell and

2 Sweeping the cavity length permits to guarantee that there is always some point where the cavity will be resonant with the laser mode.

3 The reference is not specified since it depends on the range of wavelengths we are probing.

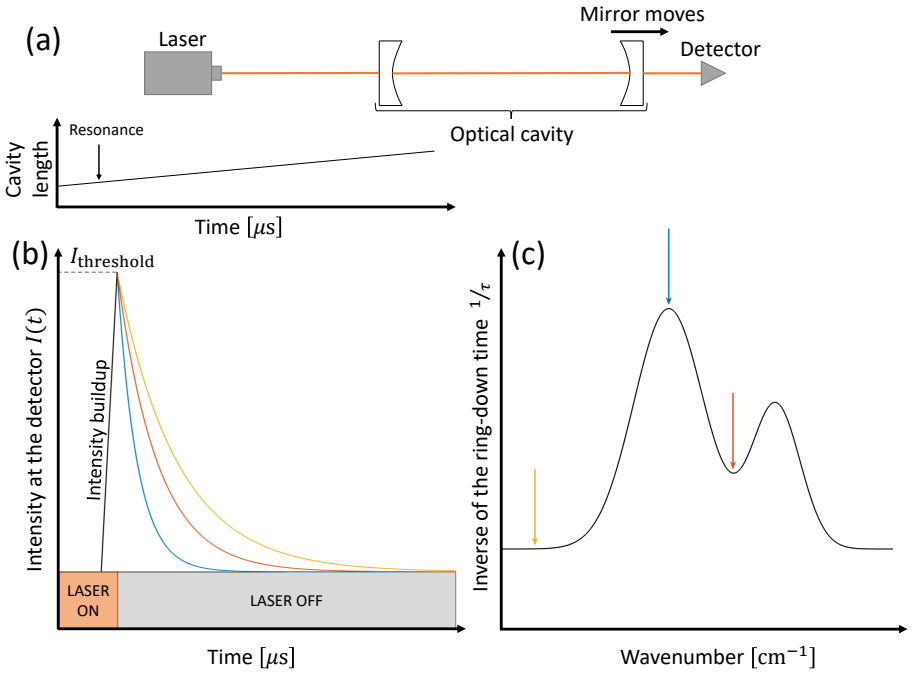


Figure 4.13: Working principle of our CRDS setup. (a) A laser with a narrow linewidth is injected in an optical cavity made of two highly reflective mirrors. A detector is placed at the output of the cavity. The cavity length is swept. (b) Intensity with respect to time measured at the detector. The laser is turned off once the intensity reaches a threshold value. The three exponential decays are recorded at different wavenumbers. (c) Inverse of the ring-down time with respect to the wavenumber. The three arrows are related to the exponential decays shown in (b).

an etalon cavity using fibered beamsplitters. The role of the etalon cavity is to have information about the relative change in wavelength of the DFB laser when modifying its temperature. It consists in two 90:10 beamsplitters (model BSX06 from Thorlabs) placed on a 7.5 cm long tubular ULE spacer with an outer diameter of 2 cm (machined by the Docter Optics company). The beamsplitters are maintained in place using heat-shrinking tubes. The tube is placed in a small vacuum chamber to isolate it from pressure fluctuations in the laboratory. A fibered acetylene cell allows to retrieve the true wavelength of the DFB laser. This absolute calibration is possible only if we encounter a molecular transition of acetylene at some point during the scan. A fibered optical isolator ensures that no light is sent back into the DFB laser head. The detector placed at the output of the cavity is an InGaAs photodiode. An integrated circuitry built in-house by our electronics workshop compares the intensity of the leakage beam at the output of the cavity with an adjustable threshold. It generates a pulse with a width that can be varied. The chosen duration depends on the decay times we are able to reach with the pair of mirrors installed and their alignment. The acquisition system is developed in Labview. It is a duplicate of the acquisition software of the *Fantasio+* setup [115, 116]. It manages the temperature control of the DFB head and therefore the wavelength it emits, the recording of the cavity's ring-downs, their fitting and the measurement of the signals from the etalon and the reference cell. It finally evaluates the absorption coefficient.

4.6 FIRST RESULTS

This section describes the results we obtained with the buffer gas cooling setup. In section 4.6.1, we describe the method we followed to obtain the first signal of cold molecules. In section 4.6.2, we characterize the lowest translational temperature we were able to reach with the setup. We present the influence of the helium density in the cold cell on the cooling of molecules.

4.6.1 *Obtaining the first signal*

The use of the CRDS for the determination of the setpoint of the buffer cooling gas setup was a two-step process: (1) we first measured the molecular fingerprint of the species under study; (2) we then placed

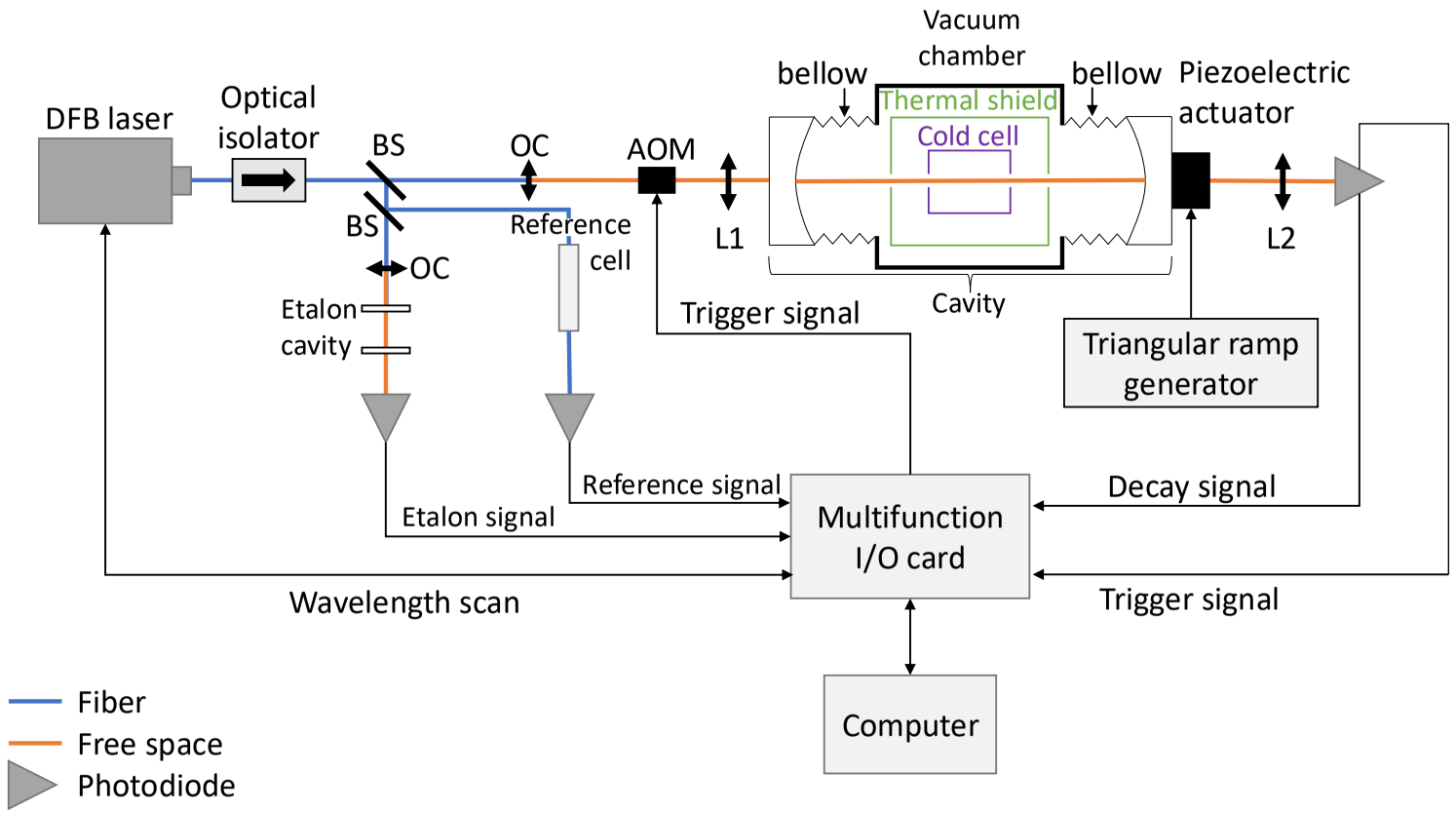


Figure 4.14: Schematic of the cavity ring-down spectroscopy setup implemented on the buffer gas cooling setup. AOM, BS, DFB, L, and OC respectively stand for acousto-optic modulator, beamsplitter, distributed feedback, lens and output coupler.

ourselves at the wavelength where absorption was supposed to be the most intense at low temperature in order to adjust the throughput of helium and of the target gas and to properly position the target gas injection pipe.

The first step is due to the fact we do not have any wavemeter on the setup that would allow us to determine, with sufficient accuracy, the exact wavelength of the DFB laser. We have instead an etalon made of ULE as a relative wavelength reference and a reference cell containing C_2H_2 (and H_2O as an impurity) for absolute calibration. Scanning the entire spectral range of the DFB laser head in presence of the species under study at room temperature allows us to observe its molecular fingerprint, and thus the temperature of the DFB head for which a specific transition occurs. In order to probe molecules at room temperature while the cold head is at cryogenic temperature, we inject the target gas in the vicinity of one of the cavity mirrors (see Appendix C.1). Alternatively, using water as the target molecule allows to observe its molecular fingerprint in the etalon and reference signals. Indeed, as illustrated in Figure 4.15(a), the water fingerprint modulates the envelope of the interference pattern of the ULE etalon. The fringes are obtained by recording the light transmitted by the etalon while scanning the emission wavelength of the DFB laser. The scan is performed by changing the temperature of the DFB head. As we can see in Figure 4.15(a), the emission wavelength varies non-linearly with the temperature, justifying the use of an etalon as a relative wavenumber reference. In Figure 4.15(b), we can observe the signal from the reference cell in which traces of water are observed. The advantage of the reference cell signal is that there are many sampled values per transition, meaning they are well defined. However, we do not know exactly at which pressure the transitions are observed.

We thus chose water, and more specifically the J_{K_a,K_c}: $1_{01} \leftarrow 1_{10}$ transition in the $\nu_1 = 2$ stretching region in order to determine an operating point for the apparatus and to familiarize ourselves with it. The line intensity of this transition should be enhanced by a factor of about 3 when cooled down at 15 K, compared to room temperature. This transition occurs at 7182.2096 cm^{-1} [117]. We employed two cavity mirrors with a reflectivity higher than 99.995% at 1392 nm (Ref. 140989 from Layertec) and the corresponding DFB head (model EP1392-DM-B01-FM from Eblana Photonics, subsequently denoted by DFB Y in the manuscript). The first transition we observed is plotted in Figure 4.16

which was corrected to remove the contribution from the emtpy cavity. As mentioned in section 4.5, the data acquisition returns the absorption coefficient α. This value includes contributions from both the empty cavity and the absorbing species. However, we are only interested in the latter. It was evaluated using the following relationship (see Ref. [118]):

$$\alpha = \frac{L}{cl}\left(\frac{1}{\tau} - \frac{1}{\tau_0}\right), \tag{4.23}$$

where L is the total cavity length, c is the velocity of light, l the length over which the sample spreads inside the cavity, τ the ring-down time in presence of the sample and τ_0 the ring-down time for an empty cavity. In our case, considering that the sample remains confined in the cold cell[4], we have $l = 0.08$ m and $L = 1.05$ m. In order to evaluate τ_0, we use the baseline of the signal. In the case of this single transition, we approximated the baseline to the mean value of the absorption coefficient in regions where there is no visible absorption. In order to determine the sensitivity of this measurement, we evaluated the standard deviation of the absorption coefficient before applying the L/l correction in the region between 7181.82 cm^{-1} and 7181.84 cm^{-1}, leading to $\alpha_{min} = 1.45 \times 10^{-9}$ cm^{-1}.

This first signal served as a starting point for the optimization (1) of the tube positioning and (2) of the helium throughput injected at the bottom of the cold cell. The goal was to minimize the ring-down time in both cases. Concerning (1), if more water molecules are injected within the cold cell, there is more absorption. In the case of (2), if the cooling process is more efficient, the line intensities of the transitions associated to the lowest energy levels are enhanced, leading to more absorption as well.

In parallel, following suggestions made by Samir Kassi, a collaborator from the University of Grenoble Alpes, a booster was placed between the optical isolator and the DFB laser (Ref. BOA1410S from Thorlabs) and we increased the diameter of the two orifices of the cold cell through which light passes from 4 mm to 7 mm. On the one hand, the booster increased the number of photons reaching the detector. On the other hand, the larger orifices allowed for the suppression of diffraction losses. These two changes allowed the CRDS setup to gain at least one order of magnitude in terms of sensitivity. Following this,

4 This assumption should be further investigated in the future.

we investigated the influence of the helium density within the cold cell on the transition linewidth and lineshape, leading to the evaluation of the translational temperature of these molecules by looking at the Doppler broadening. This study is detailed in section 4.6.2.

4.6.2 *The J_{K_a,K_c}: $1_{01} \leftarrow 1_{10}$ transition in the $2\nu_1$ overtone band of water: characterization of the translational temperature*

Assuming that the only contribution to the lineshape of the water transition is the Doppler effect, we can evaluate the translational temperature of the water molecules by fitting the transition with a Gaussian curve in order to retrieve its FWHM, denoted $\Delta\tilde{\nu}_{\text{FWHM}}$ and expressed in cm^{-1}, which is then related to the translational temperature T by the following expression (see Ref. [60]):

$$\Delta\tilde{\nu}_{\text{FWHM}} = 7.16 * 10^{-7}\tilde{\nu}_0\sqrt{\frac{T}{M}}, \tag{4.24}$$

where $\tilde{\nu}_0$ is the wavenumber at which the transition occurs and M the molar mass of the molecule, in g/mol.

Figure 4.17 is a plot of the J_{K_a,K_c}: $1_{01} \leftarrow 1_{10}$ transition in the $\nu_1 = 2$ stretching region of water that we recorded for three different helium throughputs injected at the bottom of the cold cell. In Figure 4.17(a), we can see that increasing the helium throughput reduces the FWHM of the transition while increasing its height. This is outlined by the difference in FWHM between the three curves. The increase of the absorption coefficient with the helium density partially results from the difference in population of the lower energy of the 1_{10} rotational state but it cannot be responsible for such an improvement on its own. The temperatures associated with the two higher helium throughputs are approximately equal to 20.8 K and 19.5 K while the temperature associated to the lowest one is approximately 24.8 K. Unfortunately, we were limited by the pumping capacity and we had to stop increasing the helium throughput. However, we should be cautious with these values. Indeed, in Figure 4.17(b), we observe a mismatch between the Gaussian curve and the experimental data for the three helium throughputs. We associate this discrepancy with a contribution of the non-thermalized molecules to the transition lineshape. Once normalized on the transition height, we observe a mismatch between the wings of the Gaussian fitting curve and experimental data of about 5 percent

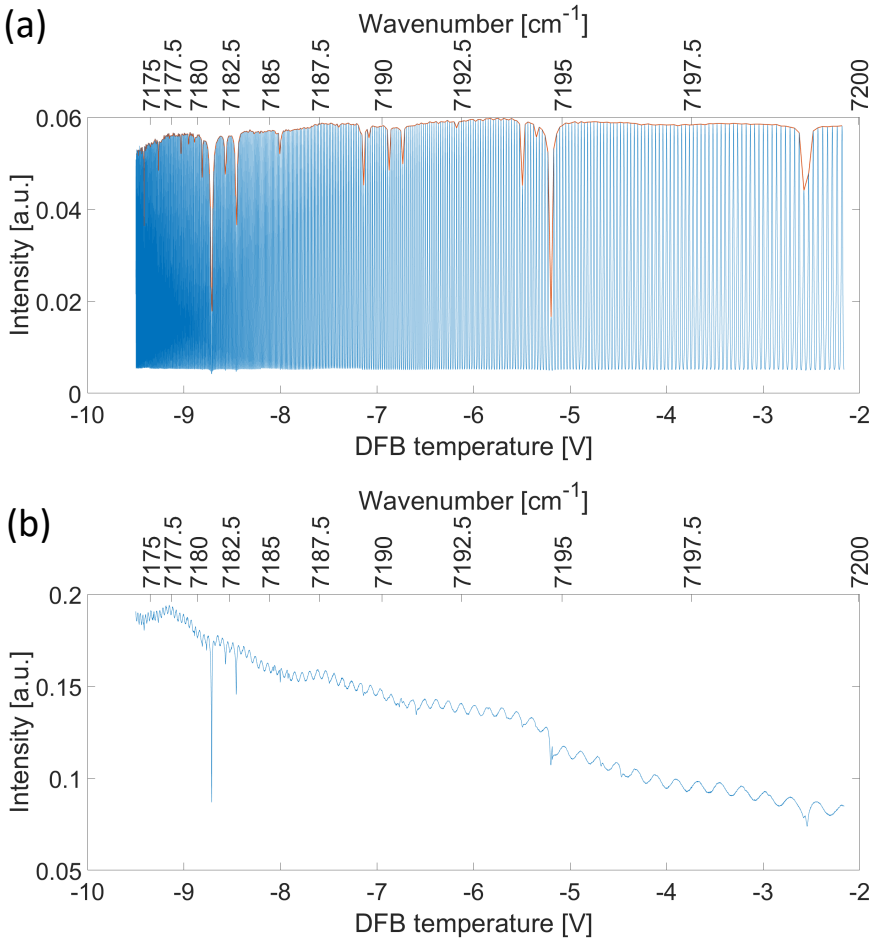


Figure 4.15: (a) Interference pattern at the output of the 75 mm long ULE etalon. The blue trace is the signal recorded while scanning the temperature. The red trace is the envelope of this signal. The change in wavelength between two adjacent maxima corresponds to an etalon FSR. (b) Signal at the output of the reference cell. Some of the transitions observed in the envelope of the etalon are visible in the signal from the reference cell. Oscillations in the reference cell baseline are imputed to a parasitic Fabry-Perot effect. Both plots were measured with the EP1388-DM-B01-FM DFB head from Eblana Photonics (DFB Z).

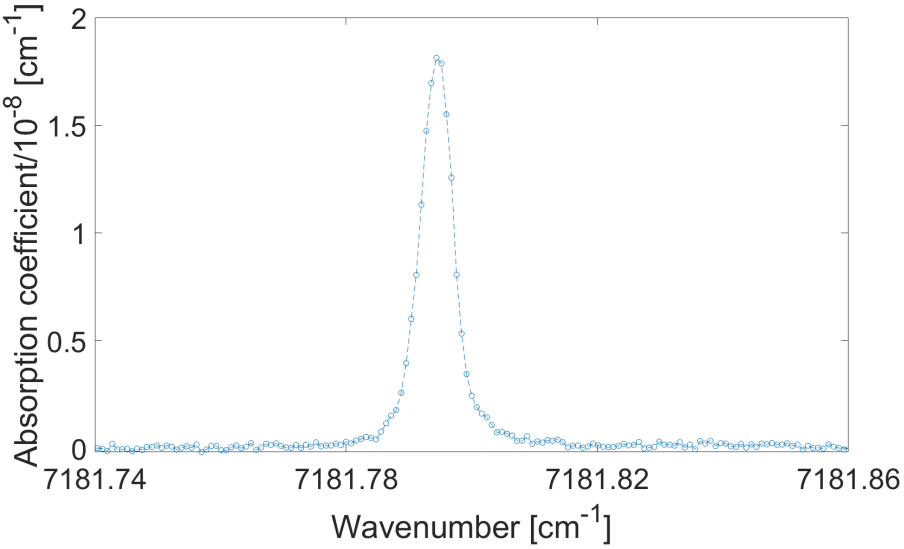


Figure 4.16: First signal obtained with the CRDS, corrected using equation (4.23). Minimum detectable absorption coefficient for an empty cavity: $\alpha_{\text{min}} = 1.45 \times 10^{-9}$ cm^{-1}, corresponding to the standard deviation of all the means of measured ring-downs (150 ring-downs per spectral element) between 7181.82 cm^{-1} and 7181.84 cm^{-1} before applying the L/l correction.

for the smallest throughput and smaller than one percent for the two higher throughputs. In Figure 4.18, we fitted the experimental data with a sum of two Gaussian curves centered on the same wavenumber value. These two Gaussian curves are associated with temperatures of 19.0 K and 148.4 K. A similar fit was performed on the data associated with the two other throughputs, leading to temperatures of 20.2 K and 191.8 K intermediate throughput and to temperatures of 19.0 K and 115.6 K for the highest throughput.

4.7 The $2\nu_1$ overtone band of methanol: characterization of the rotational temperature

The methanol is a six-atoms asymmetric top molecule. This is the smallest molecule to present internal rotation. The size of this molecule and the presence of this large amplitude motion lead to a dense and disordered rotational structure. This structure gets even more complicated when one goes up in energy with vibrational excitations. Due to its complicated spectrum, this molecule remains poorly known, especially

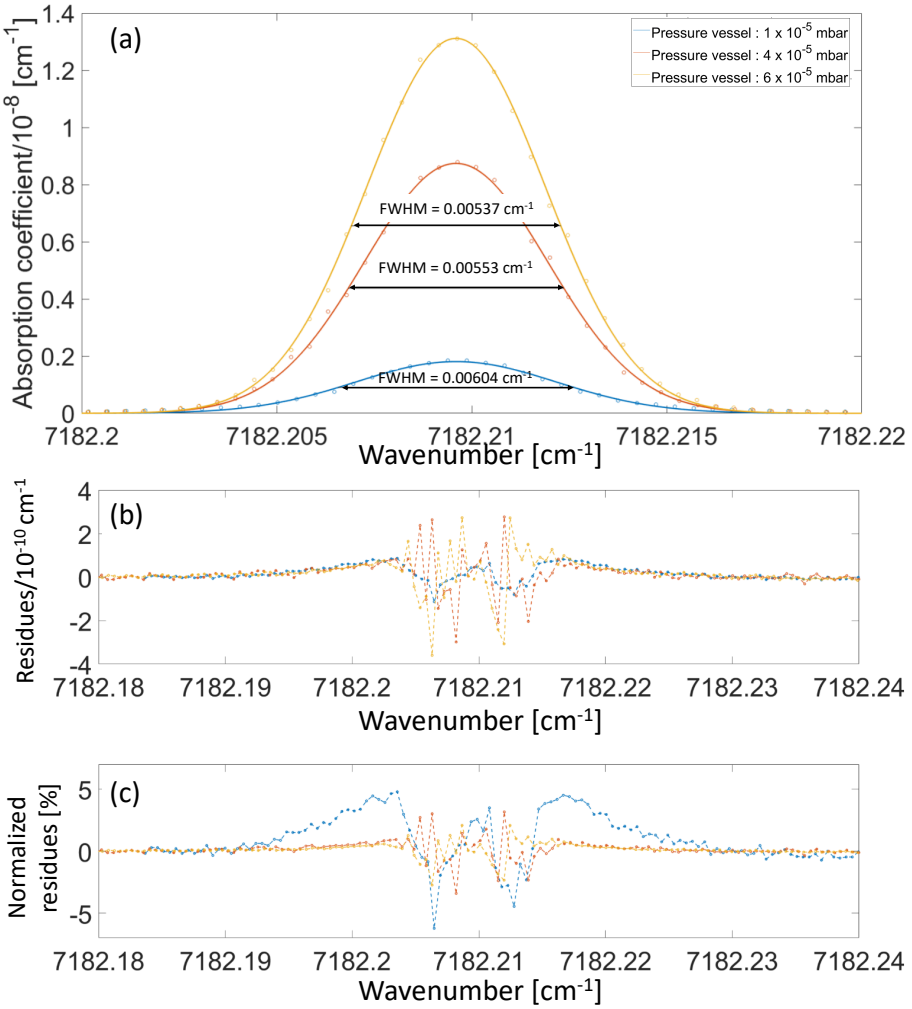


Figure 4.17: Absorption coefficient of the J_{K_a,K_c}: $1_{01} \leftarrow 1_{10}$ transition in the $\nu_1 = 2$ stretching region of the water molecule recorded using our CRDS setup. (a) Several helium throughputs are tested and fitted with a Gaussian curve. The indicated pressures are measured within the outer vacuum vessel. Translational temperatures are equal to 24.8 K, 20.8 K and 19.5 K for the blue, red and orange curves respectively. (b) Residues of the fit of the data with a single Gaussian. (c) The residues are normalized by the height of the transition.

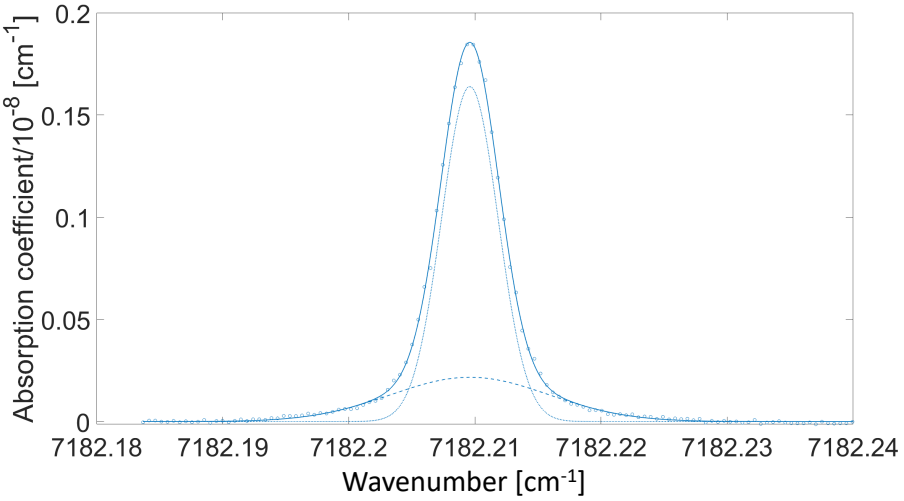


Figure 4.18: Absorption coefficient of the J_{K_a,K_c}: $1_{01} \leftarrow 1_{10}$ transition in the $\nu_1 = 2$ stretching region of the water molecule recorded using our CRDS setup for the smallest throughput (pressure vessel: 10^{-5} mbar). The curve is fitted with a sum of two Gaussian curves (continuous line). The temperatures associated with the dotted and dashed Gaussians are respectively 19.0 K and 148.4 K.

in the NIR. This frequency range was recently explored by Svoboda *et al.* [119], probing the $2\nu_1$ vibration overtone. In this report, the authors were able to assign on the order of a few percent of the observed lines. It thus seemed to be a promising candidate to challenge our ability to record and understand the spectral signature of large molecules in the overtone range using the cooling efficiency of the buffer gas cooling setup and the sensitivity of the cavity ringdown spectrometer.

During a second measurement campaign, we therefore replaced the water contained in the bubbler with methanol, otherwise kept everything else in the setup unchanged. It allowed us to probe the methanol $2\nu_1$ overtone band lying between 7180 cm^{-1} and 7220 cm^{-1}. This band was already measured by V. Svoboda *et al.* [119]. It was recorded using the DFB Y and another DFB head, the model EP1388-DM-B01-FM from Eblana Photonics, subsequently denoted by DFB Z. We spread the measurement session over three work days to cover the two DFB wavenumber ranges, leading to the spectrum presented in Figure 4.19. Once again, the contribution of the empty cavity to the absorption coefficient was removed using equation 4.23. In order to evaluate the

value τ_0, we determined the baseline of the spectrum using the peak detection algorithm presented in Appendix E. While we could only measure the translational temperature of the water transition presented in Figure 4.24, we were able to investigate the rotational temperature of the methanol spectrum presented in Figure 4.19. The rotational temperature affects the linestrength of the ro-vibrational transitions. Its characterization follows the procedure described by Santamaria *et al.* [101] and Svoboda *et al.* [119]. Their approach relies on the relationship between the line intensity at a temperature T, denoted $S(T)$, and the line intensity at a temperature T_{ref}, denoted $S(T_{\text{ref}})$, which is given by:

$$S(T) = S(T_{\text{ref}}) \left(\frac{Q_{T_{\text{ref}}}}{Q_T} \right) \frac{\exp\left(\frac{-c_2 E''}{T}\right)}{\exp\left(\frac{-c_2 E''}{T_{\text{ref}}}\right)} \frac{\left[1 - \exp\left(\frac{-c_2 \nu_{ij}}{T}\right)\right]}{\left[1 - \exp\left(\frac{-c_2 \nu_{ij}}{T_{\text{ref}}}\right)\right]}, \tag{4.25}$$

where Q_T is the total internal partition sum value for the temperature T, $Q_{T_{\text{ref}}}$ is the total internal partition sum for the temperature of T_{ref}, ν_{ij} the vacuum wavenumber of the transition, E'' its lower state energy and $c_2 = \frac{hc}{k_B}$ is the second black body radiation constant, with c the light velocity, h the Planck constant and k_B the Boltzmann constant. The reader who is interested in having further details concerning the key parameters impacting the line intensity of a transition should refer to Appendix A.8.1.

The ratio of two line intensities $S_a(T)$ and $S_b(T)$ at a temperature T is related to the ratio of their intensities, denoted $R(T)$, at a temperature T_{ref} by:

$$R(T) = \frac{S_a(T)}{S_b(T)} = \frac{S_a(T_{\text{ref}})}{S_b(T_{\text{ref}})} \frac{\exp\left(\frac{-c_2 E_a}{T}\right)}{\exp\left(\frac{-c_2 E_a}{T_{\text{ref}}}\right)} \frac{\exp\left(\frac{-c_2 E_b}{T_{\text{ref}}}\right)}{\exp\left(\frac{-c_2 E_b}{T}\right)}. \tag{4.26}$$

In order to obtain equation (4.26) from equation (4.25), the factor $\left[1 - \exp\left(\frac{-c_2 \nu_{ij}}{T}\right)\right] / \left[1 - \exp\left(\frac{-c_2 \nu_{ij}}{T_{\text{ref}}}\right)\right] \approx 1$ was neglected[5]. Svoboda *et al.* [119] assigned 12 of the hundreds transitions of the methanol molecule in the ortho configuration with certainty by cross-checking the assignment using two methods: (1) the Two-Temperature Analysis (TTA) and (2) the Ground States Combination Difference (GSCD). They also specified the linestrength of these transitions at a temperature

5 This approximation is valid since $c_2 \approx 1.4388$ cm K, ν_{ij} takes values between 7170 cm^{-1} and 7210 cm^{-1} and T and T_{ref} take values around 20 K, meaning that the two exponential terms tend to zero.

of 13 K. We were thus able to compute a theoretical value $R_{\text{th}}(T)$ for any combination of these 12 ortho transitions. In parallel, we experimentally evaluated their intensity[6], meaning that we could provide a value for the experimental line intensity ratio, R_{exp} for any combination of the 12 transitions. In order to measure the rotational temperature of the methanol molecules, we looked for the value of T such that $R_{\text{th}}(T) = R_{\text{exp}}$ for all possible combinations of transitions, leading to a rotational temperature $T_{\text{Rot}} = 20.3 \pm 7.0$ K. This temperature is in good agreement with the translational temperature of the 12 methanol transitions $T_{\text{trans}} = 21.8 \pm 1.3$ K, evaluated using equation (4.24). It is a signature of equilibrium between these two degrees of freedom. At this point, no hot bands could be identified and the vibrational temperature could not be determined. Relevant information for the temperature analysis is summarized in Table 4.2.

As a cross-check for our estimation of the translational and rotational temperatures, we compared the general shape of a small region of our spectrum with the same region of the spectrum measured by Svoboda *et al.* at 23 K (Figure 3 of Ref. [119]). Both of them are displayed in Figure 4.20. As we can see, there is a good agreement between the two of them, both in terms of transition linewidths and of relative intensities between the transitions, comforting us in our evaluation of the two temperatures. However, to obtain this plot, we had to shift of 0.0136 cm^{-1} our data towards smaller wavenumbers, meaning there might be some issues concerning the wavenumber-calibration process. This can be noticed by comparing the linecenters we measured with the values of Svoboda *et al.* [119] for the 12 transitions of Table 4.2. Indeed, there is a mean discrepancy of -0.009 cm^{-1} between the two sets of values. We might thus perform the measurement once again, but with mixing water and methanol in the bubbler this time in order to observe transitions associated to water in addition to the molecular fingerprint of methanol. It will allow us to improve the absolute wavenumber-calibration process.

Figure 4.20(b) is a zoom-in view of a small region of Figure 4.20(a) that highlights the sensitivity and the dynamic range of our measurement. We evaluated the standard deviation of this signal in the region between 7180.2 cm^{-1} and 7180.4 cm^{-1}, leading to $\alpha_{\text{min}} = 2.76 \times 10^{-10} \text{cm}^{-1}$. This value is five times smaller than the one obtained for the signal

6 The 12 transitions were fitted with Gaussian curves. The fitting coefficients were injected in equation (A.81), which, in turn, allowed to evaluate equation (A.77).

presented in section 4.6.1. One has to be cautious when comparing the two $\alpha_{\min}$ since fewer values were acquired per spectral element in the second case, meaning that the gain in sensitivity is even better than this value[7].

Finally, Figure 4.21 illustrates the advantage of recording spectra at cold temperature. In this figure, we plotted a part of the raw spectrum [8] presented in Figure 4.19 (upper frame) along with the spectrum of methanol measured when the cold cell was at 270 K and in absence of helium injected at the bottom of the cold cell (lower frame). Both plots were normalized on their most intense peak. While a forest of narrow peaks is clearly visible in the spectrum of the upper frame, we see a series of dispersed broad peaks in the lower frame. Furthermore we experience difficulties to distinguish their wings from the baseline.

4.8 CONCLUSION

In this chapter, we presented the buffer gas cooling that was developed and built in-house. The working principle behind buffer gas cooling was first detailed. Then, a complete description of the mechanical design was given, along with the dimensioning of the pumping capacity of the vacuum chamber. Considerations about the cold cell temperature measurement and control units, along with safety issues, were detailed in Appendix C. The CRDS setup that was developed to obtain the first spectra of cold molecules was detailed. Finally, the methanol $2\nu_1$ overtone band lying between 7180 cm^{-1} and 7220 cm^{-1} was recorded using the buffer gas cooling setup and the CRDS. The translational and rotational temperatures were evaluated to 21.8 ± 1.3 K and 20.3 ± 7.0 K respectively. With this measurement, we demonstrated our ability to record rovibrationally resolved spectra at relatively high frequencies, *i.e.* in the NIR region.

7 The acquisition system switches from one spectral element to the following one when it has either acquired a given number N of decay curves or it has spent more time that a timeout value $t_{\max}$. In the case of the water transition, these two parameters were set to $N = 150$ decays and $t_{\max} = 3.6$ s. In the case of the methanol spectrum, these two values were equal to $N = 50$ decays and $t_{\max} = 1.5$ s.

8 We did not use equation (4.23) to remove the contribution from the empty cavity.

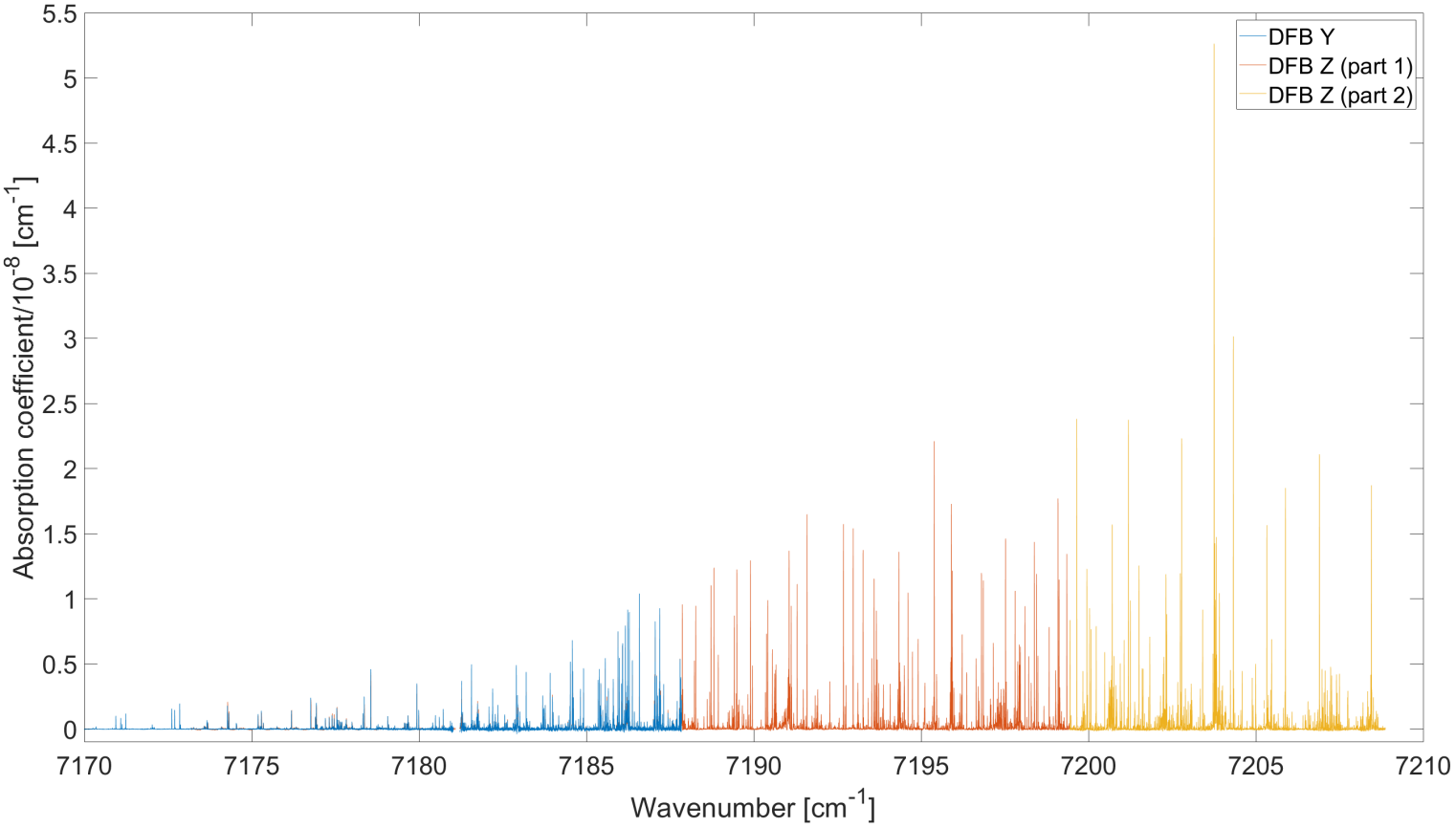


Figure 4.19: DFB Absorption spectrum of methanol between 7180 cm^{-1} and 7208 cm^{-1} recorded by using two DFB lasers (DFB Y and Z). Minimum absorption coefficient detectable for an empty cavity: $\alpha_{min} = 2.76 \times 10^{-10}$ cm^{-1}, corresponding to the standard deviation of all the values between 7181.82 cm^{-1} and 7181.84 cm^{-1} before applying the L/l correction.

Table 4.2: List of assigned transitions used for the determination of the translational and rotational temperatures of the methanol spectrum.

Measured wavenumber $[cm^{-1}]$	Integrated line intensity at 13 K $/10^{-7}$ $[cm^{-1}]$	Lower rotational level	Lower state energy $[cm^{-1}]$	Measured wavenumber $[cm^{-1}]$	Integrated line intensity $/10^{-8}$ $[cm^{-2}]$	Measured FWHM $/10^{-3}$ $[cm^{-1}]$
Ref. [119]	Ref. [119]	Ref. [119]	Ref.[120]	Our study	Our study	Our study
7197.8219	7.028	(0,0,A)	0	7197.8273	4.841	4.1611
7198.1151	6.236	(0,0,A)	0	7198.1211	4.276	4.1328
7205.3378	12.2	(0,0,A)	0	7205.3506	6.872	4.2194
7194.6216	7.246	(1,0,A)	1.61353	7194.6277	4.988	4.2793
7194.9242	4.846	(1,0,A)	1.61353	7194.9310	3.424	4.4658
7199.6677	1.279	(1,0,A)	1.61353	7199.6731	9.744	4.2360
7206.9078	11.89	(1,0,A)	1.61353	7206.9253	9.590	4.2377
7192.9815	8.154	(2,0,A)	4.84048	7192.9873	6.881	4.1544
7193.2745	7.285	(2,0,A)	4.84048	7193.2807	6.284	4.2410
7201.2051	12.98	(2,0,A)	4.84048	7201.2144	10.82	4.2194
7201.2638	5.451	(2,0,A)	4.84048	7201.2727	4.438	4.1927
7208.4607	11.07	(2,0,A)	4.84048	7208.4794	8.953	4.5341

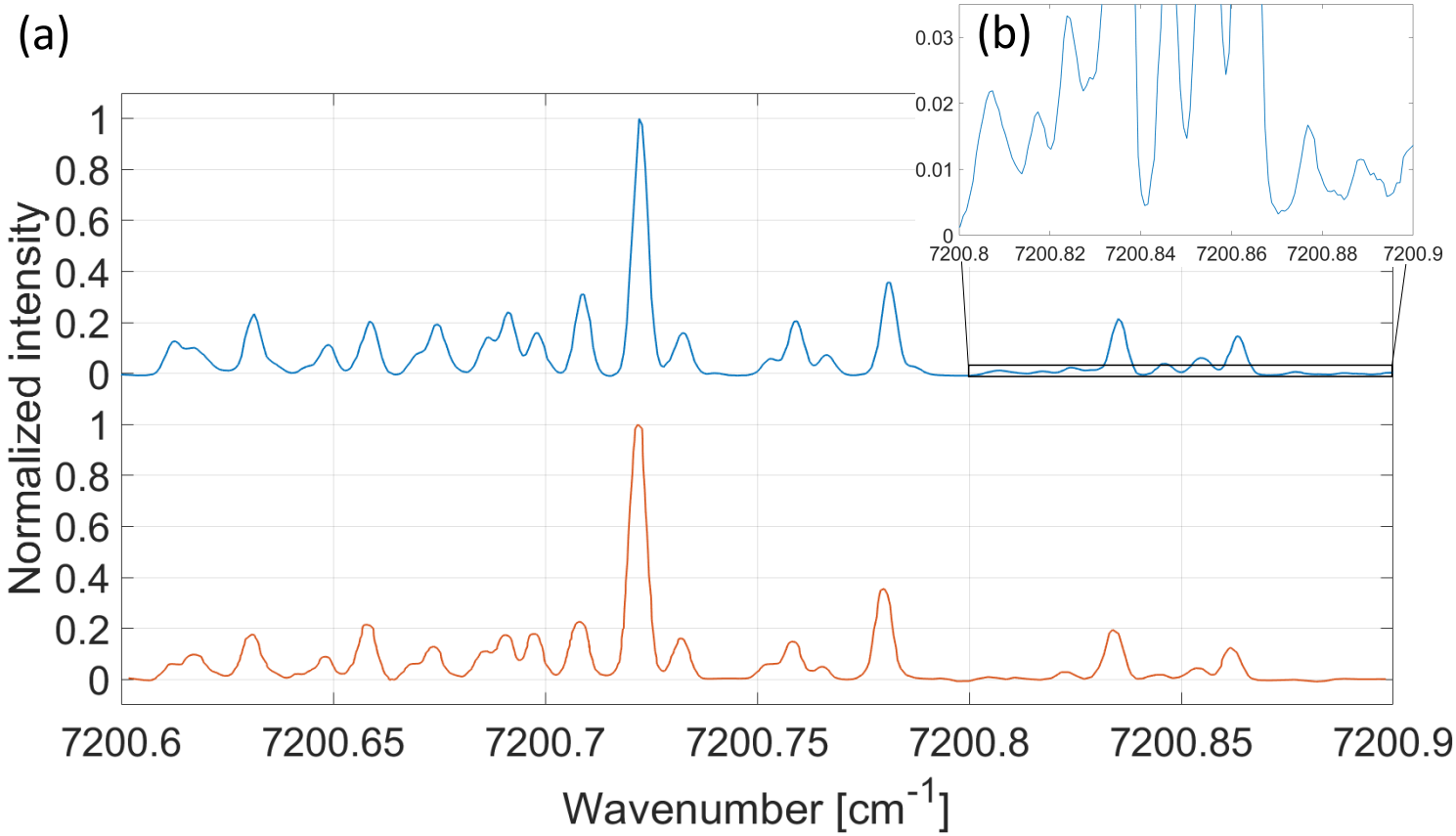


Figure 4.20: (a) Spectrum of methanol between 7200.6 cm^{-1} and 7200.9 cm^{-1} measured at 23 K by Svoboda *et al.* (Figure 3 of Ref.[119]) in red and ours in blue. The two spectra were normalized on their most intense peak. Our wavenumber scale was shifted to match theirs. Their data were retrieved from their plot using the free software *Engauge Digitizer*. (b) Zoom-in view on the *y*-scale in the region between 7200.8 cm^{-1} and 7200.9 cm^{-1}. Frame (b) illustrates the dynamic range of the measurement and the level of information hidden in the baseline.

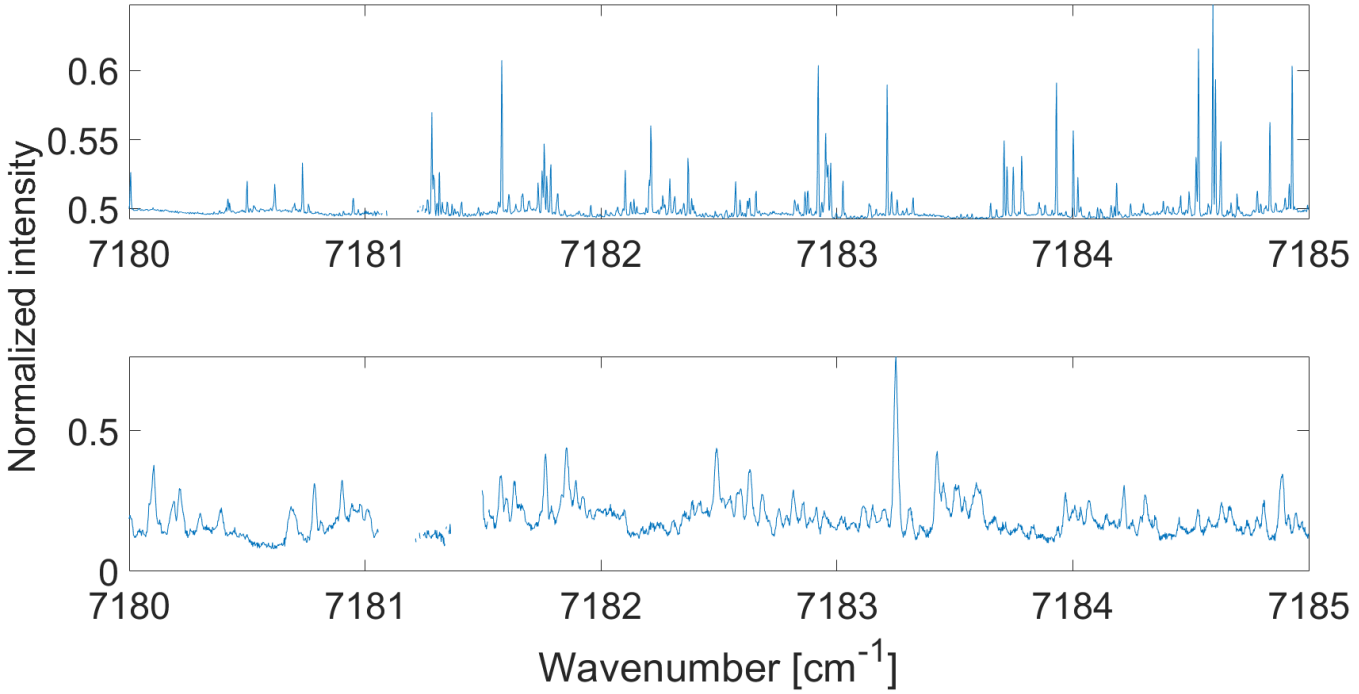


Figure 4.21: Comparison between the spectrum of methanol measured at cryogenic temperature (temperature of the cold cell equal to 15 K, helium is injected at the bottom of the cold cell) and the spectrum measured with no injection of helium at the bottom of the cold cell and for a cold cell at 270 K. The temperature of the cold cell was measured in both cases with the controller described in Appendix C.2.3. The relative intensities should not be considered as reliable in this figure but it nicely illustrates the spectral simplfication one obtains by cooling the methanol molecules.

5

PERSPECTIVES: TOWARDS BROADBAND METROLOGICAL MEASUREMENTS

5.1 INTRODUCTION

Since the construction of an ideal can be pursued in several directions, the goal of this chapter is to present perspectives and guidelines for the continuation of the presented work, and more especially for the coupling of frequency combs with optical cavities and the Fourier-transform spectrometer.

Section 5.2 introduces a technique developed in Ref. [13, 14] in order to surpass the maximum resolution of FTS when using a frequency comb as the broadband light source that will be implemented on the setup in the future.

First results concerning the stabilization of optical cavities on frequency-stabilized CW lasers and the coupling of femtosecond lasers with optical cavities are presented in section 5.3.

5.2 SURPASSING THE MAXIMUM RESOLUTION OF THE FTS

Coupling of a frequency comb with a FTS presents several advantages over conventional light sources, *i.e.* they are already collimated, they possess a high spectral brightness and they are temporally and spatially coherent. Furthermore, since the source is pulsed, it is also possible to perform some lock-in detection to reduce the noise of the measurement [15]. However, none of the aforementioned advantages actually takes advantage of the comb structure of these light sources. The group of Foltynowicz [13, 14] suggested a method relying on the comb structure to suppress the ILS of the FTS due to the finite length of its translation stage and to surpass its nominal resolution (see Appendix A.2.1 for details concerning the ILS of FTSs). This is accomplished by acquiring interferograms with delay ranges that are symmetric with respect to the centerburst and with a total length equal to c/f_{rep}. Indeed, the

ILS of a monochromatic light source, *i.e.* a single comb line, consists in a sinc function. By imposing the maximum delay to be equal to c/f_{rep}, we impose the zeros of the sinc function associated with a comb line to match the maxima of the sinc functions associated with the other comb lines. There is no more crosstalk between the different teeth of the comb and the ILS is therefore suppressed. The knowledge of the repetition and offset frequencies of the comb allows to gain precision on the wavenumber axis. It is possible to interleave spectra with different repetition and offset frequencies in order to increase the resolution of the spectrum and thus to surpass the nominal resolution of the FTS. One perspective for the instrument is to implement this paradigm. We are currently only limited by our inability to generate a frequency-stabilized frequency comb.

5.3 LOCKING OF THE FREQUENCY COMB ON AN OPTICAL CAVITY

While we have seen in chapter 2 that the coupling of SC light sources to optical cavities presents several advantages compared to conventional thermal light sources, the coupling of frequency combs with optical cavities is even better. Both the frequency comb and the optical cavity present a comb structure in the frequency domain. By imposing the optical cavity free spectral range (FSR) to be an integer multiple of the frequency comb repetition rate, the resonant teeth are transmitted through the cavity after having interacted with the sample over distances several orders of magnitude longer than the actual sample length. The spectral bandwidth over which this matching can be accomplished is only limited by the dispersion in the cavity, leading to a frequency-dependent FSR [24, 33, 80]. The situation where the comb of the femtosecond laser coincides with the one of the optical cavity is known as the *magic point* [24]. Figure 5.1 shows an oscilloscope trace showing we were able to experimentally observe the magic point with the MIRA900 femtosecond laser of Coherent matching an optical cavity nearly one meter long (meaning that one tooth over two was transmitted). The signal displayed in orange is the trigger signal associated with the triangular ramp applied to the piezoelectric actuator to sweep back and forth the cavity length around the magic point. The green trace is the intensity at the output of the optical cavity. The intensity is maximum when the cavity frequency comb structure exactly matches the frequency comb structure of the femtosecond laser and it rapidly decreases as we leave the magic point location. In order to observe

the magic point, we had to fine-tune the length of the cavity using translation stages actuated by micrometre screws (see Figure 4.11). The intensity pattern at the output of the cavity as a function of the departure from the magic point is detailed in Ref. [24].

In order to satisfy this condition during the whole measurement time, the cavity modes have to be locked on the frequency comb. The locking of the cavity on the frequency comb is equivalent to the stabilization of the cavity length. Indeed, the frequency comb structure of an optical cavity depends on its length, two adjacent teeth being distant of a FSR which can be evaluated using the following expression:

$$\mathrm{FSR} = \frac{c}{2nL}, \tag{5.1}$$

with c the velocity of light, n the refractive index of the cavity and L the cavity length. Fluctuations in the length of the cavity thus impact its frequency comb structure. These fluctuations can be due either to absorption, a slow thermal drift or to vibrations. Locking the cavity on a laser or a frequency comb thus requires the ability to modify the cavity length. This can be done thanks to a piezoelectric actuator. The correction signal applied to the piezoelectric actuator is generated by a PID controller, itself requiring some error signal, as shown in Figure 5.2.

The remaining of this section is dedicated to the generation of the error signal using the Pound-Drever-Hall method, along with the first error signal we were able to obtain and suggested improvements. It relies on Ref. [121, 122].

The Pound-Drever-Hall (PDH) stabilization scheme is a method to generate an antisymmetric error signal centred on the cavity maximum transmission point by some modulation technique rather than using one of the two fringe sides of the cavity mode. Indeed, fringe-side cavity locking presents the disadvantage of being sensitive to the laser intensity fluctuations [123]. This method relies on the reflective properties of the Fabry-Perot cavity on which the laser has to be stabilized. Indeed, when the emission frequency of a laser nearly matches the resonance frequency of an optical cavity, an intracavity standing-wave builds up. The leakage field at the input mirror of the cavity is basically in antiphase with the electric field of the laser which is directly reflected from the input mirror. The approximate cancellation of these two fields leads to a small net reflection coefficient with a phase shift which is

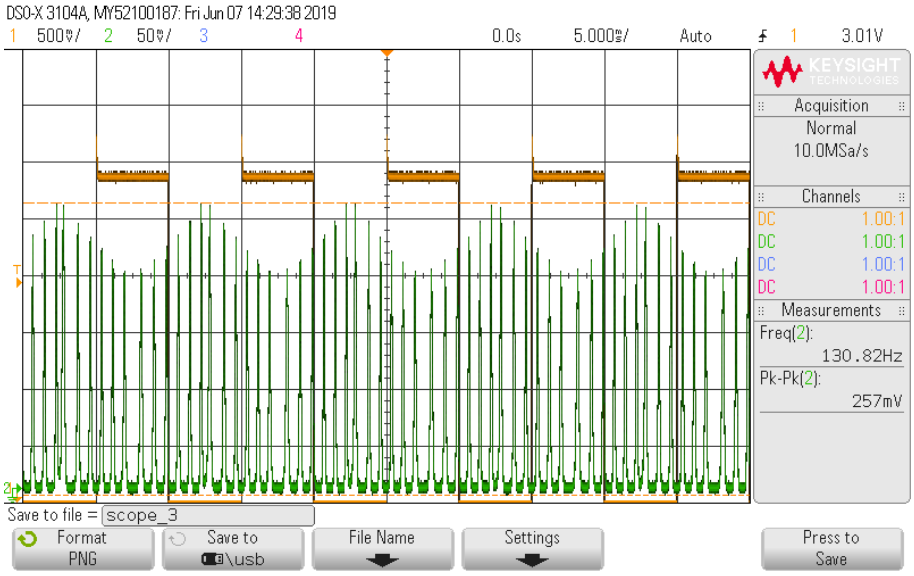


Figure 5.1: Trace of the oscilloscope displaying the observation of the magic point. The green trace corresponds to the intensity at the output of the optical cavity. The orange trace is the trigger signal associated with the voltage ramp applied on the piezoelectric actuator.

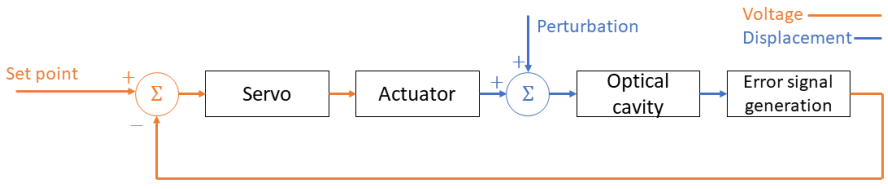


Figure 5.2: Feedback loop for the locking of an optical cavity on a femtosecond laser.

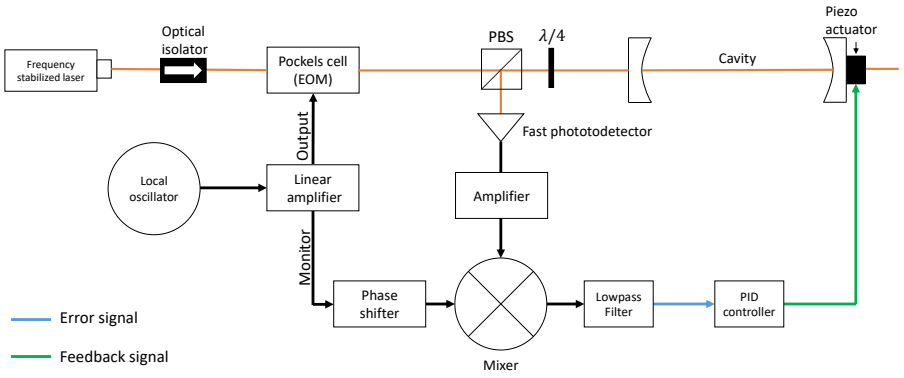


Figure 5.3: Experimental setup of the PDH stabilization scheme.

strongly frequency-dependent in the vicinity of the resonance. Furthermore, this phase shift is antisymmetric with respect to the frequency and centred on the resonance. In order to measure it, the laser beam passes through a phase modulator crystal (Pockels cell) driven by a local oscillator which produces phase-modulation sidebands. The modulation frequency is significantly larger than the cavity mode linewidth and sidebands are thus non-resonant, *i.e.* they spectrally lie outside the resonator passband. These FM sidebands are thus directly reflected from the optical cavity input mirror. They are steered to a fast photodetector, along with the net reflected carrier beam, by means of a polarizing beamsplitter and a quarter waveplate, as illustrated in Figure 5.3. The reflected signal is thus heterodyned with the sidebands. A phase demodulation against the local oscillator is finally performed, converting the symmetric minimum in the reflection coefficient into the desired antisymmetric discriminator curve required for the error signal. The complete stabilization scheme of the locking of a cavity on a frequency stabilized laser is depicted in Figure 5.3. In the case of the locking of a cavity on a frequency comb, a grating is placed before the detector in order to limit the spectral region reaching the photodiode [33, 124].

We implemented the layout presented in Figure 5.3 to attempt to lock a 150 mm long plano-concave cavity fulfilling the resonator stability condition onto the frequency-stabilized He:Ne laser presented in section 2.3.1. An optical isolator (Ref. IOT-3D-633-VLP from Thorlabs) was employed to avoid any optical feedback inside the laser cavity. The local oscillator was an arbitrary waveform generator (model 33120A

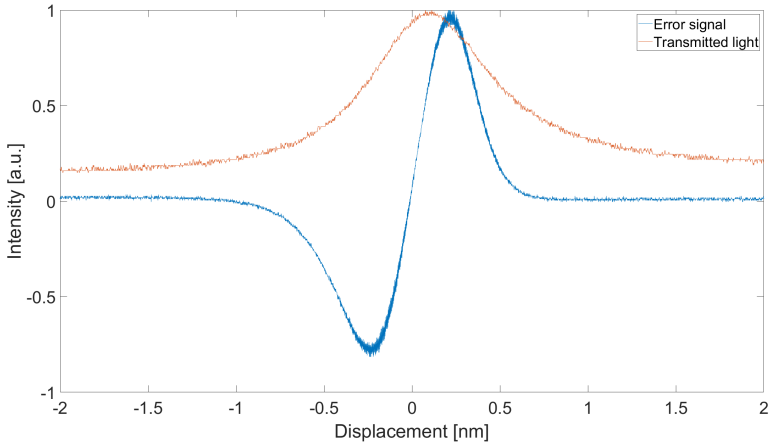


Figure 5.4: Error signal obtained experimentally.

from Agilent). The signal at its output was amplified by an old high-voltage linear amplifier (video linear amplifier VLA30 from Electro Optic Developments) and supplied to a broadband EOM (model PC22 from Electro Optic Developments). The amplifier was at the origin of important noise for modulations above 2 MHz, restricting us to slow modulations. A phase shifter (model JCPHS-2.5+ from MiniCircuits) allowed to modify the phase of the demodulation signal before it is sent into the phase mixer (ZRPD-1+ phase detector from MiniCircuits). The beam reflected from the input of the cavity was spatially separated from the incoming beam by means of a quarter waveplate (WPMQ10M-633 from Thorlabs) and a polarizing beamsplitter (PBS) (model PBS25-633/M from Thorlabs) and sent onto a fast photodetector (Model 1801 from Newport). Figure 5.4 shows the error signal we measured, along with the light leaking from the output of the cavity. We can see that the error signal is antisymmetric with the resonance but does not correspond to a typical PDH error signal (see Figure D.4 of Appendix D.1.3) due to our inability to modulate light at a sufficiently high frequency. The error signal was obtained by applying a voltage ramp to the piezoelectric actuator mounted on the output mirror of the cavity. The relationship between the voltage applied and the displacement of the piezoelectric actuator indicated in Figure 5.4 was obtained by placing the optical mount in a Michelson interferometer (see Appendix D.3 where a similar layout was obtained to characterize the frequency response of these mounts). We were able to lock the cavity using a

Digilock 110 module from Toptica as a PID controller, but we rapidly fell out of range with the piezoelectric actuator. This is due to the presence of a thermal drift of about 0.2 nm/s of the 150 mm long optical cavity. The characterization of this thermal drift is presented in Appendix D.2. In order to mitigate the thermal drift, we fastened the two mirrors of the cavity on a 1 m long spacer made of Invar in the case of the buffer gas cooling setup presented in Chapter 4. Another possibility to overcome the problem is to implement a unlock-relock system, such as the ones detailed in Ref. [125, 126].

One way of improvement is the use of a resonant EOM rather than a broadband one. Indeed, there is no need to adjust the modulation frequency as long as it is high enough to be in the fast-modulation regime presented in Appendix D.1.3. Two new resonant EOMs were already purchased (models PMR-3-40-AR700-900-6.25MHz and PMR-3-40-AR1300-1600-6.25MHz from Leysop). We also purchased a dual-channel arbitrary waveform generator (model 4054B from BK Precision). The first output will be amplified by a linear amplifier (ZX60-100VH+ from MiniCircuits) and will supply the EOM. The second will track the first output with an eventual phase shift and will be injected into the mixer in order to demodulate the signal reaching the fast photodiode. Choice was made to select a 6.25 MHz modulation frequency since it matches with the pre-defined modulation frequency of the Digilock 110 module from Toptica. However, we do not restrict ourselves to this PID controller, others being available in the laboratory (LB1005 from New Focus, FSC from MogLabs and D2-125 from Vescent photonics). As a proof of concept for the use of the above-listed (opto-)electronic devices for PDH applications, we measured the error signal generated by sweeping the wavelength of a DFB laser (model NLK1556STG from NEL) coupled to an optical cavity made of an ULE spacer and two high reflectivity mirrors (Ref. 102102 and 154209 from Layertec), leading to a finesse of 2050 (measured experimentally). This error signal is shown in Figure 5.5. Its shape is typical of PDH error signals (see Figure D.4 of Appendix D.1.3)).

As shown in Figure 5.2, the stabilization of the optical cavity requires to implement a feedback loop which can suffer from stability issues. One source of instability is the presence of mechanical vibrations, as detailed in Ref. [127], which limit the bandwidth of the feedback. We needed vacuum-tight piezo-actuated cavity mirror mounts. Our design is described in section 2.3.4 and shown in Figure 2.5. A test

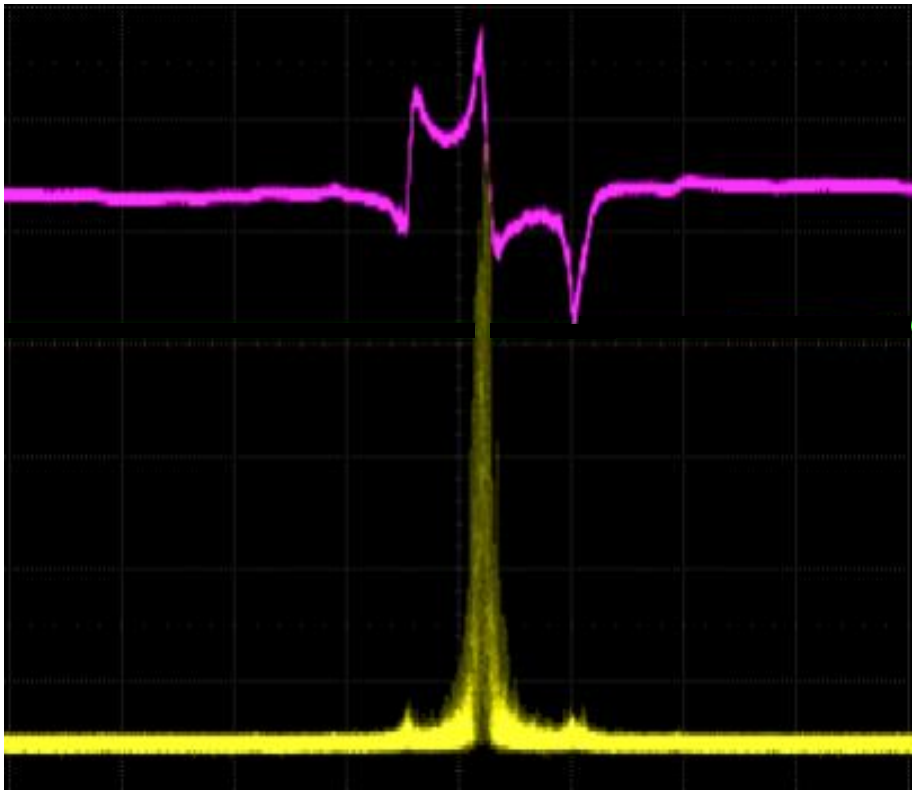


Figure 5.5: Oscilloscope trace showing the signal at the output of the optical cavity in yellow and the error signal in magenta as the DFB wavelength is swept. We can see the two sidebands generated by the EOM on the yellow curve and the typical shape of a PDH error signal on the magenta curve.

bench relying on a Michelson interferometer was set in order to test the frequency response of our mounts. It is presented in Appendix D.3, along with the frequency response of our current mounts. The first resonance at 130 Hz is very limiting but can be electronically overcome using different techniques such as notch filtering or the use of a differentiator stage to compensate for the phase lagging introduced by the resonance. These techniques are detailed in Ref. [127]. They add complexity to the design of the feedback loop and are valid until we reach another mechanical resonance. Designs of piezoelectric-actuated mirrors with a very high servo bandwidth can be found in literature [128–131], but they are not vacuum-tight. However, they can be used as a guideline for a proper design of vacuum-tight mounts with enough bandwidth to overcome, amongst others, vibrations induced by the vacuum pumping unit and the cryogenic refrigerator (see Ref. [107] for the characterization of the vibrations induced by the cold head). Such a design will open the door to the locking of the frequency comb on the optical cavity which is required to perform CEAS.

5.4 CONCLUSION

Due to their structure in the frequency domain, frequency combs can be efficiently coupled to optical cavities, allowing for ultra-sensitive measurements with a very good signal-to-noise ratio. They also permit to considerably increase the precision of the FTS, to suppress their ILS and to overcome the path-limited resolution of such instruments. Moreover, to perform broadband CEAS measurements of molecules cooled down to a few Kelvin using the buffer gas cooling setup and the FTS presented in chapter 2, we will have to interleave spectra. Indeed, at 20 K, the FWHM of Doppler-broadened molecules with a molecular mass 32 amu[1] is 0.0055 cm^{-1}, a bit more than the resolution of the FTS 0.002 cm^{-1}.

This chapter presented the first results regarding the coupling of frequency combs with optical cavities and briefly introduced the advantages of using them as a light source in a high-resolution FTS.

1 like Methanol

6

CONCLUSION

The ideal instrument in optical molecular spectroscopy embodies a series of characteristics : it has to be broadband, precise, sensitive and it has enough resolution to distinguish the complex structure of molecular spectra. We have seen throughout this manuscript that the design and fabrication from scratch of such an instrument is a complex but feasible task. It is possible to meet the different aforementioned features by combining a frequency-comb light source with an optical cavity and a Fourier transform spectrometer. The cooling of the gaseous sample at cryogenic temperatures simplifies the spectra, allowing to extend the use of the instrument to the study of more complex molecules. This thesis aimed at presenting our methodology and at justifying our choices concerning the design of the different elements of such a setup.

Chapter 2 presented the Fourier transform spectrometer which is the most advanced part of the setup, rivaling commercial instruments in terms of sensitivity. Details concerning both the hardware and the software of the instrument were given, allowing for other groups to rapidly build their own instrument. There are still possible improvements for this part of the setup. Indeed, the FTS should be placed under vacuum to get rid of the light absorption due to molecules in ambient air, especially water. We also highlighted the detrimental impact of mechanical vibrations on the ILS of the instrument. The replacement of the translation stage will therefore improve the SNR of the measurements, and ultimately its sensitivity. Small changes in the data processing pipeline of the FTS have to be made in order to implement the new paradigms presented in Chapter 5 that allow to suppress the ILS due to the finite length of the translation stage of FTS and to surpass the resolution of the FTS.

In chapter 3, we presented the first results concerning the fabrication of a homemade frequency comb, including both the design of the femtosecond resonator and its stabilization in terms of frequency. Once operational, this part of the setup will be responsible for the broadband and precision aspects of the measurement. Currently, the laser

resonator is able to work in the KML operation, with pulses as short as 60 fs. However, it is not stabilized yet. We also detailed our first attempts to measure the offset frequency of the MIRA900 femtosecond laser of Coherent using a $1f - 2f$ interferometer, a mandatory step for the stabilization of the offset frequency of femtosecond resonators. We showed that we were only limited by the duration of the pulses emitted by the Mira 900 resonator, avoiding us to generate the coherent octave-spanning supercontinuum required for the application. The homemade femtosecond resonator will make a big difference concerning this limitation and opens up new perspectives for this part of the setup.

Chapter 4 was dedicated to the design and fabrication of the buffer gas cooling setup. This setup permits to decongest the complex molecular spectra while reducing the Doppler broadening. It thus renders the attribution of complex spectra more tractable. In this chapter, a complete description of the mechanical design was given, along with the selection of the cold head and the estimation of the vacuum-pumping capacity required by the setup. We also suggested an innovative geometrical design for the thermal shield that presents a very large molecular conductance. This geometry allowed us to circumvent our inability to use cryopumping for the helium exiting the cold cell because of the limited performances of the cold head. Considerations about safety issues and the gas injection management were also developed. The CRDS setup used to seek the first cold molecules was described. Finally, we validated the setup by looking at the evolution of the linewidth of the $J_{K_a,K_c} : 1_{01} \leftarrow 1_{10}$ transition in the $\nu_1 = 2$ stretching region of the water molecule as the helium throughput was increased. We also measured the $2\nu_1$ overtone band of methanol lying between 7180 cm^{-1} and 7220 cm^{-1} and we evaluated its rotational and translational temperatures. They were respectively equal to 21.8 ± 1.3 K and 20.3 ± 7.0 K. This measurement illustrates our ability to actually record ro-vibrationally resolved spectra of large and complex molecules in the overtone range, opening the door to go beyond the state of the art in terms of molecular complexity with the study of large and heavy molecules at relatively high frequencies (NIR,VIS).

Perspectives associated with the coupling of a frequency comb with optical cavities and with the FTS are given in chapter 5. Once implemented, the ILS due to the limited OPD that can be induced by the FTS will be suppressed and the coupling of the frequency comb with the

optical cavity will be very efficient, improving even more the sensitivity of the setup. Ultimately, all the above-mentioned specifications will be fulfilled, giving us the ideal instrument for applications in optical molecular spectroscopy.

A

FOURIER TRANSFORM SPECTROMETER: SUPPLEMENTARY MATERIALS

The aim of this appendix is to give further details concerning the Fourier transform spectrometer. The generation of an interferogram in a Michelson interferometer is given in section A.1. The notion of instrumental lineshape function (ILS) is introduced in section A.2, along with intrinsic limitations of Fourier transform spectrometers. Considerations about the sampling of the interferogram are given in section A.3. Section A.4 is about the stabilization scheme of the He:Ne laser employed for the proper sampling of the interferogram. The reference signal and the broadband light source signal are filtered in the time domain at the beginning of the data processing pipeline, the design of the numerical filters is developed in section A.5. Section A.6 details the algorithm employed for the determination of the zero-crossings of the reference laser interference pattern sampled at uniform time intervals, allowing for the generation of a constant OPD grid. The concept of ideal reconstruction of a uniformly sampled signal is given in section A.7, it allows for the correct resampling of the broadband light source signal on the constant OPD grid. Finally, procedures for the determination of the sensitivity of the instrument for both single-pass measurements and cavity-enhanced measurements are detailed in section A.8.

Sections A.1, A.2, A.3 and A.4 are taken from Ref. [31].

A.1 GENERATION OF AN INTERFEROGRAM IN A MICHELSON INTERFEROMETER

This section relies on Ref. [2, 29, 132].

A.1.1 *The Michelson interferometer*

FTS are based on Michelson interferometers. The Michelson interferometer is depicted in Figure A.1. In its simplest form, it consists of a beamsplitter (BS), a compensator (C) and two mirrors (M1 and M2). The ray coming from the source is split in two at the beamsplitter, one part is transmitted while the other is reflected. Both beams travel in free space until they reach one of the two mirrors. Both mirrors then reflect light beams back to the beamsplitter where they are recombined. Part of the recombined beam returns in direction of the source, the remaining part travels in the direction of the photodetector. Usually, one of the mirrors (M1) is maintained fixed and the other is mobile (M2) so that the relative distance traveled by light in the two arms before recombination can be varied. In other words, moving the mirror of one arm of the interferometer allows to introduce a phase difference with respect to the second arm before recombination at the beamsplitter. Interference between the two beams occurs if they have a good spatial overlap from the beamsplitter to the photodetector. The measured intensity is then a function of the optical path difference, *i.e.* the difference of distance traveled by light in the two arms. The signal recorded at the photodetector for a purely monochromatic wave that undergoes an OPD equal to one wavelength is represented in Figure A.1. It consists in a sine wave of period equal to the wavelength of the monochromatic source. A formal derivation of the interference pattern is detailed in the next section.

Light is subject to dispersion in the beamsplitter, leading to an optical path difference that depends on the wavelength λ. Indeed, light travels a greater distance in the material of the beamsplitter for one of the two arms. This is shown in Figure A.1 where the beamsplitter is decomposed in a blue part corresponding to the material and a black part corresponding to the reflecting coating. One can see in this figure that light passes three times in the material of the beamsplitter for the arm with mirror M1 and only once for the arm with mirror M2. Adding a replica of the beamsplitter, with the exception of the reflecting coating, in the arm with mirror M2 ensures that light travels the same distance in the material for both arms. This replica is the so-called compensator. The compensator is mandatory in quantitative applications that involve broadband sources, as it is the case for Fourier transform

spectroscopy [34]. Nowadays, the compensator and the beamsplitter are built together, resulting in a single optics on the optical bench.

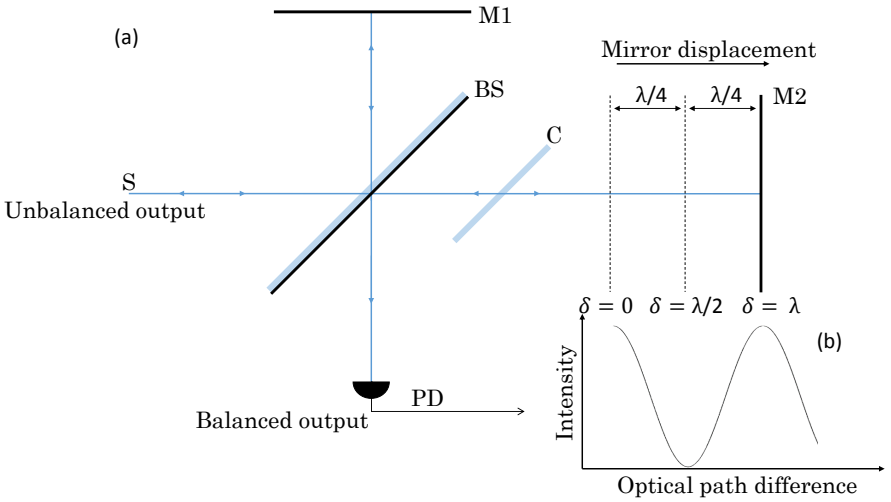


Figure A.1: (a) schematic of a Michelson interferometer. BS stands for beamsplitter, C for compensator, PD for photodetector and S for source. M1 and M2 are respectively the fixed and the mobile mirrors. (b) Intensity at the photodetector with respect to retardation δ of a purely monochromatic source is shown. This figure is inspired by Ref. [133].

A Michelson interferometer has two outputs ports. The unbalanced output denotes the part of light which returns in direction of the source, whereas the balanced output corresponds to light that actually reaches the photodetector (PD). Both beams undergo a single reflection and a single transmission at the beamsplitter in the case of the balanced output. The source and the unbalanced output beams are overlapped in Figure A.1, avoiding the recording of the signal of the unbalanced output. If retroreflectors are used instead of mirrors, the source and the unbalanced output are spatially separated, allowing the measurement of the two output signals. This configuration is depicted in Figure A.2. Advantages of measuring the unbalanced output and the balanced output simultaneously are emphasized in section A.1.2.

The two optical axes of the interferometer are shown in Figure A.2. They are imaginary lines that correspond to the directions along which light travels in the setup. They make a 45-degree angle with the beamsplitter. For the arm with the movable retroreflector, the optical

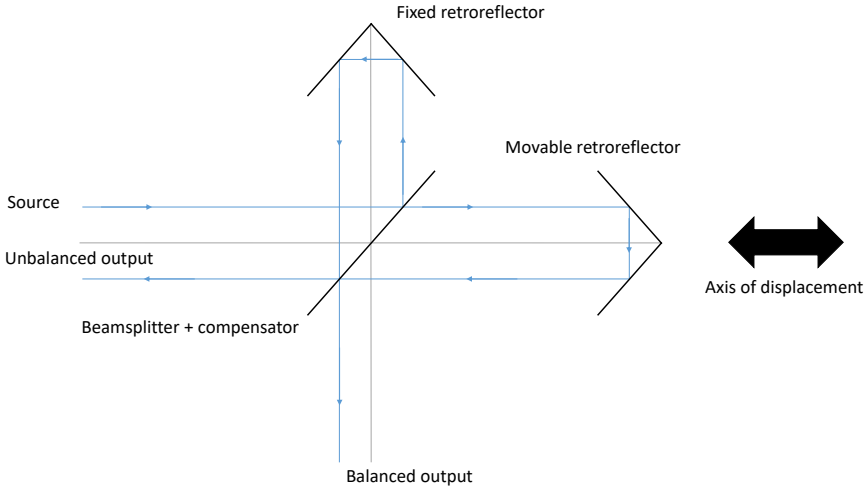


Figure A.2: Schematic of a Michelson interferometer using retroreflectors. The grey lines correspond to the two optical axes of the interferometer.

axis also corresponds to the locus engendered by the translation of the apex of the retroreflector during its displacement.

A.1.2 *Generation of an interferogram*

This section introduces the main concepts of Fourier transform spectroscopy step by step. Section A.1.2 first describes what happens when a purely monochromatic source is injected into a FTS by evaluating the intensity measured at the two outputs as a function of the mirror displacement. This measurement is the so-called interferogram. The usefulness of measuring both outputs is pointed out. Section A.1.2 then generalizes the results for a polychromatic source and it demonstrates how to recover the source irradiance spectrum from the interferogram.

Interferogram of a monochromatic source

This section relies on Ref. [2, 34].

In order to understand what happens in a Fourier transform spectrometer and how the spectrum is related to the Fourier transform of the measured signal, it is necessary to subdivide the problem by considering each arm separately. Figure A.3 supports the demonstration given

just below. It is convenient to have a look at it while reading the demonstration. This figure shows the influence of each optical component on the amplitude of the electric field of a source of monochromatic radiation producing an infinitely narrow and perfectly collimated beam. The importance of light collimation will appear obvious after the reading of section A.2.2. This hypothesis allows considering plane waves which propagate parallel to the optical axes.

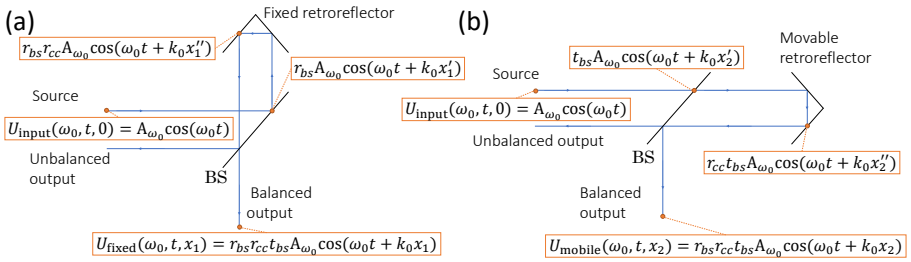


Figure A.3: Expression of the electric field of a monochromatic source of angular frequency ω_0 at several positions (red dots) in the interferometer. The two arms are treated separately: (a) arm with the static retroreflector; (b) arm with the movable retroreflector. $A_{\tilde{\nu}_0}$ is the electric field amplitude, r_{cc} is the effective reflection coefficient of the retroreflectors, r_{bs} and t_{bs} are respectively the external reflection coefficient and the transmission coefficient of the beamsplitter.

Light emitted by a source of monochromatic radiation producing an infinitely narrow and perfectly collimated beam is best described by its electric field U which depends on both time t and position x:

$$U(\omega_0, t, x) = A_{\tilde{\nu}_0}\cos(\omega_0 t + 2\pi \mathrm{j}\tilde{\nu}_0 x) = \frac{1}{2}A_{\tilde{\nu}_0}\mathrm{e}^{\mathrm{j}\omega_0 t}\mathrm{e}^{2\pi \mathrm{j}\tilde{\nu}_0 x} + \text{c.c.}, \quad \text{(A.1)}$$

where ω_0 is the angular frequency of the monochromatic wave and $A_{\tilde{\nu}_0}$ is its amplitude. The notation c.c. stands for conjugate complex. Equation (A.1) is the equation of a plane wave propagating parallel to the optical axes. The electric field depends on the source angular frequency ω_0, the time t and the position x in which the field is observed. Finally, $\tilde{\nu}_0$ denotes the wavenumber of the wave and is defined as the inverse of the wavelength, *i.e.* $\tilde{\nu}_0 = \frac{1}{\lambda_0}$. The wavenumber is linked to the angular frequency by the following equation:

$$\omega_0 = 2\pi c\tilde{\nu}_0, \quad \text{(A.2)}$$

with c the velocity of light.

The source is located in $x = 0$ and the electric field U_{input} at the source is therefore given by:

$$U_{\text{input}}(\omega_0, t, 0) = A_{\tilde{\nu}_0} \cos(\omega_0 t) = \frac{1}{2} A_{\tilde{\nu}_0} e^{j\omega_0 t} + \text{c.c.}, \tag{A.3}$$

The beamsplitter splits the beam in two, one part is transmitted while the other is reflected on its surface. They next travel a certain distance in free space before being reflected back to the beamsplitter where they recombine. The electric field at the balanced output is obtained by summing the electric fields of both arms and is therefore given by:

$$U_{\text{balanced output}} = U_{\text{fixed}} + U_{\text{mobile}}. \tag{A.4}$$

Based on Figure A.3, U_{fixed} and U_{mobile} at the photodetector and at time t are given by:

$$U_{\text{fixed}}(\omega_0, t, x_1) = \frac{1}{2} A_{\tilde{\nu}_0} r_{cc} r_{bs} t_{bs} e^{j\omega_0 t} e^{2\pi j \tilde{\nu}_0 x_1} + \text{c.c.}, \tag{A.5}$$

$$U_{\text{mobile}}(\omega_0, t, x_2) = \frac{1}{2} A_{\tilde{\nu}_0} r_{cc} r_{bs} t_{bs} e^{j\omega_0 t} e^{2\pi j \tilde{\nu}_0 x_2} + \text{c.c.}, \tag{A.6}$$

where r_{bs} is the external amplitude reflection coefficient at the beamsplitter, t_{bs} is the transmission coefficient of the beamsplitter and r_{cc} is the effective reflection coefficient of the retroreflector which takes into account the multiple reflections taking place in the retroreflector. Light travels a distance x_1 between the source and the photodetector if it goes through the arm with the fixed retroreflector. The distance between the source and the photodetector is equal to x_2 in the case of the arm with the movable retroreflector. The difference $\delta = x_2 - x_1$ is the optical path difference (OPD) or retardation. If light travels the same distance in both arms, the path difference is equal to zero, and the movable mirror is said to be at zero path difference (ZPD).

Injecting equations (A.5) and (A.6) into equation (A.4) leads to:

$$U_{\text{balanced output}} = \frac{1}{2} A_{\tilde{\nu}_0} r_{cc} r_{bs} t_{bs} e^{j\omega_0 t} \left(e^{2\pi j \tilde{\nu}_0 x_1} + e^{2\pi j \tilde{\nu}_0 x_2} \right) + \text{c.c.}. \tag{A.7}$$

The photodetector does not directly measure the light electric or magnetic field but rather a time-averaged intensity of the signal. This is due to the very high frequencies of optical signals (10^5 GHz for a 3000 nm wavelength), compared to the bandwidth of the photodetector (up to a

few GHz for the best detectors available). The time-averaged intensity at the balanced output is given by the following relationship:

$$I_{\text{balanced output}} = \left|U_{\text{balanced output}}\right|^2, \tag{A.8}$$

Injecting equation (A.7) in equation (A.8) leads to:

$$\begin{aligned} I_{\text{balanced output}}(\delta, \tilde{\nu}_0) &= 2A_{\tilde{\nu}_0}^2 R_{cc} R_{bs} T_{bs} \left(1 + \cos\left(2\pi\tilde{\nu}_0\delta\right)\right) \\ &= 2I_{\tilde{\nu}_0} R_{cc} R_{bs} T_{bs} \left(1 + \cos\left(2\pi\tilde{\nu}_0\delta\right)\right), \end{aligned} \tag{A.9}$$

where $R_{bs} = r_{bs}^2$ and $R_{cc} = r_{cc}^2$ are the intensity reflection coefficients of the beamsplitter and of the retroreflectors, and $T_{bs} = t_{bs}^2$ is the intensity transmission coefficient of the beamsplitter. $I_{\tilde{\nu}_0}$ stands for the intensity of the input radiation of wavenumber $\tilde{\nu}_0$. An ideal beamsplitter exhibits a 50% transmittance and a 50% reflectance on its entire bandwidth. Equation (A.9) can be rewritten by regrouping all the factors before the brackets in a single wavenumber-dependent factor $B_{\tilde{\nu}_0}$, leading to the following relation:

$$I_{\text{balanced output}}(\delta, \tilde{\nu}_0) = B_{\tilde{\nu}_0} \left(1 + \cos\left(2\pi\tilde{\nu}_0\delta\right)\right). \tag{A.10}$$

The intensity at the output is composed of a constant term and a modulated one. The modulated term is the so-called interferogram and it is the one of interest in spectroscopic measurements. For a monochromatic source, intensity at the photodetector varies in a sinusoidal manner with respect to the optical path difference, as depicted in Figure A.4. It is convenient to remove the constant term from the signal since it is unnecessary and it adds noise at the amplifier. It can be done either with the use of a highpass filter or with the use of both the balanced and the unbalanced outputs, as it will be explained in the next section. The interferogram is then given by:

$$I_{\text{balanced output}}(\delta, \tilde{\nu}_0) = B_{\tilde{\nu}_0} \cos\left(2\pi\tilde{\nu}_0\delta\right). \tag{A.11}$$

There is neither creation nor destruction of energy in the process. Instead, energy is redistributed between balanced and unbalanced outputs depending on the retardation and they are therefore complementary. For an input of intensity $I_{\tilde{\nu}_0}$ and if there are only losses at the retroreflectors, then the sum of the two outputs is constant and equal to $R_{cc} I_{\tilde{\nu}_0}$:

$$I_{\text{balanced output}} + I_{\text{unbalanced output}} = \text{Constant} = R_{cc} I_{\tilde{\nu}_0}, \tag{A.12}$$

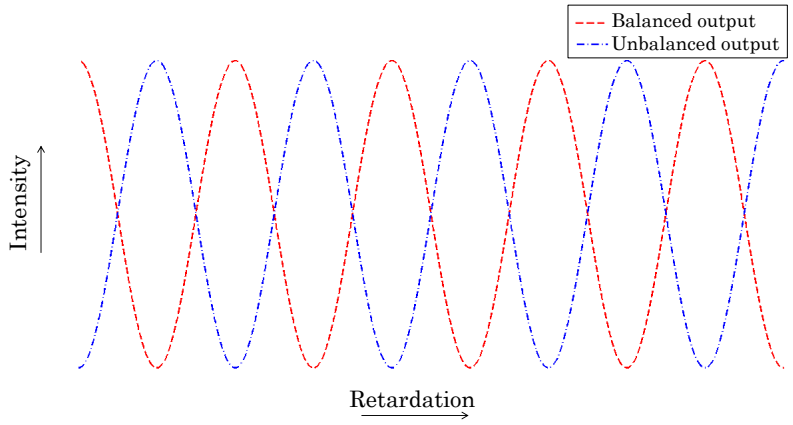


Figure A.4: Intensity with respect to retardation for a purely monochromatic source.

Injecting equation (A.9) into equation (A.12) and solving for $I_{\text{unbalanced output}}$ leads to:

$$I_{\text{unbalanced output}} = I_{\tilde{\nu}_0} R_{cc} \left(1 - 4R_{bs}T_{bs}\left(\frac{1+\cos\left(2\pi\tilde{\nu}_0\delta\right)}{2}\right)\right). \quad \text{(A.13)}$$

This expression can be rewritten as follows:

$$\begin{aligned} I_{\text{unbalanced output}} =& 4I_{\tilde{\nu}_0}R_{cc}R_{bs}T_{bs}\left(\frac{1-\cos\left(2\pi\tilde{\nu}_0\delta\right)}{2}\right) \\ &+ I_{\tilde{\nu}_0}R_{cc}\left(1-4R_{bs}T_{bs}\right). \end{aligned} \quad \text{(A.14)}$$

The unbalanced output is out of phase of π compared to the signal of the balanced output, *i.e.* equation (A.9). Both outputs thus contain the same information because they receive about the same amount of photons. Intensity at the output of the interferometer for a purely monochromatic source is shown in Figure A.4 as well.

Subtracting the unbalanced output from the balanced output allows doubling the signal strength and to get rid of most of the dc term which is responsible for adding extra noise to the signal:

$$\begin{aligned} I_{\text{balanced output}} - I_{\text{unbalanced output}} =& 4R_{cc}R_{bs}T_{bs}\cos\left(2\pi\tilde{\nu}_0\delta\right) \\ &- I_{\tilde{\nu}_0}R_{cc}\left(1-4R_{bs}T_{bs}\right). \end{aligned} \quad \text{(A.15)}$$

In the previous equation, the term which is subtracted is nearly equal to zero because $R_{bs} \approx T_{bs} \approx \frac{1}{2}$.

Another advantage of measuring both outputs is to remove time-domain intensity variations of the source by adding both signals together [38].

Interferogram of a polychromatic source

This section relies on Ref. [2, 134].

In the case of polychromatic sources, that is when more than one frequency is emitted by the source, the measured interferogram is a superposition of the interferograms of each different frequency. The contribution of each individual interferogram to the measured interferogram is weighted by a factor named spectral irradiance. Spectral irradiance characterizes the total amount of radiant power going through a unit area at wavenumber $\tilde{\nu}$. The objective of a Fourier transform spectrometer is to measure the spectral irradiance of a source on an interval of wavenumbers. The plot of the source spectral irradiance with respect to the wavenumber is the so-called spectrum. As mentioned in the previous section, optical elements and detectors are frequency-dependent, and the setup therefore modifies the true spectrum of the source. The measured irradiance spectrum is denoted by $B(\tilde{\nu})$. Influence of several instrument parameters on the true irradiance spectrum will be studied in section A.2.

For a continuum source, the intensity measured at a retardation δ is obtained by integrating equation (A.11) over all the wavenumbers, leading to:

$$I(\delta) = \int_0^{+\infty} B(\tilde{\nu}) \cos(2\pi\tilde{\nu}\delta)\, \mathrm{d}\tilde{\nu}. \tag{A.16}$$

The quantity of interest is the spectral distribution $B(\tilde{\nu})$, which can be obtained by taking the inverse transform of the interferogram, that is:

$$B(\tilde{\nu}) = \int_0^{+\infty} I(\delta) \cos(2\pi\tilde{\nu}\delta)\, \mathrm{d}\delta. \tag{A.17}$$

Equations (A.16) and (A.17) only consider positive optical path differences and positive wavenumbers. An interferogram that only takes positive optical path differences is said to be single-sided. Since retarding one beam or the other must be equivalent, the interferogram is ideally an even function of retardation, *i.e.* $I(-\delta) = I(\delta)$. A double-sided interferogram is an interferogram measured on a symmetrical

range of retardation around the zero path difference (ZPD). Extending the integral boundaries of equation (A.16) to minus infinity leads to:

$$I(\delta) = \frac{1}{2}\int_{-\infty}^{+\infty} B(\tilde{\nu})\cos\left(2\pi\tilde{\nu}\delta\right)\mathrm{d}\tilde{\nu}. \tag{A.18}$$

Although negative wavenumbers have no physical meaning, it is necessary to extend integral boundaries from minus infinity to plus infinity in equation (A.17) to ensure complete symmetry in transforming back and forth from the interferogram domain to the spectral domain. This extension can be easily done since $\cos(2\pi\tilde{\nu}\delta) = \cos(-2\pi\tilde{\nu}\delta)$, $B(\tilde{\nu})$ should just be an even function of $\tilde{\nu}$ (*i.e.* $B(\tilde{\nu}) = B(-\tilde{\nu})$) to produce identical interferograms.

Equation (A.17) simply becomes

$$B(\tilde{\nu}) = \frac{1}{2}\int_{-\infty}^{+\infty} I(\delta)\cos\left(2\pi\tilde{\nu}\delta\right)\mathrm{d}\delta. \tag{A.19}$$

In practice, it is more convenient to use Fourier transforms instead of cosine Fourier transforms. Equations (A.18) and (A.19) are then given by:

$$I(\delta) = \frac{1}{2}\int_{-\infty}^{+\infty} B(\tilde{\nu})\mathrm{e}^{-2\pi\mathrm{j}\tilde{\nu}\delta}\mathrm{d}\tilde{\nu}, \tag{A.20}$$

$$B(\tilde{\nu}) = \frac{1}{2}\int_{-\infty}^{+\infty} I(\delta)\mathrm{e}^{2\pi\mathrm{j}\tilde{\nu}\delta}\mathrm{d}\delta. \tag{A.21}$$

The use of equation (A.21) instead of equation (A.17) does not modify the spectrum as long as $I(\delta)$ is an even function of δ. This can be shown by rewriting $I(\delta)$ as a sum of an even function $E(\delta)$ and an odd function $O(\delta)$:

$$I(\delta) = \frac{1}{2}\left[I(\delta) + I(-\delta)\right] + \frac{1}{2}\left[I(\delta) - I(-\delta)\right] = E(\delta) + O(\delta). \tag{A.22}$$

Injecting the previous equation in equation (A.21) leads to

$$B(\tilde{\nu}) = \int_{-\infty}^{+\infty}\left(E(\delta) + O(\delta)\right)\mathrm{e}^{2\pi\mathrm{j}\tilde{\nu}\delta}\mathrm{d}\delta, \tag{A.23}$$

or equivalently:

$$\begin{aligned} B(\tilde{\nu}) = \int_{-\infty}^{+\infty}&\left(\frac{1}{2}\left[I(\delta) + I(-\delta)\right] + \frac{1}{2}\left[I(\delta) - I(-\delta)\right]\right) \\ &\times\left(\cos(2\pi\tilde{\nu}\delta) + \mathrm{j}\sin(2\pi\tilde{\nu}\delta)\right)\mathrm{d}\delta. \end{aligned} \tag{A.24}$$

Since the integral of an odd function on a symmetrical interval with respect to 0 is vanishing, equation A.24 is equal to:

$$B(\tilde{\nu}) = \int_{-\infty}^{+\infty} E(\delta)\cos(2\pi\tilde{\nu}\delta)\,\mathrm{d}\delta + \mathrm{j}\int_{-\infty}^{+\infty} O(\delta)\sin(2\pi\tilde{\nu}\delta)\,\mathrm{d}\delta. \quad \text{(A.25)}$$

As long as $I(\delta)$ is even, that is $O(\delta) = 0$, and real, $B(\tilde{\nu})$ is real.

Even if all the information on the source spectrum can be theoretically recovered from the positive retardation interferogram by evaluating equation (A.16), the use of equation (A.21) exhibits two main advantages. First, information about the phase and the ability to correct it are mandatory and imply the use of Fourier transforms instead of cosine Fourier transforms. Phase errors arise from the discrete sampling of the interferogram. Also, dispersive phenomena taking place in optical elements make the optical path difference to be a function of the wavenumber and they are therefore at the origin of phase errors too [34]. These phase errors would modify the spectrum if negative retardation was not considered. Secondly, it is computationally more efficient to evaluate Fourier transforms instead of cosine Fourier transforms.

Figure A.5 shows the double-sided interferogram of a blackbody source with its associated spectrum. All the waves interfere constructively at ZPD. It results in a bright central fringe, the so-called centerburst. On both sides of that peak, there are ripples that extend to large optical path differences. These ripples contain most of the information, as it will be explained in section A.2.1. The spectrum is recovered from the interferogram by taking its Fourier transform.

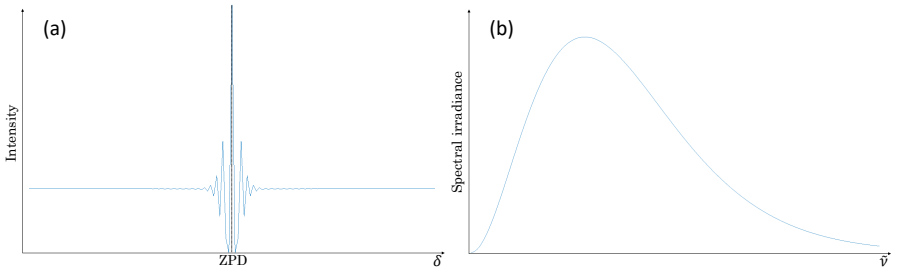


Figure A.5: Interferogram of a blackbody source in panel (a) and its associated spectrum in panel (b).

A.2 INSTRUMENTAL LINESHAPE FUNCTION

Section A.1 introduced the working principle of a perfect instrument. The spectrum that was obtained was the true spectrum of the source. However, all physical instruments exhibit deviations from this perfect apparatus, leading to the notion of instrumental lineshape function. The ILS is formally defined as the instrumental response to a monochromatic input signal [2, 34].

Two physical phenomena that have an influence on the instrumental lineshape function are the maximum path difference and the finite dimension of the source. They are respectively the topics of section A.2.1 and section A.2.2. In each of these two sections, a comprehensive and intuitive way to understand what happens is first presented. Then, a more formal approach is given.

A.2.1 *Effect of maximum path difference*

This section relies on Ref. [29, 34].

The maximum path difference allowed by the spectrometer, denoted by $\delta_{\max}$, determines the maximum achievable spectral resolution $\Delta\tilde{\nu}$ of the spectrometer. The spectral resolution of the spectrometer measures its ability to distinguish two spectral peaks that are close to each other.

The relationship between $\delta_{\max}$ and $\Delta\tilde{\nu}$ is given by the following equation:

$$\Delta\tilde{\nu} = \frac{1}{\delta_{\max}}. \tag{A.26}$$

An intuitive way to illustrate it is to consider the beating between two monochromatic waves of slightly different frequencies $\tilde{\nu_1}$ and $\tilde{\nu_2}$ such that $\Delta\tilde{\nu} = \tilde{\nu_2} - \tilde{\nu_1}$. The interferogram, along with its spectrum, is depicted in Figure A.6. It is necessary to measure a complete period of the beat pattern to distinguish the two frequencies that build the interferogram, imposing the optical path difference to be greater than $(\Delta\tilde{\nu})^{-1}$. The smaller the frequency interval between the two lines, the greater the retardation before the cosine waves become in phase again. The spectral resolution thus depends on the maximum optical path difference the interferometer can perform.

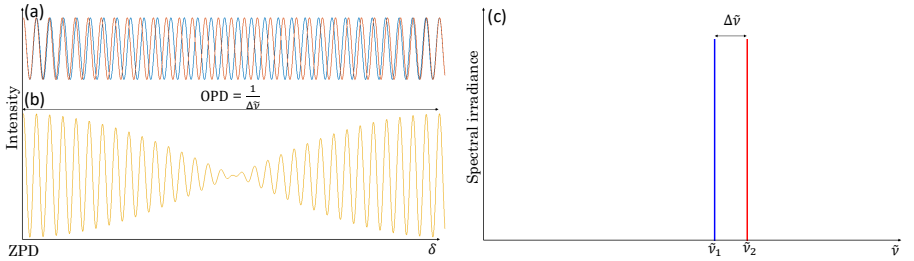


Figure A.6: Interferogram of two monochromatic waves with slightly different wavenumbers. (a) Interferogram of each single monochromatic wave. (b) Interferogram resulting from the beating between the two monochromatic waves. (c) The spectrum consists of two lines of equal intensity.

The statement of equation (A.26) can be formally derived by multiplying the complete interferogram $I(\delta)$ (*i.e.* extending from $\delta = -\infty$ to $\delta = +\infty$) by a boxcar truncation function $D(\delta)$ that is equal to unity for $|\delta| < \delta_{\text{max}}$, and zero otherwise:

$$D(\delta) = \begin{cases} 1 & \text{if } -\delta_{\text{max}} \leq \delta \leq \delta_{\text{max}} \\ 0 & \text{otherwise.} \end{cases} \tag{A.27}$$

The spectrum is then obtained by taking the Fourier transform of the product $I(\delta)D(\delta)$, that is by evaluating the following relationship:

$$B(\tilde{\nu}) = \int_{-\infty}^{+\infty} D(\delta)I(\delta)\mathrm{e}^{2\pi\mathrm{j}\tilde{\nu}\delta}\mathrm{d}\tilde{\nu}. \tag{A.28}$$

Since the Fourier transform of a product of two functions is equal to the convolution of the Fourier transforms of the two functions, the measured spectrum is equal to the true spectrum convolved by the Fourier transform of $D(\delta)$. The Fourier transform of a boxcar function of width $2\delta_{\text{max}}$ is the sinc function given by:

$$f(\tilde{\nu}) = 2\delta_{\text{max}}\frac{\sin\left(2\pi\tilde{\nu}\delta_{\text{max}}\right)}{2\pi\tilde{\nu}\delta_{\text{max}}} = 2\delta_{\text{max}}\text{sinc}\left(2\pi\tilde{\nu}\delta_{\text{max}}\right). \tag{A.29}$$

The interferogram of a truncated cosine and its associated spectrum are depicted in Figure A.7. The sinc function is centred about $\tilde{\nu} = \tilde{\nu}_0$. The width of the first lobe is equal to $\frac{1}{\delta_{\text{Max}}}$. The full width at half maximum (FWHM) of the sinc function is known as the theoretical maximum resolution $R_{\text{theoretical}}$ achievable by the FTS and is given by:

$$\text{FWHM} = R_{\text{theoretical}} = \frac{1.207}{2\delta_{\text{Max}}}. \tag{A.30}$$

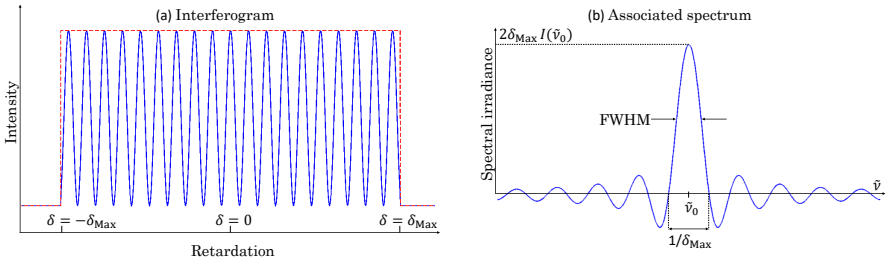


Figure A.7: Influence of finite path length on a monochromatic source of wavenumber $\tilde{\nu_0}$. (a) The cosine signal is truncated at $\delta = \pm\delta_{\text{Max}}$. (b) The resulting spectrum consists in a sinc function centred in $\tilde{\nu} = \tilde{\nu}_0$. The width between the two first zero-crossings of the sinc function is equal to $\frac{1}{\delta_{\text{Max}}}$.

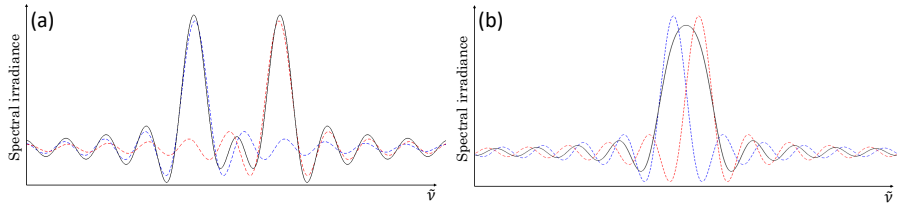


Figure A.8: Spectra of two single lines of equal intensity modified by the finite length of the translation stage which is the same for both figures. The relative position of the two lines varies from one figure to another. (a) The maximum path difference is long enough to clearly distinguish the two peaks, *i.e.* $\Delta\tilde{\nu}$ is large enough. (b) The maximum path difference is too short to resolve the two peaks, *i.e.* $\Delta\tilde{\nu}$ is too small.

Figure A.8 shows how the two lines of Figure A.6 are modified by the measurement of the interferogram on a finite path difference. Each line is broadened by a sinc function with a width that depends on the maximum path difference. In Figure A.8(a), the maximum path difference is long enough to resolve both peaks while the translation stage is too short to clearly distinguish them in Figure A.8(b).

A.2.2 *Effect of beam divergence*

This section relies on Ref. [2, 29, 34, 135].

Plane waves, all moving parallel to the optical axes, were considered in section A.1, but light issuing from a finite aperture size is never perfectly collimated. Instead, it travels through the spectrometer on

a range of off-axis angles that limit the achievable resolution of the spectrometer, as shown in Figure A.9. The two extreme rays are traced. α_{max} denotes the maximum angle that can be accepted by the entrance aperture which is located at the focus of the collimating lens. A similar situation is encountered in sources of finite size, such as laser beams.

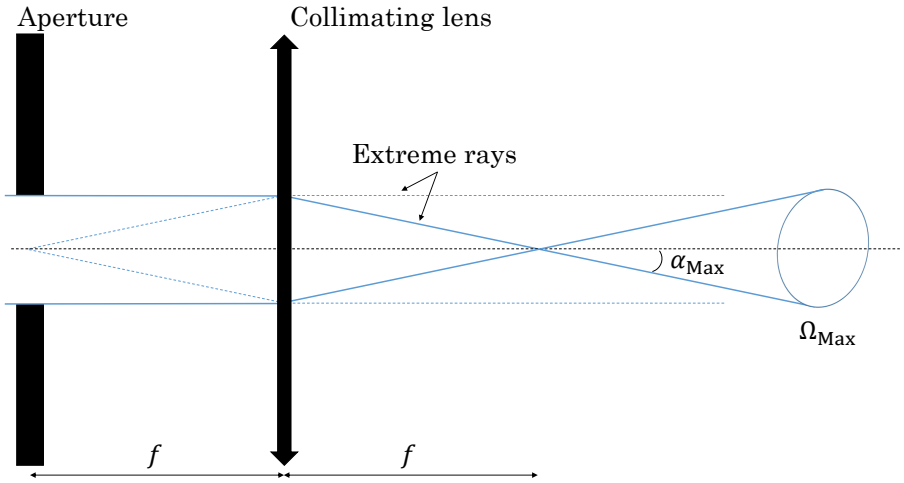


Figure A.9: Schematic of the interferometer entrance aperture. The aperture is located at the focus of the collimating lens. Extreme rays are traced in blue. This figure is inspired by Ref. [2].

In order to study the consequences of a source of finite size, it is convenient to consider a unique point source located at the focus of the collimating lens but aside from the optical axis of the instrument, as represented in Figure A.10. Rays entering the spectrometer at a specific angle take different paths depending on the position of the moving mirror. The change in optical path difference can be evaluated by considering two interfering rays issued from the same wavefront. Figure A.10 sketches the situation. In this figure, ray 1 interferes with the ray issued from the fixed arm (ray A) at ZPD while ray 2 interferes with this same ray A for a mechanical displacement l.

For a better insight of what is going on, it is convenient to look at Figure A.11 which is a zoom of Figure A.10 on the movable mirror. Both rays travel the same distance before reaching points B and C. However, ray 1 travels the supplementary distance BA compared to ray 2 whereas ray

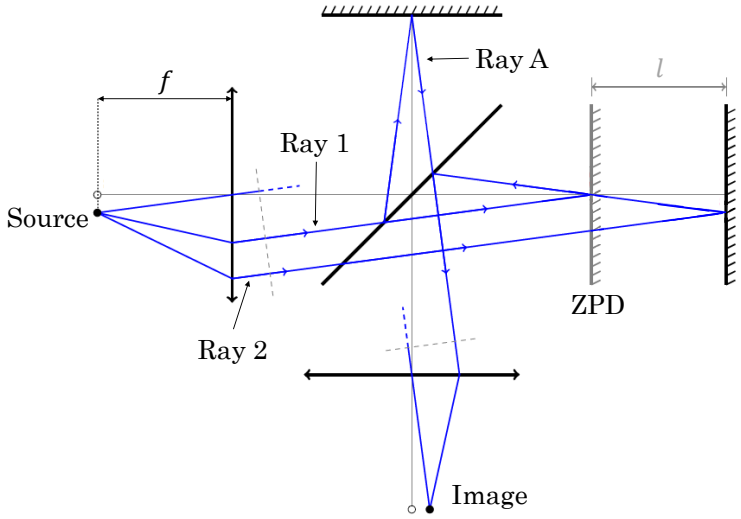


Figure A.10: Ray tracing of a point source away from the centre of the optical axis and injected in a Michelson interferometer. The point source is in the focal plan of the collimating lens. The wavefront is represented by the dashed grey lines. This figure is adapted from Ref. [135].

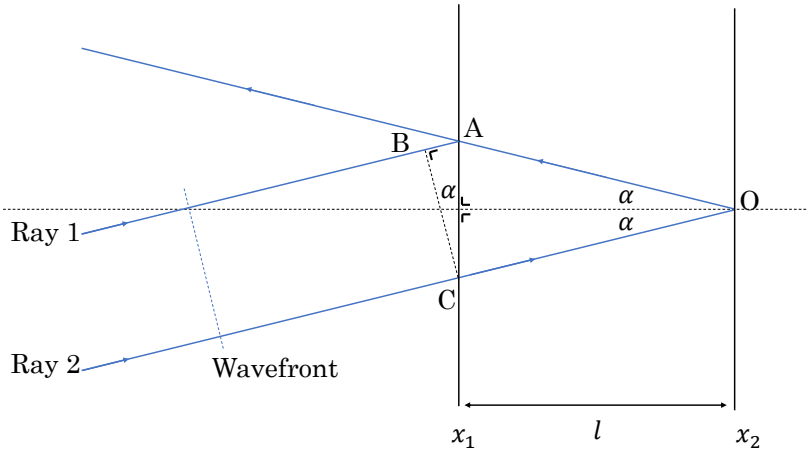


Figure A.11: Schematic of an off-axis ray striking the mobile mirror at different mirror displacements. This figure is adapted from Ref. [135].

2 travels the supplementary distances OA and CO with respect to ray 1, leading to an optical path difference δ' between the two paths given by:

$$\delta' = OA + CO - BA. \tag{A.31}$$

Applying some geometry and trigonometry leads to:

$$\delta' = 2l\cos(\alpha) = \delta\cos(\alpha), \tag{A.32}$$

where δ is the on-axis optical path difference.

Optical path difference induced by a mechanical displacement l of the mirror is dependent on the divergence angle and equation (A.10) has to be modified to take into account off-axis rays:

$$I(\delta, \tilde{\nu}, \alpha) = B(\tilde{\nu})\left(1 + \cos\left(2\pi\tilde{\nu}\delta\cos\left(\alpha\right)\right)\right). \tag{A.33}$$

Since α can take a continuum of values between zero and $\alpha_{\max}$, a same mechanical displacement leads to a set of apparent wavenumbers or measured wavenumbers, denoted $\tilde{\nu}_{\mathrm{m}}$, that depends on the off-axis angle:

$$\tilde{\nu}_{\mathrm{m}} = \tilde{\nu}\cos(\alpha). \tag{A.34}$$

It is necessary to consider all divergence angles for a single wavenumber. This is done by integrating over all the solid angles Ω that can be subtended by the entrance aperture (see Figure A.9). This is done by integrating equation (A.33) with respect to Ω. A second integration over all the wavenumbers gives the measured intensity as a function of the on-axis optical path difference:

$$I(\delta) = \int_{-\infty}^{+\infty}\int_{0}^{\Omega_{\mathrm{Max}}} B(\tilde{\nu})\cos\left(2\pi\tilde{\nu}\delta\cos(\alpha)\right)\mathrm{d}\tilde{\nu}\mathrm{d}\Omega. \tag{A.35}$$

The divergence angle α is related to the solid angle Ω by the following definite integral:

$$\Omega = \int_{0}^{2\pi}\int_{0}^{\alpha'}\sin(\alpha')\mathrm{d}\alpha\mathrm{d}\phi = 2\pi\left(1 - \cos(\alpha)\right), \tag{A.36}$$

where ϕ is the azimuthal angle.

Substituting the $\cos(\alpha)$ of equation (A.35) by the expression of equation (A.36) leads to:

$$I(\delta) = \int_{-\infty}^{+\infty}\int_{0}^{\Omega_{\mathrm{Max}}} B(\tilde{\nu})\cos\left(2\pi\tilde{\nu}\delta\left(1 - \frac{\Omega}{2\pi}\right)\right)\mathrm{d}\tilde{\nu}\mathrm{d}\Omega. \tag{A.37}$$

This expression can be rewritten in a more convenient way by applying consecutively the three following trigonometric identities and by integrating with respect to Ω:

$$\cos(a-b) = \cos(a)\cos(b) + \sin(a)\sin(b), \quad \text{(A.38)}$$

$$\sin(a-b) = \sin(a)\cos(b) - \cos(a)\sin(b), \quad \text{(A.39)}$$

$$\sin(a) + \sin(b) = 2\sin\left(\frac{a+b}{2}\right)\cos\left(\frac{a-b}{2}\right), \quad \text{(A.40)}$$

giving:

$$I(\delta) = \Omega_{\text{Max}} \int_{-\infty}^{+\infty} B(\tilde{\nu}) \text{sinc}\left(\frac{\tilde{\nu}\delta\Omega_{\text{Max}}}{2}\right) \cos\left(2\pi\tilde{\nu}\delta\left(1 - \frac{\Omega_{\text{Max}}}{4\pi}\right)\right) \text{d}\tilde{\nu}. \quad \text{(A.41)}$$

Figure A.12 consists of a plot of equation (A.41) for a monochromatic source with three different maximum divergence angles. For each wavenumber, the interferogram consists of a cosine of wavenumber $\frac{\tilde{\nu}(1+\cos(\alpha_{\text{Max}}))}{2}$ multiplied by a sinc function vanishing for the first time for an optical path difference equal to $\pm\frac{1}{\tilde{\nu}(1-\cos(\alpha_{\text{Max}}))}$. A large entrance aperture leads to a more rapid decrease in contrast as the optical path difference increases. This phenomenon is named self-apodization. It should be pointed out that the interferogram, given by equation (A.41), is also multiplied by Ω_{Max}, meaning that increasing the throughput at the entrance aperture increases the signal at the photodetector. Since the sinc function depends on the wavenumber, the sinc will first vanish for important wavenumbers leading to a decrease in signal. Opening of the entrance aperture represents a trade-off between optical throughput and the spectral resolution that must be achieved.

In order to obtain the instrumental lineshape function, a monochromatic source of wavenumber $\tilde{\nu}_0$ is considered. Equation (A.41) simply becomes:

$$I(\delta) = \Omega_{\text{Max}} B(\tilde{\nu}_0) \text{sinc}\left(\frac{\tilde{\nu}_0\delta\Omega_{\text{Max}}}{2}\right) \cos\left(2\pi\tilde{\nu}_0\delta\left(1 - \frac{\Omega_{\text{Max}}}{4\pi}\right)\right). \quad \text{(A.42)}$$

The product between the cosine function (interferogram) and the sinc function gives rise to a convolution in the spectral domain. The spectrum is then given by:

$$I(\tilde{\nu}) = \begin{cases} \frac{B(\tilde{\nu}_0)\Omega_{\text{Max}}}{\tilde{\nu}_0(1-cos\alpha_{\text{Max}})} & \text{if } \tilde{\nu}_0\cos(\alpha_{\text{Max}}) \leq \tilde{\nu} \leq \tilde{\nu}_0 \\ 0 & \text{otherwise.} \end{cases} \quad \text{(A.43)}$$

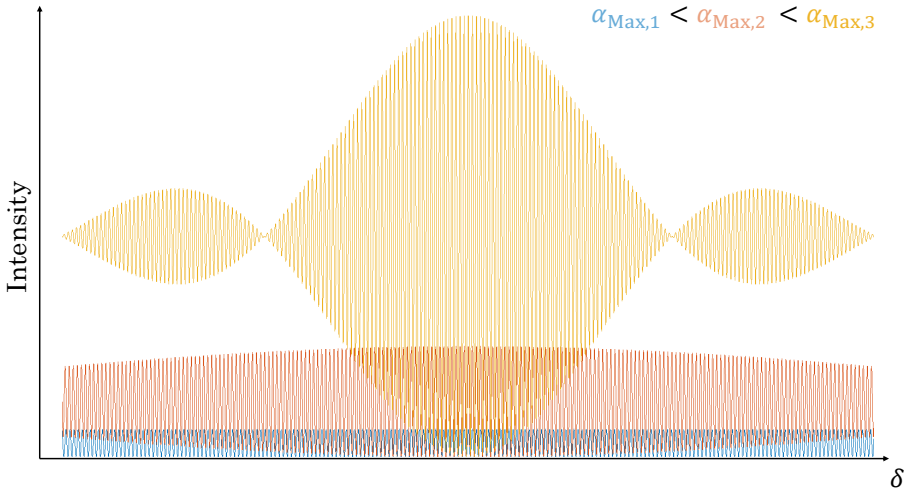


Figure A.12: Interferogram of a coherent monochromatic source for three maximum divergence angles.

It is a boxcar function centred in $\frac{\tilde{\nu}(1+\cos(\alpha_{Max}))}{2}$, with a width equal to $\tilde{\nu}_0\,(1-\cos\,(\alpha_{Max}))$. It should be emphasized that the width of the boxcar depends on the wavenumber,

Another phenomenon resulting from beam divergence is the spatial interference pattern observable in the image field of view if a monochromatic source is injected in the interferometer. It is the so-called Haidinger fringe pattern that is represented in Figure A.13(a). A lens is used to condense light at the photodetector. Light propagating at an angle α is brought into focus at a distance $r = f\sin(\alpha)$ from the optical axis, with f the focal length. The situation is shown in Figure A.13(b). Interference between rays that propagate at a given angle in the two arms will occur since they are spatially overlapped in the image plane. There is no azimuthal dependence in the optical path difference, leading to a pattern that consists of concentric circular disks of equal inclination. The distance between the bright fringes is a function of the optical path difference and of the wavenumber.

The simultaneous detection of several disks leads to a decrease in contrast of the interference pattern. If all the disks were measured with a single photodetector, there would be no overall change of intensity with respect to the retardation. The dimension of the entrance aperture is chosen so that only the central filled disk can be formed [29].

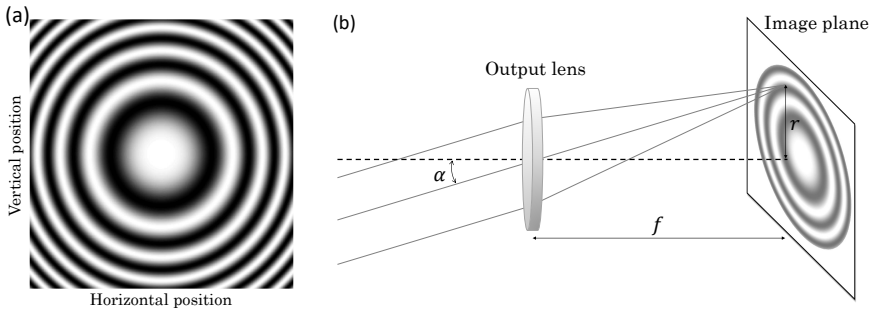


Figure A.13: Haidinger Fringe pattern. Rays with a same inclination angle are mapped at a same distance r from the optical axis.(a) Pattern in the image plane. (b) Action of a lens on rays of equal inclination.

A.3 SAMPLING

Interferograms are continuous functions of the retardation, but digitally convert them imposes their discretization. In practice, the interferogram can be either sampled at uniform OPD or at uniform time intervals. However, the final interferogram should be sampled on a constant OPD sampling grid to recover the spectrum (see equation (A.21)). Both sampling methods imply the use of a spatial reference which usually consists in a helium-neon (He:Ne) laser. Its role is detailed in section A.3.1.

For the discrete signal to be mathematically equivalent to the continuous interferogram, requirements on the sampling frequency must be satisfied. These requirements are described in section A.3.2.

A.3.1 *Reference Laser*

This section relies on Ref. [29, 30].

The spectrum is retrieved from the interferogram by applying a Fourier transform. This operation implies that the interferogram was first sampled at uniform OPD spacing. Therefore, it is mandatory to have a spatial reference to generate the constant OPD sampling grid. Continuous wave (CW) lasers usually serve this purpose in a Fourier transform spectrometer. Indeed, injecting a quasi-monochromatic light in a Michelson interferometer leads to a cosine signal when varying the OPD. The period of this cosine signal is equal to the wavelength of the

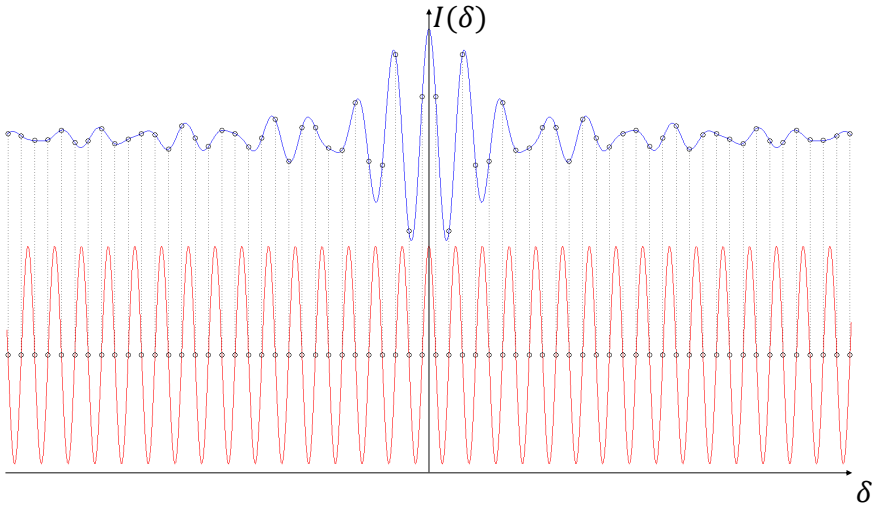


Figure A.14: The interferogram is sampled at each zero-crossing of the He:Ne reference laser (black bullets). The red curve corresponds to the interferogram of the He:Ne reference laser and the blue curve to the interferogram of the light source.

laser and can be used as a spatial reference. The sampling process is shown in Figure A.14.

He:Ne lasers are typically used as reference lasers in Fourier transform spectrometers. Sampling the interferogram can be performed in two different ways using the He:Ne laser. The first method consists in detecting the zero crossings with an analog circuit which then triggers the analog-to-digital converter (ADC). The second method makes use of an ADC with two channels that are simultaneously triggered by an external stable clock. One of the channels records the interferogram of interest while the other records the He:Ne interferogram. The sampling at constant OPD of the interferogram is done at the software level with the help of the reference laser signal.

The sampling grid obtained with the reference laser also permits to add several interferograms in order to improve the signal-to-noise ratio (SNR).

A.3.2 *Sampling frequency and aliasing*

This section relies on reference [61].

Sampling the continuous interferogram implies to take measurements at some specific moments. This operation is mandatory to numerically represent and manipulate the signal. However, one has to be careful when determining the sampling frequency to avoid spectrum distortion due to aliasing. This section describes the origin of aliasing for a continuous signal $x(t)$ uniformly sampled at time intervals T_s.

The sampled function $x_s(t)$ can be mathematically expressed as the product of the original continuous function $x(t)$ with an impulse train, that is a comb of impulse functions uniformly spaced by the sampling period T_s.

$$x_s(t) = x(t) \cdot \sum_{n=-\infty}^{\infty} \delta(t - nT_s). \tag{A.44}$$

In this equation, $\delta(t)$ corresponds to the impulse function which is defined as follows:

$$\delta(t) = \begin{cases} 1 & \text{if } t = 0 \\ 0 & \text{if } t \neq 0. \end{cases} \tag{A.45}$$

The sampled function thus only takes non-zero values at times $t = nT_s$, where n is an integer. Figure A.15(a) depicts the situation for the continuous function $x(t) = \text{sinc}^2(t)$. Its Fourier transform, denoted by $X(f)$, is the triangular function which is shown in Figure A.15(b). The bandwidth of the spectrum extends from $-f_{\text{Max}}$ to f_{Max}.

The Fourier transform of a product of two functions is equal to the convolution[1] of the Fourier transforms of each function. The Fourier transform of equation (A.44) is thus given by the convolution of the spectrum of $x(t)$ with the Fourier transform of the impulse train. The Fourier transform of a comb of impulse functions, each spaced by an interval T_s is another comb with each impulse separated by a value $f_s = \frac{1}{T_s}$ and scaled by a factor $\frac{1}{T_s}$. The spectrum of the sampled signal of equation (A.44) is therefore given by:

$$X_s(f) = X(f) \circledast \frac{1}{T_s} \sum_{k=-\infty}^{\infty} \delta(f - kf_s). \tag{A.46}$$

1 The convolution product is written $\circledast$

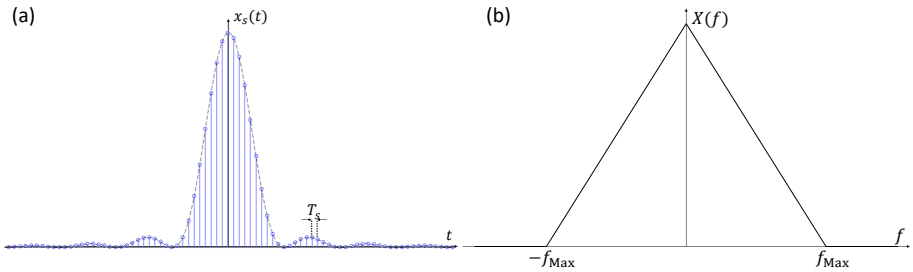


Figure A.15: (a) Sampled squared sinc function. The black dashed curve corresponds to the continuous function. The comb of delta functions is represented by blue lines ended by a circle. (b) Fourier transform of the continuous squared sinc function.

A function convoluted with an impulse function remains unchanged. Thus, a function convoluted with a comb of impulse functions simply repeats itself with a spacing f_s between two consecutive repetitions:

$$X_s(f) = \frac{1}{T_s} \sum_{k=-\infty}^{\infty} X(f - kf_s). \tag{A.47}$$

These repetitions will overlap if the sampling frequency is not large enough compared to the frequency extend of the sampled signal. This phenomenon is called aliasing and it causes a distortion of the signal. Figure A.16 represents the Fourier transform of the sampled sinc^2 of Figure A.15(a) for two distinct sampling frequencies. On the left figure, the sampling frequency is high enough to avoid signal distortion. On the right figure, the sampling frequency is too low for the signal. Consecutive replicas of the spectrum add together, modifying its shape. Thus, the spectrum of the sampled signal cannot be employed to analyze the original continuous-time signal.

In order to prevent aliasing, the sampling frequency f_s must be equal to or greater than twice the maximum frequency component f_{Max} of the signal that has to be sampled:

$$f_{\text{Max}} \leq \frac{1}{2} f_s. \tag{A.48}$$

In a Fourier transform spectrometer, different methods are employed to avoid aliasing. One way is to use optical filters as lowpass filters. It allows a control on the shortest wavelength that can reaches the photodetector. Another way relies on anti-aliasing lowpass electronic filters.

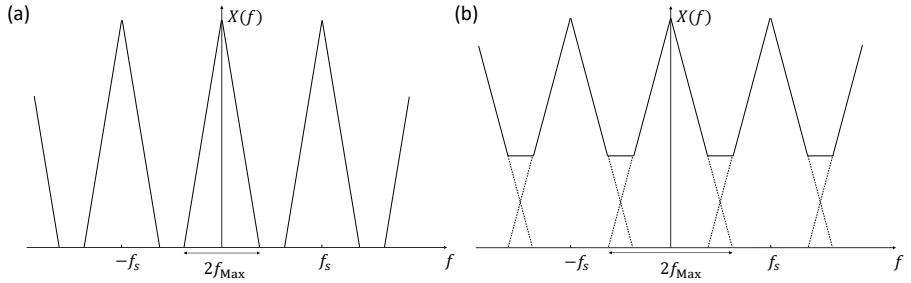


Figure A.16: Fourier transform of a sampled squared sinc function. (a) The sampling theorem is satisfied: the spectrum is not distorted. (b) The sampling theorem is not satisfied: aliasing occurs, leading to spectrum distortion.

The second category has the advantage to suppress high-frequency noise as well [2, 29].

A.3.3 *Uniform time sampling versus uniform space sampling*

The irradiance spectrum of the source is retrieved from the interferogram by applying a Fourier transform, the Fourier conjugate variables being the wavenumber $\tilde{\nu}$ and the OPD δ. Thus, the interferogram has to be sampled at constant OPD before the transformation. The uniform OPD grid is obtained thanks to the use of a spatial reference; the He:Ne laser in our case. Two different approaches allow achieving a spatial uniform sampling: either the data acquisition is triggered electronically from the zero-crossings of the He:Ne interferogram or the spatial uniform sampling is performed at the software level by recording both the He:Ne laser and the supercontinuum interferograms at uniform time intervals. Both techniques present advantages but they also suffer from some drawbacks. They are compared in the next two paragraphs, alongside with the justification of the use of the uniform time-sampling technique for our homemade Fourier-transform spectrometer.

The first approach is a hardware approach. The clock signal of the ADC is generated by a circuit which detects the rising zero-crossings. The advantage is that the interferogram recorded following this method can readily be Fourier transformed. The computation time needed to obtain the spectrum is thus seriously reduced. Spectrometry at wavelengths smaller than 1265.6 nm cannot be performed if the interferogram of the supercontinuum is sampled only once per period of the He:Ne laser, otherwise aliasing will occur. Thankfully, it is possible to double

the sampling frequency by detecting both rising and falling edges, extending the inferior wavelength limit to 632.8 nm. If the He:Ne signal is integrated/differentiated in order to generate another signal in quadrature with the first one and the falling and rising edges are detected on this new signal as well, it is even possible to extend the spectral range of the instrument down to 316.4 nm [2]. Unfortunately, these reference fringe subdivision methods are subject to sampling errors. For example, if there is any offset in the comparators used to sense the zero-crossings, a periodic error at the reference laser frequency could appear, leading to ghost lines in the irradiance spectrum [48].

A second approach consists in measuring both the He:Ne and the supercontinuum interferograms at uniform time intervals and to generate a constant-OPD grid via a software evaluation of the zero-crossings of the He:Ne laser interferogram. It is then possible to create a denser constant-OPD grid from the knowledge of the times of the zero-crossings via a cubic interpolation. The supercontinuum interferogram is then resampled by interpolating it at the times of the reference fringe subdivisions [41, 48]. Furthermore, measuring the two channels gives important information concerning speed variations of the carriage which allows for a better ressampling of the signal of interest [48, 136]. It is possible to retrieve information about the fringe visibility with respect to the optical path difference. This information is relevant concerning the data intensity calibration [136]. Moreover, this technique permits to get rid of the matching of the time delays of the different channels since it can be done at the postprocessing level [136]. It also permits to filter and perform equalization before ressampling [34]. Last but not least, this technique permits to take advantage of commercial ADCs at an affordable price which are developed for other domains of applications, like the audio market, in which high-sampling frequencies ($\approx$ 1 Megasamples per second) and high resolution ($>$ 20 bits) are both required [41, 48]. For all these reasons, choice was made to implement the second method for obtaining the constant-OPD grid.

A.3.4 *ADC resolution*

ADCs convert analog signals into digital ones. The binary representation of the digital signal limits the resolution of the converter, that is

2 Another way to do it is by employing a $\lambda/4$ plate, a PBS and another detector to obtain two signals in quadrature by optical means

precision with which it can convert an analog signal into a digital one. The resolution of the ADC is characterized by the number of bits that can be used to represent the analog signal. An ADC with N bits will be able to generate 2^N distinct discrete values. The full-scale voltage range, that is the range of voltages that can be coded by the ADC, is divided in $2^N - 1$ intervals. Two analog signals which lie in a same interval will be represented by a same discrete value. Most of the information is contained in the small ripples away from the centerburst. Inability to resolve them lowers the FTS resolution, no matter the maximum OPD allowed by the translation stage. The problem is even more important than the dynamic range of the interferogram, *i.e.* the ratio of the maximum intensity to the root-mean-noise level, is usually larger than 10^5 [29]. Figure A.17 illustrates the consequences of a too-low ADC resolution by comparing the digitalized signals of a same interferogram sampled at two different ADC resolutions. The ripples on both sides of the centerburst are rapidly digitalized to zero in Figure A.17(a) while they are discernible everywhere on the interferogram shown in Figure A.17(b).

Currently, a NI-PXI 5922 is employed for the acquisition of the He:Ne and SC channels. It allows digitalization on 24 bits for frequencies up to 500 kHz which is sufficient for the optical path difference induced by the translation stage [26].

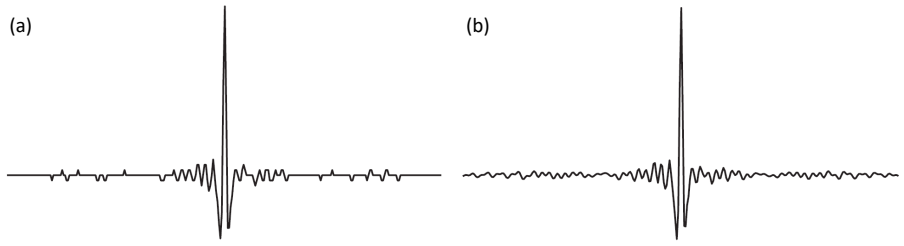


Figure A.17: Same interferogram measured with the same FTS and sampled with (a) a 6-bits ADC (b) a 16-bits ADC. From Ref. [29].

The two interferograms have to be sampled over a certain sampling frequency to ensure that there are enough data to recover the true signals. At least two experimental data have to be measured on each period of the He:Ne laser to unequivocally define it. But, in practice, a minimum of 4 points per period must be taken to correctly evaluate the zero-crossings. Taking 4 points per period of the He:Ne also permits

to measure enough information on the supercontinuum signal to perform spectrometry at wavelengths down to 316.4 nm without aliasing to occur. Since the data are recorded at uniform time intervals, the minimum sampling frequency is imposed by the speed of the carriage by the following formula:

$$f_s = 16v\tilde{\nu}_{\text{He:Ne}}, \tag{A.49}$$

where f_s is the sampling frequency, v is the carriage speed in cm s^{-1} and $\tilde{\nu}_{\text{He:Ne}}$ is the wavenumber of the He:Ne laser in cm^{-1}. The factor 16 is due to the fact that 4 points are measured on a single period of the He:Ne laser and to the fact that the optical path difference is related by a factor 4 to the carriage displacement in our configuration, *i.e.* with the two corner cubes placed back-to-back in the carriage. Injecting the numerical value of the He:Ne wavenumber into equation (A.49) leads to:

$$f_s = 253v \text{ [kHz]}. \tag{A.50}$$

A sampling frequency of 50 kHz for a carriage moving at 0.2 cm s^{-1} gives good results.

A.4 STABILIZATION OF THE HE:NE LASER

As explained in section A.3.1, a CW laser is used as a spatial reference in the FTS. In our setup, a He:Ne laser plays this role for several reasons: it provides an intense collimated beam, a narrow bandwidth, a high mechanical stability and good visibility [137]. Stringent constraints on the stability of the laser output frequency are imposed whenever precision length measurements are involved. Even slight variations in the laser cavity length lead to significant changes in the output frequency. In our case, these changes are mainly induced by thermal expansion of the discharge tube. Tight control of the cavity length is mandatory to stabilize the output frequency of the He:Ne laser. This section is divided into four subsections. The theoretical background necessary to understand the stabilization scheme is first introduced in section A.4.1. Section A.4.2 then explains how stabilization is actually performed.

A.4.1 *Theoretical background*

Lasers usually consist of an amplification medium placed in an optical cavity. Both the amplification medium and the optical cavity geometry vary with the nature of the laser. These two features influence the output frequency of the laser. In the case of the He:Ne laser, the amplification medium is a gas mixture composed of helium and neon placed in a discharge tube. In our case, the cavity mirrors that build the optical cavity are directly sealed onto the ends of the discharge tube. The amplification medium and the optical cavity are introduced separately in the two following subsections. Each time, the factors that influence the output frequency are emphasized.

Amplification medium

He:Ne lasers are CW gas lasers that are based on radiative transitions in neon atoms. Composition of the gas mixture is approximately 85%He-15%Ne and the total pressure is about 1 Torr. Helium atoms are placed in the metastable energy level 2^1S_0 thanks to an electric discharge. These excited helium atoms provide selective excitation of the neon atoms by means of collisions. During the collisions, neon atoms are excited to the 5s energy level and they can then undergo stimulated radiative emissions to the 3p level. The wavelength of the photon emitted during this process is equal to 632.8 nm, the so-called red line of the He:Ne lasers.[3] Atoms in the 3p level then undergo a fast radiative decay to the 3s level. A last transition, from the 3s to the ground state ($1s^2 2s^2 2p^6$), occurs when neon atoms collide with the walls of the gas reservoir. Population inversion is easily maintained since the lifetime of the 5s energy level ($\approx$ 110 ns) is about five times longer than the lifetime of the level 3p ($\approx$ 20 ns). The energy-level diagram of Figure A.18 summarizes all the information given in this paragraph [60, 132, 138].

Since the He:Ne laser is based on the 632.8 nm radiative transition of neon atoms, the profile of the gain curve should be approximated to a Lorentzian centred on the transition frequency with a FWHM equal to the A_{21} Einstein coefficient of the 5s $\rightarrow$ 3p transition, that is about 3.39 MHz [138]. In practice, it is not the case because the transition is broadened by the Doppler effect and the gain curve is

3 In practice, more than 200 other laser lines can be produced by neon atoms but they are of no interest for our purpose and they will not be discussed throughout this report.

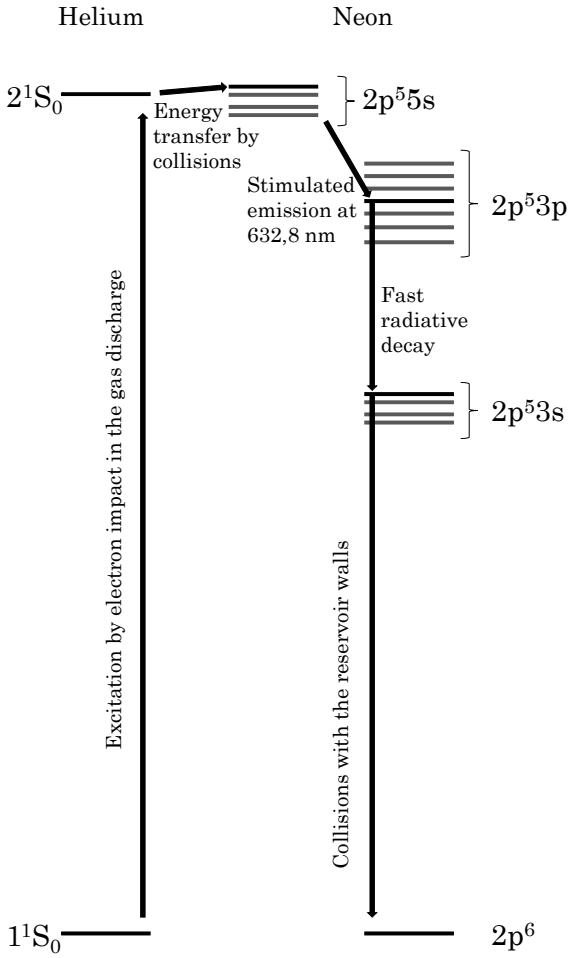


Figure A.18: Partial energy level diagram of the helium and neon atoms relevant for the He:Ne laser emission at 632.8 nm.

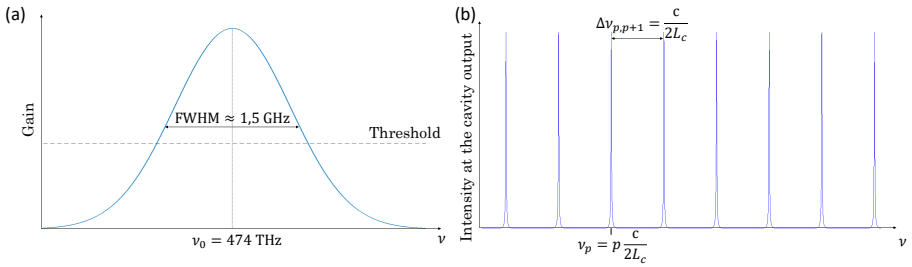


Figure A.19: (a) Gain curve for a Doppler broadened He:Ne gas laser. The curve is approximated by a Gaussian centred in $\nu = 474$ THz with a FWHM of about 1.5 GHz. Light amplification occurs when the gain overcomes the losses, that is for a gain above threshold. (b) Intensity at the output of an optical cavity with respect to the frequency. L_c denotes the cavity length. The width of each peak depends on the cavity finesse.

best described by a Voigt profile, *i.e.* the convolution of the Lorentzian function resulting from the effective lifetime of the energy level with the Gaussian function associated with the Doppler broadening which is evaluated using the Maxwell-Boltzman velocity distribution (FWHM $\approx$ 1.5 GHz). Because of the several orders of magnitude between the FWHM of the Lorentzian and the FWHM of the Gaussian, the gain curve can be approximated to a Gaussian centred on the 5s $\rightarrow$ 3p transition frequency of the neon. Light amplification will occur only if the gain overcomes the losses. Thus, only the frequencies that are above a certain threshold represented by the dashed line in Figure A.19 can result in light amplification [60].

Optical cavity

The optical cavity consists of two mirrors that are placed at both extremities of the tube in which the gas discharge takes place. The two mirrors form the so-called Fabry-Perot interferometer. Light bounces back and forth between the two mirrors that build the cavity. At each reflection, some light passes through the mirrors. If they have a high reflection coefficient, only light that is resonant with the cavity is significantly transmitted. The optical cavity ensures that light travels a long distance before leaving the laser to maximize light amplification. One of the mirrors is a high reflector coated for maximum reflectivity, while the other transmits 0.5% to 1% of light [60].

A second feature of the cavity is to restrict oscillations to longitudinal modes that have frequencies determined by the cavity attributes (cavity

length, mirror reflection coefficients, etc.). The frequency of the p^{th} mode can be approximated to:

$$\nu_p = p\frac{c}{2L_c}, \tag{A.51}$$

where L_c is the cavity length. The difference in frequency between two consecutive modes is the free spectral range (FSR) of the cavity. It is given by:

$$\Delta\nu_{p+1,p} = \nu_{p+1} - \nu_p = \frac{c}{2L_c}. \tag{A.52}$$

The intensity spectrum of the optical cavity consists of a comb of narrow peaks with a width that depend on the reflectivity of the mirrors, each peak being spaced by a frequency $\Delta\nu$ from adjacent peaks. The situation is depicted in Figure A.19(b). The cavity is also responsible for the directivity of the laser and for the transverse spatial profile of the laser beam. The divergence of the laser is lower than in the absence of the cavity [60].

When the amplification medium is placed between the two mirrors that build the cavity and if there is a population inversion between the energy levels involved in the stimulated optical transition, light will be emitted at frequencies for which the longitudinal modes of the cavity have a gain high enough to overcome the losses. In the case of the He:Ne laser, the spectral width of these longitudinal modes are very much narrower compared to the gain curve of the amplification medium [60]. The cavity of the He:Ne used in our setup is about 24 cm long. From equation (A.52), difference of frequency between the two modes is equal to 625 MHz. Up to three modes can be simultaneously emitted by the He:Ne laser for one atomic transition. Because of mode competition, two adjacent modes of the He:Ne laser have perpendicular polarizations [35].

A.4.2 *Implementation*

Since instabilities in the emission frequency of the He:Ne laser are mainly due to variations in the cavity length, tight control of the distance between the two mirrors of the resonator maintain these frequency variations to a minimum. One way to control the cavity length relies on the use of a heater placed around the plasma tube of the He:Ne laser. The heater allows making use of the thermal expansion of the

discharge tube to control the cavity length. The behaviour of the heater is controlled by a feedback system.

For the feedback system to work properly, a setpoint has to be defined. The setpoint permits to define an error signal that characterizes the departure of the output signal from it. An appropriate response is generated from the error signal and allows correcting the output frequency of the He:Ne laser. An astute way to generate an error signal relies on the measurement of the intensity of the two modes that are sustained within the gain curve of the He:Ne laser. Indeed, the intensity of a mode depends on its position in the gain curve, as shown in Figure A.20. The error signal is obtained by subtracting the intensity of one mode from the other. If the two modes are symmetric with respect to the neon transition, as shown in Figure A.20(a), the error signal is equal to zero. However, if one mode is more intense than the other, like in Figure A.20(b), it results in a non-zero error signal that is processed by the feedback system which in turns controls the flow of current in the heater to counteract the change in intensity. A feedback system based on the intensity of the two modes sustained by the laser allows stabilizing the output frequency as well since the frequency is related to the intensity by means of the gain curve. It should be pointed out that the laser would be stable in any situation where the difference of output voltages at the photodetectors is kept constant [36]. However, imposing the two modes to have equal intensities permits to have a very good sensitivity on any frequency change since $\frac{\mathrm{d}I}{\mathrm{d}\nu}$ is maximum at this point [35].

To measure the intensity of each mode, they need to be spatially separated. Since the two lasing modes are polarized orthogonal to each other, a polarizing beamsplitter (PBS) allows to spatially separate them. Each mode is then measured by a distinct photodetector. Output voltages issuing from these two detectors are then subtracted from each other to create the error signal. The error signal is then processed by the feedback system which in turn controls a transistor that determines the current passing through the heater [35, 138]. The whole stabilization setup is depicted in Figure A.21. It should be stressed that the stabilization system uses the low power output of the He:Ne laser. Therefore, stabilizing the laser does not put any constraint on the high power output that can be used for the FTS.

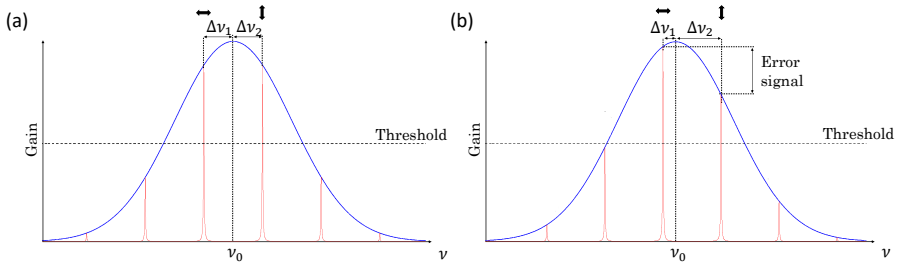


Figure A.20: Gain profile of the He:Ne laser. The cavity modes are represented in orange. They determine the emission frequencies of the laser. Their position in the gain curve determines the emission intensity. Double-sided arrows indicate the polarization of the modes. (a) The two modes are symmetric with respect to the transition line at ν_0 ($\Delta\nu_1 = \Delta\nu_2$). They have the same intensity and the error signal is equal to zero. (b) The two modes are not symmetric with respect to the transition line at ν_0 ($\Delta\nu_1 \neq \Delta\nu_2$). They do not have the same intensity, resulting in a non-zero error signal.

It is common practice to set the response of the system proportional to the instantaneous value of the error. However, the feedback system response is improved by adding integral and derivative responses as well. The integral part takes past values of the error into account in order to get rid of steady-state errors while the derivative part allows to avoid overshooting the setpoint and to damp out oscillations around it [35, 139]. These three responses form the so-called Proportional-Integral-Derivative control system (PID).

Fabrication of the stabilization setup was performed by Marc Daman who based himself on Ref. [35] for the implementation of the PID circuit.

A.5 TIME-DOMAIN FILTERING OF THE TWO CHANNELS

Filtering of the reference channel is twofold. On one hand, removing the dc and the low frequencies terms allows to ensure that the signal baseline is as close to zero as possible. This is necessary for the determination of the constant OPD grid from the signal sampled at uniform time intervals. On the other hand, reducing the the noise equivalent bandwidth of the signal should reduce uncertainties in the location of the zero-crossings. In the case of the supercontinuum channel, filtering allows to reduce the noise equivalent bandwidth, avoids aliasing and suppresses the unmodulated signal, *i.e.* the low-frequency content [34].

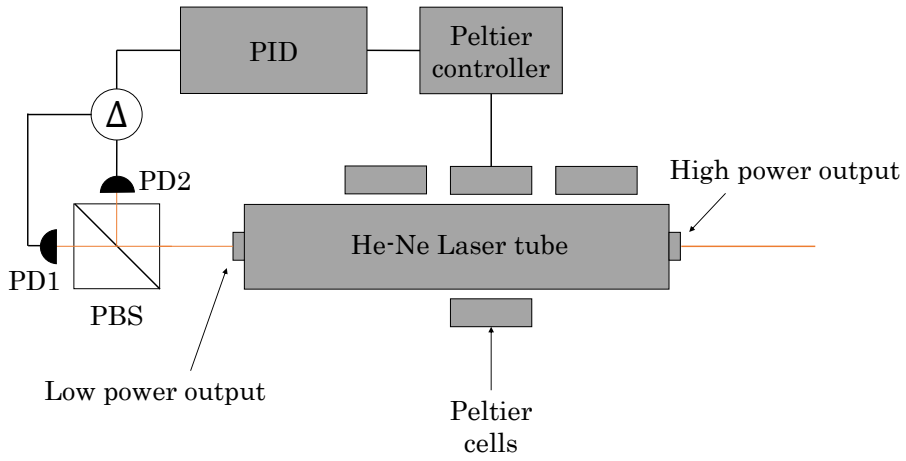


Figure A.21: Laser Stabilization scheme. An error signal is generated thanks to the two orthogonal modes sustained by the He:Ne laser. This error signal is treated by the PID system which controls the Peltier cells placed around the plasma tube.

The two filters are bandpass finite impulse response (FIR) filters designed with the *Filter design and analysis toolbox* of *Matlab*. The bandwidth of the passband should be large enough to do not affect variations in the signal frequency due to velocity fluctuations, as mentioned by Ref. [34]. The two filters have an identical response, depicted in Figure A.22. As we can see, the phase is linear. This is a desired property, justifying our choice to employ FIR filters rather than infinite impulse response (IIR) filters. Indeed, a linear phase in the frequency domain can easily be compensated since it results in a constant delay in the temporal domain. On the other hand, the phase nonlinearity of IIR filters is a problem. Indeed, to a single wavenumber corresponds a range of frequencies due to velocity fluctuations. A given wavenumber will undergo different phase shifts depending on the carriage velocity, resulting in increased phase noise [34]. Even if different frequency responses are applied to the two signals, it is important to design filters with the same order since different delays will result in a shift between the OPD grid generated by the He:Ne and the target channel, leading to sampling errors and ultimately to the measurement of a noisier spectrum [34, 140].

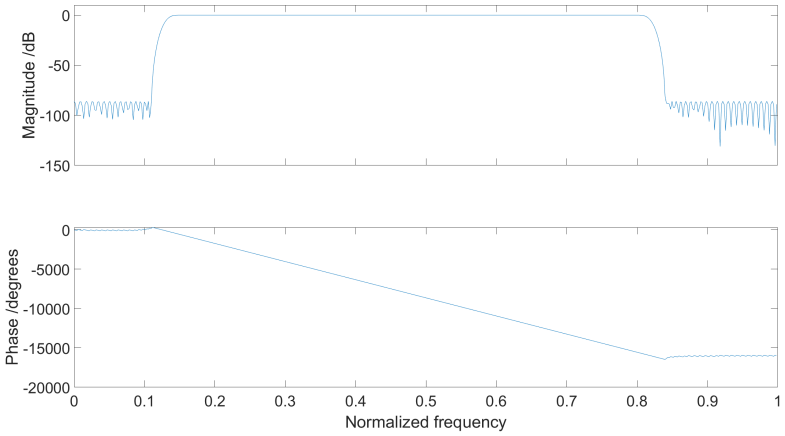


Figure A.22: Frequency response of the FIR filters of the reference and the target channels.

A.6 ZERO-CROSSINGS DETERMINATION

After having filtered the reference signal, the times of the zero-crossings can be estimated with high accuracy. The method suggested by Yang *et al.* (see Ref. [41]) consists in interpolating between the data to determine the times of the zero-crossings. Since zero-crossings provide information about the carriage position, interpolation of the supercontinuum signal at the times of the zero-crossings allows to retrieve a constant OPD-grid from the He:Ne interference pattern sampled at uniform time intervals. For a correct estimation of the zero-crossings, at least four points per period of the He:Ne signal are needed. This value was determined by evaluating the mean percentage error and the mean absolute error between the computed zero-crossings and the analytic zero-crossings of an analytical sinusoidal function. The algorithm for the determination of the constant OPD grid from the He:Ne interference pattern was implemented in *Matlab*. The function returns a vector containing the fractional indexes for which the He:Ne signal is vanishing. Its working principle is illustrated in Figure 2.8 and it is developed step by step just below.

1. Supplementary data points are generated thanks to the function `interp` of *Matlab*, which inserts zeros into the original signal and then applies a lowpass interpolating filter to the expanded sequence. The amount of data is multiplied by 8, as suggested

by Yang *et al.* (Ref. [41]). The supplementary data points are represented by red bullets in Figure 2.8 while the blue crosses correspond to the input data.

2. The indexes of the points located just before a zero-crossing are determined using the following formula:

$$\texttt{diff}(\texttt{sign}(signal))) = 0, \tag{A.53}$$

where the function `sign` returns the sign of each entry of the vector *signal*, that is +1 if $signal > 0$, -1 if $signal < 0$ and 0 if $signal = 0$. The function `diff` returns a vector containing the differences between adjacent entries of a vector in *Matlab*. When there is a zero-crossing, the difference is equal to zero. The indexes of the zero-crossings are then determined by finding all the entries that are equal to zero in the vector resulting from the use of the above formula.

3. For each detected zero-crossing:

   a) 3 samples are taken from both sides of the zero-crossing and these data are interpolated by a cubic function which is traced in black in Figure 2.8;

   b) The root of the cubic function that is nearest to the zero-crossing is evaluated using the Newton-Raphson method. The root corresponds to the fractional index at which the signal is vanishing. The zero-crossings are depicted by the black diamonds in Figure 2.8.

Finding the polynomial that best approximates the set of data involves solving a system of linear equations:

$$Ax = y, \tag{A.54}$$

where A is the Vandermonde matrix, x is a column vector containing the coefficients of the polynomial and y is a column vector containing the data that need to be fitted. High-resolution spectra involve to perform this step several millions of times which is time-consuming. Indeed, for each zero-crossing, it is necessary to evaluate the QR decomposition of the A matrix, also known as its QR factorization, which consists in rewriting the A matrix as a product of two matrices Q and R:

$$A = QR. \tag{A.55}$$

where Q is an orthogonal matrix, meaning that $Q^{-1} = Q^T$, and R is an upper right triangular matrix. The system of equation (A.54) becomes:

$$QRx = y. \tag{A.56}$$

Multiplying on the left both equations by Q^{-1} or alternatively by Q^T leads to:

$$Rx = Q^T y. \tag{A.57}$$

The resulting problem is trivial since R is a triangular matrix.

Since the abscissa correspond to evenly spaced values in the time domain, the system of equations that needs to be solved is the following one:

$$\begin{bmatrix} (k-2)^3 & (k-2)^2 & (k-2) & 1 \\ (k-1)^3 & (k-1)^2 & (k-1) & 1 \\ k^3 & k^2 & k & 1 \\ (k+1)^3 & (k+1)^2 & (k+1) & 1 \\ (k+2)^3 & (k+2)^2 & (k+2) & 1 \\ (k+3)^3 & (k+3)^2 & (k+3) & 1 \end{bmatrix} \begin{bmatrix} p1 \\ p2 \\ p3 \\ p4 \end{bmatrix} = \begin{bmatrix} y_{k-2} \\ y_{k-1} \\ y_k \\ y_{k+1} \\ y_{k+2} \\ y_{k+3} \end{bmatrix}. \tag{A.58}$$

where k is the index of the sample just before the zero-crossing, p_1 and p_2 are the coefficients of the third degree polynomial $y = p_1 x^3 + p_2 x^2 + p_3 + p_4$. Finally, y_k is the value of the k$^{\text{th}}$ sample. The first matrix in this problem is the so-called Vandermonde matrix. This matrix has a similar form for all the roots that need to be precisely determinate, at the exception of the value of k. In order to avoid to find the QR decomposition of the Vandermonde matrix for each of the millions of zero-crossings that need to be found, which is time-consuming, the problem can be shifted around zero by setting $k = 0$. The value of the zero-crossing is shifted back by k after the system is solved. Thus, only a single QR decomposition has to be evaluated, that is the one of the matrix

$$v = \begin{bmatrix} (-2)^3 & (-2)^2 & (-2) & 1 \\ (-1)^3 & (-1)^2 & (-1) & 1 \\ 0^3 & 0^2 & 0 & 1 \\ (1)^3 & (1)^2 & (1) & 1 \\ (2)^3 & (2)^2 & (2) & 1 \\ (3)^3 & (3)^2 & (3) & 1 \end{bmatrix}. \tag{A.59}$$

The R matrix of the QR decomposition is of the following form

$$R = \begin{bmatrix} & & & \\ a_1 & a_2 & a_3 & a_4 \\ 0 & b_2 & b_3 & b_4 \\ 0 & 0 & c_3 & c_4 \\ 0 & 0 & 0 & d_4 \\ 0 & 0 & 0 & 0 \\ 0 & 0 & 0 & 0 \end{bmatrix}. \tag{A.60}$$

We can express the coefficients p_4, p_3, p_2 and p_1 as a function of $a_{1,2,3,4}$, $b_{2,3,4}$, $c_{3,4}$ and d_4 and Q as follows:

$$p_4 = \frac{Q^T \times y}{d_4}; \tag{A.61}$$

$$p_3 = \frac{Q^T \times y - c_4 p_4}{c_3}; \tag{A.62}$$

$$p_2 = \frac{Q^T \times y - b_4 p_4 - b_3 p_3}{b_2}; \tag{A.63}$$

$$p_1 = \frac{Q^T \times y - a_4 p_4 - a_3 p_3 - a_2 p_2}{a_1}. \tag{A.64}$$

$$\tag{A.65}$$

In order to find the root of interest of the polynomial $y = p_1 x^3 + p_2 x^2 + p_3 x + p_4$, the Newton-Raphson method was implemented. The first guess for the zero-crossing location x is $x_0 = \frac{1}{2}$, meaning that the root is at equal distance of the k and $k+1$ samples. The actual zero-crossing is obtained by shifting the zero-crossing determined by the shifted problem by k, that is

$$x_k = k + x. \tag{A.66}$$

A.7 IDEAL RECONSTRUCTION OF A SAMPLED SIGNAL: THE SINC INTERPOLATION

This section relies on Ref. [61].

The problem of reconstructing the continuous-time signal from its samples on a uniform sampling grid is most easily solved in the frequency domain with the use of the Fourier transform.

The Fourier transform representation of the sampled signal, denoted $X_\delta(\mathrm{j}\omega)$, is given by:

$$X_\delta(\mathrm{j}\omega) = \frac{1}{T_s} \sum_{k=-\infty}^{+\infty} X(\mathrm{j}\omega - \mathrm{j}k\omega_s), \tag{A.67}$$

where $X(\mathrm{j}\omega)$ is the Fourier transform of the continuous-time signal, T_s is the sampling interval and ω_s is the sampling frequency. The goal of the reconstruction is to apply some operation to $X_\delta(\mathrm{j}\omega)$ that converts it back to $X(\mathrm{j}\omega)$. Any such operation must eliminate the replicas or images of $X_\delta(\mathrm{j}\omega)$ that are centred at $k\omega_s$. This is accomplished by multiplying $X_\delta(\mathrm{j}\omega)$ by

$$H_r(j\omega) = \begin{cases} T_s & \text{for} \quad |\omega| \leq \frac{\omega_s}{2} \\ 0 & \text{for} \quad |\omega| > \frac{\omega_s}{2}. \end{cases} \tag{A.68}$$

The spectrum is then given by:

$$X(j\omega) = X_\delta(\mathrm{j}\omega) H_r(\mathrm{j}\omega). \tag{A.69}$$

Multiplication in the frequency domain transforms to convolution in the time domain. Therefore, we have in the time domain:

$$\begin{aligned} x(t) &= x_\delta(t) \star h_r(t) \\ &= h_r(t) \star \sum_{n=-\infty}^{+\infty} x[n]\delta(t - nT_s) \\ &= \sum_{n=-\infty}^{+\infty} x[n] h_r(t - nT_s), \end{aligned} \tag{A.70}$$

with

$$h_r(t) = \mathrm{sinc}\left(\frac{\omega_s t}{2\pi}\right). \tag{A.71}$$

Finally, the signal at any time t can be obtained by evaluating the following expression:

$$x(t) = \sum_{n=-\infty}^{+\infty} x[n] \mathrm{sinc}\left(\frac{\omega_s(t - nT_s)}{2\pi}\right). \tag{A.72}$$

This operation is commonly referred to as ideal band-limited interpolation, since it indicates how to interpolate between the samples of a bandlimited signal in order to get the exact value of x at time t. In practice, this interpolation cannot be implemented for two reasons:

- it represents a non-causal system because the output depends on past and futures values of the input.
- the influence of each sample extends over an infinite amount of time because $h_r(t)$ has an infinite duration.

However, since the sinc function rapidly tends to zero and because we perform the interpolation at the post-processing level, we use equation (A.72) for the resampling process of the FTS, as described in Section 2.4.2.

A.8 INSTRUMENT SENSITIVITY

As mentioned in section 2.5.3, absorption spectroscopy relies on the measurement of the frequency-dependent attenuation of light after its interaction with the sample which is described using the Beer-Lambert's law. It specifies that the attenuation is proportional to the optical path through the sample:

$$\mathrm{d}I = -I(\tilde{\nu})\alpha(\tilde{\nu})\mathrm{d}l, \tag{A.73}$$

with $I(\tilde{\nu})$ the intensity of light at wavenumber $\tilde{\nu}$ and $\alpha(\tilde{\nu})$ the wavenumber-dependent absorption coefficient which depends on both the line intensity and the amount of the species under study, $\mathrm{d}I$ the intensity variation after interacting with the sample on a distance $\mathrm{d}l$. The sensitivity of the instrument is characterized by the smallest value of $\alpha(\tilde{\nu})$ the instrument can measure, denoted α_{min}.

The interaction path length is a function of the absorption in optical cavities and procedures to estimate the instrument sensitivity will be different for cavity-based or non-cavity-based measurements. The calibration procedure is performed by using the knowledge of the line intensities of a well-known molecule listed in the Hitran database in both cases.

Section A.8.1 presents the estimation of the sensitivity of measurements performed in a single-path configuration or in a multi-pass configuration considering the use of a multi-path cell.

Section A.8.2 describes the estimation of the instrument sensitivity in the case of a cavity-enhanced measurement.

A.8.1 *absorption coefficient in absence of an optical cavity*

This section relies on Ref. [141] and [142].

Evaluating the sensitivity of the instrument requires the knowledge of the partial pressure P_{Mol} of the calibration species, the line intensities S_{ij} of the transitions $i \rightarrow j$ used for the calibration and the interaction length l between light and the sample. The observed line intensity S_L is given by:

$$S_L = S_{ij}^{\star} \frac{B}{B_T} \frac{296}{T} N_L P_{Mol} l, \tag{A.74}$$

where $N_L = 2.6867661(47) \times 10^{19}$molecules cm^{-3}atm^{-1} is the Loschmidt number, B is the isotope abundance in the atmosphere being modelled, B_T the isotope abundance in the terrestrial atmosphere and T the temperature in Kelvin at which the transition is observed. In equation (A.74), $S_{ij}^{\star}$ denotes the temperature-corrected line intensity. This correction is due to the fact that the line intensities S_{ij} are tabulated for a temperature of 296 K in the Hitran database. $S_{ij}^{\star}$ can computed using the following formula:

$$S_{ij}^{\star} = S_{ij} \left(\frac{Q_{296\mathrm{K}}}{Q_T} \right) \frac{\exp\left(\frac{-c_2 E''}{T}\right)}{\exp\left(\frac{-c_2 E''}{296}\right)} \frac{1 - \exp\left(\frac{-c_2 \tilde{\nu}_{ij}}{T}\right)}{1 - \exp\left(\frac{-c_2 \tilde{\nu}_{ij}}{296}\right)}, \tag{A.75}$$

where Q_T is the total internal partition sum value for the calculation temperature, $Q_{296\mathrm{K}}$ is the total internal partition sum for the temperature of 296 K, $\tilde{\nu}_{ij}$ the vacuum wavenumber of the transition, E'' its lower state energy and $c_2 = \frac{hc}{k}$ is the second black body radiation constant, with c the light velocity, h the Planck constant and k the Boltzmann constant. All the parameters of equation (A.75) are tabulated in the Hitran database.

The wavenumber-dependent absorbance $A(\tilde{\nu})$ is related to S_L as follows:

$$A(\tilde{\nu}) = f(\tilde{\nu}) S_L, \tag{A.76}$$

where $f(\tilde{\nu})$ is the normalized lineshape profile. Since the profile lineshape is a normalized function, integrating both members of equation (A.76) leads to:

$$\int_{-\infty}^{+\infty} A(\tilde{\nu}) \mathrm{d}\tilde{\nu} = \int_{-\infty}^{+\infty} f(\tilde{\nu}) S_L \mathrm{d}\tilde{\nu} = S_L. \tag{A.77}$$

Combining equations (A.74) and (A.77) leads to:

$$\int_{-\infty}^{+\infty} A(\tilde{\nu})\mathrm{d}\tilde{\nu} = S_{ij}^{\star}\frac{B}{B_T}\frac{296}{T}N_L P_{Mol} l. \tag{A.78}$$

In order to evaluate the sensitivity of the instrument, we need to find the value of the interaction length l:

$$l = \frac{\int_{-\infty}^{+\infty} A(\tilde{\nu})\mathrm{d}\tilde{\nu}}{S_{ij}^{\star}\frac{B}{B_T}\frac{296}{T}N_L P_{Mol}}. \tag{A.79}$$

The experimental wavenumber-dependent absorbance $A(\tilde{\nu})$ is obtained from the experimental wavenumber-dependent transmittance $T(\tilde{\nu})$ using the following expression:

$$A(\tilde{\nu}) = -\log(T(\tilde{\nu})), \tag{A.80}$$

where log is the natural logarithm. To evaluate L in equation (A.79), $A(\tilde{\nu})$ needs to be integrated. To do so, the experimental data are fitted by a function, and the integral of this function is evaluated analytically. At low pressures, the lineshape is dominated by the Doppler effect, resulting in a Gaussian profile. We thus have:

$$\begin{aligned}\int_{-\infty}^{+\infty} A(\tilde{\nu})\mathrm{d}\tilde{\nu} &= \int_{-\infty}^{+\infty} a\exp\left(\frac{-(\tilde{\nu}-b)^2}{c^2}\right)\mathrm{d}\tilde{\nu} \\ &= \frac{-1}{2}\sqrt{\pi}ac\left[\mathrm{erf}\left(\frac{b-\tilde{\nu}}{c}\right)\right]_{-\infty}^{+\infty} = \sqrt{\pi}ac.\end{aligned} \tag{A.81}$$

This result allows for the determination of the experimental interaction length l:

$$l = \frac{\sqrt{\pi}ac}{S_{ij}^{\star}\frac{B}{B_T}\frac{296}{T}N_L P_{Mol}}. \tag{A.82}$$

Indeed, a and c are obtained from the line fit, B, T and P_{Mol} are experimental parameters that are either known or easily measured, N_L is a physical constant and $S_{ij}^{\star}$ is retrieved from the Hitran database.

The last step to determine the sensitivity of the measurement consists in dividing the experimental wavenumber-dependent absorbance by the interaction length in order to obtain the absorption coefficient. The minimum absorption coefficient that can be unambiguously distinguished from the noise corresponds to the sensitivity we are looking for.

A.8.2 *Cavity-enhancement of absorption*

This section relies on Ref. [143].

When absorption spectroscopy is performed within an enhancement cavity, the determination of the sensitivity of the measurement is more complicated since the number of back-and-forth travels that light undergoes within the cavity depends upon the line strength, leading to a variable absorption enhancement [144]. The evaluation of the absorption coefficient from the transmittance thus requires to take into account the response of the cavity.

This can be done by evaluating the expression of the light transmitted by a linear cavity of length l with mirror reflectivities R_1 and R_2 and with extra-losses L inside the cavity due to species absorption. The derivation of this expression relies on Figure A.23. In this figure, we make the distinction between the path length d for a single path through the sample and the length l of the cavity.

The intensity at the output of the cavity is given by the sum of the intensities after an even number of reflections in the cavity:

$$\begin{aligned} I =& I_{\text{in}}(1-R_1)(1-L)(1-R_2) && \text{zeroth path} \\ &+ I_{\text{in}}(1-R_1)(1-L)R_2(1-L)R_1(1-L)(1-R_2) && \text{(first path)} \\ &+ ... \\ &+ I_{\text{in}}(1-R_1)(1-R_2)R_1^n R_2^n (1-L)^{2n+1} && n^{\text{th}} \text{ path} \\ =& I_{\text{in}}(1-R_1)(1-R_2)(1-L)\sum R_1^n R_2^n (1-L)^{2n}. && \text{(A.83)} \end{aligned}$$

Since the mirror reflectivities R_1, R_2 and the cavity losses L are smaller than 1, this geometric series converges and equation (A.83) becomes:

$$I = I_{\text{in}} \frac{(1-R_1)(1-R_2)(1-L)}{1-R_1R_2(1-L)^2}. \tag{A.84}$$

For an empty cavity, $L = 0$, and the time-integrated transmitted intensity I_0 is given by:

$$I_0 = I_{\text{in}} \frac{(1-R_1)(1-R_2)}{1-R_1R_2}. \tag{A.85}$$

The transmittance T is defined as the ratio of I over I_0, giving:

$$T = \frac{I}{I_0} = \frac{(1-L)(1-R_1R_2)}{1-R_1R_2(1-L)^2}, \tag{A.86}$$

which can be rewritten as follows:

$$(1-L)^2 R_1 R_2 \frac{I}{I_0} + (1-L)(1-R_1R_2) - \frac{I}{I_0} = 0. \tag{A.87}$$

Solving for this second order equation in $1-L$ leads to:

$$1-L = \sqrt{\frac{1}{4}\left(\frac{I_0}{I}\frac{(1-R_1R_2)}{R_1R_2}\right)^2 + \frac{1}{R_1R_2}} - \frac{1}{2}\frac{I_0}{I}\frac{(1-R_1R_2)}{R_1R_2}. \tag{A.88}$$

Supposing that the losses are only due to Lambert-Beer absorption, we can replace $1-L$ by $\exp(-\alpha d)$ (see equation (A.73)) into equation (A.88) and solve for the absorption coefficient α:

$$\alpha = \frac{1}{d}\left|\ln\left(\frac{1}{2R_1R_2}\left(\sqrt{4R_1R_2 + \left(\frac{I_0}{I}(1-R_1R_2)\right)^2} - \frac{I_0}{I}(1-R_1R_2)\right)\right)\right|. \tag{A.89}$$

This is a general expression of the absorption coefficient where no approximation was made regarding neither the size of α nor the mirror reflectivities R_1 and R_2, meaning that the expression is valid even for strong absorption and small mirror reflectivities. However, when determining the measurement sensitivity, it is more convenient to work with the following approximation:

$$\alpha = \frac{1}{d}\left(\frac{I_0}{I} - 1\right)\left(1 - \sqrt{R_1R_2}\right), \tag{A.90}$$

which was obtained by supposing low losses for a single path ($L \to 0$) and high mirrors reflectivities $R_{1,2} \to 1$.

From a glance at either equation (A.89) or equation (A.90), we can see that the determination of the minimum absorption coefficient, denoted $\alpha_{\min}$, requires the knowledge of the reflectivities of the two mirrors. We will suppose their reflectivities to be equal and evaluate the effective reflectivity R of both mirrors. This can be done by combining equations (A.74), (A.77) and (A.90), leading to the following expression (see Ref. [16]):

$$R = 1 - \frac{NdS_{ij}}{\int_{-\infty}^{+\infty}\left(\frac{I_0(\tilde{\nu}}{I(\tilde{\nu}} - 1\right)\mathrm{d}\tilde{\nu}}, \tag{A.91}$$

with N the number density of the gas. This expression is only valid for small absorption losses and high mirrors reflectivities. Its use for the determination of the mirrors reflectivities requires the presence of a calibration gas with well known line intensities and gas density.

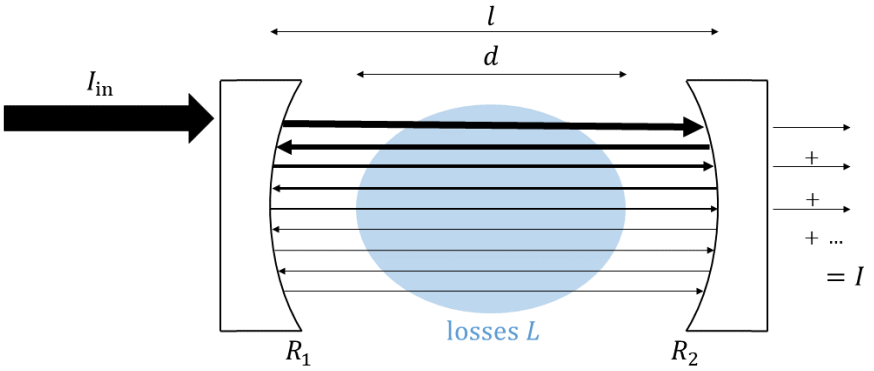


Figure A.23: Intensity at the output of an optical cavity consisting of two mirrors separated by a distance d. Light undergoes losses L at each passage in the gaseous sample spread over a distance d in the cavity. Adapted from Ref. [143]

B

FREQUENCY COMBS: SUPPLEMENTARY MATERIALS

The aim of this appendix is to give further details concerning the frequency combs. It is divided in two sections. Section B.1 details the second-order autocorrelator developed in the laboratory for the characterization of the pulse duration while section B.2 gives the relevant characteristics of the optics constituting the resonator built in-house.

B.1 MEASURING THE DURATION OF THE PULSES

Ability to characterize the pulse duration is necessary in this project for two reasons: (1) to ensure that pulses emitted by the MIRA900 femtosecond laser are short enough to generate a coherent octave spanning spectrum in the nonlinear fiber placed before the $1f - 2f$ interferometer [93] and (2) to characterize the pulse duration of the homemade femtosecond laser. However, no direct measurement of the pulse duration is possible in the femtosecond domain because there are neither detectors nor electronics that are fast enough to measure events in the sub-picosecond domain. Instead, nonlinear autocorrelation techniques are employed to perform the task. They consist in measuring the intensity autocorrelation pattern whose width is proportional to the pulse duration. The proportionality factor is known as the deconvolution factor and depends on the temporal envelope of the pulse [60]. However, nonlinear autocorrelation techniques do not allow to retrieve precise information on the temporal profile and some assumption on its shape has to be made to select the right deconvolution factor. Furthermore, an erroneous guess can lead to inconsistent or inaccurate results, especially for the shortest pulses with only a few electric field cycles [71, 145]. Being aware of that, information given by nonlinear autocorrelation techniques is sufficient since we mainly want to have a good estimate of the pulse duration and to optimize it. In this type of measurement, two replicas of the pulse are generated which are delayed with respect to each other. An instantaneous nonlinear optical effect, such as second-harmonic generation is used to form the

product of the two replicas, which depends on the temporal overlap of the replicas. Effectively, this allows converting measurement of a time into the measurement of a distance [71]. In section B.1.1, the working principle of interferometric autocorrelators is developed.

In section B.1.2, the homemade autocorrelator is presented, along with the data-processing pipeline.

B.1.1 *Working principle*

This section relies on Ref. [60, 67].

The concept behind intensity autocorrelators consists in creating a copy of the pulse and to use it as a probe for characterizing the pulse duration. Most intensity autocorrelators rely on Michelson-type interferometers to create a copy of the pulse and to delay it with respect to the original pulse. Other interferometers can be employed to perform the task such as the Mach-Zhender type [146] . A second harmonic generation (SHG) crystal is placed in front of the detector to measure the intensity autocorrelation pattern rather than the electric field-autocorrelation pattern. The optical layout is shown in Figure B.1. The expression of the electric field at the detector is given by:

$$E_{\text{det}} = [E(t) + E(t-\tau)]^2, \tag{B.1}$$

where $E(t)$ is the pulse electric field amplitude and τ the delay induced by the mobile arm. The detector responds to the electric field intensity $I(t) \equiv |E(t)|^2$ rather than the electric field amplitude. Also, the detector response is slow so that it integrates the signal over the entire pulse, meaning that for a given delay τ, we actually measure:

$$\begin{aligned} S(\tau) &= \int_{-\infty}^{+\infty} \left([E(t) + E(t-\tau)]^2 \right)^2 \mathrm{d}t. \\ &= \int_{-\infty}^{+\infty} \left(|E(t)|^2 + |E(t-\tau)|^2 + \right. \\ &\quad \left. \underbrace{2\mathrm{Re}(E(t)E(t-\tau)^*)}_{\text{interference}} \right)^2 \mathrm{d}t. \end{aligned} \tag{B.2}$$

By retaining only the interferometric term, we obtain the intensity autocorrelation $A(\tau)$ which is given by:

$$A(\tau) = \int_{-\infty}^{+\infty} I(t)I(t-\tau)\mathrm{d}t \tag{B.3}$$

Table B.1: Deconvolution factors for different pulse shapes with a temporal profile $I(t)$ of FWHM duration τ_p. The FWHM of the autocorrelation above the background level is τ_{ac}. From Ref. [60].

I(t)	τ_{ac}/τ_p
top hat	1
$\exp\left(-\ln 2 \frac{t}{\tau_p}\right)$	2
$\exp\left(-4\ln 2 \left(\frac{t}{\tau_p}\right)^2\right)$	$\sqrt{2}$
$\mathrm{sech}^2\left(1.76\frac{t}{\tau_p}\right)$	1.54

where $I(t)$ is the intensity of the electric field of the pulse which is a function of time. The autocorrelation signal is always symmetric about $\tau = 0$ even for non-symmetrical pulse envelopes, avoiding to determine their exact shape. In order to make a more quantitative estimate of the pulse duration, it is necessary to assume the shape of the pulse envelope in order to select the best deconvolution factor that links the full width at half maximum (FWHM) of the pulse to the one of the autocorrelation pattern. Several deconvolution factors for different pulse shapes are given in Table B.1.

In practice, it is possible to measure only the interferometric term by mixing the electric fields issuing from the two arms in a non-collinear configuration, as depicted in Figure B.2. Indeed, when mixing two waves of frequency ω with angles of incidence (AOI) equal to $\pm\theta$ in a type I SHG crystal, the frequency doubled resultant exits the crystal at normal incidence. This statement is illustrated in Figure B.2(a) while the optical layout that allows this background free measurement is shown in Figure B.2(b). The aperture allows to suppress the background signal while preserving the interferometric signal.

B.1.2 *Design of our interferometric autocorrelator*

In order to characterize the duration of the pulses emitted by the MIRA900 and by our homemade femtosecond laser, we built an interferometric autocorrelator based on the layout presented in Figure B.2. A picture of the setup is given in Figure B.3. Most of the optics employed (the beamsplitter and the two retroreflectors) for its implementation were scavenged from a broken autocorrelator found in the laboratory

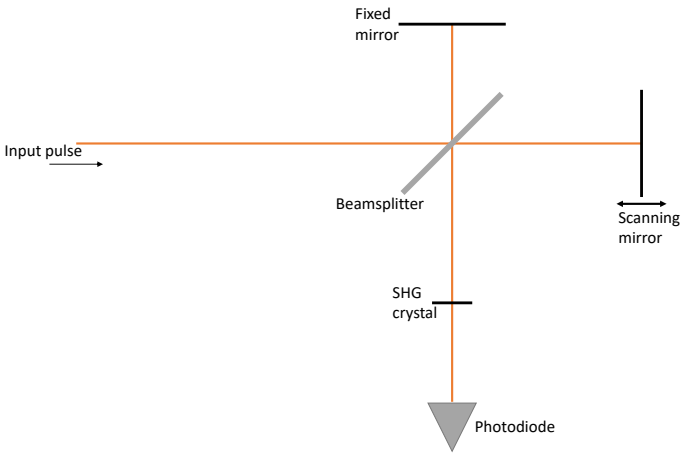


Figure B.1: Layout of an interferometric autocorrelator based on a Michelson interferometer.

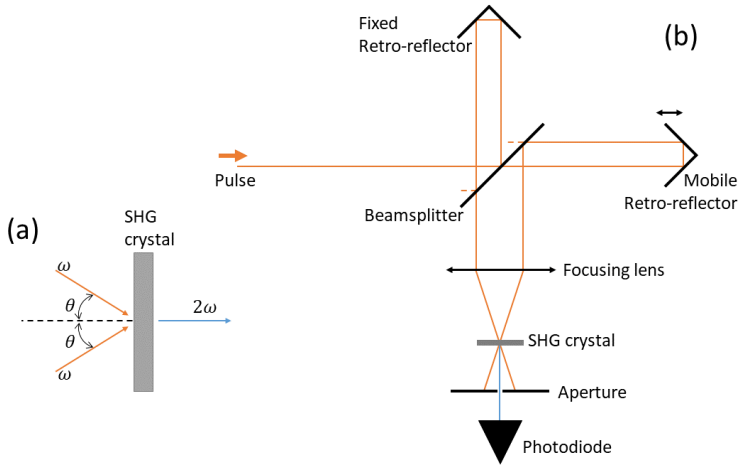


Figure B.2: Background-free interferometric autocorrelation. (a) Interaction of two waves of frequency ω with an AOI equal to $\pm\theta$ in a Type I SHG crystal. The frequency doubled term exits at normal incidence. (b) Layout of an interferometric autocorrelator based on a Michelson interferometer allowing background-free measurements. The beams coming from the two arms are focused in a SHG crystal, the frequency-doubled light beam is measured with a photodiode. The beams participating to the background are suppressed by means of a circular aperture.

from APE. A plano-convex lens with a focal length of 25 mm is used to focus the beams coming from the two arms of the interferometer in a type-I BBO SHG crystal which was also available in the laboratory. The optical path length is modified in one of the two arms by means of a P-290.00 piezoelectric linear translation stage from PI instrument (1 mm maximum stroke for a -1000V applied voltage). A triangular voltage signal is applied on the piezoelectric crystal, inducing a displacement of the mobile retro-reflector. The ramp is recorded along with the signal of interested which is measured with a PDA25K2 photodiode from the Thorlabs catalog. The Tie-Pie ADC is used to sample the two channels.

The displacement induced by the piezoelectric crystal was calibrated with a frequency-stabilized He:Ne laser. The translation stage was placed in one of the two arms of a Michelson interferometer, allowing to measure the He:Ne interference pattern as a function of the voltage applied on the piezoelectric crystal. It ultimately allowed the determination of the relationship between the displacement and the voltage. Indeed, since we are only interested in the width of the envelope of the intensity autocorrelation pattern, we do not have to sample the signal at specific values. The different stages of the calibration process are shown in Figure B.5. We can see that the voltage ramp is recorded along with the He:Ne interference pattern at the same sampling times. To a given index in these two vectors is associated a given sampling time. The voltage ramp is first fitted with a straight line to remove the noise. The indices of the zero-crossings of the He:Ne interference pattern are determined using the function described in Appendix A.6 that was initially written for the Fourier-transform spectrometer. They are spaced by an OPD of 316.4 nm. OPD is thus known at the fractional indices of the zero-crossings. The OPD grid is interpolated at the integer indices, allowing for an one-to-one correspondence between the voltage ramp and the OPD.

In order to evaluate the pulse duration, the signal at the output of the layout depicted in Figure B.2 is recorded along with the voltage ramp applied on the piezoelectric crystal which is filtered at the software level by means of a linear fit. The next stage consists in converting the voltage ramp into optical path difference (OPD) thanks to the prior determination of the voltage-displacement relationship. Dividing the OPD by the velocity of light gives access to the time delay induced in the mobile arm. We are now able to plot the intensity autocorrelation pattern with respect to the delay and to extract its envelope. To illustrate

Table B.2: Specifications of the Ti:Sapphire crystal of the homemade femtosecond resonator.

Material	Ti:Sapphire laser crystal
Face dimensions	5.23 mm x 6.00 mm
Path length	2 mm
Orientation:	C-axis parallel to E-vector of light beam
alpha	7 cm^{-1} at 532 nm
FOM	> 200
End faces	Brewster cut
Clear aperture	> 90 %
Coating	uncoated
surface quality	10-5 scratch-dig
Surface flatness	lambda/10
Parallelism	< 30 arcsec

this, experimental data recorded with the MIRA900 femtosecond laser are shown in Figure B.6. In this plot, the blue curve corresponds to the intensity autocorrelation pattern. The last stage of the analysis consists in fitting the intensity autocorrelation pattern with the appropriate function. We tried both the hyperbolic secant and the Gaussian function. The goodness of the fits was better when using the Gaussian function. The pulse duration is finally estimated by dividing the FWHM of the Gaussian fit by $\sqrt{2}$ (see Table B.1).

B.2 OPTICS OF THE HOMEMADE FEMTOSECOND RESONATOR

The characteristics of the Ti:Sapphire crystal employed in our setup are given in Table B.2. Figures B.7, B.8 and B.9 give the GDD curves of the four mirrors building the resonator.

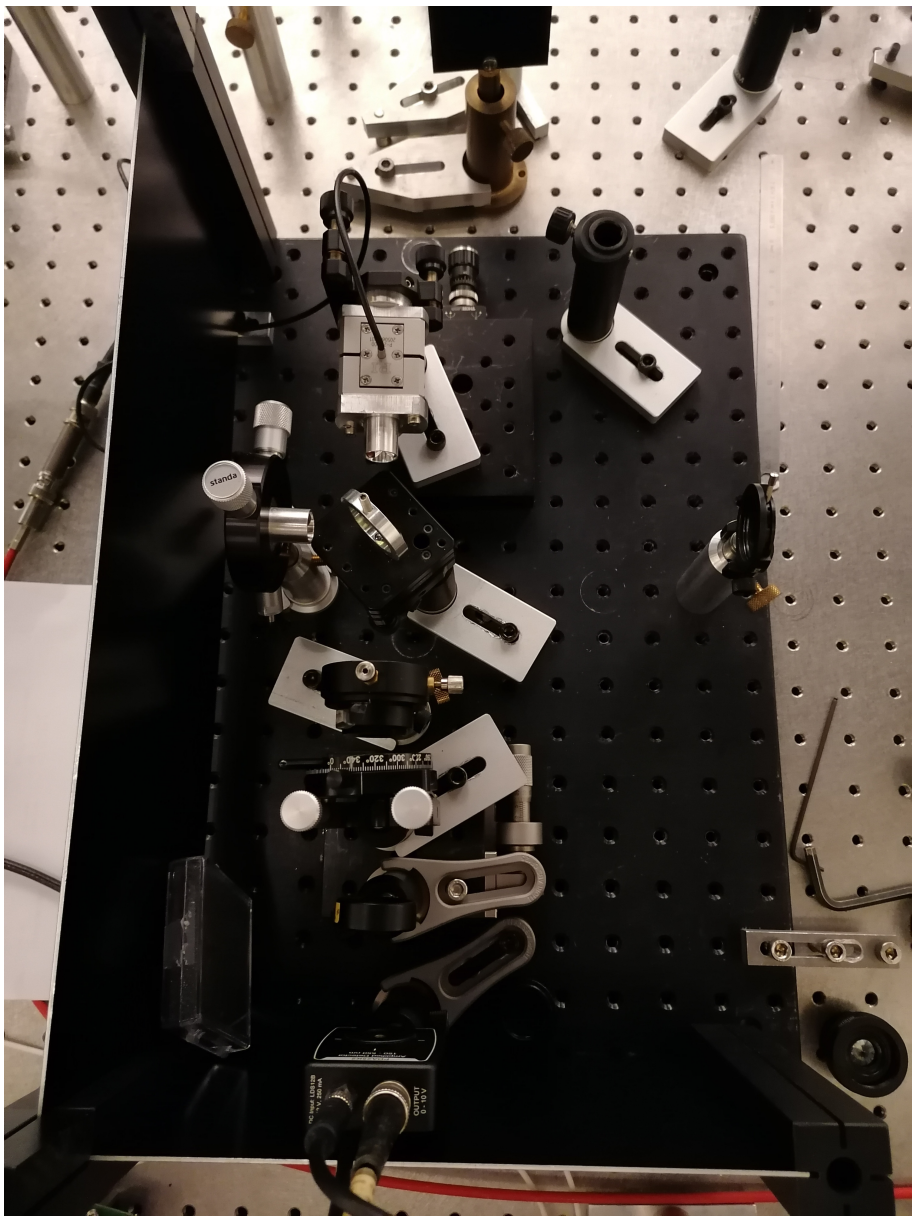


Figure B.3: Picture of our experimental setup.



Figure B.4: Butterfly pattern at the output of the properly aligned autocorrelator. The blue part contains the interferometric information of interest while the red wings only participate to the background signal. They are removed by means of a circular aperture place in front of the detector

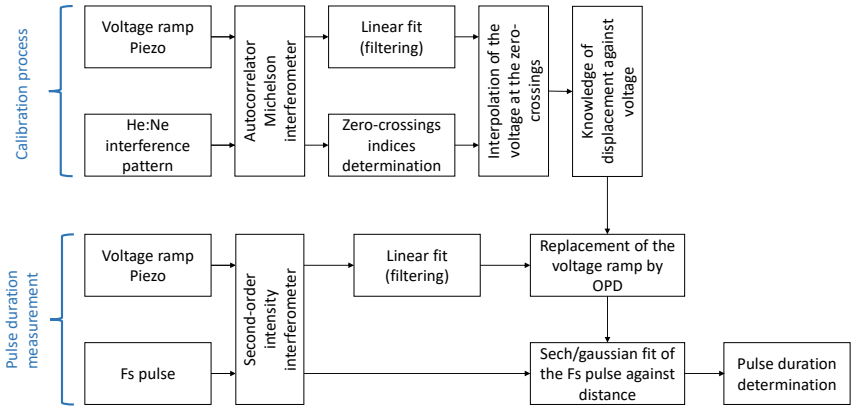


Figure B.5: Data processing pipeline of the second order optical autocorrelator implemented in Matlab.

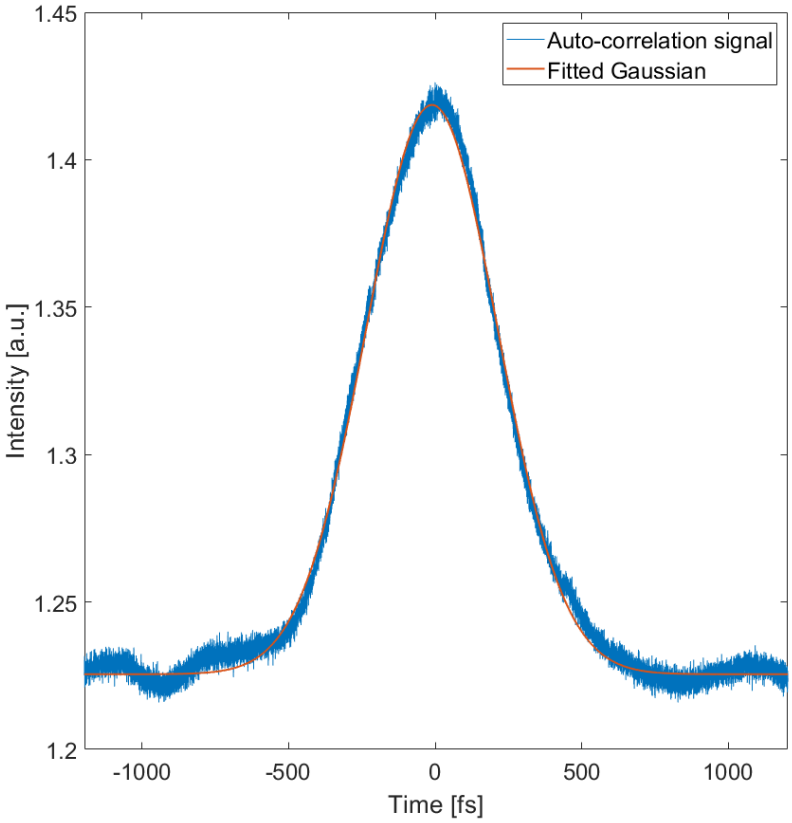


Figure B.6: Background-free aucorrelation pattern at the output of the MIRA900. The measured pulse duration is equal to 373 fs (Gaussian pulse).

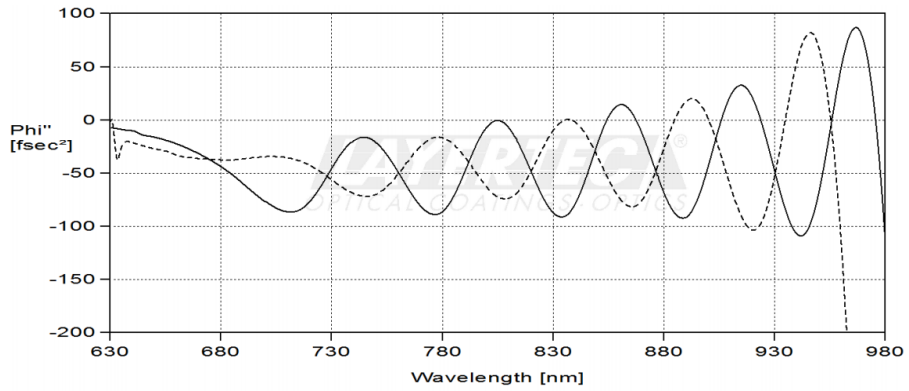


Figure B.7: Calculated GDD of the folding chirped mirrors pair employed in our cavity (Ref. 142348, Layertec) at 0° angle of incidence. Figure given in the chirped mirror pair datasheet available on the Layertec company website.

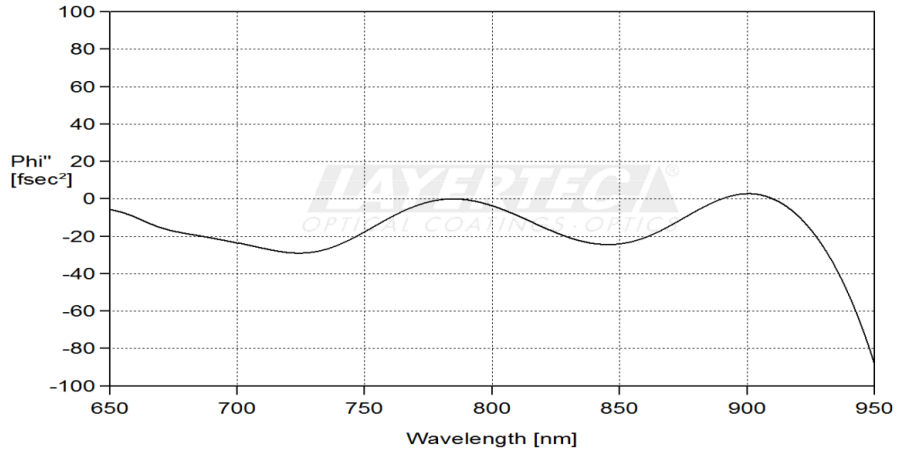


Figure B.8: Calculated GDD of the output coupler employed in our cavity (Ref. 101907, Layertec) at 0° angle of incidence. Figure given in the chirped mirror pair datasheet available on the Layertec company website.

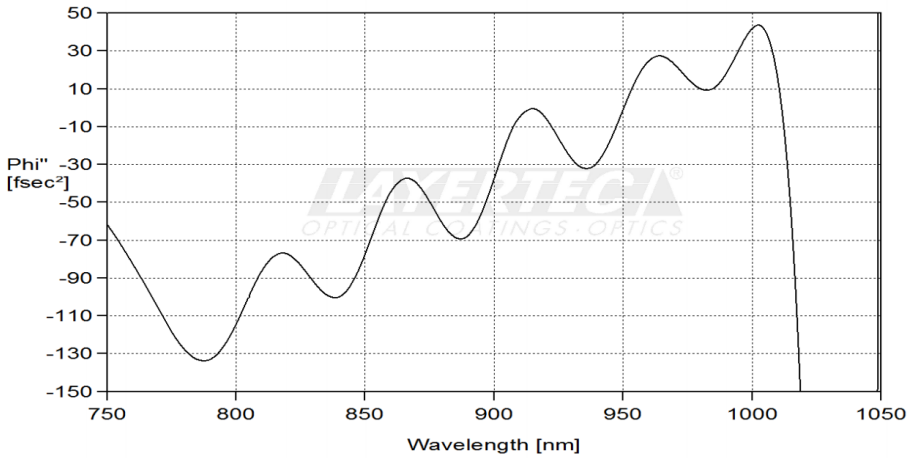


Figure B.9: Calculated GDD of the chirped end-mirror employed in our cavity (Ref. 104219, Layertec) at 0° angle of incidence. Figure given in the chirped mirror pair datasheet available on the Layertec company website.

C

BUFFER GAS COOLING SETUP: SUPPLEMENTARY MATERIALS

This appendix gives more information about the buffer gas cooling setup. Section C.1 describes the management of the vacuum and gas injection of the apparatus. The description of the temperature measurement and control system of the cold cell and the thermal shield is given in section C.2. Finally, the safety aspects of the setup are detailed in section C.3.

C.1 VACUUM AND GAS INJECTION MANAGEMENT - DETAILED

As already mentioned at the beginning of section 4.3, the cold cell and the thermal shields are placed in a vacuum chamber in order to reduce the heat load on the cold cell and to reach the desired helium and target gas densities inside it. Therefore, we need a way to inject both gases inside the cold cell (and thus in the vacuum chamber) in a controllable manner. We also want to be able to re-align the optical cavity without breaking the vacuum. Finally, the setup needs to be safe for the user. A series of valves, gauges, vacuum pumps, etc. are placed on the setup in order to deal with the aforementioned requirements and features. Figure C.1 is a schematic of our setup from the perspective of vacuum and gas injection management. In the remaining of this subsection, we describe the layout of elements displayed in Figure C.1.

Three vacuum pumps allow to generate a vacuum in two distinct parts of the setup: the vacuum chamber and the purge line. The role of the purge line is to remove the gas of some regions of the setup without passing through the vacuum chamber. A rough vacuum is enough for the purge line. It is generated using a rotary vane vacuum pump (Edwards, model 5, 2-stages). To avoid oil back streaming when the pump is turned off, the PL2 valve allows to isolate the pump from the purge line. Pressure inside the purge line is measured using a Pirani vacuum gauge (TTR91 gauge, from Leybold). On the other hand, the use of the cold cell requires a high vacuum in the vacuum chamber,

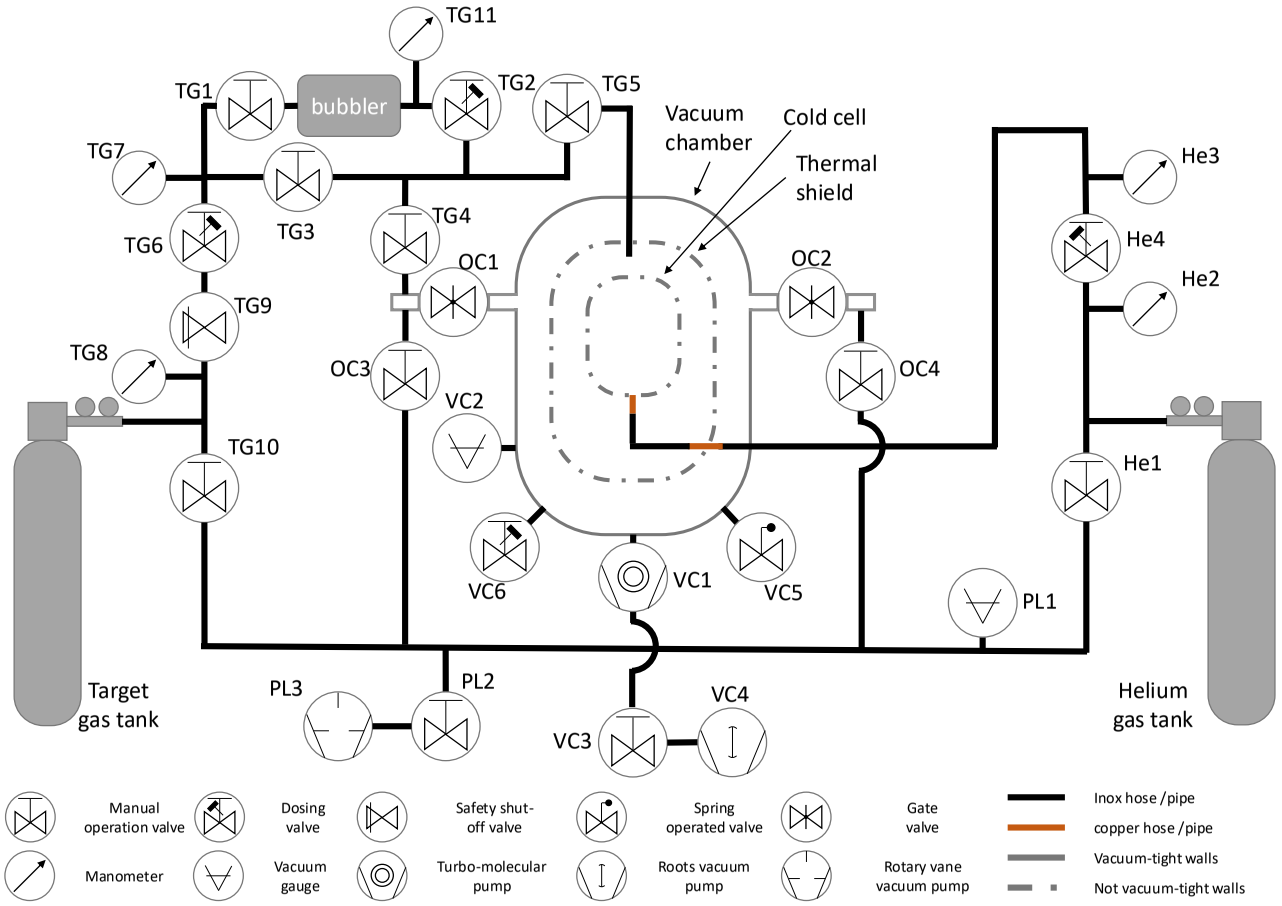


Figure C.1: Layout for the vacuum and gas injection management of the buffer gas cooling setup.

as discussed in section 4.4 where the dimensioning of the pumping capacity is made explicit. It is generated by combining a turbomolecular pump (HiPace 700, from Pfeiffer) and a multi-stage roots pump (ACP40, from Pfeiffer). The foreline pump, *i.e.* the ACP40, can be isolated from the vacuum chamber by means of the valve VC3 shown in Figure C.1. Closing it allows to gently heat up the cold cell by injecting a few mbar of helium in the vacuum chamber. Pressure inside the vacuum chamber is measured using a full range gauge (PTR90 N, from Leybold). Valve VC5 is a pressure relief valve (Ref. 120VUS040 from Pfeiffer). Its role is to prevent any risk of failure due to an overpressure in the vacuum chamber. The outlet of the valve being connecting to the gas exhaust line. Valve VC6 is a manual venting valve (Ref. 120VBE010 from Pfeiffer) allowing to gently break the vacuum when required.

We chose to use dosing valves instead of flow controllers in order to adjust in a repeatable way the throughputs with which helium and the target gas are injected inside the cold cell, and thus their density inside it. Indeed, while mass flow controllers allow for both controllable and repeatable gas flows, we did not find any affordable reference covering the desired range of throughputs for the application (see section 4.4). Furthermore, the knowledge of the true throughput is not necessary, what really matters are the helium and target gas densities in the cold cell. This is why we decided to use dosing valves (Ref 21124-KE0X-0003 from VAT) instead of mass flow controllers. These valves have a digital position display to which we can associate a throughput thanks to a calibration curve (given in the datasheet and shown in Figure C.2 if the pressure drop between the inlet and outlet connections of the valve is equal to 1 bar). We thus placed manometers upstream and downstream the two dosing valves He4 and TG6 (one valve for the helium gas line, the other for the target gas line) to have a reading of the pressure drop across the two valves. They respectively correspond to items TG7 and TG8 and to items He2, He3 for the target gas line and for the helium gas line. They are placed on a panel, along with the bellows-sealed valves He1 et TG5 that allow for purging the two gas lines up to the two dosing valves. Photographs of the front and rear views of the panel are given in Figure C.3.

The setup offers the possibility to study gas molecules stored in a gas tank or molecules initially stored in the liquid phase. The target gas tank of Figure C.1 is replaced by a helium gas tank which is used as a carrier gas for species that are liquid at ambient temperature. Helium

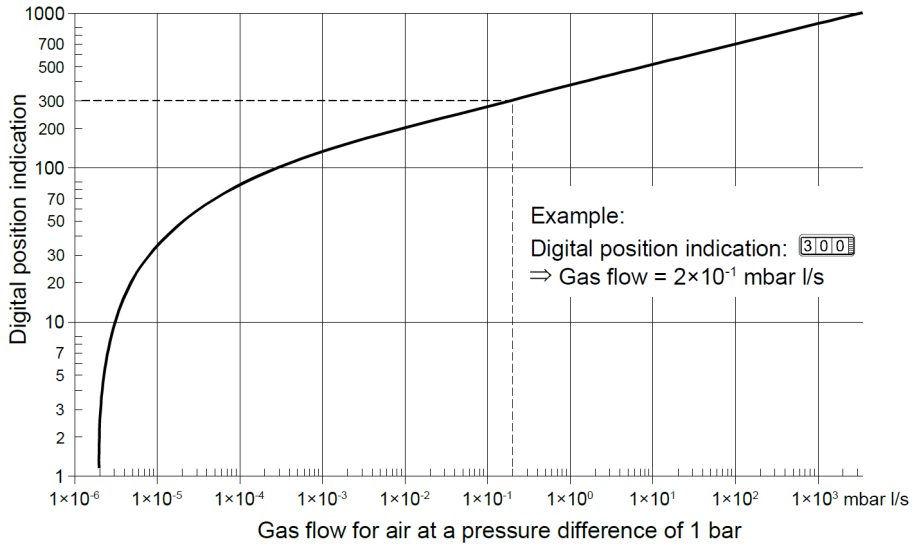


Figure C.2: Gas flow curve of the 21124-KE0X-000 dosing valve of VAT. Curve given in the operating manual of the dosing valve.

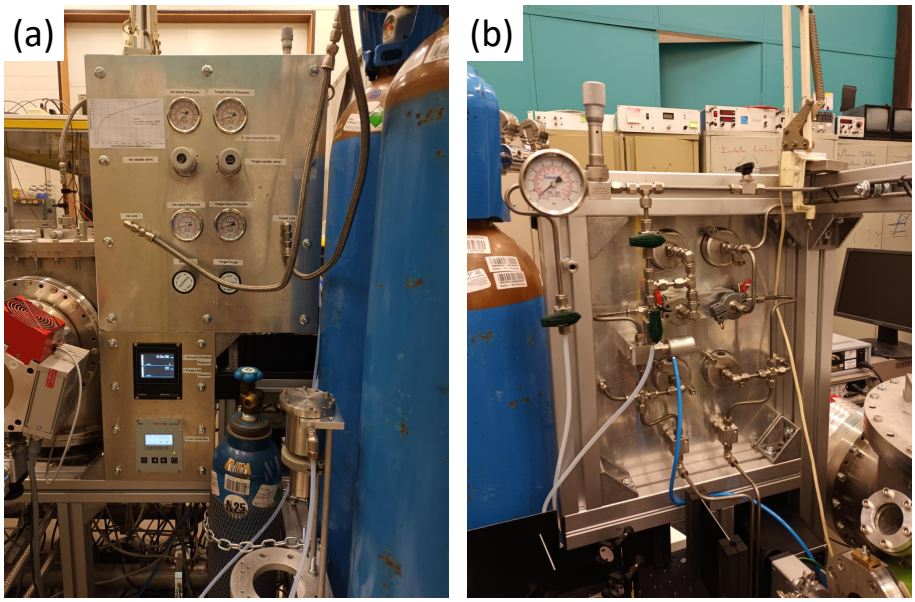


Figure C.3: Photographs of the gas injection panel. (a) Front view. (b) Rear view.

passes through a bubbler to carry out the species of interest with it inside the cold cell. The system of valves TG1, TG2 and TG3 allows to bypass or not the bubbler. The valve TG2 is a needle valve. It serves to maintain a pressure high enough at the surface of the liquid to avoid reaching its boiling point. The manometer TG11 allows to have a reading of the pressure at the surface of the liquid to adjust the opening of valve TG2.

Valves OC1, OC2, OC3 and OC4 permit to change/clean the HRMs of the optical cavity without breaking the vacuum inside the vacuum chamber. The method is detailed in section 4.3.5.

As we can see in Figure C.1, the target gas can be injected inside the vacuum chamber either above the cold cell or in the vicinity of one of the two HRMs constituting the optical cavity depending on the settings of valves TG4 and TG5. Doing the latter allows to easily tune the DFB laser wavelength employed in the CRDS setup (see section 4.5) on a specific molecular transition in order to adjust the target gas and the helium throughputs and to align the pipe position of the target gas line with the cold cell, as discussed below.

Finally, we placed a normally closed pneumatic valve (Ref. SS-BNS6MM-C from Swagelok) just after the target gas inlet (valve TG9 in Figure C.1). This pneumatic valve is connected to the pressurized air service. A solenoid valve interrupts the supply in pressurized air of the pneumatic valve in case of a failure (see section C.3 for further details), the pneumatic valve then stops the target gas injection inside the vacuum chamber.

The techniques employed to inject the target gas and helium inside the cold cell were described in section 4.3.4. They will be not further addressed.

C.2 TEMPERATURE MEASUREMENT AND CONTROL

C.2.1 *Choice of cryogenic temperature sensors*

There are mainly three types of temperature sensors when dealing with cryogenic applications: thermocouples, resistive thermometer devices and thermometer diodes. Thermocouples are devices that rely on the Seebeck effect to measure the temperature. While, their use only requires a voltmeter to perform the measurement and despite their

low cost, they need an in-situ calibration and their sensitivity rapidly decreases at temperatures below 70K, making them bad candidates for measuring the temperature of the cold cell but remain possible candidates for the thermal shield [110, 147]. Resistive thermometer devices rely on the change of the resistance of materials to measure temperature. Some of them are self-calibrated. Furthermore, they are low-dissipation devices, which reduces the heat load on the part of the setup that is probed. However, they require strain-free mountings and the electronics which is necessary to drive them is usually more expensive compared to thermometer diodes. Thermometer diodes rely on the forward voltage drop across a diode traveled by a constant forward current when temperature changes. They follow a standard voltage-temperature curve which is plotted in Figure C.4, making them easy to use. These sensors possess a high sensitivity at temperatures down to a few Kelvin and better resist to thermal shock than their resistive sensor counterparts. They cover the 1.4K-500K range, but suffer from a decrease in sensitivity above 30K. They dissipate a few μW and are subject to the switching phenomenon, but this does not represent a problem at the temperatures we want to reach (10K-20K range). Switching consists in abrupt drops in the voltage that can ultimately lead to erroneous measurements [148]. These sensors will be employed in our setup, and more specifically the DT-670C-CU model from Lake Shore. Measurement is performed following a four-lead measurement scheme. One pair of leads is dedicated to the constant forward current and the second pair of leads to the measurement of the voltage drop. The current excitation source and the ADC for the reading of the voltage drop are generated by circuitry built in-house and which is further detailed in subsection C.2.3.

We placed four cryogenic temperature sensors, two on the cold cell and two on the thermal shield. Placing two sensors on each element, one on the bottom plate and another one on the top plate allows to check for the eventual presence of a thermal gradient. Installation of the diodes was done following recommendations of the manufacturer (see Ref. [149]). The diodes are installed in a bored package allowing to screw them on the cold cell and on the thermal shield. Apiezon N cryogenic grease is utilized to ensure a good thermal anchoring. In order to avoid that heat is conducted through the wires from elements at room temperature, thermal anchoring of the wires is performed on the thermal shield for the two sensors probing its temperature, and on

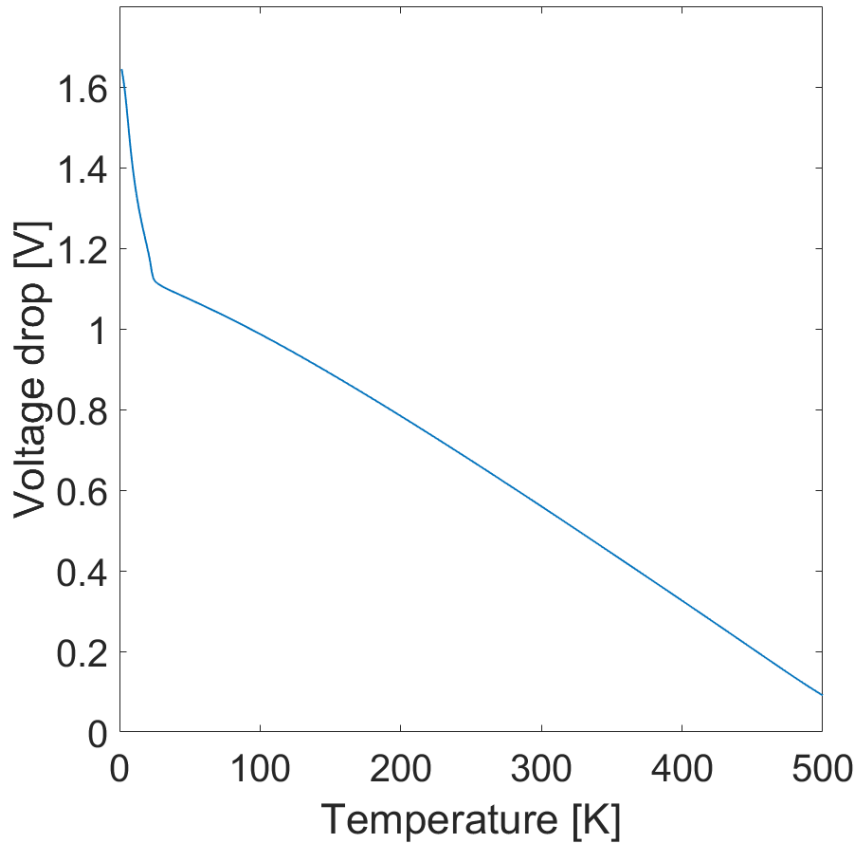


Figure C.4: Standard temperature-voltage curve of the DT670 temperature diode of Lake Shore for a forward current of 10 μA.

the thermal shield and the cold cell for the two other sensors. Thermal anchoring is accomplished by performing several wraps with the leads around a copper bobbin and bonding them to it using cryogenic varnish (GE Varnish from CMR).

C.2.2 *Choice of the heaters*

The use of heaters for the cold cell and the thermal shield is three-folded: (1) the heaters allow to precisely control the temperature of the two stages of the cold head and (2) they permit to safely bring back the setup to room temperature when reactive species have been trapped on the cold cell (see section C.3).

Six cartridge heaters were purchased (model HTR-25-100 from Lake Shore): two for the bottom plate of the thermal shield, two for its lid, one for the bottom plate of the cold cell and one for its lid. They will be inserted in tight holes in the different elements.

C.2.3 *Temperature control*

A temperature controller built in-house by the electronic workshop allows for the temperature measurement and control. It is composed of four 16-bit differential ADCs with an integrated 10 μA current source for the excitation of the temperature sensors, four 24 V power supplies controlled by pulse-width modulation (PWM), four analog outputs with voltages up to 24 V and a LCD screen for display purposes. All these elements are controlled with a microcontroller (Arduino Due). Figure C.5 is a schematic of the temperature control layout. To each temperature sensor is associated an independent power supply allowing for temperature-stabilizing each sub-element if required. The analog outputs can serve to control safety elements such as solenoid valves. Currently, only one analog port is utilized for the safety shutoff valve TG9.

While not implemented yet, controlling the temperature of the cold cell and thermal shield will give us the ability to manage the regeneration sequence of the cold head by heating it up progressively, with eventual temperature plateaus to permit selective desorbing of molecular species trapped on the cold elements. It will ultimately open the field to the study of chemical reactions since we will be able to inject in the cold cell species that would strongly react in the exhaust line in the absence of selective desorption.

C.3 SAFETY ASPECTS OF THE BUFFER GAS COOLING SETUP

When particles, molecules or atoms, collide with a surface, there is a probability that they remain adsorbed on it. This probability increases as the temperature of the surface decreases. This phenomenon is at the heart of cryo-pumping. It consists in cooling down a surface at cryogenic temperatures with the objective to remove particles from the vacuum chamber. Bond strengths are usually weak (Van der Waals forces) and the number of particles that can be stuck to the surface depend on its temperature, the physicochemical properties of the gas

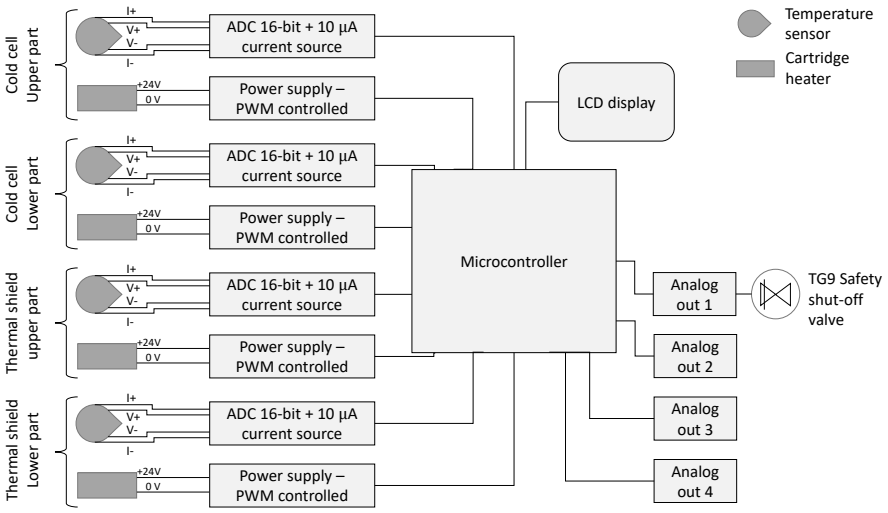


Figure C.5: Schematic of the temperature control layout.

and surface, its roughness, etc. Because the cold cell reaches cryogenic temperatures, it behaves as a cryo-pump for the molecules under study, meaning that large amounts of gas can be fixed on it during a measurement session. It requires to interleave regeneration sessions between measurement sessions in order to definitely extract molecules from the vacuum vessel. These regeneration sessions should be performed at a controlled rate, limited by the pumping capacity of the vacuum system [106]. If the temperature increases too quickly, important amount of gas can be released rapidly, eventually leading to a pressure surge. A pressure relief valve was placed on the vacuum chamber to avoid any detrimental consequence.

A second safety element that we placed in the setup is the normally closed valve TG9 placed just after the target gas tank (see Figure C.1).

Currently, the regeneration process is performed by turning off the compressor and waiting for the setup to gently warm up, allowing for a progressive desorption of the molecules stuck on the cold head. If the warming up has to be done rapidly, we close the valve between the turbomolecular pump and the foreline vacuum pump after having turned off both the turbomolecular pump and the compressor and we inject about 10 mbar of helium in the vacuum vessel. These procedures will not be applied in presence of reactive/explosive species because of safety issues, detailed below.

In the case where an explosive gas is injected in the buffer gas setup in order to perform spectroscopy, special attention should be given to the warming-up stage of the cold cell to avoid that important amount of explosive gas is located in the vacuum chamber or in the exhaust line. Heating up has to be performed progressively and in a controlled manner in order to continuously remove molecules desorbing from the cold surface. An inert gas, *i.e.* nitrogen, should be injected before the foreline vacuum pump to dilute the explosive gas so that it remains below its low explosive limit if the vacuum chamber also contains a significant amount of oxygen. In any case, nitrogen gas should be used after the foreline vacuum pump to dilute the explosive gas. The exhaust line should be made of metal and grounded. Finally, the regeneration process should be performed very often to prevent important accumulation of explosive gas on the cold head [150].

As mentioned in section C.2.3, the use of heater cartridges will allow to study chemical reactions at low temperatures, the risk of chemical reactions in the exhaust line being excluded by selectively desorbing molecules during the warming-up sequence. The heater cartridges permit to control the heat load on the two stages of the cold head while it is turned on, allowing to perform a sequence of temperature ramps and plateaux while warming up the setup.

D

PERSPECTIVES: SUPPLEMENTARY MATERIALS

This appendix concerns the stabilization and characterization of high-finesse optical cavities. An overview of optical cavities and Fabry-Perot interferometers is given in Appendix F. In section D.1, a mathematical framework for the Pound Drever Hall (PDH) stabilization scheme is given. The PDH scheme is used as an error signal generator to lock a laser to a cavity or the other way around. Section D.2 describes the method we developed to characterize the length drift of optical cavities. Finally, we present the optical bench we put in place for the testing of the frequency response of cavity-mirror mounts in section D.3.

D.1 POUND-DREVER-HALL (PDH) STABILIZATION SCHEME: THEORETICAL BACKGROUND

This section relies on Ref. [122, 151, 152].

To get a better insight of the PDH stabilization scheme, the general expression of the signal measured by the fast photodetector of Figure D.1 is derived in section D.1.1. Sections D.1.2 and D.1.3 present the two limiting cases where the frequency modulation is slow and fast respectively when compared to the cavity mode linewidth. The active optical element responsible for the modulation is the electro-optic modulator. It is presented in section D.1.4.

The PDH method is similar to the well-known frequency-modulation spectroscopy technique [153]. Keeping this in mind eases the understanding of this section.

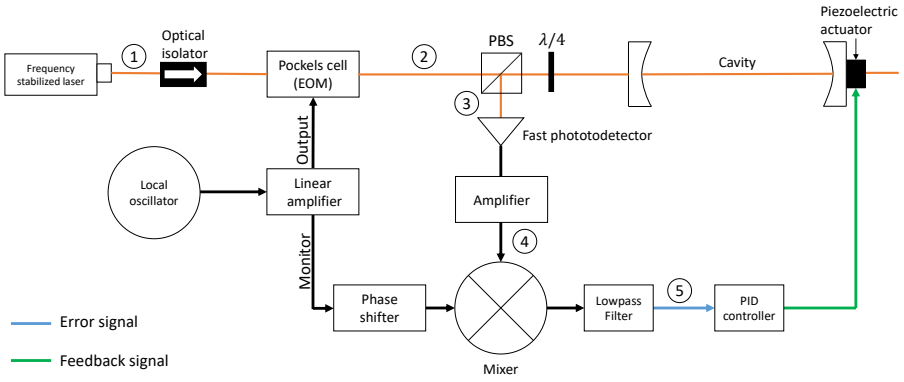


Figure D.1: Exerimental setup of the PDH stabilization scheme.

D.1.1 *General expression at the input of the cavity*

The PDH stabilization scheme uses the light reflected from the cavity to do so. The reflection coefficient F of the cavity with respect to the angular frequency ω is given by:

$$F(\omega) = \frac{E_{\text{ref}}}{E_{\text{inc}}} = \frac{r\left(\exp\left(\mathrm{j}\frac{\omega}{\Delta\nu_{\text{fsr}}}\right) - 1\right)}{1 - r^2\exp\left(\mathrm{j}\frac{\omega}{\Delta\nu_{\text{fsr}}}\right)}. \tag{D.1}$$

with r the reflection coefficient of each mirror and $\Delta\nu_{\text{fsr}}$ the free spectral range (FSR) of the cavity of length L. Figure D.2 depicts the magnitude and the phase of the reflection coefficient of a Fabry-Perot cavity. The reflection beam consists of two terms: a promptly reflective beam and a leakage beam from the cavity. At resonance, these two beams have the same amplitude and are 180 degrees out of phase, resulting in a destructive interference. Near resonance, the phase between the two beams is not exactly 180 degrees and they will not perfectly cancel each other. This phase is antisymmetric with respect to the resonance and gives information about which side of the resonance the laser is. Furthermore, the leakage beam contains information about the phase of the light at a former time. The cavity acts like a phase storage element for optical frequencies. If one is able to measure this phase, then he will know the correction to apply to the cavity to lock it on the laser. In order to do so, light is phase-modulated at a frequency Ω, resulting in sidebands at frequencies $\omega \pm \Omega$, with ω the center frequency of the laser. These sidebands have the same phase as the center frequency. Measuring the beating pattern between the leakage beam

and the sidebands and mixing it to the local oscillator gives rise to a DC and a 2Ω terms. The DC term corresponds to the phase we were looking for. The setup that accomplishes this task is depicted in Figure 5.3. A frequency-stabilized laser is first linearly polarized and then phase-modulated using an electro-optic modulator (EOM) driven by a local oscillator working at a frequency Ω. The beam passes through the optical isolator which consists of a $\lambda/4$ waveplate and a polarizing beamsplitter (PBS). The reflected beam is sent onto a fast photodiode in order to measure the beating pattern. To retrieve the phase, the signal is mixed with the oscillator and lowpass filtered, leading to the antisymmetric error signal. In this section, the electric field at the different positions designated by numbers in Figure D.1 will be made explicit in order to get a good insight of the PDH locking scheme.

At the output of the laser (location 1 in Figure D.1), the electric field at time t is given by

$$E_{\text{inc}} = E_0 \mathrm{e}^{\mathrm{j}\omega t}. \tag{D.2}$$

After passing through the EOM (location 2 in Figure D.1), the electric field has its phase modulated and becomes

$$E_{\text{inc}} = E_0 \mathrm{e}^{\mathrm{j}(\omega t + \beta \sin(\Omega t))}. \tag{D.3}$$

In this expression, β denotes the modulation depth, Ω the phase modulation frequency and ω the carrier frequency, *i.e.* the laser frequency. Supposing that the modulation depth is small, equation (D.3) can be rewritten as follows[1]:

$$\begin{aligned} E_{\text{inc}} &\approx E_0 \mathrm{e}^{\mathrm{j}\omega t} \left[1 + \beta \mathrm{j} \sin(\Omega t)\right] \\ &= E_0 \mathrm{e}^{\mathrm{j}\omega t} \left[1 - \frac{\beta}{2} \mathrm{e}^{-\mathrm{j}\Omega t} + \frac{\beta}{2} \mathrm{e}^{\mathrm{j}\Omega t}\right]. \end{aligned} \tag{D.4}$$

The reflected electric field (location 3 in Figure D.1) is obtained by multiplying each of the different terms by the reflection coefficient at the appropriate frequency. Doing so leads to:

$$E_{\text{ref}} = E_0 \left[F(\omega)\mathrm{e}^{\mathrm{j}\omega t} - \frac{\beta}{2} F(\omega - \Omega)\mathrm{e}^{\mathrm{j}(\omega-\Omega)t} + \frac{\beta}{2} F(\omega + \Omega)\mathrm{e}^{\mathrm{j}(\omega+\Omega)t}\right]. \tag{D.5}$$

1 We used the approximation $\exp(\mathrm{x}) = 1 + x$.

The photodetector measures the power of the reflected beam (location 4 in Figure D.1), *i.e.* $P_{\text{ref}} = |E_{\text{ref}}|^2$, rather than its electric field:

$$\begin{aligned} P_{\text{ref}} &= P_0|F(\omega)|^2 + P_0\left(\frac{\beta}{2}\right)^2\left\{|F(\omega+\Omega)|^2 + |F(\omega-\Omega)|^2\right\} \\ &+ \beta P_0\ \text{Re}\left[F(\omega)F^*(\omega+\Omega) - F^*(\omega)F(\omega-\Omega)\right]\cos(\Omega t) \\ &+ \beta P_0\ \text{Im}\left[F(\omega)F^*(\omega+\Omega) - F^*(\omega)F(\omega-\Omega)\right]\sin(\Omega t) \\ &+ 2\Omega \text{ terms.} \end{aligned} \tag{D.6}$$

The reflected power consists of a constant term and of a beating pattern at two frequencies: (1) the terms in Ω resulting from the beating between the carrier and the two sidebands and (2) the terms in 2Ω resulting from the beating between the sidebands. The terms of interest are the ones in Ω because they are proportional to the phase of the reflected carrier.

In order to isolate the Ω term from the DC term and the 2Ω term, the signal at the output of the photodiode is first mixed with the signal from the local oscillator and then lowpass filtered (location 5 in Figure D.1). The output of the mixer is the product of its inputs:

$$\sin(\Omega t)\sin(\Omega' t) = \frac{1}{2}\left\{\cos\left[(\Omega-\Omega')t)\right] - \cos\left[(\Omega+\Omega')t\right]\right\}. \tag{D.7}$$

where Ω is the frequency of the local oscillator and Ω' is the frequency of the local oscillator. Since $\Omega = \Omega'$, the output of the mixer consists in a DC term and a term at high frequency. The term at high frequency is removed thanks to the lowpass filter. However, if the beating pattern and the local oscillator are 90 degrees out of phase, the signal at the output of the mixer is given by:

$$\sin(\Omega t)\cos(\Omega' t) = \frac{1}{2}\left\{\sin\left[(\Omega-\Omega')t)\right] - \sin\left[(\Omega+\Omega')t\right]\right\}. \tag{D.8}$$

The DC term vanishes because $\sin(0) = 0$, making necessary the use of a phase shifter to adjust the relative phase between the local oscillator and the beating pattern.

D.1.2 *Slow modulation*

In the case where the modulation frequency is small with regard to the FSR, the standing wave in the optical cavity is in equilibrium with the

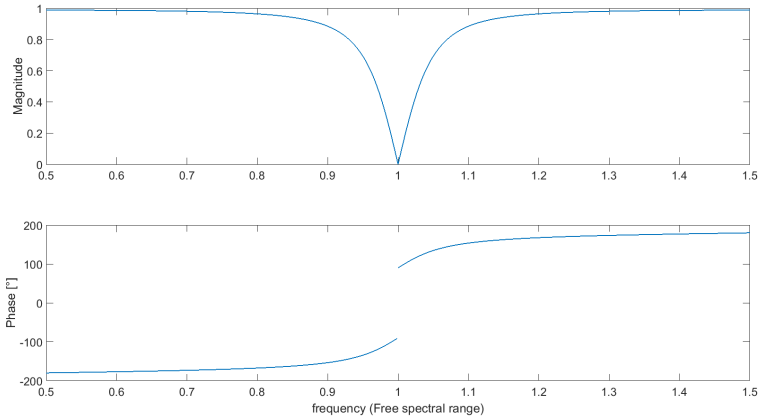


Figure D.2: Magnitude and phase of the reflection coefficient of a Fabry-Perot cavity.

incident beam. In such a case, the reflected power is simply an image of the instantaneous frequency:

$$\omega(t) = \frac{\mathrm{d}}{\mathrm{d}t}(\omega t + \beta \sin(\Omega t)) = \omega + \Omega\beta\cos(\Omega t). \tag{D.9}$$

The reflected power $P_{\mathrm{ref}} = P_0|F(\omega)|^2$ then varies with time as follows:

$$\begin{aligned} P_{\mathrm{ref}}(\omega + \Omega\beta\cos(\Omega t)) &\approx P_{\mathrm{ref}}(\omega) + \frac{\mathrm{d}P_{\mathrm{ref}}}{\mathrm{d}\omega}\Omega\beta\cos(\Omega t) \\ &\approx P_{\mathrm{ref}}(\omega) + P_0\frac{\mathrm{d}|F(\omega)|^2}{\mathrm{d}\omega}\Omega\beta\cos(\Omega t). \end{aligned} \tag{D.10}$$

The previous approximation was obtained by making a Taylor expansion around ω since $\Omega\beta \ll \omega$. The factor $\frac{\mathrm{d}|F(\omega)|^2}{\mathrm{d}\omega}$ can be developed as follows:

$$\begin{aligned} \frac{\mathrm{d}|F(\omega)|^2}{\mathrm{d}\omega}\Omega &= \left[\frac{\mathrm{d}F(\omega)}{\mathrm{d}\omega}F^*(\omega) + F(\omega)\frac{\mathrm{d}F^*(\omega)}{\mathrm{d}\omega}\right]\Omega \\ &= \left[-\left(-\frac{\mathrm{d}F(\omega)}{\mathrm{d}\omega}\Omega F^*(\omega) + F^*(\omega)F(\omega)\right)\right. \\ &\quad \left. + \left(F(\omega)F^*(\omega) + F(\omega)\frac{\mathrm{d}F^*(\omega)}{\mathrm{d}\omega}\Omega\right)\right] \\ &= F(\omega)F^*(\omega+\Omega) - F^*(\omega)F(\omega-\Omega) \\ &= 2\mathrm{Re}\left\{F(\omega)\frac{\mathrm{d}}{\mathrm{d}\omega}F^*(\omega)\right\}\Omega. \end{aligned} \tag{D.11}$$

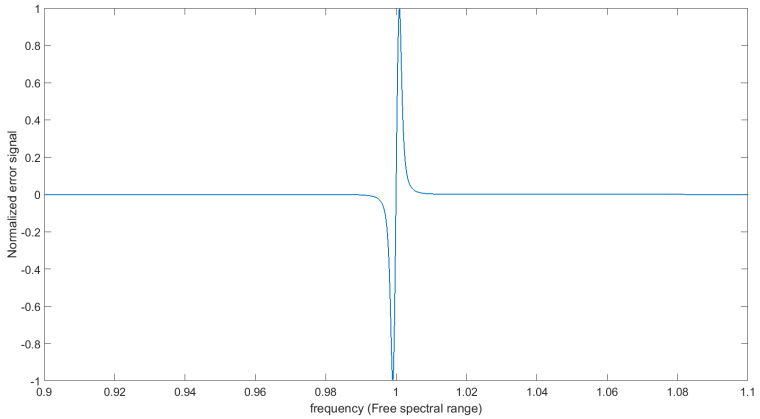


Figure D.3: Error signal for a slow modulation frequency. The modulation frequency is about half a linewidth or about 0.001 of a FSR, with a cavity finesse of 1000. This figure is inspired by Ref. [151].

This expression is purely real. A close look at the third equation of (D.10), the second equation of (D.11) and equation (D.6) gives:

$$P_{\text{ref}} = \text{ constant terms} + P_0 \frac{\mathrm{d}|F(\omega)|^2}{\mathrm{d}\omega} \Omega\beta \cos(\Omega t) + 2\Omega \text{ terms.} \quad \text{(D.12)}$$

All the terms but the one in $\cos(\Omega t)$ will be filtered out after the mixing and lowpass filtering stages. The amplitude of this signal is the error signal we were looking for. A plot of the error signal with respect to the angular frequency ω is given in Figure D.3.

D.1.3 *Fast modulation*

When the carrier is near resonance and the modulation frequency is high enough that the sidebands are not, we can assume that the sidebands are totally reflected: $F(\omega \pm \Omega) \approx -1$, then the expression below:

$$F(\omega)F^*(\omega+\Omega) - F^*(\omega)F(\omega-\Omega) \approx -2\text{Im}\left\{F(\omega)\right\} \quad \text{(D.13)}$$

is purely imaginary. In this regime, the cosine term in equation (D.6) is negligible, and the reflected power becomes:

$$\begin{aligned} P_{\text{ref}} = &\text{ constant terms} \\ &+ P_0\beta\text{Im}\left\{F(\omega)F^*(\omega+\Omega) - F*(\omega)F(\omega-\Omega)\right\}\sin(\Omega t) \quad \text{(D.14)} \\ &+ 2\Omega \text{ terms.} \end{aligned}$$

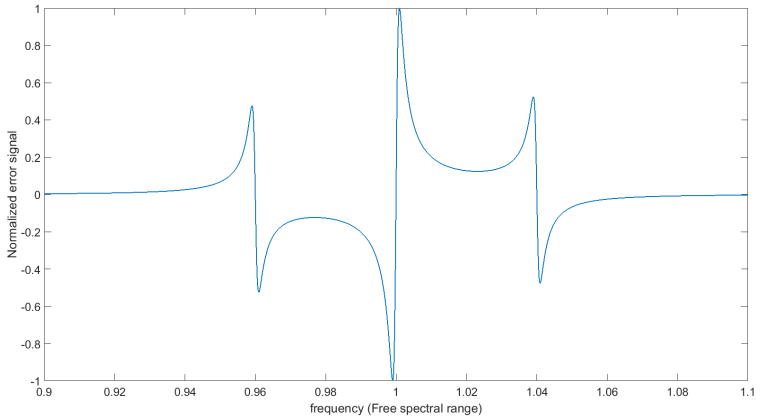


Figure D.4: Error signal for a fast modulation frequency. The modulation frequency is about 20 linewidths or about 0.04 of a FSR, with a cavity finesse of 1000. This figure is inspired by Ref. [151].

The constant terms are equal to $P_0 \left(\frac{\beta}{2}\right)^2$ because $|F(\omega)|^2 \approx 0$ near resonance. After the mixer and the lowpass filter, the only remaining term is the term in $\sin(\Omega t)$, which is the error signal. Figure D.4 shows a plot of this error signal. Advantages of employing the fast modulation are that the sidebands are not transmitted at all by the optical cavity while gaining in sensitivity compared to the slow modulation error signal. Also, when stabilizing the laser to the optical cavity, the error signal is not limited by the optical cavity response time since it is the promptly reflected sidebands which interfere with the leakage beam.

D.1.4 *Electro-optic modulator and the generation of sidebands in practice*

This section relies on Ref. [122].

In order to generate the sidebands necessary for the heterodyne detection, we use an electro-optic modulator (EOM). An EOM is an optical device which can be used for controlling the power, phase or polarization of a laser beam by applying an electrical signal to a transparent material through which light passes. It relies on the property of some crystals to change their refractive index when an external electric field is applied to them, the change being proportional to the field strength. When used as a phase modulator, the EOM consists in a Pockels cell,

where an electric field changes the phase delay of a laser beam traveling in the crystal. This phase delay can be rapidly varied. If the electric field is sinusoidally modulated at frequency $\Omega/(2\pi)$ and if the input field is given by:

$$E_{\text{inc}} = E_0 e^{j\omega t}, \tag{D.15}$$

then, the field at the output of the EOM is given by:

$$E_{\text{inc}} = E_0 e^{j(\omega t + \beta \sin(\Omega t))}. \tag{D.16}$$

with β the modulation depth, Ω the phase modulation frequency and ω the carrier frequency. Equation (D.16) can be rewritten as follows:

$$\begin{aligned} E_{\text{inc}} &\approx E_0 e^{j\omega t} \left[1 + \beta j \sin(\Omega t)\right] \\ &= E_0 e^{j\omega t} \left[1 - \frac{\beta}{2} e^{-j\Omega t} + \frac{\beta}{2} e^{j\Omega t}\right]. \end{aligned} \tag{D.17}$$

There are now three different components in the beam: the main component at frequency ω and two sidebands at frequencies $\omega \pm \Omega$.

Several considerations had to be fulfilled to select the right EOM for our setup. First, the crystal had to be transparent in the spectral range of interest and it should have anti-reflection coatings to minimize insertion losses. Since we were interested in a single modulation frequency $\Omega/(2\pi)$ that had to be high enough to obtain the PDH error signal, we preferred resonant devices over the broadband ones. It has the advantage of reducing the constraints on the voltage's driver unit at the expense of flexibility. Also, the open aperture had to be large enough so as to not truncate the beam. Finally, special care was given to avoid that the damage threshold is reached when injecting the femtosecond laser beam into the EOM.

A proper mechanical mount is also required in order to correctly align the modulator in the various directions and to ensure that the input beam polarization is aligned with one of the optical axes of the crystal, so that the polarization state is not changed.

D.2 LENGTH DRIFT OF THE OPTICAL CAVITY

In order to characterize the length drift associated with the optical cavity, we implemented the optical layout presented in Figure D.5(a). A frequency-stabilized He:Ne laser is coupled to an optical cavity. A triangular ramp voltage is applied on the piezoelectric transducer. The

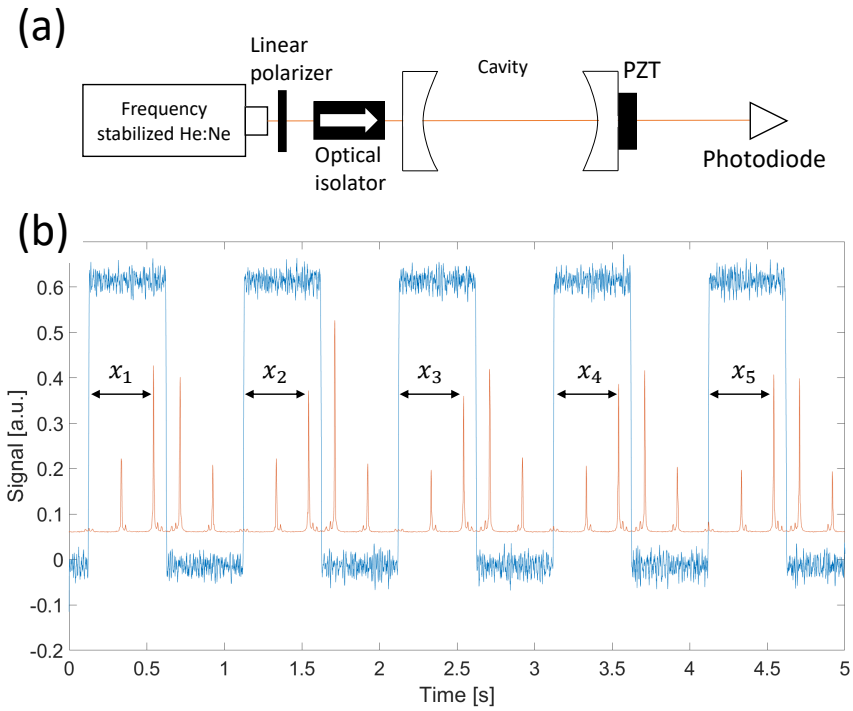


Figure D.5: Procedure for the characterization of the optical cavity length drift. (a) optical layout. (b) recorded pattern. The blue trace is the trigger of the triangular ramp generator, the red trace is the signal at the output of the cavity.

signal at the output of the cavity and the trigger signal associated with the ramp voltage are simultaneously recorded. They are displayed in Figure D.5(b). We determined the difference of indices separating the rising edge of the repetitive square pattern with a same transmission peak, *i.e* x_1, x_2, x_3, etc. We then subtracted the first value, that is x_1 to all subsequent values. The expression of the length drift in terms of distance was obtained thanks to a prior calibration of the piezoelectric transducer displacement to the voltage ramp in a Michelson interferometer (see Figure D.7(a) of section D.3). We associated the deviation from x_1 to the length drift of the cavity. We then plotted the values in Figure D.6. We can see that the length of the cavity varies with respect to time. A drift of about 40 nm is observed on a 200 s time interval. This drift can be mitigated with the use of an invar spacer.

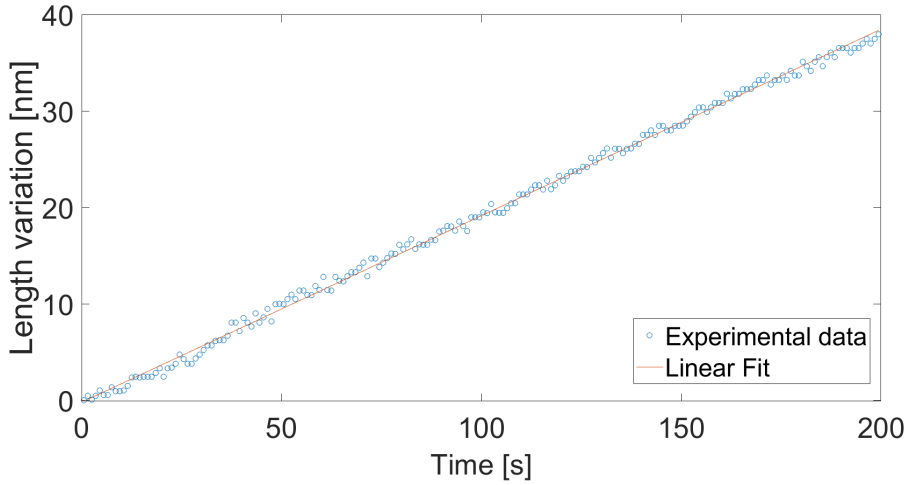


Figure D.6: Length drift of a 150 mm long optical cavity in an unconditioned laboratory. The two mirrors are fastened on the optical bench.

D.3 CHARACTERIZATION OF THE FREQUENCY RESPONSE OF THE OPTICAL MOUNTS

In order to characterize the frequency response of the optical mounts, we implemented the layout presented in Figure D.7(a) which consists in placing the optical mount with a plane mirror mounted in it in the moving arm of a Michelson interferometer. A frequency-stabilized He:Ne laser is injected into the interferometer. A square voltage function is applied on the piezoelectric transducer. It is recorded along with the signal at the output of the interferometer with a photodiode (with the Handyscope HS5 oscilloscope from Tie Pie). A trace is displayed in Figure D.7(b). Retrieval of the displacement associated with the interference pattern requires the prior determination of the signal voltage versus displacement relationship. This is accomplished by applying a voltage ramp to the piezoelectric actuator to record the interference pattern of the He:Ne laser, its wavelength being supposed to be known and equal to 632.8 nm. The signal is then fitted with a sine function. The fitting coefficients are employed to retrieve the displacement from the interference pattern, taking into account the fact that the sine function is not bijective. The calibration procedure is illustrated in Figure D.8.

Applying a step function to a system gives tremendous information concerning its behaviour, as we can see in Figure D.9, where a small

step voltage was applied on the piezoelectric transducer of the cavity vacuum-tight mount. Two curves are displayed, one corresponds to the mirror mount installed in a KM200 mount from Thorlabs, the other one in a Polaris K2T1 mount from Thorlabs. The latter better maintains the cavity mount, reducing the amplitude of the oscillations and damping them. Peaks at 100 Hz and 200 Hz that are visible in the red curve are due to fluctuations in the laser intensity.

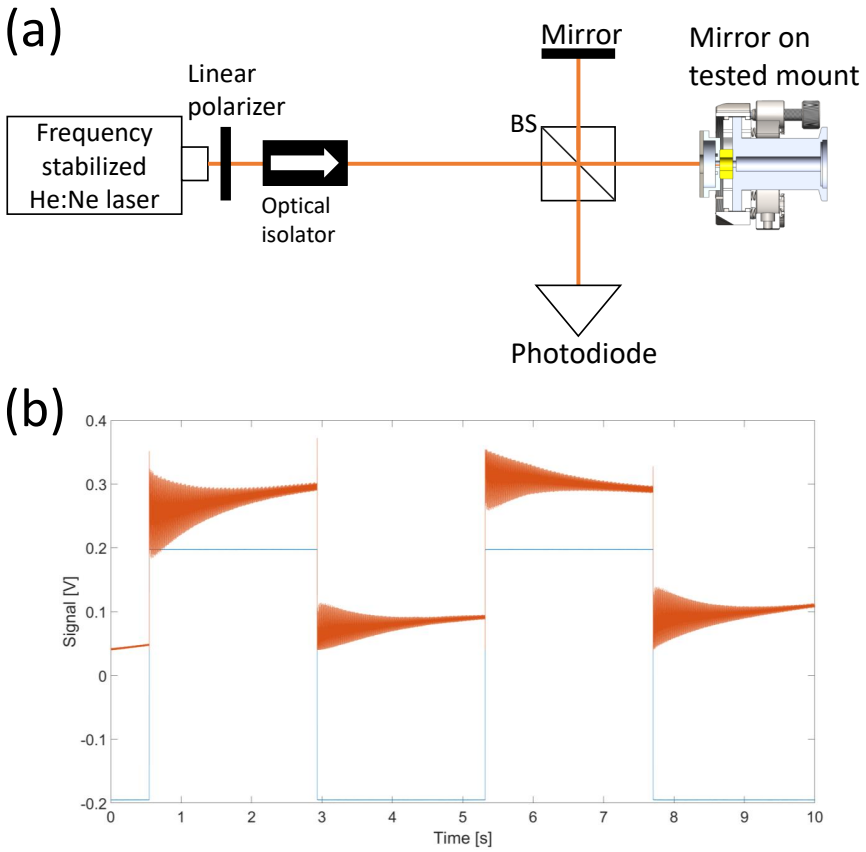


Figure D.7: Layout for the characterization of the mirror mounts. (a) Optical layout. (b) Oscilloscope trace when a square function is applied to the piezoelectric transducer. The red trace is the intensity at the output of the interferometer. The blue trace is the square signal applied to the piezoelectric transducer.

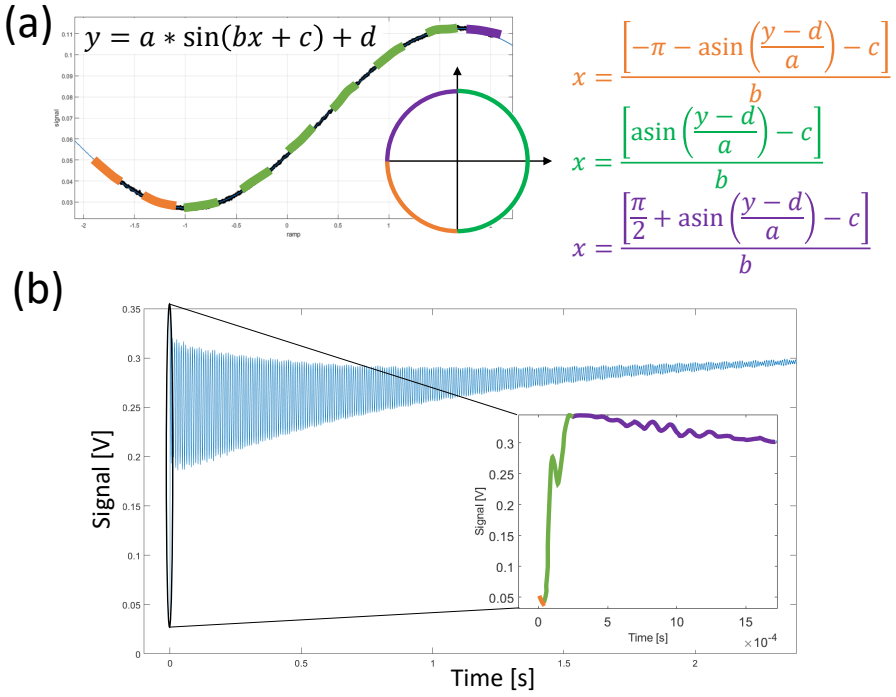


Figure D.8: Calibration procedure for the determination of the displacement from the knowledge of the intensity at the output of the Michelson interferometer. (a) Fit of the He:Ne interference pattern and reversed expressions for the retrieval of the associated displacement. (b) Retrieval of the mount displacement from the intensity at the output of the interferometer.

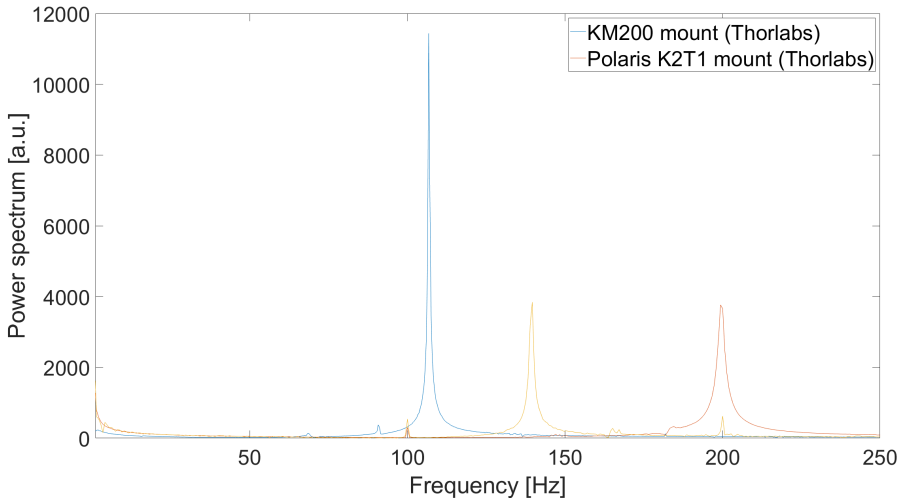


Figure D.9: Transfer functions of the piezo-mount when installed in a KM200 optical mount from Thorlabs or a Polaris K2T1 from Thorlabs.

E

PEAK DETECTION ALGORITHM AND BASELINE DETERMINATION

This appendix presents an algorithm we adapted from Ref. [154, 155]. It is employed to discriminate the molecular fingerprint against the spectrum baseline in order to preserve the molecular transitions while fitting the baseline using the Weighted Penalized Least Squares (WPLS) method or Whittaker algorithm [51, 156, 157]. The ability to properly determine the baseline is of prime importance when we are unable to record sample-free spectra. This situation was encountered for the cavity-enhanced spectrum of H_2O presented in Figure 2.12 of chapter 2 for example.

The appendix is divided in two. In section E.1, we present the part of the algorithm responsible for detecting the molecular transitions, *i.e.* the peaks, in the measured data. The goal is to generate a mask that will hide the peaks when performing the WPLS fit in order to retrieve the spectrum baseline, as detailed in the second part of this appendix, that is section E.2.

E.1 PEAK DETECTION

This section relies on Ref. [154, 155].

Detection of the peaks in the recorded spectrum relies on the continuous wavelet transform (CWT). Basically, the CWT $C(a,b)$ coefficient of a function $f(x)$ is defined as follows:

$$C(a,b) = \int_{-\infty}^{+\infty} f(x)\Psi_{a,b}(x)\mathrm{d}x, \tag{E.1}$$

with

$$\Psi_{a,b} = \frac{1}{\sqrt{a}}\Psi\left(\frac{x-b}{a}\right), \tag{E.2}$$

where $\Psi(x)$ is the mother wavelet, $a \in R^+$ is the wavelet scale and $b \in R$ the shifting value. The wavelet scale corresponds to the number

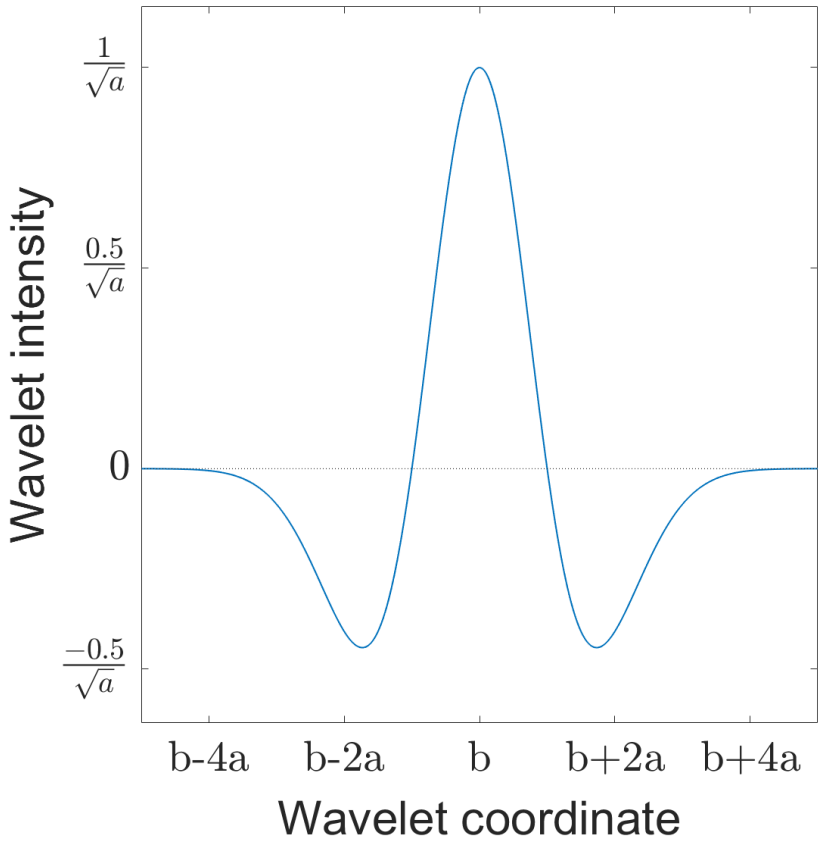


Figure E.1: Mexican hat wavelet.

of data samples over which the wavelet spreads (the larger the scale, the more the wavelet spreads). Intuitively, the CWT $C(a, b)$ reflects the pattern matching between the signal $f(x)$ and the wavelet $\Psi_{a,b}$. The higher the value of C, the better the match.

In order to detect the peaks present in the data, we thus need to choose a wavelet with a shape similar to the one of a peak. The Mexican hat wavelet, also known as the Lorentzian of Gaussian wavelet, fulfills this condition, as one may notice with a glance at Figure E.1. The analytic expression of the Mexican hat mother wavelet is given by:

$$\Psi(x) = \left(\frac{2}{\sqrt{3}}\pi^{-\frac{1}{4}}\right)(1 - x^2)\mathrm{e}^{-\frac{x^2}{2}}. \tag{E.3}$$

The two wings of the Mexican wavelet have a surface equal to the one of the main lobe, but opposite in sign. This allows to directly apply the CWT-based pattern matching to the data, without any pre-processing step. Supposing that the raw data $f(x)$ of equation (E.1) can be decomposed as follows:

$$f(x) = P(x) + B(x) + C, x \in [x_1, x_2], \tag{E.4}$$

where $P(x)$ is the real peak, $[x_1, x_2]$ is the supporting region of the peak, and $B(x) + C$ is the baseline function that is locally approximated as a constant C plus an odd function $B(x)$ defined in the peak support region and with the peak center as the original point. This decomposition is valid as long as the baseline is slowly varying and locally monotonic in the peak support region. Injecting equation (E.4) into equation (E.1) leads to:

$$\begin{aligned} C(a,b) = &\int_{-\infty}^{+\infty} P(x)\Psi_{a,b}(x)\mathrm{d}x \\ &+ \int_{-\infty}^{+\infty} B(x)\Psi_{a,b}(x)\mathrm{d}x + \int_{-\infty}^{+\infty} C\Psi_{a,b}(x)\mathrm{d}x. \end{aligned} \tag{E.5}$$

Because $\Psi_{a,b}(x)$ has a zero mean and $B(x)\Psi_{a,b}(x)$ is an odd function integrated on a symmetric interval, the last two terms are equal to zero. Only the peak contributes to $C(a,b)$. By generating a 2D CWT map, $C(a,b)$, with all the possible shifting values b and a relevant set of scaling values a ranging from 1 to $a_{\max}$, the CWT coefficients at each scale will be maximum around the peak center. Starting from scale $a = 1$, the amplitude of the local maximum corresponding to the peak will gradually increase as a increases. It will reach a maximum for the scale that best matches the peak and it will then gradually decrease for higher values of a, as shown in Figure E.2(a). Du *et al.* [154] suggested to make use of this redundancy in the 2D CWT map to reduce the number of false positives/negatives. If one draws the analogy between the 2D CWT map and an elevation map, the presence of a peak is similar to a mountain ridge (see Figure E.2(b)) in the CWT map, with a preferred direction towards increasing values of a. Detection of peaks in the raw data now consists in detecting ridges in the 2D CWT map. The ridge identification algorithm is fully detailed in Ref. [154, 155]. Once all the ridges have been detected, we disregard the ones which are shorter than a threshold length and we determine the couples of points (a,b) where the remaining ridges take a maximum value. These couples of points are finally used to generate a mask that will allow to

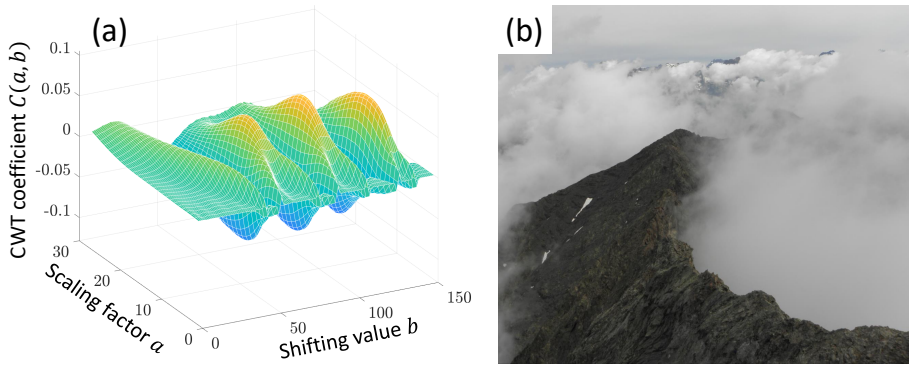


Figure E.2: (a) Generation of the 2D map of CWT coefficients $C(a,b)$. The presence of peaks in the raw data leads to the creation of hills in the 2D CWT map. (b) Analogy with mountain ridges.

preserve the peaks when performing the WPLS fit described in section E.2.

Figure E.3 shows a small part of the buffer gas cooled spectrum of methanol that was presented in section 4.6, along with the associated cwt map and detected ridges. As we can see in this figure, peaks have various heights and may be very congested, compared to signals presented in Ref. [154, 155]. The problem with congested spectra is that the negative wings resulting from the convolution of the Mexican hat function with the most intense peaks of these crowded regions hide the smaller peaks which therefore remain undetected. Furthermore, we apply a global threshold when determining the local maxima building up the ridges, leaving small peaks undetected as well. We troubleshot these two problems by applying the peak detection algorithm several times to the data, detected peaks being removed between two successive function calls.

E.2 WEIGHTED PENALIZED LEAST SQUARES FOR THE BASELINE EVALUATION

Once the peaks have been properly discriminated against the baseline, the latter can be estimated. To do so, the baseline is fitted using the WPLS method which consists in finding the values that best satisfy a balance of two conflicting goals, that is (1) fidelity to the data and (2)

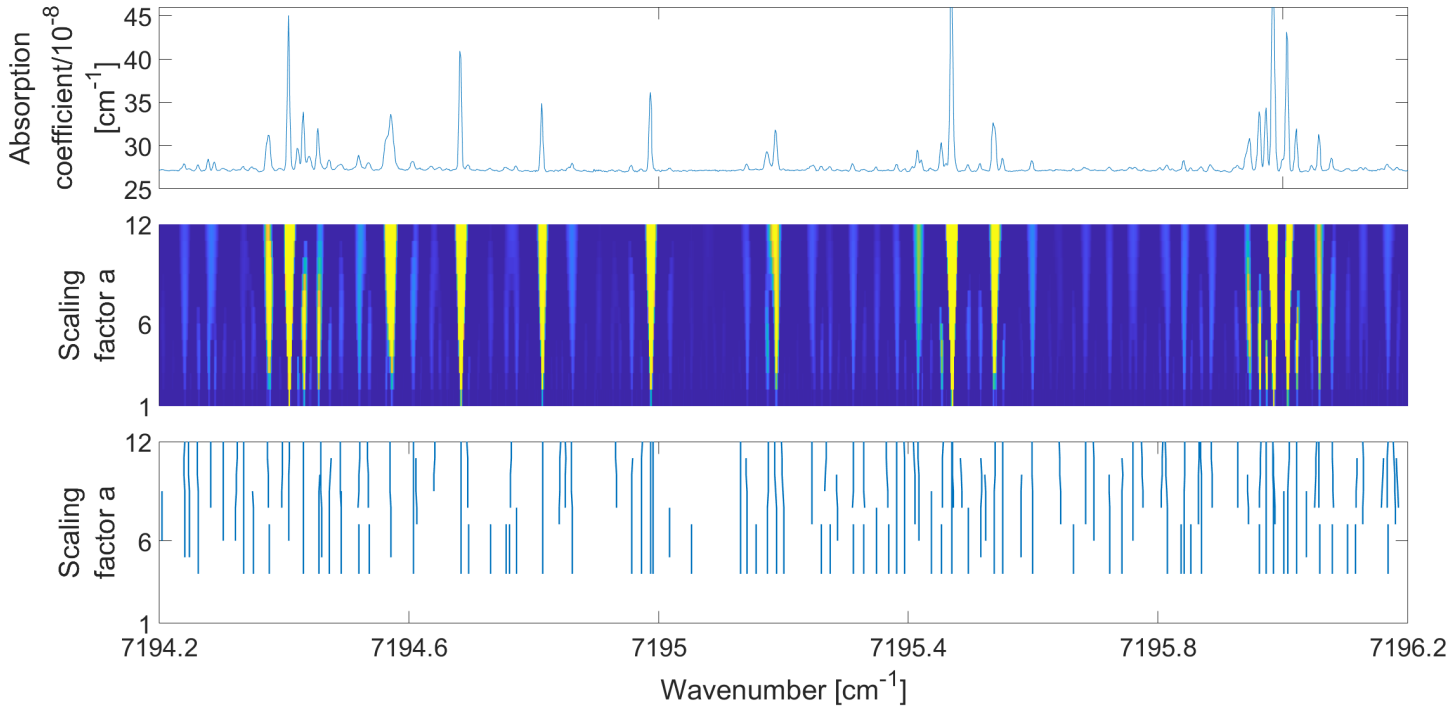


Figure E.3: Illustration of the peak detection algorithm. Upper frame: raw data. Middle frame: generated 2D cwt map. Lower frame: detected ridges after 4 iterations of the peak detection algorithm.

smoothness. This algorithm is well detailed in Ref. [51, 156, 157] and briefly described below.

The fidelity to the data can be expressed as:

$$S = \sum_i (y_i - z_i)^2, \tag{E.6}$$

where z_i is the desired value and y_i is the original raw value. Smoothness can be expressed by the squared differences between neighbors:

$$R = \sum_i (z_i - z_{i-1})^2 = \sum_i (\Delta z_i)^2. \tag{E.7}$$

A balanced combination of the two goals is the sum

$$Q = S + \lambda R, \tag{E.8}$$

where λ is a user-defined parameter. Finding the values z_i consists in solving the linear system

$$z = \left(I + \lambda D^t D\right) / y. \tag{E.9}$$

where D is the derivative of the identity matrix I. The mask M, that was determined using the peak detection algorithm presented in section E.1, is introduced in the fidelity term:

$$S = \sum_i m_i (y_i - z_i)^2. \tag{E.10}$$

The system becomes:

$$(M + \lambda D^t D) z = My. \tag{E.11}$$

If the matrices S and D are sparse matrices, finding the values z_i takes less than a second on up-to-date computers. Once the baseline is obtained, *i.e.* the values of z_i are known, it can be employed, amongst others, to suppress the contribution of the empty cavity to the absorption coefficient in the case of CRDS or it can be employed to estimate the transmittance from a spectrum measured with the FTS.

Figure E.4(a) shows part of the raw methanol spectrum presented in section 4.19, along with the detected baseline. The latter was employed to correct the absorption coefficient in order to remove the contribution of the empty cavity on the absorption coefficient. Figure E.4(b) shows a small portion of the methanol spectrum. The shaded patch indicates

the detected peaks. As one may notice, the pedestal of some peaks in crowded regions are truncated (for example between 7177.5 cm^{-1} and 7178 cm^{-1}) . An improvement to cope with these highly congested spectra is suggested by Bao *et al.* [158]. They iteratively evaluate the baseline to avoid that the computed baseline-free spectrum takes negative values in these crowded regions. This improvement is left as a perspective.

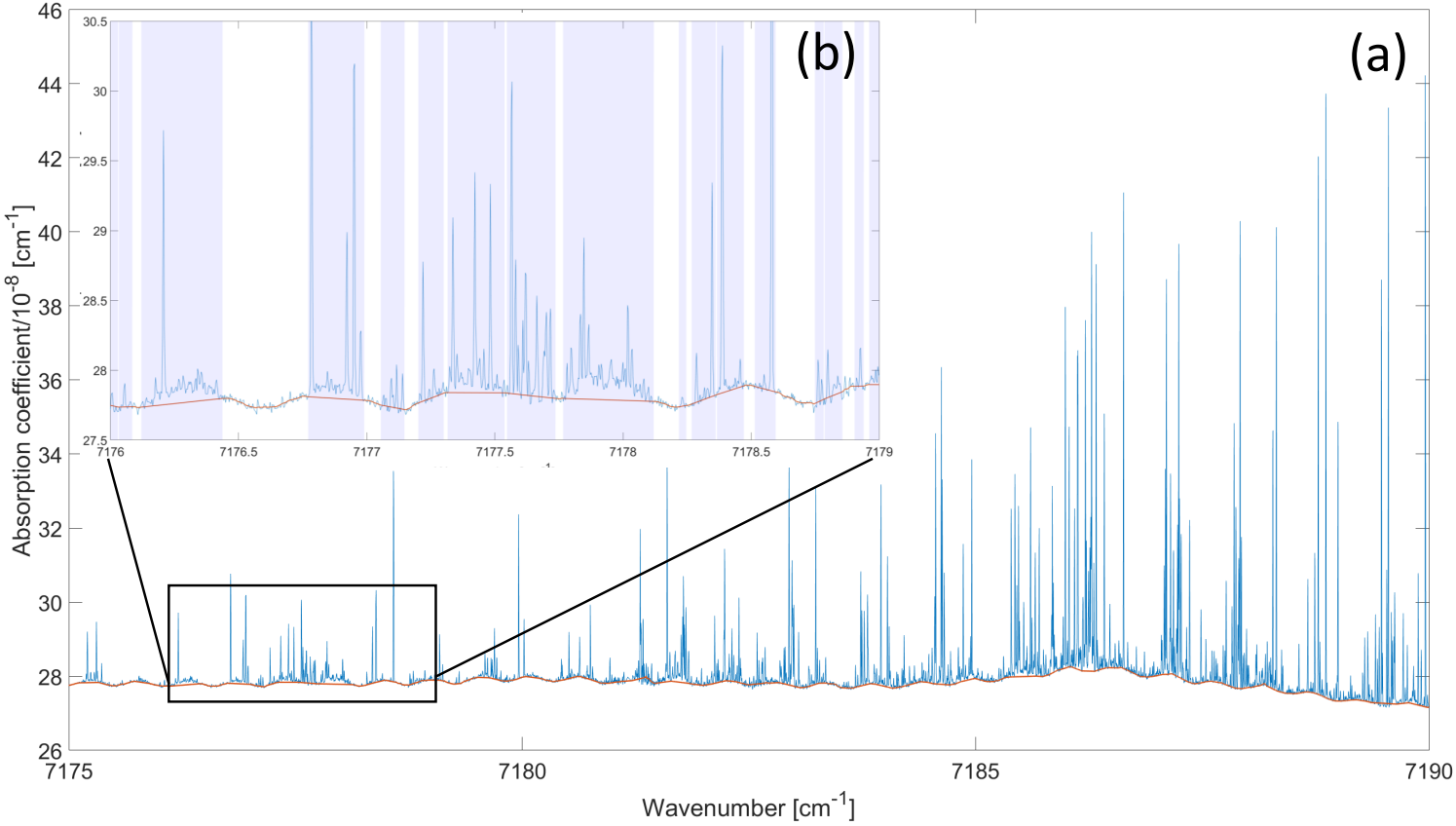


Figure E.4: (a) Portion of the raw spectrum of methanol between 7175 cm^{-1} and 7190 cm^{-1} measured with the buffer gas cooling setup. The red curve is the estimated baseline. (b) Zoom on the region between 7175 cm^{-1} and 7190 cm^{-1}. Shaded area are the regions masked to the WPLS fit.

F

STUDY OF A HIGH-FINESSE CAVITY

This appendix presents the laboratory protocol I implemented for the course of optics and lasers. A video showing the transverse modes scrolling as the cavity length is swept is accessible using the following URL link: `https://www.youtube.com/watch?v=JDjYMttcKqs&ab_channel=AlexisLibert`.

F.1 INTRODUCTION

Optical cavities are fundamental in optics. They are one of the key elements of lasers, but they also serve as reference etalons or as spectrum analyzers. They can also be used to increase the interaction path length between light and a sample during spectroscopic experiments. They are also present in gravitational wave detectors.

During this laboratory, you will study some features of a plano-concave Fabry-Perot optical cavity : (i) light transmission and reflection patterns, (ii) stability conditions and (iii) transverse modes. You will also characterize the finesse F of the cavity.

A Fabry-Perot interferometer, reduced to its simplest terms, consists of two partially reflective surfaces parallel to each other and separated by a distance L_c, the cavity length. Light bounces back and forth between these two surfaces, part of the light being transmitted through the two mirrors at each reflection. The amplitude of the transmitted and reflected electric fields are given by

$$E_t = \frac{T}{1 - R\mathrm{e}^{-\mathrm{i}\varphi}} E_0 \mathrm{e}^{\mathrm{i}\omega t}, \tag{F.1}$$

$$E_r = \frac{\sqrt{R}\left(1 - \mathrm{e}^{-\mathrm{i}\varphi}\right)}{1 - R\mathrm{e}^{-\mathrm{i}\varphi}} E_0 \mathrm{e}^{\mathrm{i}\omega t}, \tag{F.2}$$

where R is the intensity reflection coefficient and T is the intensity transmission coefficient, φ is the phase shift due to one round trip of cavity and $E_0\mathrm{e}^{\mathrm{i}\omega t}$ is the electric field of the incident light.

Multiplying the two previous equations by their conjugate complex yields to the transmitted and reflected intensities which are then given by

$$I_t = I_i \frac{1}{1 + F \sin^2\left(\frac{\varphi}{2}\right)} \tag{F.3}$$

$$I_r = I_i \frac{F \sin^2\left(\frac{\varphi}{2}\right)}{1 + F \sin^2\left(\frac{\varphi}{2}\right)} \tag{F.4}$$

where I_i is the intensity of the light incident on the interferometer. These two functions are plotted in Figure F.1. The optical cavity transmits light for $\varphi = 1$, or alternatively at frequencies $\nu_p = \frac{pc}{2L_c}$, where p is an integer that corresponds to the order of interference and c is the speed of light.

The difference of frequencies between two adjacent modes p and $p+1$ is the so-called free spectral range (FSR):

$$\Delta\nu_{\text{FSR}} = \nu_{p+1} - \nu_p = \frac{c}{2L_c}. \tag{F.5}$$

This parameter, along with the finesse which is defined as the ratio of the FSR to the full width at half maximum of the transmission peaks $\Delta\nu_{\text{FWHM}}$ is a characterization metric of paramount importance for optical cavities. It can be shown that the finesse mainly depends on the reflectivity of the mirrors, as follows:

$$F = \frac{\pi \sqrt[4]{R_1 R_2}}{1 - \sqrt{R_1 R_2}}. \tag{F.6}$$

The previous equation is a generalization of the finesse for cavities with mirrors of different reflectivities R_1 and R_2.

F.2 EXPERIMENTAL SETUP

A schematic of the setup is depicted in Figure F.2. It consists of a frequency-stabilized He:Ne laser, an optical isolator and a plano-concave optical cavity. The beam emitted by the stabilized He:Ne laser first passes through an optical isolator which ensures that no light can go back into the laser cavity. Indeed, this would disturb the correct functioning of the laser. The beam is then directed in the axis of the cavity using the injection optics. A lens allows to ensure mode matching between the laser beam and the optical cavity. This consideration is

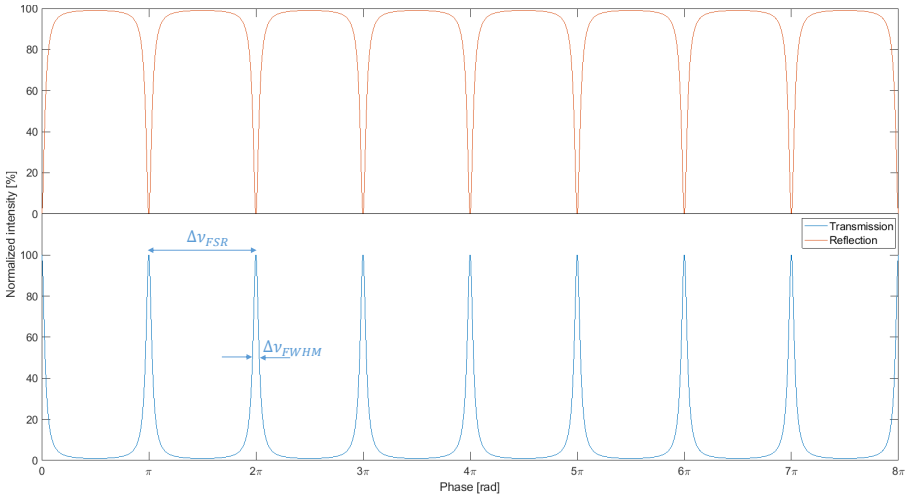


Figure F.1: Normalized reflected and transmitted light intensities by a Fabry-Perot cavity.

discussed in section F.2.1. The combination of a polarizing beamsplitter (PBS) and a correctly oriented $\lambda/4$ waveplate allows to spatially separate the incoming laser beam from the reflected beam issuing from the optical cavity. The optical cavity itself consists of a plane mirror and a concave one. The distance d between the two is constrained because of stability considerations. These considerations are also discussed in section F.2.1.

Transmitted and reflected light beams are both detected using two photodetectors and displayed on the oscilloscope. The photodetectors are placed at the focus of a lens to collect all the light on the active area of the detector. A beamsplitter is placed at the output of the interferometer to deviate part of the beam on a CCD camera in order to analyze the different TEM cavity modes. TEM modes are introduced in section F.2.2.

A piezoelectric crystal is placed on one of the two mirrors to slightly change the length of the optical cavity. The deformation of the piezoelectric crystal is proportional to the voltage applied to its extremities. The length of the cavity is progressively modified by applying a triangular voltage ramp. This ramp signal is displayed as well on the oscilloscope. The scanning of the cavity is discussed in section F.2.3.

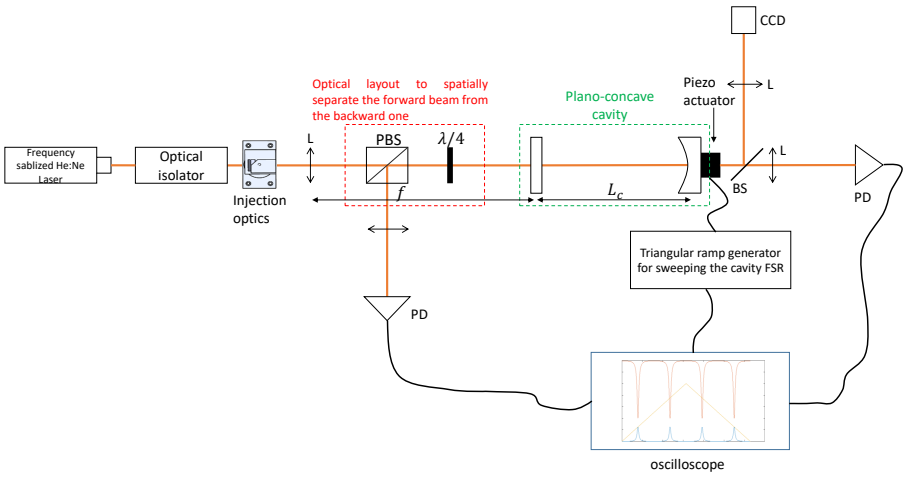


Figure F.2: Schematic of the experimental setup. PD stands for photodetector, PBS for polarizing beamsplitter, BS for beamsplitter, L for lens and CCD for Charge-Coupled Device which corresponds to the camera.

F.2.1 *Conditions of stability and mode matching*

Due to diffraction, light tends to naturally exit the cavity, avoiding to reach the very important number of back and forth reflections of light inside optical cavities with high finesse, as it is the case for the laboratory. To overcome diffraction, concave mirrors are used instead of the plan reflective surfaces of the theoretical Fabry-Perot. Concave mirrors allow to focus and recenter the laser beam during each round trip of the light in the cavity. Moreover, for an optical cavity to be stable, the light beam has to overlap with itself after one round trip between the two mirrors. To do so, the following condition must be satisfied:

$$0 \leq \left(1 - \frac{L_c}{R_a}\right)\left(1 - \frac{L_c}{R_b}\right) \leq 1, \tag{F.7}$$

where R_a and R_b are the radii of curvature of the two mirrors and L_c is the cavity length, *i.e.* the distance between the two mirrors.

- **Given that $R_a = 150$ mm and $R_b = +\infty$ (plane mirror), what is the maximum cavity length ?**
- **Evaluate the free spectral range (FSR) which corresponds to the frequency range between two adjacent modes for a cavity of length $L_c = L_{c,\,\mathbf{max}} - 5$ mm.**

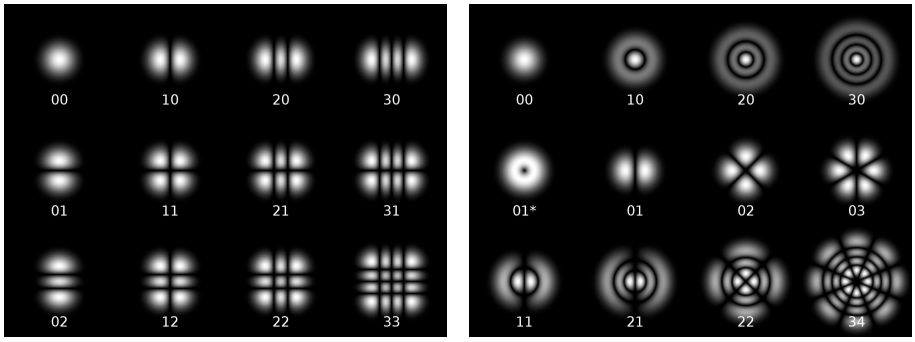


Figure F.3: TEM_{mn} modes labelled with m, n of beams with (left) a planar symmetry (right) a cylindrical symmetry. From Ref. [159].

F.2.2 *Transverse modes*

In addition to the longitudinal modes of the cavity, which correspond to a standing wave along the cavity optical axis, different transverse modes can be sustained as well. They correspond to the cross section of the beam in different regions, as shown in Figure F.3. These transverse modes are the so-called TEM_{mn} modes, for Transverse Electric and Magnetic modes. The m and n modes correspond to the number of nodes in the transverse plan of the cavity. A single TEM_{mn} is associated with a specific longitudinal mode frequency, each of them being separated by the free spectral range, adding evenly spaced peaks on the transmitted and reflected intensities by the cavity.

F.2.3 *Scanning the cavity*

A piezoelectric actuator is a component that changes shape when a difference of voltage is applied to its extremities. A ring piezoelectric actuator is fixed to one of the optical mounts in order to slightly change the cavity length. It allows to sweep the different modes of the cavity on at least a complete free spectral range (FSR). In order to estimate the voltage ramp that has to be applied on the piezoelectric actuator for scanning the whole FSR, you first need to evaluate the displacement that has to be imposed on the piezoelectric actuator by evaluating the following expression:

$$\Delta\nu_p = 1\ \mathrm{FSR} = \left|\frac{\partial\nu_p}{\partial L_c}\right| \Delta L_c. \tag{F.8}$$

The voltage set on the triangular ramp generator is linked to the displacement by the following formula :

$$V_{\text{gen}} = (1.25\text{e}6) * \Delta L_c \tag{F.9}$$

Determine the value V_{gen} to scan three times the FSR (evaluated in section F.2.1).

F.3 EXPERIMENTS AND OBSERVATIONS

Alignment of the cavity

Your first goal is to align the optical cavity. In order to do so, you will perform the following steps:

1. You will first place the back mirror which is the one fixed to the piezoelectric actuator. The reflected beam has to be perfectly overlapped with the incoming beam. To ensure it is the case, you can use a card with a tiny hole to see where goes the reflected beam and to correct its trajectory.
2. You will then place the second mirror. As for the first one, the reflected beam has to be perfectly overlapped.
3. You will sweep the mirror back and forth using the piezoelectric actuator, you should see peaks on the oscilloscope. Try to maximize them in order to fine tune the alignment.

Be careful not to touch anything else on the setup, the rest being already aligned to save some time.

Light transmitted by the cavity

In the first part of this laboratory, you will observe light transmitted by the optical cavity. Does it correspond to the formula you derived during the exercise session and introduced in the introductory part of this document ?

Light reflected by the cavity

You should now display the signal from the light that is reflected back to the laser on the oscilloscope, along with the trace of the transmitted

light. What can you conclude concerning interferometers using energy conservation considerations ?

Measurement of the finesse of the cavity

The finesse is a metric of the quality of a Fabry-Perot interferometer. it is defined as the ratio of the free spectral range to that of the full width at half maximum of the transmission peaks. Using the measurement cursors of the oscilloscope, evaluate the effective finesse of the cavity.

Observation of the different TEM modes

By decreasing the amplitude on the piezoelectric actuator and by modifying the offset, you can scan one peak at a time in order to observe it on the television screen connected to the CCD camera. You should observe some TEM modes.

G

PHOTOMETRY AND IMAGING TO INFER THE NUMBER, THE SIZE AND THE DYNAMICS OF EXHALED DROPLETS.

This work is not related to remaining of the manuscript. It was realized in the framework of the COVID-19 pandemic. It is currently in the peer-reviewing process for the journal "Applied optics". Authors are, in order of appearance, Alexis Libert, Baptiste Fabre, Thomas Corbo, Marc Daman and Clément Lauzin.

G.1 ABSTRACT

A new light scattering measurement method is presented in this work along with the developed setup and the associated data analysis. In addition to the ability to achieve static, dynamic or tracking analysis, this method allows, for the first time, to measure the size of aerosols by absolute photometric measurements. Experimentally, a coherent monochromatic light sheet crosses liquid droplets suspended in air and scattered light is collected by a camera placed at 45°, with respect to the light propagation direction.This geometry provides an improvement of a factor 10 in sensitivity compared to the common perpendicular configuration, while still keeping the filming capability of the camera thanks to specific optics. This increased sensitivity allows to detect more and smaller particles. A procedure to transform a commercial camera into an absolute photometer is presented and this capability is then used in conjunction with predictions from the Mie's theory to infer the equivalent diameter of liquid droplets. This method is first validated and then applied to characterize the dynamics of exhaled droplets by someone yelling. The post-processing evaluation of droplets trajectories permits to retrieve information on transport mechanisms and overcome the bias in the droplet size determination. The size distribution, the trajectories and the lifetime of the generated droplets are determined from our measurements. Those results are put in regards with recent published studies in the framework of the COVID-19 pandemics.

Characterization of aerosols suspended in the gas phase is of prime importance for a series of fundamental[160] and industrial processes[161]. Accordingly, a large series of methods have been developed to estimate the number of aerosol particles, to infer their dynamics and to measure their size. Those techniques are for example, the diffraction glare point[162], the Laser Doppler Anemometry[163], the shadow imagery[164] or the Particle Image Velocimetry[165]. Those techniques present pros and cons in terms of sensitivity, available size range or field of view and the combination of such techniques, combined with careful dedicated analysis, provides complementary information. The large majority of these techniques are based on optics and light-matter interaction properties. In particular, measurements based on the collection of scattered light are usually qualified as static, dynamic or tracking analysis[166]. Such measurements are at the basis of the determination of fine particles concentration using optical particle counters[167, 168]. The experimental method presented in this article combines all these features and use the scattered light as the experimental observable. It associates predictions from Mies's theory, as detailed in section G.3, and absolute photon counting of scattered light to infer the size of liquid droplets. The instrument, presented in section G.4, employs a single-lens reflex camera (imaging ability) with a tilt-and-shift objective to observe the scattered light at angles around 45° with respect to the laser propagation direction in order to increase the signal by a factor of 10 when compared to previous works [169]. The data processing is presented in section G.5. In particular, a procedure to use the camera as an absolute photometer is detailed in section G.5.2. An algorithm, detailed in section G.5.4, was implemented to retrieve the individual particle trajectories from the information on their position in the field of view of consecutive frames. It provides the particle position in the laser sheet thickness in order to avoid any underestimation of the particle sizes which is a common concern in typical particle counters [170]. It also permits to study the decay mechanisms and to determine the lifetime of droplets suspended in air. Finally, the knowledge of the trajectories allows to perform anemometry measurements with our setup. The procedure is validated on millimetric isopropanol droplets for which the size can additionally be retrieved thanks to geometrical optics and white light imaging. This validation process is described in section G.6.1. The instrument was then used to study the size distribu-

tion and decay mechanisms of droplets in suspension in air that were exhaled by someone yelling. These last results are presented in sections G.6.2 and G.6.3. Those results are discussed in regards of the literature and in particular Ref. [171, 172] where the half-life of such droplets was evaluated to be in the range of 10 minutes by tracking light scattering as a function of time. In this manuscript, aerosol, droplets and particles all designate liquid droplets of equivalent diameters ranging from 100 nm to 3 mm .

G.3 APPLICATION OF MIE SCATTERING TO DROPLET SIZE DETERMINATION

In order to get an estimation of the droplet size distribution, it is possible to use the elastic scattering of light whose description relies on the Mie's theory. In this theory, based on the Maxwell's equations, the scattering particles are considered as homogeneous spheres with complex refractive index m. This model is well adapted for particles greater than $\lambda/10$, where λ is the light wavelength. For smaller particles, Mie's theory is no longer valid, and a better description is obtained using Rayleigh's scattering theory. In the present study, all the calculations were performed in the Mie's theory framework since the particle size was in the range of 0.1 to 200 µm and the incident wavelength equal to 532 nm. For these calculations, we used the open source python library `PyMieScatt` [173], in which Mie's equations have recently been incorporated, that allows the computation of the angular scattering intensity functions.

As illustrated in the panel (a) of Figure G.1, the incident light polarization is vertical, following the x axis, while the scattering light is collected in the yOz horizontal plane. We will thus restrict the calculation, using the `PyMieScatt` Python library [173] to the perpendicular intensity $|S_1|^2$ (see panel (b) in Figure G.1). Furthermore, due to the vertical polarization configuration, scattered light is maximum in the (scattering) plane perpendicular to the polarization axis, following a $\sin^2(\varphi)$ shape emission diagram. The number of scattered photons that one should be detecting can be evaluated in an absolute manner when one has information concerning the polarization, the wavelength, the laser power, the solid angle probed and the time of exposition. In these conditions, the number N of photons scattered in the detection cone

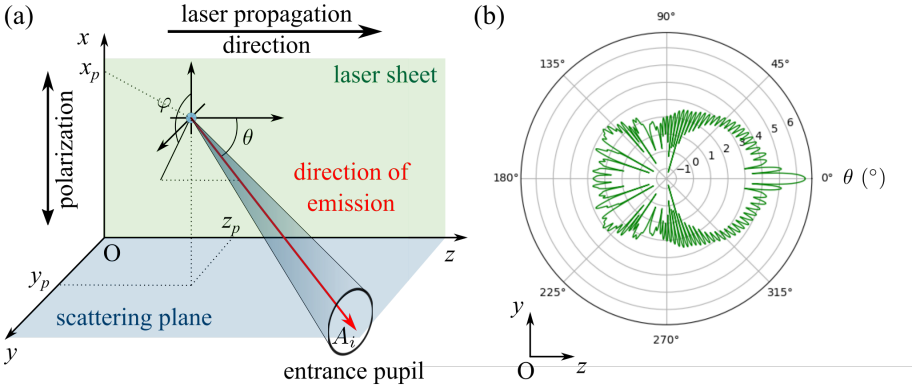


Figure G.1: (a) Geometry of the scattering process from the emission to the detection through the entrance pupil. Polarization of the laser field is along the x axis and the scattering particle is located at position (x_p, y_p, z_p). (b) Angular scattering intensity function ($|S_1|^2$) in log-scale computed with the `PyMieScatt` Python library (Ref. [173]) for a particle diameter equal to 10 µm, vertical polarization and wavelength $\lambda = 532$ nm. Laser propagation direction corresponds to $\theta = 0°$.

whose base is defined by the surface A_i of the entrance pupil is given by:

$$N = N_{inc} \frac{\iint_{A_i} |S_1|^2 \sin^2 \varphi \, d\Omega}{\int_0^{\pi} \int_0^{2\pi} |S_1|^2 \sin^2 \varphi \, d\Omega} \tag{G.1}$$

where N_{inc} is the number of incident photons defined as:

$$N_{inc} = \frac{P\tau\lambda}{hcS} \pi \left(\frac{d_{sphere}}{2} \right)^2 \tag{G.2}$$

with P the laser power, τ the exposition time, S the section of the light sheet in the xOy plane (see Figure G.1) and d_{sphere} the diameter of the considered particle assumed to be spherical.

Considering the particle position in the light sheet (corresponding to angles θ distributed around the 45° orientation with respect to the laser propagation direction) and the specific experimental features described in the next sections, we can generate predictions on the number of

scattered photons for a particle considered as a homogeneous sphere of diameter d_{sphere}, as presented in Figure G.2 in the case of isopropanol droplets. It has to be noted that the number of collected photons strongly depends on the position of the particle in the light sheet, not only through the angular dependence of $|S_1|^2$ but also because of change in the detection cone. A particular attention has then been paid in the integration on the 45°-tilted entrance pupil surface. This integration has been done numerically using the `dblquad` function from python `scipy.integrate` library [174]. By considering only the Mie scattering, we neglected any inelastic scattering and/or any absorption. This is a reasonable approximation considering the relative weights of the different processes when one is working in the visible with a quasi-monochromatic source (1 MHz linewidth). Another solution, based on a geometrical treatment of the scattering process could have been performed to speed up the computation time at the cost of a loss of accuracy, as described in Ref. [175].

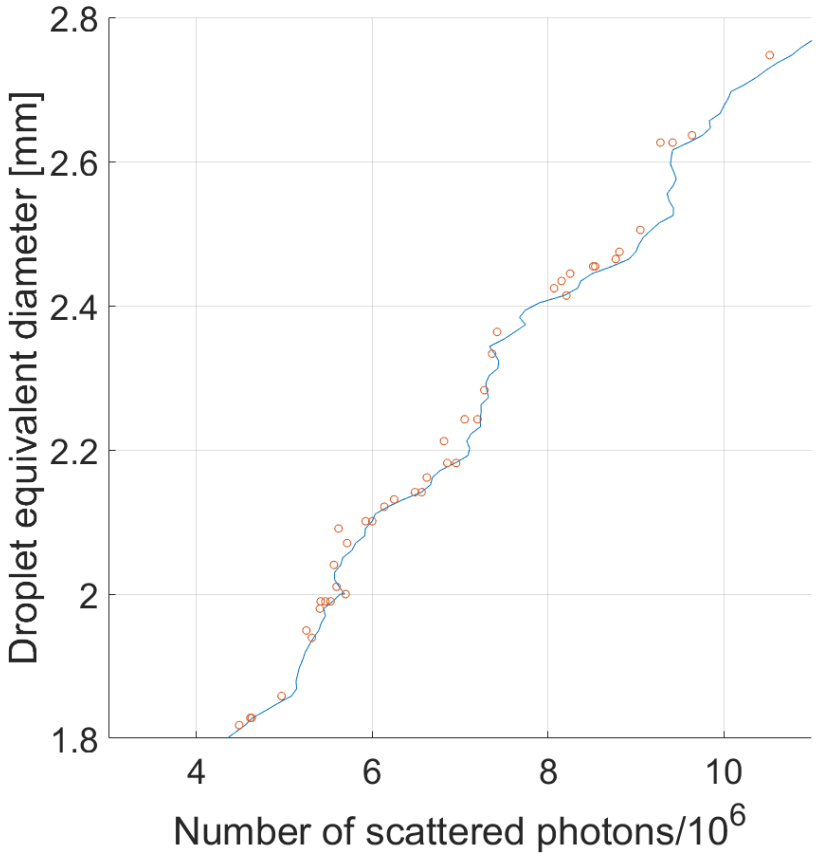


Figure G.2: Scattering particle equivalent diameter with respect to the number of scattered photons for isopronanol droplets ($n = 1.3851$) and a laser power of 0.25 mW. The blue curve corresponds to the calculated number of scattered photons for a given droplet equivalent diameter at the middle height of the light sheet. Red bullets are experimental measurements for isopropanol droplets located at 7.75 cm from the box entry (z coordinate) and taking into account their height (x coordinate) in the light sheet, as described later in the text.

G.4 DESCRIPTION OF THE EXPERIMENTAL SETUP AND PROCEDURE

The experimental setup is presented in Figure G.3. It consists of a Verdi V-10 laser, from Coherent ©, emitting at 532 nm with an adjustable power up to 10 W, a pair of plane mirrors for aligning the laser beam, two cylindrical lenses that permit to expand the laser beam in the vertical plane in order to obtain a light sheet of about 3×90 mm^2, a Nikon D800 camera equipped with a tilt-and-shift objective (Nikkor 45 mm, f/2.8D PC-E) and a $300 \times 300 \times 300$ mm^3 box made of black-anodized aluminum and associated with a mechanically assisted air exhaust. A 45×90 mm^2 hole in the front plane of the box allowed for the candidate to speak in the direction perpendicular to the light sheet that passes through the box via a pair of 8×100 mm^2 vertical slits on each side. A hole at the top of the box allows to easily clean the inside and to place a calibration card to adjust the camera.

A hygrometer and a thermometer were used to record both the relative humidity and the ambient temperature during a measurement. The complete setup was placed on an optical bench installed under an HEPA filtering unit. Even with the filtering fan unit and after several cleaning of the laboratory, some dust still remained in suspension and a third (portable) HEPA system was placed on the optical bench (Dyson Pure Cool Me) to decrease further the amount of dust suspended in air. A measurement consists in filming the scene and detecting as a function of time and position the light scattered by any particle passing through the light sheet.

As already discussed, the amount of light scattered by droplets in air increases as the scattering angle, with respect to the forward light propagation direction, decreases. In Mie scattering measurements of exhaled droplets, the camera is generally placed perpendicularly with respect to the light sheet. Such a relative orientation is chosen since common camera objectives allow to focus in a plane parallel to the sensor, so that no region of the light sheet is blurry. We overcome this limitation by using a tilt-and-shift objective that relies on the Scheimpflug principle to focus in a plane that is not parallel to the camera sensor. This objective allowed us to observe the scattering of light by particles at angles around 45 degrees with respect to the light propagation direction, increasing the sensitivity of measurements by a factor of about 10 compared to a 90° configuration. Figure G.4 illustrates the Scheimpflug principle. A ruler is oriented at an angle of

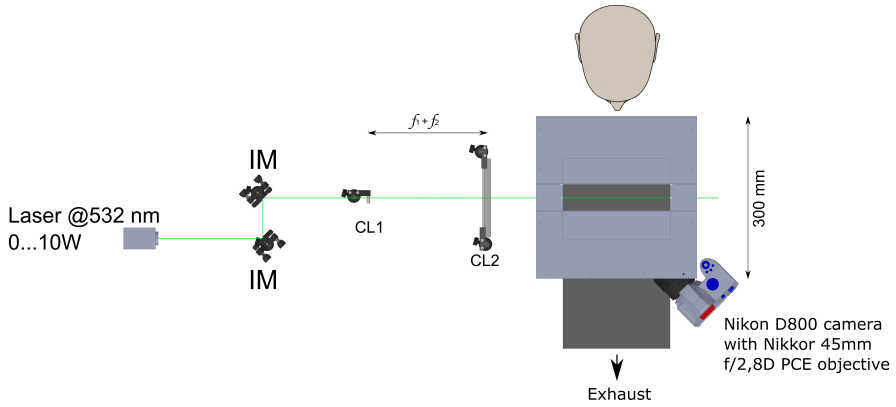


Figure G.3: Experimental setup. IM stands for injection mirror and CL for cylindrical lens. CL1 has a focal length f_1 of 10 mm. CL2 has a focal length f_2 of 200 mm.

45 degrees with respect to the camera sensor, the tilt-and-shift objective is adjusted so that the plane of focus of the camera matches with the plane of the ruler, resulting in a sharp image of the whole ruler. This effect works even when taking pictures with a small f-number (large clear aperture), resulting in pictures with a small depth of field but that allow to gather more light. The picture of Figure G.4 was taken with a f-number of 3.5, so that we were rapidly out-of-focus in the foreground and background parts of the photograph but the ruler is not blurred. Another advantage of filming at 45 degrees is that the hole for the speaker is not centred on the field of view of the camera, avoiding to trigger on false events when analyzing the data. Furthermore, the objective being manual, we do not need to place an object such as a needle in the beam for the autofocus to work properly, as it is the case in Ref. [171]. However, the main drawback is that images are distorted and different pixels will not cover the same area of the observation scene. This is illustrated in Figure G.4(b) by the fact that graduations on the ruler are not equidistant. Positioning and focus adjustment of the camera were performed using a graph paper stuck on a metallic plate. This latter is placed in the plane of the laser light sheet thanks to grooves on the top of the box. The focus is adjusted so that the graph paper appears sharp on the camera. The clear aperture is set

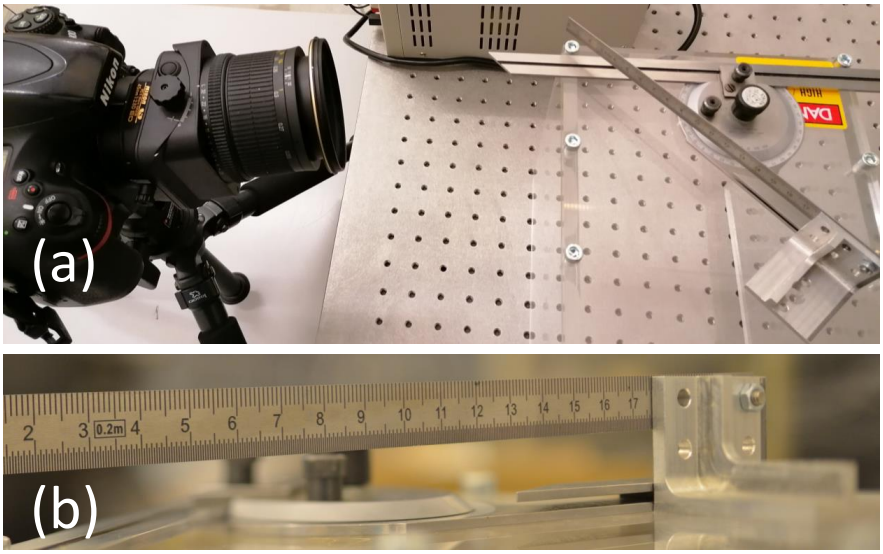


Figure G.4: (a) Illustration of the tilt-and-shift photography and the Scheimpflug principle. A ruler is placed in a plane at 45 degrees with respect to the sensor and the objective is adjusted to properly focus on the ruler (b) Resulting photograph. The edges of the picture were truncated. Exposure time: 1/60 s, f-number: f/3.5, sensitivity: 2000 ISO.

to f/5.6, which represents a good compromise between the amount of light gathered and the sensitivity to camera misalignment.

G.5 DATA ANALYSIS

G.5.1 *Principles and general overview*

The data-processing pipeline applied to each image in order to determine the number of particles, their location and size are schematized in Figure G.5.

First, the green component from each Red, Green and Red (RGB) frame of the film is extracted. The goal of the background suppression is to remove stray light due to optics and mechanical elements that diffuse/reflect light by subtracting a mean frame obtained by co-adding all the frames pixel by pixel and dividing the obtained frame by the total number of frames participating to the sum. The third stage of the data-processing pipeline is the retrieval of the energy map from the pixel values, that will be further detailed in the next subsection.

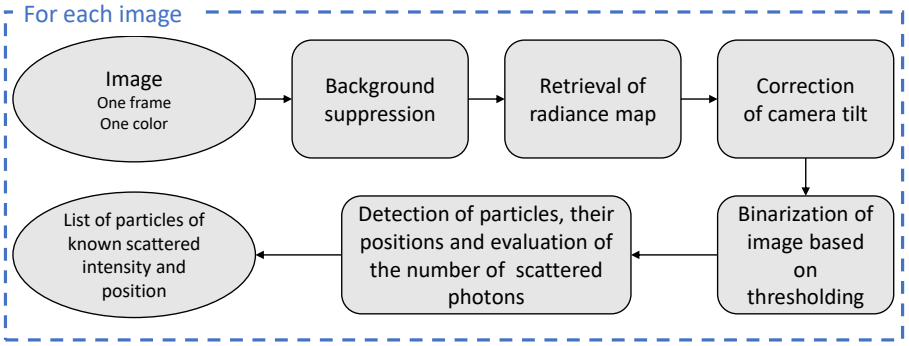


Figure G.5: Data processing pipeline applied to each image of the video.

In the following stage of the process, the resampling of the image on a uniform spatial grid is performed. The image is then binarized using a global threshold value, all values above the threshold are set to 1, and considered as particles, all values below the threshold are set to zero and belong to the background. If adjacent pixels have a 1 value, they are grouped together to form a single particle using the Matlab function `bwconncomp`. This function also returns the indices of the concerned pixels. Thanks to a prior absolute calibration of the sensor, it is possible to ultimately determine the total energy scattered by the different particles, and therefore to infer their size using the simulation based on Mie's theory. Figure G.6 shows an image of the laser sheet taken 30 seconds after someone yelled during 30 seconds in front of the box, along with the same image obtained by applying all data processing stages up to the binarization process.

Determination of the threshold value represents a trade-off between sensitivity to small particles and the background noise level. We observed that for too-small threshold values, a constant baseline was present in measurements while the signal of interest remained nearly unchanged. We iteratively increased the value of the threshold until a baseline-free measurement was obtained while preserving the signal of interest. We associated this baseline, as a function of its magnitude, to either small particles that were not removed by the different HEPA filters units or to sensor noise. The threshold value we obtained imposes a size sensitivity limit of 100 nm of equivalent diameter.

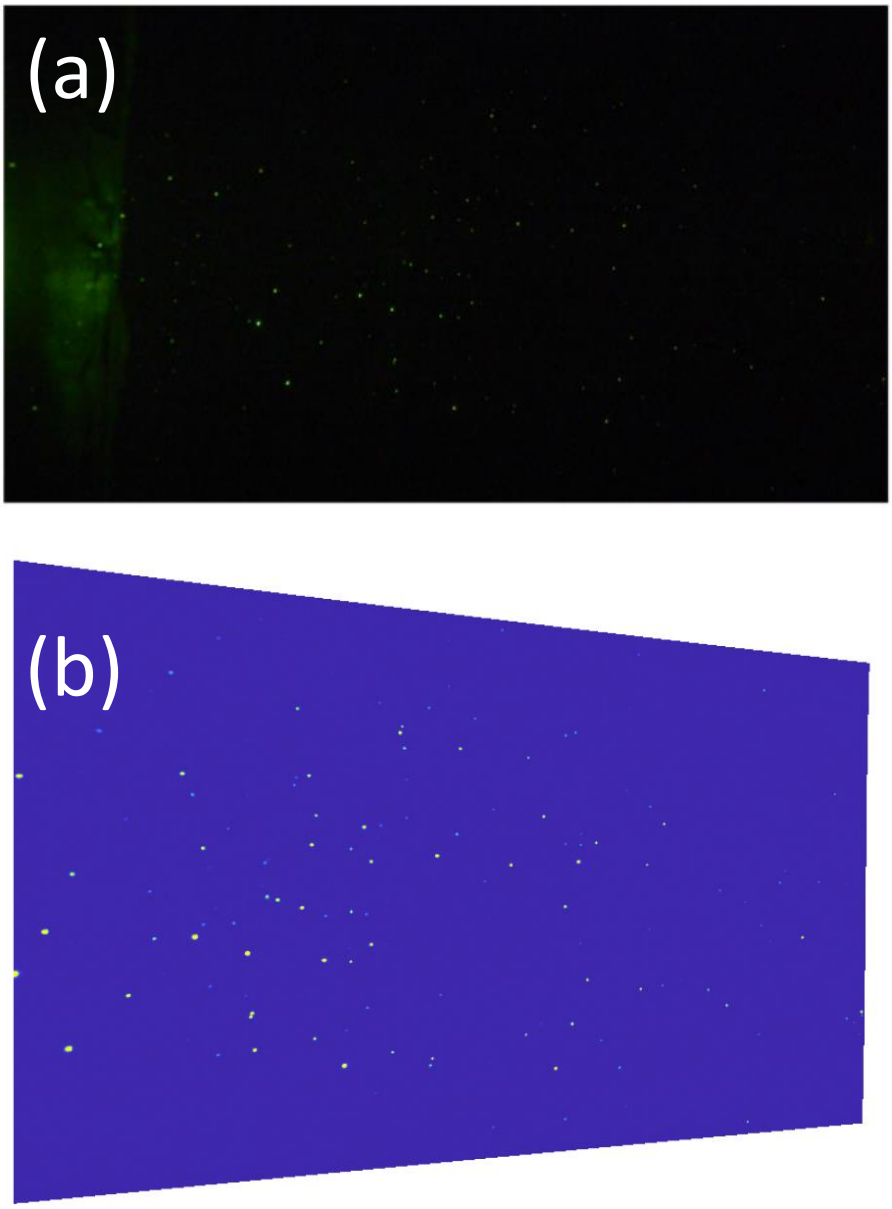


Figure G.6: Image of the laser sheet, 30 seconds after someone yelled the word "particle" during 30 seconds in front of the box hole. (a) Original image. (b) Image just before the binarization process of the data processing pipeline. Experimental parameters: Verdi laser at 4 W, exposure time: 1/400 s, f-number: f/5.6, sensitivity: 2500 ISO.

G.5.2 *Energy map retrieval*

The encoding function between the energy deposited on each pixel and the resulting integer digital value is a nonlinear function. The mapping function is specific to the camera and it is *a priori* unknown. We used the algorithm developed by Debevec *et al.* [176] which is usually employed by photographers to combine photographs taken with different exposure times in order to perform high dynamic range (HDR) photography. The idea relies on the fact that to a given light exposure X (*i.e.* energy) reaching the pixel i is associated a single digital value Z_{ij} given by:

$$Z_{ij} = f(X) = f(R_i \Delta t_j) \tag{G.3}$$

where R_i is the scene radiance illuminating a surface associated with a pixel i and Δt_j the exposure time, with $X = R_i \Delta t_j$. (G.3) can be rewritten as follows:

$$\ln f^{-1}\left(Z_{ij}\right) = g\left(Z_{ij}\right) = \ln R_i + \ln \Delta t_j, \tag{G.4}$$

where $g = \ln f^{-1}$. The function g is supposed to be monotonic and smooth. This function, once determined, allows to retrieve the relative energy map or, equivalently, the relative radiance map from the pixel value Z. Supposing that the scene radiance remains unchanged during the observation time, it is possible to determine the g function and the radiance R_i by taking several pictures of the same scene at several exposure times. By selecting a series of pixels on these photographs, we obtain a set of linear equations that can be solved in a least-squared error sense [176]. We can therefore determine both the unknown radiance values R_i and the g function. In the case of RGB pictures, three g functions are determined, one per color channel. The used algorithm is fully described in Ref. [176] and it is implemented in a built-in Matlab function named `camresponse`. Figure G.7 shows the series of photographs employed for the determination of the g function. They were taken in an outdoor environment within a 2-minute interval to guarantee an almost constant scene radiance. One g function was measured for each sensor sensitivity (ISO value) employed in this work. Figure G.8 shows the g curve of the Nikon D800 obtained with the photographs of Figure G.7. This curve is used to substitute the digital values Z of each image by the corresponding amount of energy $\exp(g(Z))$. A gridded interpolation is performed using the Matlab function `griddedInterpolant` in order to obtain the relative energy

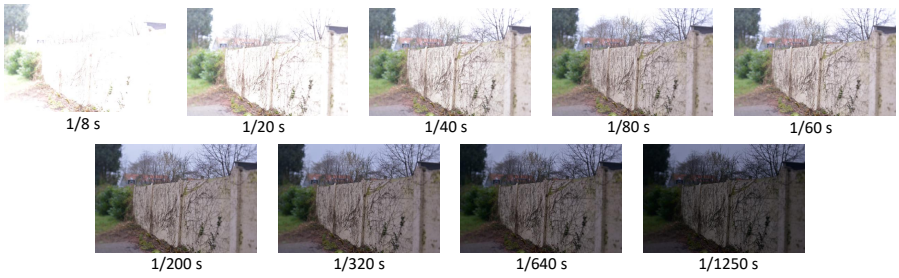


Figure G.7: Several photographs of an outdoor wall, taken at 9 exposure times from 1/8 seconds to 1/1250 seconds within a 2-minute interval to guarantee a constant scene radiance. Recorded with the Nikon D800 camera equipped with the Nikkor 45 mm, f/2.8D PC-E objective. F-number: f/5.6, sensitivity: 1250 ISO.

reaching each pixel. The absolute energy of each pixel can be obtained by multiplying the relative energy by a scaling factor k. The scaling factor was determined by illuminating the camera with the Verdi laser employed in the setup. The absolute energy deposited by the laser was determined using a powermeter and a series of neutral density filters of known attenuation. The total relative energy deposited by the laser is obtained by summing all the pixels excited by the beam, allowing for the determination of the scaling factor. For the green channel, we evaluated a k factor equal to 5×10^4. The number of scattered photons is finally obtained by computing $k \exp(g)$.

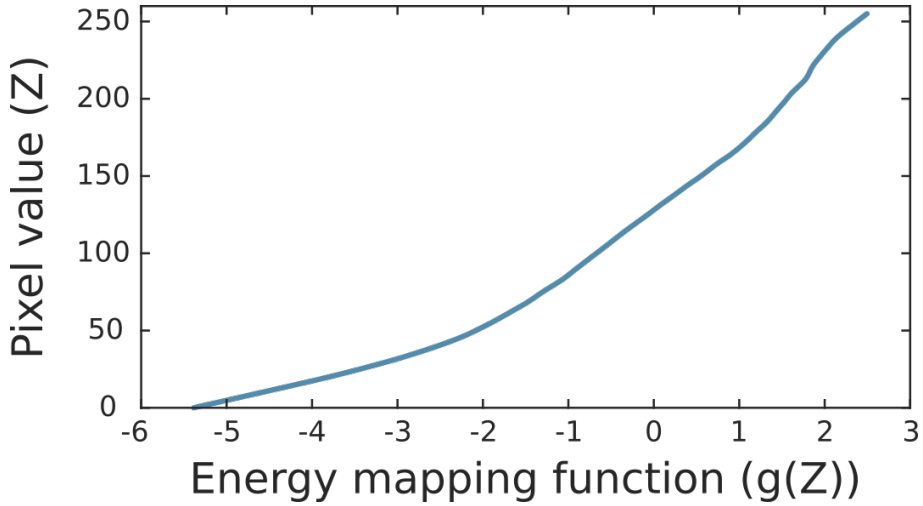


Figure G.8: g-curve of the Nikon D800 green channel obtained with a sensitivity of 1250 ISO. See text for more details.

G.5.3 *Tilt angle correction*

While filming the scene with a 45-degree tilt angle configuration presents the advantage of the sensitivity, it also results in a distortion of the scene. A pixel covers a different area of the field of view depending on its location, either in the foreground or in the background of the scene. In order to apply a single intensity threshold to the whole image and to easily interpret the particle position coordinates, the distortion is corrected by applying a remapping of the image on a uniform spatial grid. The remapping function is obtained thanks to the graph paper also employed for the camera alignment and positioning. Coordinates of a series of control points are determined in the original image. The distorted coordinates are corrected through a two-dimensional 4^{th} degree polynomial mapping function constructed using these estimated true positions and evaluated using the Matlab function `fitgeotrans`. The Matlab function `imwrap` was first used as it manages all the aspects of the remapping procedure but is time consuming as it takes about 0.9 seconds per image to perform the remapping (*i.e.* interpolation). A twenty-minute video recorded at 50 frames per second would take about 45 hours to be properly resampled. We took advantage of the fact that the interpolation grid does not change from frame to frame, allowing to estimate once the grid. The gridded interpolation function is thus created once. Only the values of the interpolation function are

updated, reducing the execution time to about 0.02 seconds per image. A picture of the graph paper before and after correction is presented in Figure G.9. Selected control points for the remapping function are also shown in this figure.

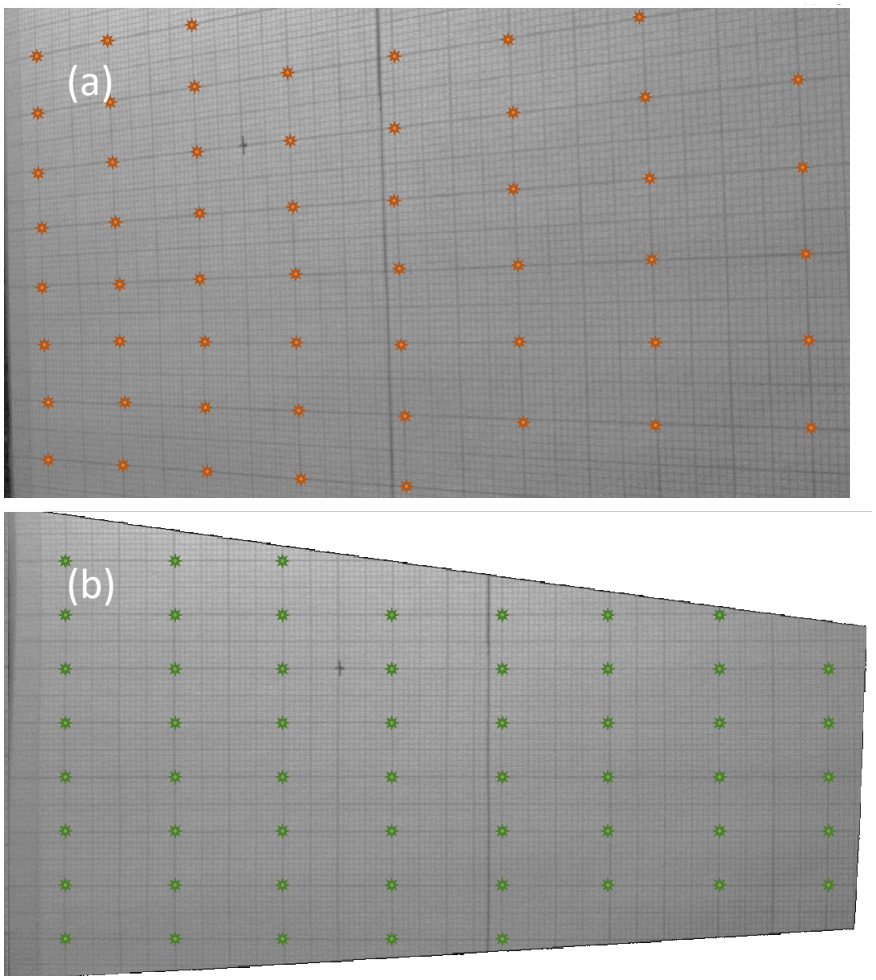


Figure G.9: Illustration of the tilt-angle correction. The graph paper before and after correction are presented in panels (a) and (b) respectively. The green and red asterisks are the control points used to determine the remapping function.

G.5.4 *Determination of particles trajectories*

For particles smaller than the light sheet thickness, the laser light intensity will vary with respect to the position of the particles in the light sheet section. Indeed, light intensity in the edges of the Gaussian beam is much smaller than at its center. This intensity variation will directly impact the number of scattered photons and the size determination from absolute photometric measurement. To minimize any experimental bias [170], we placed a vertical slit in the beam path to remove the edges of the Gaussian beam. We also implemented an algorithm to determine the trajectory followed by a particle detected on several consecutive frames. A flowchart explaining the algorithm is given in Figure G.10 and the principle of the trajectory (left panel) and the associated size determination (right panel) are presented in Figure G.11.

A trajectory is defined as a 4-column matrix containing the time at which the particle is detected, its 2D position coordinates and the number of scattered photons. The process is initialized by assigning a trajectory to each particle visible in the first frame. Then, for each frame (*i.e.* at each time step), and for each trajectory, all the non-assigned particles below a certain distance from the end of the considered trajectory are detected. We set this distance to 12 pixels, limiting the velocity of particles, in the plane of the laser sheet, to a maximum of 0.102 $m.s^{-1}$. This distance is represented for the frame t_{i+3} as a dashed orange circle in the left panel of Figure G.11. When a particle is appended to an existing trajectory with a length equal to or greater than 3, it is tagged as *assigned* and it is not further considered. However, when the trajectory to which the particle is appended is made of at most two elements, we are less confident in the fact that the particle can be associated with the trajectory. It therefore remains tagged as *non-assigned*, meaning that a same particle can be appended to several trajectories as long as it is not assigned to a trajectory with more than 3 elements. New trajectories are also created for every *non-assigned* particle once all existing trajectories have been considered. For a particle present on more than two frames, when the distance criterion is respected, we assumed the particle cannot turn around and is going forward with an angular dispersion of $\pm$ 30° as illustrated in Figure G.11. In this figure, particles A and B and C all satisfy the distance criterion, but only particles A and B are in the forward direction. The algorithm will append particle A rather than

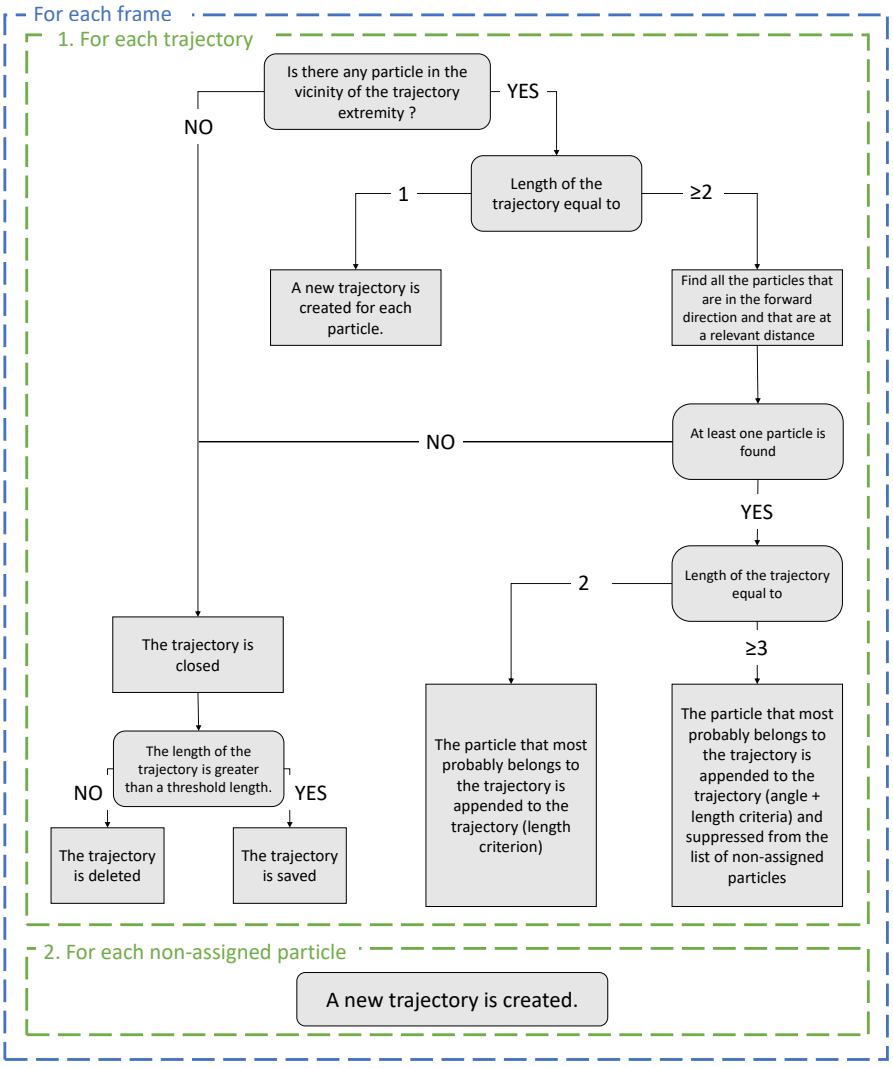


Figure G.10: Flowchart for the determination of the particle trajectories.

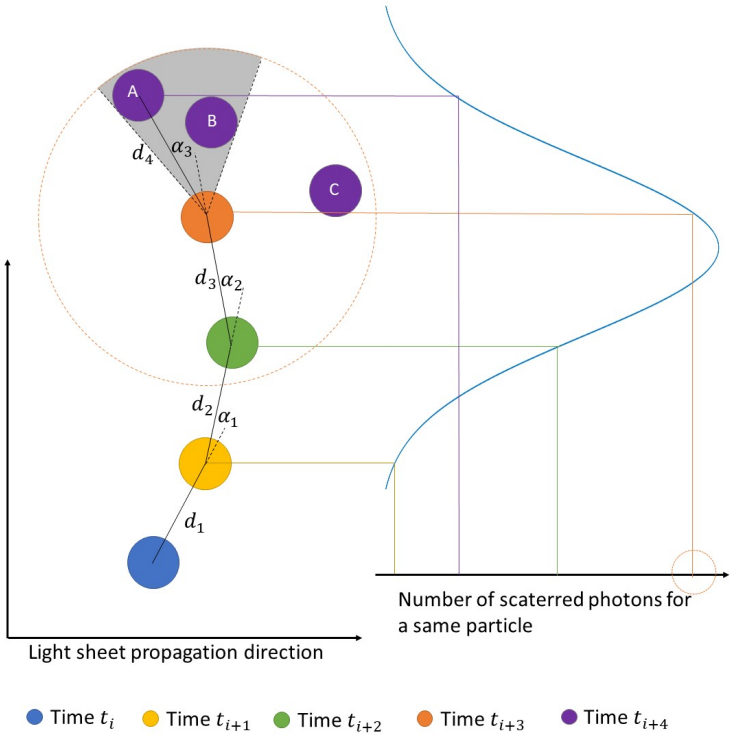


Figure G.11: Schematic illustrating the algorithm for the determination of the particle trajectories. One particle is illustrated in different colors for different frames. The dashed circle illustrates the notion of maximum distance traveled by a particle between two consecutive frames. The gray area defines the forward direction in Figure G.10. On the side the Gaussian profile in the depth of the laser sheet with the corresponding modulation on the detected scattered photons. The maximum of this distribution is chosen for size determination. $\alpha_{1,2,3}$ is the deflection angle of the trajectory, $d_{1,2,3,4}$ is the distance traveled by the particle between two consecutive detections.

particle B because it is the one that minimizes both the deviation from the mean distance traveled by the particle between two consecutive time steps and the trajectory mean deflection angle. If this optimum particle deviates too much from the trajectory (distance deviating from more than ± 1 pixel compared to the mean distance between consecutive particles constituting the trajectory), this detection is not appended and the trajectory is defined as closed.
For the size determination, we consider the frame corresponding to the largest number of photons detected during the trajectory as illustrated in Figure G.11. The largest number of frames in the trajectory, the best we sample the Gaussian profile, as illustrated in the right panel of Figure G.11. In any future analysis, we restrict ourselves to trajectories longer than 5, meaning that the particle remained in the light sheet for at least 0.083 seconds for a video sampled at 60 frames per second and that there is no ambiguity on the trajectory. Figure G.12 illustrates particle trajectories for a time window of 0.5 seconds measured after 7 seconds (panel (a)) and after 110 seconds (panel (b)) after the last repetition of the word "particle" without the use of a fan.

We can see, in panel (a), that a vortex is generated by the speaker. This vortex is no more visible 16 seconds after yelling. We also see, in panel (b) at longer times, that a flow directed in the direction of the box entry drives the particles outside of the box.

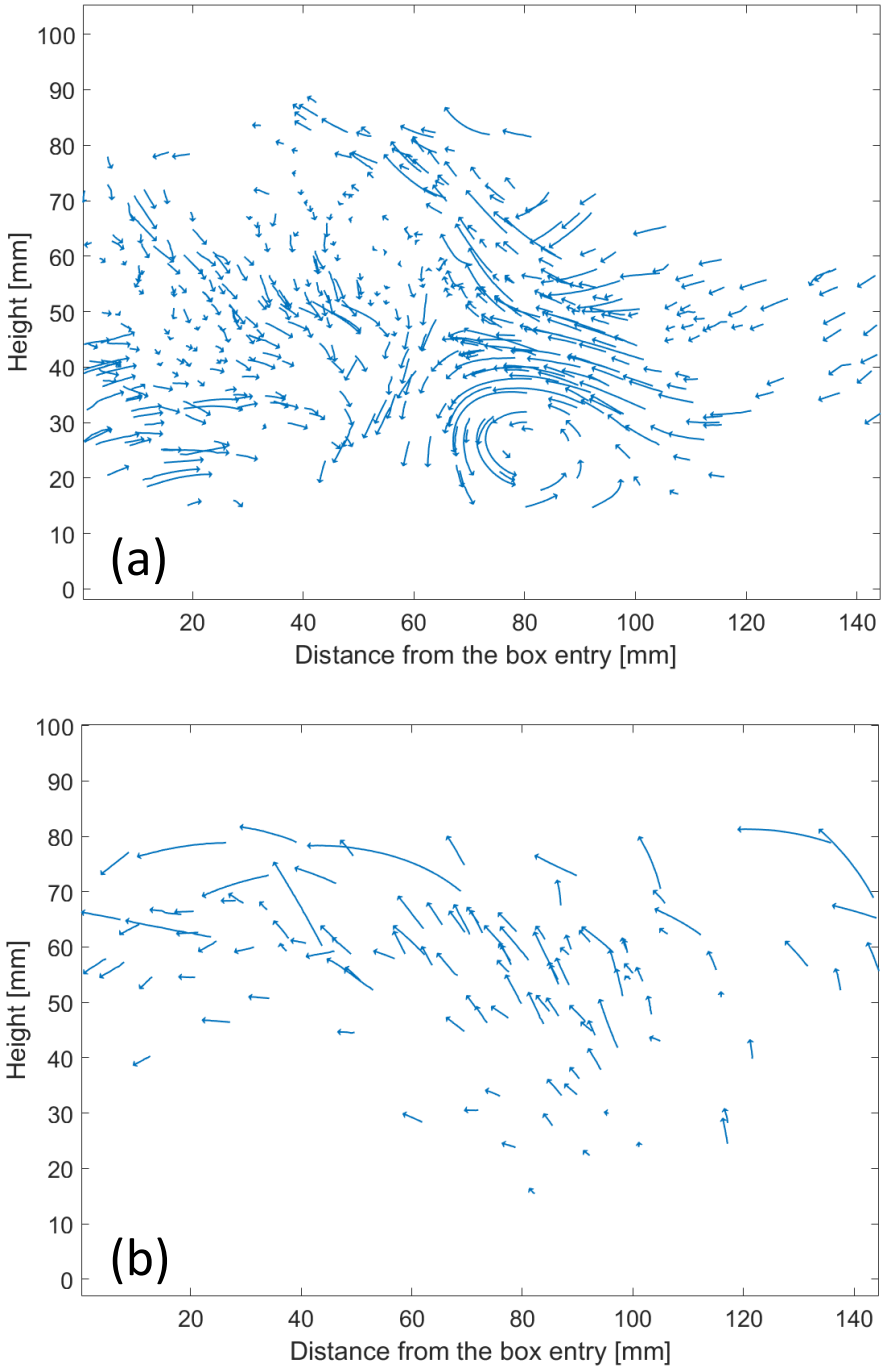


Figure G.12: Trajectories followed by particles in this study (a) on a 0.5 second interval starting 7 seconds after yelling (b) on a 5-second interval starting 110 seconds after yelling.

G.6 RESULTS AND DISCUSSION

G.6.1 *Validation of the size determination procedure*

In order to validate this new method, the measurement procedure and the data-processing pipeline, we used isopropanol droplets generated at the tip of a 28-gauge needle actuated with a liquid controller dropper (model 982, SD&ZC). We then measured their diameters by absolute photometry and independently by two other methods. On the one hand, we employed a white light lamp to directly image the droplets with the camera, as shown in Figure G.13, we obtained from the ratio of lengths, a droplet diameter at the exit of the needle of 2.2 ± 0.3 mm. On the other hand, for the second independent evaluation of the droplet size, we used direct spatial dependency of scattered light. This dependency can be rationalized from geometrical optics consideration, *i.e.* the Snell-Descartes law with the geometry of interaction and observation. Indeed, two spots are observed for each droplet, as illustrated in Figure G.14(b). One spot is due to the light that is directly reflected from air-isopropanol interface, the second one is due to the light that is refracted twice. Since we observed the two rays at the same angle, we can determine the droplet diameter from the distance along the laser propagation direction from the geometrical construction presented in Figure G.14(a). Experimentally, the needle tip was placed at the centre of the laser light sheet using the resulting shadow. The power of the laser was attenuated with a calibrated neutral density filter to 0.28 mW. We could then measure (i) the integrated number of scattered photons and (ii) the distance between the two spots for each droplet in order to retrieve the beam diameter in both cases. These measurements lead to droplet sizes presented for (i) in blue and for (ii) in red in Figure G.13, with a distribution centred at 2.1 mm for (i) and 2.22 mm for (ii). The data presented in the histogram are limited to droplets that fall in the axis of the needle and a correction was applied to take into account the non-uniform light intensity distribution in the vertical direction for the absolute photometric measurements.

The photometric measurements lead to a slight underestimation of the size of the droplet by about 5 %. This can be understood by the relatively large diameter of the droplets compared to the laser sheet thickness of 2.25 mm considered in these measurements ($1/e^2$ criterion). We used a constant mean value for the light intensity in the y direction.

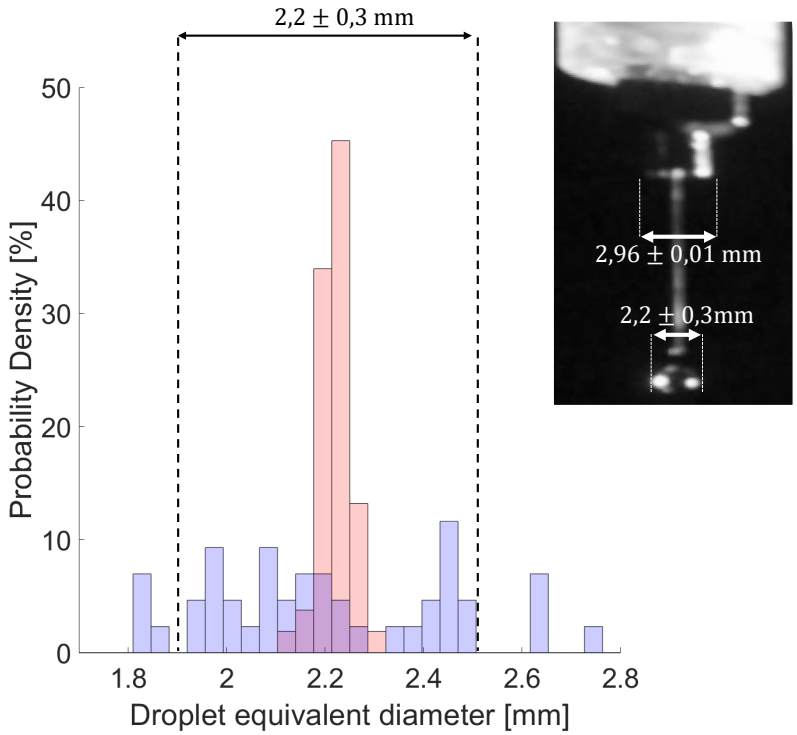


Figure G.13: Size distribution of isopropanol droplets generated with the liquid controller dropper. The blue histogram corresponds to the size estimated using photometric measurement and Mie's theory, the red histogram is obtained thanks to the geometrical optics considerations as detailed in the text and in Figure 13. The double arrow line represents the size range of the droplet determined from white light illumination and ratio of the lengths as measured on the photograph on the right side of the Figure.

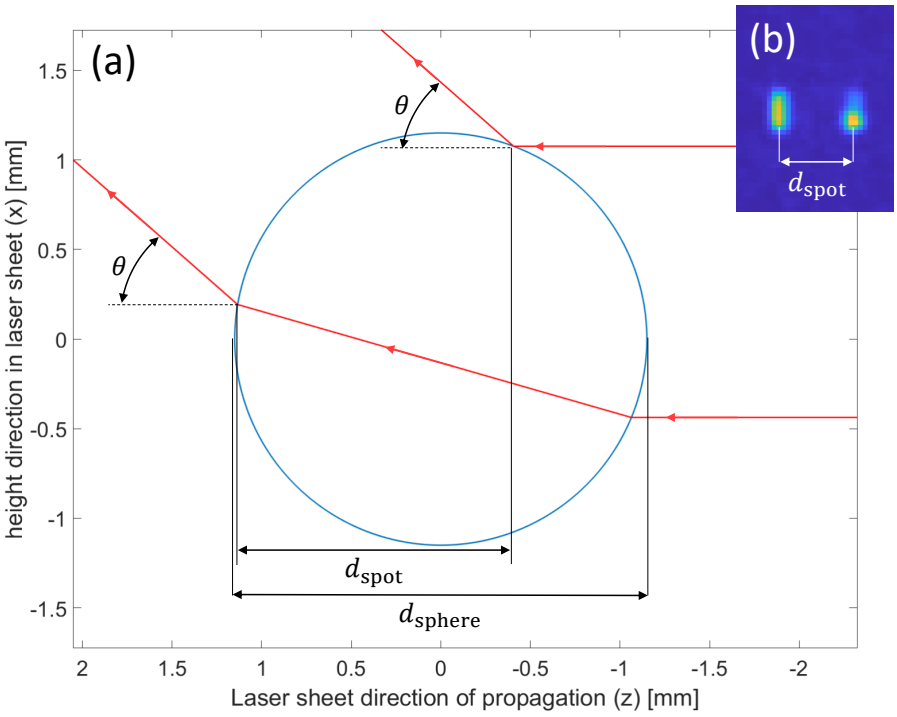


Figure G.14: Geometrical method for the determination of the droplet diameter. (a) Tracing of the rays reaching the camera for an isopropanol droplet with a 2.2 mm diameter located in a uniform light sheet. The droplet diameter d_{sphere} is proportional to the distance d_{spot} between the two spots shown in (b). The proportional factor depends on the observation angle θ.

This is justified, in the case of small particles, since a slit is placed in the beam path to select the center of the Gaussian profile, as it is the case for the other measurements presented in the present manuscript. However, due to the relative important size of the isopropanol droplets, the slit had to be removed for this specific set of measurements. The larger distribution of photometric measurements in Figure G.13 can be understood in terms of variations of the alignment of the droplet compared to the laser sheet. Figure G.2 shows the droplet size with respect to the number of scattered photons obtained in the Mie's theory framework for isopropanol droplets.

G.6.2 *Application to the dynamics of produced aerosols while yelling*

The setup aimed at studying the lifetime and size distribution of droplets generated by talking or yelling in the framework of the current COVID-19 pandemic. Two datasets were produced in this context. Both of them consist in a 20-minute video with the following time sequence: during the first three minutes, the background is recorded, then the speaker, a male of 27 years, yelled as many times as possible the French word "particule" in a 30-second interval of time at a sound level of approximately 100 dB in the box (see Figure G.3). The decay of the number of particles is recorded during the 17 remaining minutes. The two datasets differ by the presence or the absence of a 12 V muffin fan in the box for dataset 2 and 1 respectively. The fan was placed in dataset 2, in order to reproduce the experimental protocol of Stadnytskyi *et al.*, Ref. [171] . The muffin fan was turned on 20 seconds before yelling and turned off 10 seconds after yelling. The authors of Ref. [171] justified its use as a way to homogenize the particles distribution inside the box. In both measurements, the power of the laser was set to 4 W, that is the same power used by Stadnytskyi *et al.* [171]. The exposure time, f-number and sensitivity of the Nikon D800 were respectively 1/400 s, f/5.6 and 2500 ISO in any case. The two videos were recorded at 60 frames per second. The temperature and relative humidity were equal to 19.7°C and 42 % during the two measurements.

Aerosol size determination from photometric measurement

Using the trajectories determined from the analysis of the video, we can infer the size distribution of droplets exhaled by someone yelling. This leads to the distribution presented in Figure G.15 for dataset 1.

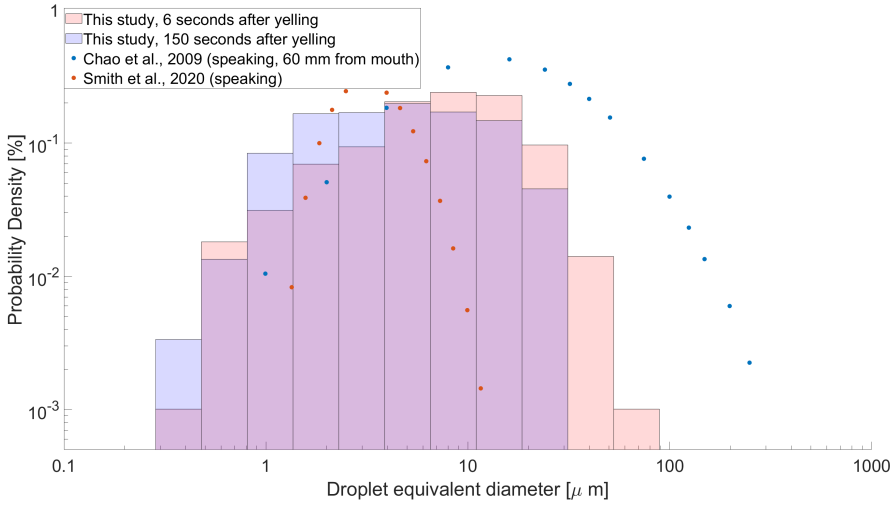


Figure G.15: Size distribution of droplets of the measurement without any fan. The red histogram corresponds to the distribution on a 0.5 seconds interval 6 seconds after yelling, the blue histogram corresponds to the distribution on a 30-second interval 150 seconds after yelling. The red dots are the values obtained by Smith *et al.* [177]. The blue dots are the values obtained by Chao *et al.* [178].

The distribution in blue is determined on a 0.5 second time interval 6 s after yelling and the red one on a 30-second time interval 150 s after yelling. We can observe a slight shift of the distributions towards smaller particles for larger times. This is a sign of either evaporation and/or a faster evacuation of larger droplets from the plane of observation. The increased sensitivity of the current setup allows to detect particles with diameters as small as 100 nm according to the minimum number of photons we are able to detect at 532 nm (around 250). These distributions are plotted against results obtained from Ref. [177, 178]. The distribution of this work can be considered in good agreements with those previous studies [177, 178], when one considers the variation between these two works. This type of distribution and their description using parameterized analytical expressions has recently been reviewed in Ref. [179].

G.6.3 *Characterization of aerosols lifetimes*

In order to characterize the persistence of aerosols produced while yelling and compare our results with the ones obtained by Stadnytskyi

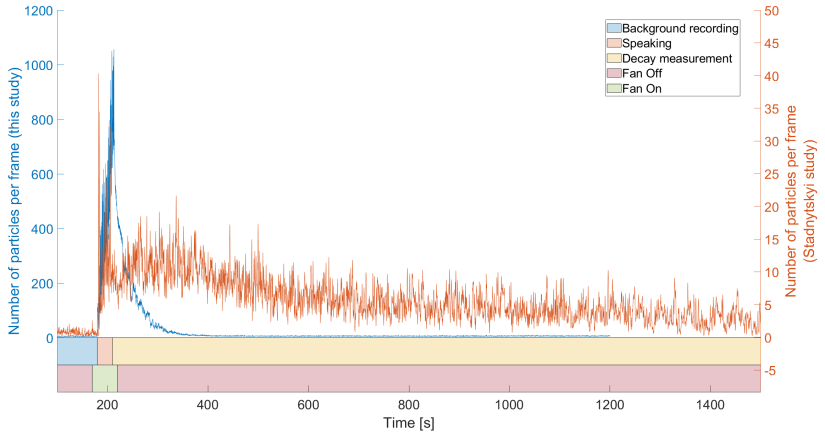


Figure G.16: Comparison between Stadnytskyi *et al.*, Ref. [171], in orange and this work, in blue. A 21-sample Gaussian moving average was applied to both measurements and the time sequence was identical in both cases.

et al., Ref. [171], we followed a similar experimental procedure (see dataset 2). Experimentally, for our measurements, a slit with a 1.78 mm opening was placed to truncate the edges of the Gaussian beam in the thickness of the light sheet. The number of detected particles on each frame with respect to time is shown in Figure G.16 for both studies. Our results are presented in blue and show a typical decay time of **23.9** seconds. The decay was fitted to a decreasing exponential 10 seconds after the fan was turned off. In the work of Stadnytskyi *et al.*, in Ref. [171], the data were fitted by two exponential decays presumably associated to two ranges of sizes providing half-lives of **480** and **840** s. Our value is thus more than one order of magnitude smaller than the results published by Stadnytskyi *et al.* for comparable laser light sheet, 1x150 mm^2 in Ref. [171] and 3x90 mm^2 in this work. Using the tools developed in this work we tried to rationalize this significant difference in lifetimes, keeping in mind the importance of the dynamics of aerosol droplets in the frame of pandemics [179].

The data of Ref. [171] were thus reanalysed using the algorithm developed in this work and the movie available in supplementary material of Ref. [171]. The number of detected particles per frame, one of the results of this analysis, is also displayed in Figure G.16 as an orange curve. The comparison of the two curves highlights the significant difference in dynamics and in signal-to-noise ratio (SNR). The differ-

ence in SNR illustrates the present sensitivity gain obtained thanks to the favorable geometry of our experimental setup (it has to be noticed that the vertical scales are different). A 21-sample Gaussian moving average was applied and shows a slight bump around 250 s for the orange curve. This bump can be associated with the use of a fan to disperse the particles in the box. This bump was not visible in Figure 1 of Ref. [171], due to the lowpass filtering effect of the 576 sample running average applied on the original data. Those trajectories for the beginning of the measurement and after a time on the order of the lifetime published in Ref [171] (movie times=260 s and 610 s) are presented in Figure G.17. From this figure, we can notice that a convective motion is still present 50 seconds after yelling and we clearly see the sedimentation taking place 350 seconds later. From this observation we can re-evaluate the data of the Figure G.16, and fit an exponential decay starting at a time of 500 s (300 s after yelling) to guarantee that we actually only characterize the sedimentation dynamics. We then obtain a half-life of **650** s, about 3 minutes longer than firstly reported. This discrepancy can be attributed to the fact that on this previous study, they were not able to properly distinguish between convective and sedimentation dynamics. They overcame the problem by using two exponential decays associated with different size distributions rather than changing the temporal window of the fitted data to deal with the change in the decay dynamics. In our case, as illustrated in Figure G.12 and on the video accessible on (https://youtu.be/EfJSfobX79I), we stay in the convective regime with a continuous escape of the particles from the box towards the left. Surprisingly when we blocked the three apertures on the left of the box, we have not observed a significant difference in particle lifetime. From the trajectory determination, the average flow towards the escape was determined. A mean value of 0.03 $m.s^{-1}$ was obtained, which is 10 times smaller than airflow of ventilation, *i.e.* 0.3 $m.s^{-1}$ provided in Ref. [180]. We also turned off all the HEPA filter units and it led to an increase of the decay time to **83** s, at the expense of a considerable deterioration of the SNR due to dust in suspension, precluding the trajectories determination. We also characterized the lifetime as a function of the particle size for our measurement as presented in Figure G.18. As expected we observe faster decay for larger particles. In conclusion, the times presented by Stadnytskyi *et al.* (Ref. [171]), are an upper bound of the typical lifetime of aerosols in enclosed room and a slight ventilation decreases this lifetime dramatically. Indeed, even while turning off all the source

of possible perturbations we found significantly shorter lifetimes for suspended particles (**83** s instead of **650** s). The present results are calling for future analysis but the conclusions go along with the work reported in Ref. [181] where the authors used a portable optical particle counter and found no significant amount of aerosols in common places except in restrooms, unventilated living rooms and elevators.

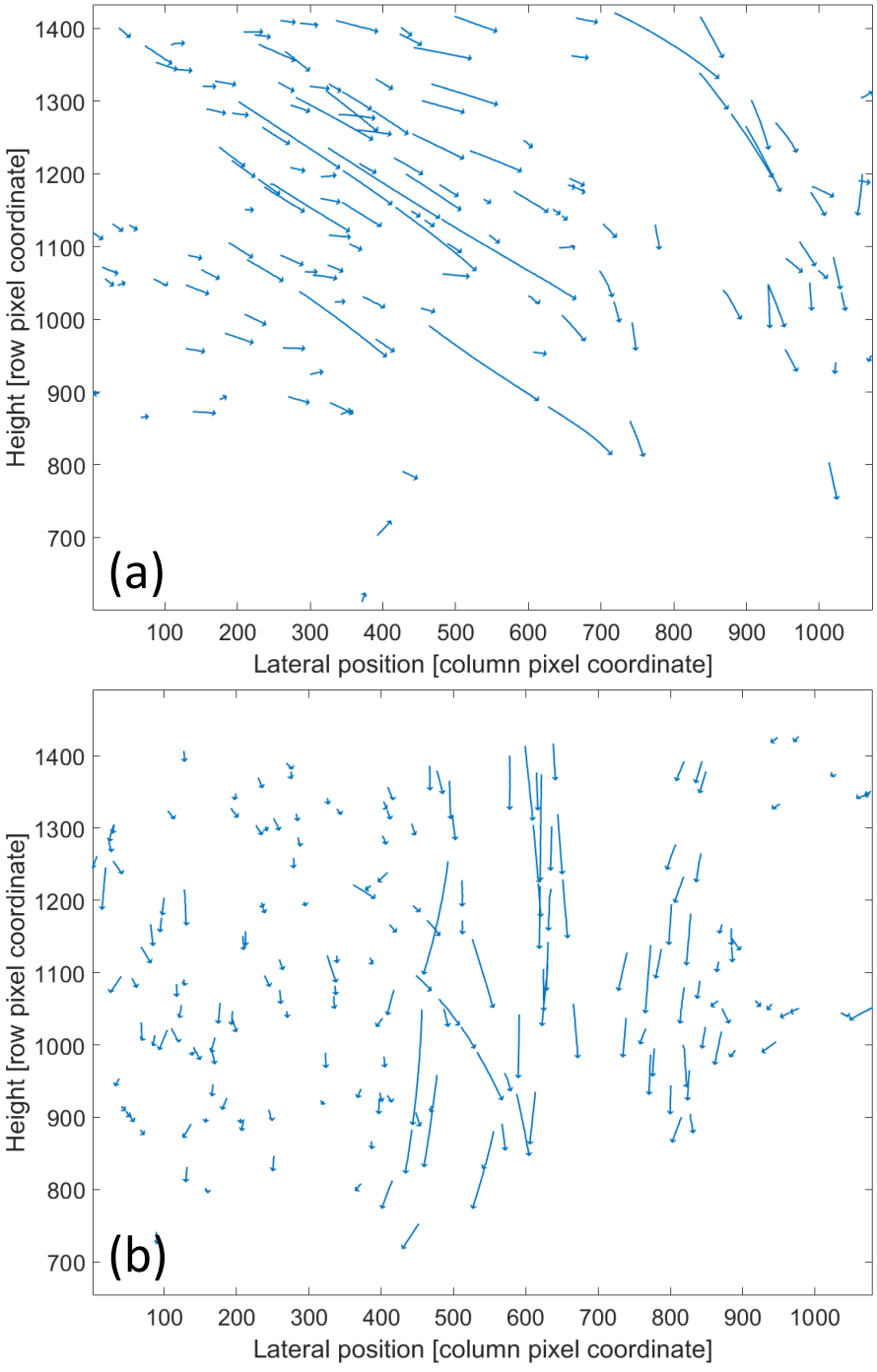


Figure G.17: Trajectories followed by particles in the study of Stadnytskyi *et al.* [171] (a) on a 20 seconds interval starting 50 seconds after yelling and b) on a 50 seconds interval starting 400 seconds after yelling.

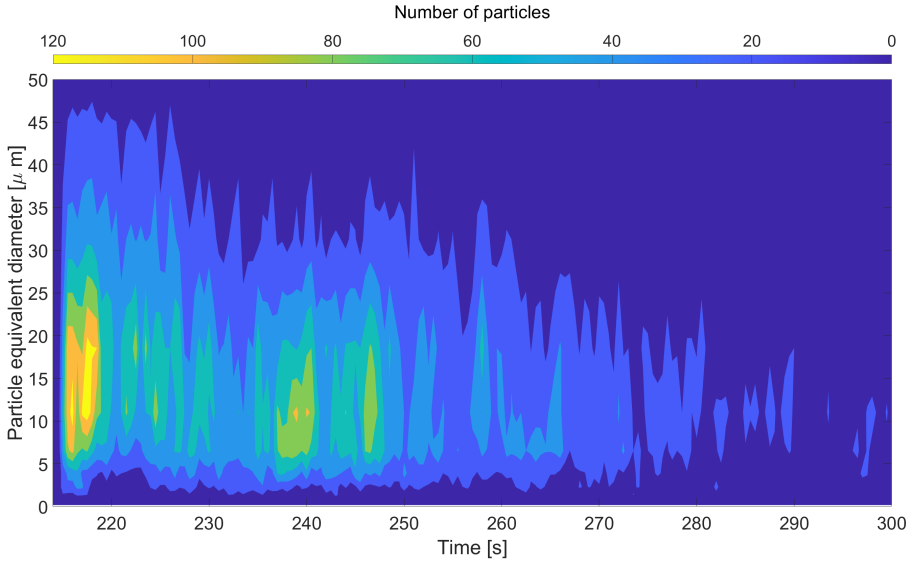


Figure G.18: Evolution of the size distribution of droplets with respect to time. The temporal resolution is of 1 second.

G.7 CONCLUSION AND PERSPECTIVES

This work presents for the first time the combination of filming and absolute photometric capabilities. Those features with post-processing analysis allow to measure the number, the size and to characterize the dynamics of aerosols in air. The absolute photometry provides measurements which are free of any further calibration (or correction) factors, the only input being the refractive index of the considered species. This capability is accompanied by the possibility to record a scene and thus to retrieve information on the dynamics of the particles. This is characterized by trajectories determined by post-processing treatment. The method has been applied to the measurement of the lifetime of particles exhaled while yelling. Our measurements and postprocessing analysis show a dramatic decrease of the lifetime of particles in presence of small airflow (0.03 $m.s^{-1}$) and allow to re-estimate the lifetime published in a previous study. This previous measurement presents a SNR from 10 to 100 times smaller. Impressively, the setup presented in this work can still be optimized especially in terms of the used camera and the laser beam profile. Imaging technology is improving quickly and a HDR, a kHz acquisition rate and/or an intensified camera could be envisioned for a gain in dynamics, time resolution or sensitivity

respectively. For the uniformity of the laser sheet, the use of a top-hat profile instead of a Gaussian profile could also be considered.
The technique presented in this work represents a step forward in the characterization of nanoparticles present in air and could be used in a large panel of applications in particular in the domains of air quality assessment and atmospheric sciences.

G.8 ACKNOWLEDGMENTS

This work was supported by the Fonds de la Recherche Scientifique - FNRS under Grants n°: J.0129.20 and the ARC 18/23-090. Olivier Leblanc is warmly thanked for fruitful discussions. Anthony Roucou is acknowledged for having provided constructive comments on this manuscript.

G.9 DATA AVAILABILITY

The raw data that support the findings of this study are available from the corresponding author upon reasonable request. A video showing post-processed data is available on Youtube (link to the unlisted video: https://youtu.be/EfJSfobX79I).

BIBLIOGRAPHY

[1] J.-L. Basdevant, *Lectures on quantum mechanics*. Springer, 1 ed., 2007.

[2] D. Sumner, M. Abrams, and J. Brault, *Fourier transform spectrometry*. Academic Press, 2001.

[3] D. Sprecher, C. Jungen, W. Ubachs, and F. Merkt, "Towards measuring the ionisation and dissociation energies of molecular hydrogen with sub-mhz accuracy," *Faraday discussions*, vol. 150, pp. 51–70, 2011.

[4] L. Clarisse, C. Clerbaux, F. Dentener, D. Hurtmans, and P.-F. Coheur, "Global ammonia distribution derived from infrared satellite observations," *Nature Geoscience*, vol. 2, no. 7, pp. 479–483, 2009.

[5] H. H. Funke, B. L. Grissom, C. E. McGrew, and M. W. Raynor, "Techniques for the measurement of trace moisture in high-purity electronic specialty gases," *Review of scientific instruments*, vol. 74, no. 9, pp. 3909–3933, 2003.

[6] B. Henderson, A. Khodabakhsh, M. Metsälä, I. Ventrillard, F. M. Schmidt, D. Romanini, G. A. Ritchie, S. te Lintel Hekkert, R. Briot, T. Risby, *et al.*, "Laser spectroscopy for breath analysis: towards clinical implementation," *Applied Physics B*, vol. 124, no. 8, pp. 1–21, 2018.

[7] M. J. Thorpe, D. Balslev-Clausen, M. S. Kirchner, and J. Ye, "Cavity-enhanced optical frequency comb spectroscopy: application to human breath analysis," *Optics Express*, vol. 16, no. 4, pp. 2387–2397, 2008.

[8] P. B. Changala, M. L. Weichman, K. F. Lee, M. E. Fermann, and J. Ye, "Rovibrational quantum state resolution of the c60 fullerene," *Science*, vol. 363, no. 6422, pp. 49–54, 2019.

[9] I. Gordon, L. Rothman, R. Hargreaves, R. Hashemi, E. Karlovets, F. Skinner, E. Conway, C. Hill, R. Kochanov, Y. Tan, *et al.*, "The

hitran2020 molecular spectroscopic database," *Journal of Quantitative Spectroscopy and Radiative Transfer*, vol. 277, p. 107949, 2022.

[10] A. Foltynowicz, L. Rutkowski, I. Silander, A. C. Johansson, V. S. de Oliveira, O. Axner, G. Soboń, T. Martynkien, P. Mergo, and K. K. Lehmann, "Sub-doppler double-resonance spectroscopy of methane using a frequency comb probe," *Physical Review Letters*, vol. 126, no. 6, p. 063001, 2021.

[11] V. Di Sarno, R. Aiello, M. De Rosa, I. Ricciardi, S. Mosca, G. Notariale, P. De Natale, L. Santamaria, and P. Maddaloni, "Lamb-dip spectroscopy of buffer-gas-cooled molecules," *Optica*, vol. 6, no. 4, pp. 436–441, 2019.

[12] I. Galli, S. Bartalini, S. Borri, P. Cancio, D. Mazzotti, P. De Natale, and G. Giusfredi, "Molecular gas sensing below parts per trillion: radiocarbon-dioxide optical detection," *Physical Review Letters*, vol. 107, no. 27, p. 270802, 2011.

[13] P. Maslowski, K. F. Lee, A. C. Johansson, A. Khodabakhsh, G. Kowzan, L. Rutkowski, A. A. Mills, C. Mohr, J. Jiang, M. E. Fermann, *et al.*, "Surpassing the path-limited resolution of Fourier-transform spectrometry with frequency combs," *Physical Review A*, vol. 93, no. 2, p. 021802, 2016.

[14] L. Rutkowski, P. Masłowski, A. C. Johansson, A. Khodabakhsh, and A. Foltynowicz, "Optical frequency comb fourier transform spectroscopy with sub-nominal resolution and precision beyond the voigt profile," *Journal of Quantitative Spectroscopy and Radiative Transfer*, vol. 204, pp. 63–73, 2018.

[15] J. Mandon, G. Guelachvili, and N. Picqué, "Fourier transform spectroscopy with a laser frequency comb," *Nature Photonics*, vol. 3, no. 2, pp. 99–102, 2009.

[16] D. M. O'Leary, A. A. Ruth, S. Dixneuf, J. Orphal, and R. Varma, "The near infrared cavity-enhanced absorption spectrum of methyl cyanide," *Journal of Quantitative Spectroscopy and Radiative Transfer*, vol. 113, no. 11, pp. 1138–1147, 2012.

[17] A. Libert, X. Urbain, B. Fabre, M. Daman, and C. Lauzin, "Design and characteristics of a cavity-enhanced fourier-transform spectrometer based on a supercontinuum source," *Review of Scientific Instruments*, vol. 91, no. 11, p. 113104, 2020.

[18] A. Korobenko, K. Johnston, M. Kubullek, L. Arissian, Z. Dube, T. Wang, M. Kübel, A. Y. Naumov, D. Villeneuve, M. F. Kling, *et al.*, "Femtosecond streaking in ambient air," *Optica*, vol. 7, no. 10, pp. 1372–1376, 2020.

[19] P. Fellgett, *Theory of infra-red sensitivites and its application to investigations of stellar radiation in the near infra-red*. PhD thesis, University of Cambridge, 1951.

[20] P. Jacquinot, "17e Congres du GAMS," 1954.

[21] J. Connes and P. Connes, "Near-infrared planetary spectra by Fourier spectroscopy. I. Instruments and results," *JOSA*, vol. 56, no. 7, pp. 896–910, 1966.

[22] P. R. Griffiths, "The early days of commercial FT-IR spectrometry: a personal perspective," *Applied spectroscopy*, vol. 71, no. 3, pp. 329–340, 2017.

[23] A. A. Ruth, J. Orphal, and S. E. Fiedler, "Fourier-transform cavity-enhanced absorption spectroscopy using an incoherent broadband light source," *Applied optics*, vol. 46, no. 17, pp. 3611–3616, 2007.

[24] T. Gherman and D. Romanini, "Mode–locked cavity–enhanced absorption spectroscopy," *Optics Express*, vol. 10, no. 19, pp. 1033–1042, 2002.

[25] W. Denzer, G. Hancock, M. Islam, C. Langley, R. Peverall, G. A. Ritchie, and D. Taylor, "Trace species detection in the near infrared using Fourier transform broadband cavity enhanced absorption spectroscopy: initial studies on potential breath analytes," *Analyst*, vol. 136, no. 4, pp. 801–806, 2011.

[26] A. Foltynowicz, T. Ban, P. Masłowski, F. Adler, and J. Ye, "Quantum-noise-limited optical frequency comb spectroscopy," *Physical review letters*, vol. 107, no. 23, p. 233002, 2011.

[27] K. C. Cossel, *Techniques in molecular spectroscopy : from broad bandwidth to high resolution*. PhD thesis, California Institute of Technology, 2014.

[28] B. Guislain, R. Harvey, D. Tokaryk, A. Ross, P. Crozet, and A. Adam, "An alternative approach to interferogram collection

and processing for a vintage Bomem DA3 Fourier transform spectrometer," *Journal of Molecular Spectroscopy*, p. 111181, 2019.

[29] P. Griffiths and J. De Haseth, *Fourier transform infrared spectrometry*, vol. 171. John Wiley & Sons, 2007.

[30] V. Saptari, *Fourier transform spectroscopy instrumentation engineering*. SPIE Optical Engineering Press, 2003.

[31] A. Libert, "Design of a Fourier transform spectrometer for high resolution spectroscopy," Master's thesis, Universite catholique de Louvain, 2016.

[32] A. Foltynowicz, P. Masłowski, T. Ban, F. Adler, K. Cossel, T. Briles, and J. Ye, "Optical frequency comb spectroscopy," *Faraday discussions*, vol. 150, pp. 23–31, 2011.

[33] A. Foltynowicz, P. Masłowski, A. J. Fleisher, B. J. Bjork, and J. Ye, "Cavity-enhanced optical frequency comb spectroscopy in the mid-infrared application to trace detection of hydrogen peroxide," *Applied Physics B*, vol. 110, no. 2, pp. 163–175, 2013.

[34] J. Genest and P. Tremblay, *Understanding Fourier-transform spectrometers*. Centre d'optique, photonique et laser, Université Laval, 20017.

[35] Y. Zhao, "Implementing thermal feedback control of a helium-neon laser for frequency stabilization," Master's thesis, Ward Melville High School, East Setauket, NY, 2008.

[36] R. Balhorn, H. Kunzmann, and F. Lebowsky, "Frequency stabilization of internal-mirror helium–neon lasers," *Applied optics*, vol. 11, no. 4, pp. 742–744, 1972.

[37] H. Shirvani-Mahdavi and Y. Narges, "Frequency stabilization of ambience-isolated internal-mirror He–Ne lasers by thermoelectric-cooling thermal compensation," *Journal of Theoretical and Applied Physics*, vol. 10, no. 4, pp. 315–321, 2016.

[38] G. Guelachvili, "Distortion free interferograms in fourier transform spectroscopy with nonlinear detectors," *Applied optics*, vol. 25, no. 24, pp. 4644–4648, 1986.

[39] P. C. Hobbs, "Ultrasensitive laser measurements without tears," *Applied optics*, vol. 36, no. 4, pp. 903–920, 1997.

[40] J. L. Hall, M. S. Taubman, and J. Ye, "Laser stabilization," in *Handbook of Optics IV* (J. M. Enoch, E. V. Stryland, and W. L. Wolves, eds.), ch. 27, Washington D.C.: McGraw-Hill, New York, 2000.

[41] H. Yang, P. R. Griffiths, and C. J. Manning, "Improved data processing by application of Brault's method to ultra-rapid-scan FT-IR spectrometry," *Applied spectroscopy*, vol. 56, no. 10, pp. 1281–1288, 2002.

[42] D. A. Naylor, T. R. Fulton, P. W. Davis, I. M. Chapman, B. G. Gom, L. D. Spencer, J. V. Lindner, N. E. Nelson-Fitzpatrick, M. K. Tahic, and G. R. Davis, "Data processing pipeline for a time-sampled imaging Fourier transform spectrometer," in *Imaging Spectrometry X*, vol. 5546, pp. 61–72, International Society for Optics and Photonics, 2004.

[43] W. Herres and J. Gronholz, "Understanding FT-IR data processing," *Part*, vol. 1, pp. 352–356, 1984.

[44] D. A. Naylor and M. K. Tahic, "Apodizing functions for Fourier transform spectroscopy," *JOSA A*, vol. 24, no. 11, pp. 3644–3648, 2007.

[45] J. W. Brault, "High precision fourier transform spectrometry: The critical role of phase corrections," *Microchimica Acta*, vol. 93, pp. 215–227, Jan 1987.

[46] L. Mertz, "Auxiliary computation for Fourier spectrometry," *Infrared Physics*, vol. 7, no. 1, pp. 17–23, 1967.

[47] M. L. Forman, W. H. Steel, and G. A. Vanasse, "Correction of asymmetric interferograms obtained in Fourier spectroscopy," *JOSA*, vol. 56, no. 1, pp. 59–63, 1966.

[48] J. W. Brault, "New approach to high-precision Fourier transform spectrometer design," *Applied Optics*, vol. 35, no. 16, pp. 2891–2896, 1996.

[49] L. Comolli and B. Saggin, "Analysis of disturbances in the Planetary Fourier Spectrometer through numerical modeling," *Planetary and Space science*, vol. 58, no. 5, pp. 864–874, 2010.

[50] L. S. Rothman, I. E. Gordon, A. Barbe, D. C. Benner, P. F. Bernath, M. Birk, V. Boudon, L. R. Brown, A. Campargue, J.-P. Champion, *et al.*, "The HITRAN 2008 molecular spectroscopic database," *Journal of Quantitative Spectroscopy and Radiative Transfer*, vol. 110, no. 9-10, pp. 533–572, 2009.

[51] J. C. Cobas, M. A. Bernstein, M. Martín-Pastor, and P. G. Tahoces, "A new general-purpose fully automatic baseline-correction procedure for 1D and 2D NMR data," *Journal of Magnetic Resonance*, vol. 183, no. 1, pp. 145–151, 2006.

[52] R. Learner, A. Thorne, and J. W. Brault, "Ghosts and artifacts in Fourier-transform spectrometry," *Applied optics*, vol. 35, no. 16, pp. 2947–2954, 1996.

[53] M. L. Salit, J. C. Travis, and M. R. Winchester, "Practical wavelength calibration considerations for UV–visible Fourier-transform spectroscopy," *Applied optics*, vol. 35, no. 16, pp. 2960–2970, 1996.

[54] M. L. Salit, C. J. Sansonetti, D. Veza, and J. C. Travis, "Investigation of single-factor calibration of the wave-number scale in fourier-transform spectroscopy," *JOSA B*, vol. 21, no. 8, pp. 1543–1550, 2004.

[55] R. Hawkins, M. Hoke, and J. Shaw, "Wavenumber calibration of Fourier transform spectra," *Applied Spectroscopy*, vol. 37, no. 2, pp. 134–139, 1983.

[56] S. E. Fiedler, A. Hese, and A. A. Ruth, "Incoherent broad-band cavity-enhanced absorption spectroscopy," *Chemical physics letters*, vol. 371, no. 3-4, pp. 284–294, 2003.

[57] P. Masłowski, K. Cossel, A. Foltynowicz, and J. Ye, "Cavity-enhanced direct frequency comb spectroscopy," in *Cavity-Enhanced Spectroscopy and Sensing*, pp. 271–321, Springer, 2014.

[58] M. Abbas, K. Jahromi, M. Nematollahi, R. Krebbers, N. Liu, G. Woyessa, O. Bang, L. Huot, F. Harren, and A. Khodabakhsh, "Fourier transform spectrometer based on high-repetition-rate mid-infrared supercontinuum sources for trace gas detection," *Optics Express*, vol. 29, no. 14, pp. 22315–22330, 2021.

[59] M. L. Weichman, P. B. Changala, J. Ye, Z. Chen, M. Yan, and N. Picqué, "Broadband molecular spectroscopy with optical frequency combs," *Journal of molecular spectroscopy*, vol. 355, pp. 66–78, 2019.

[60] S. Hooker and C. Webb, *Laser Physics*. Oxford Master Series in Physics, OUP Oxford, 2010.

[61] S. Haykin and B. V. Veen, *Signals and systems*. John Wiley & Sons, 2007.

[62] F. W. Helbing, G. Steinmeyer, and U. Keller, "Carrier-envelope offset phase-locking with attosecond timing jitter," *IEEE Journal of Selected Topics in Quantum Electronics*, vol. 9, no. 4, pp. 1030–1040, 2003.

[63] L. Gallmann and U. Keller, "Femtosecond and attosecond light sources and techniques for spectroscopy," *Handbook of High-resolution Spectroscopy*, 2011.

[64] E. P. Ippen, "Principles of passive mode locking," *Applied Physics B*, vol. 58, no. 3, pp. 159–170, 1994.

[65] S. Yefet and A. Pe'er, "A review of cavity design for kerr lens mode-locked solid-state lasers," *Applied Sciences*, vol. 3, no. 4, pp. 694–724, 2013.

[66] C. Spielmann, P. F. Curley, T. Brabec, and F. Krausz, "Ultrabroadband femtosecond lasers," *IEEE Journal of quantum electronics*, vol. 30, no. 4, pp. 1100–1114, 1994.

[67] M. Wollenhaupt, A. Assion, and T. Baumert, "Femtosecond laser pulses: linear properties, manipulation, generation and measurement," *Springer Handbook of Lasers and Optics, ISBN 978-0-387-95579-7. Springer-Verlag New York, 2007, p. 937*, p. 937, 2007.

[68] R. Adams and E. C., *Calculus : a complete course*. Pearson, 7 ed., 1940.

[69] S. T. Cundiff, "Phase stabilization of ultrashort optical pulses," *Journal of Physics D: Applied Physics*, vol. 35, pp. R43–R59, apr 2002.

[70] S. T. Cundiff and J. Ye, "Colloquium: Femtosecond optical frequency combs," *Reviews of Modern Physics*, vol. 75, no. 1, p. 325, 2003.

[71] G. Steinmeyer, D. Sutter, L. Gallmann, N. Matuschek, and U. Keller, "Frontiers in ultrashort pulse generation: pushing the limits in linear and nonlinear optics," *Science*, vol. 286, no. 5444, pp. 1507–1512, 1999.

[72] M. Fox, *Optical properties of solids*. Oxford master series in condensed matter physics, Oxford university press, 2 ed., 2010.

[73] B. F. and N. Treps, *Le laser*. Une introduction à..., EDP Sciences, 2016.

[74] G. Cerullo, S. De Silvestri, V. Magni, and L. Pallaro, "Resonators for kerr-lens mode-locked femtosecond ti: sapphire lasers," *Optics letters*, vol. 19, no. 11, pp. 807–809, 1994.

[75] I. Walmsley, L. Waxer, and C. Dorrer, "The role of dispersion in ultrafast optics," *Review of Scientific Instruments*, vol. 72, no. 1, pp. 1–29, 2001.

[76] B. Tsermaa, B. K. Yang, J. M. Seo, and J. S. Kim, "A sub-10-fs ti: sapphire oscillator with a simple four-mirror cavity," *JOURNAL-KOREAN PHYSICAL SOCIETY*, vol. 52, no. 4, p. 1043, 2008.

[77] F. Helbing, G. Steinmeyer, J. Stenger, H. Telle, and U. Keller, "Carrier–envelope-offset dynamics and stabilization of femtosecond pulses," *Applied Physics B*, vol. 74, no. 1, pp. s35–s42, 2002.

[78] J. Reichert, R. Holzwarth, T. Udem, and T. W. Haensch, "Measuring the frequency of light with mode-locked lasers," *Optics communications*, vol. 172, no. 1-6, pp. 59–68, 1999.

[79] M. J. Thorpe and J. Ye, "Cavity-enhanced direct frequency comb spectroscopy," *Applied Physics B*, vol. 91, no. 3, pp. 397–414, 2008.

[80] F. Adler, M. J. Thorpe, K. C. Cossel, and J. Ye, "Cavity-enhanced direct frequency comb spectroscopy: technology and applications," *Annual Review of Analytical Chemistry*, vol. 3, pp. 175–205, 2010.

[81] M. L. Weichman, P. B. Changala, J. Ye, Z. Chen, M. Yan, and N. Picqué, "Broadband molecular spectroscopy with optical frequency combs," *Journal of molecular spectroscopy*, vol. 355, pp. 66–78, 2019.

[82] I. Coddington, N. Newbury, and W. Swann, "Dual-comb spectroscopy," *Optica*, vol. 3, no. 4, pp. 414–426, 2016.

[83] V. Magni, G. Cerullo, and S. De Silvestri, "Closed form gaussian beam analysis of resonators containing a kerr medium for femtosecond lasers," *Optics communications*, vol. 101, no. 5-6, pp. 365–370, 1993.

[84] H. Kogelnik and T. Li, "Laser beams and resonators," *Applied optics*, vol. 5, no. 10, pp. 1550–1567, 1966.

[85] V. Magni, G. Cerullo, and S. De Silvestri, "Abcd matrix analysis of propagation of gaussian beams through kerr media," *Optics Communications*, vol. 96, no. 4-6, pp. 348–355, 1993.

[86] A. Yariv, *Quantum Electronics*. Wiley, 1989.

[87] I. H. Malitson, "Refraction and dispersion of synthetic sapphire," *JOSA*, vol. 52, no. 12, pp. 1377–1379, 1962.

[88] P. E. Ciddor, "Refractive index of air: new equations for the visible and near infrared," *Applied optics*, vol. 35, no. 9, pp. 1566–1573, 1996.

[89] H. Burton, C. Debardelaben, W. Amir, and T. A. Planchon, "Temperature dependence of ti: Sapphire fluorescence spectra for the design of cryogenic cooled ti: Sapphire cpa laser," *Optics express*, vol. 25, no. 6, pp. 6954–6962, 2017.

[90] D. J. Jones, S. A. Diddams, J. K. Ranka, A. Stentz, R. S. Windeler, J. L. Hall, and S. T. Cundiff, "Carrier-envelope phase control of femtosecond mode-locked lasers and direct optical frequency synthesis," *Science*, vol. 288, no. 5466, pp. 635–639, 2000.

[91] S. T. Cundiff, J. Ye, and J. L. Hall, "Optical frequency synthesis based on mode-locked lasers," *Review of Scientific Instruments*, vol. 72, no. 10, pp. 3749–3771, 2001.

[92] H. R. Telle, G. Steinmeyer, A. E. Dunlop, J. Stenger, D. H. Sutter, and U. Keller, "Carrier-envelope offset phase control: A novel concept for absolute optical frequency measurement and ultrashort pulse generation," *Applied Physics B*, vol. 69, no. 4, pp. 327–332, 1999.

[93] J. M. Dudley, G. Genty, and S. Coen, "Supercontinuum generation in photonic crystal fiber," *Reviews of modern physics*, vol. 78, no. 4, p. 1135, 2006.

[94] P. B. Changala, B. Spaun, D. Patterson, J. M. Doyle, and J. Ye, "Sensitivity and resolution in frequency comb spectroscopy of buffer gas cooled polyatomic molecules," *Applied Physics B*, vol. 122, no. 12, p. 292, 2016.

[95] B. Spaun, P. B. Changala, D. Patterson, B. J. Bjork, O. H. Heckl, J. M. Doyle, and J. Ye, "Continuous probing of cold complex molecules with infrared frequency comb spectroscopy," *Nature*, 2016-05 2016.

[96] D. Patterson and J. M. Doyle, "Cooling molecules in a cell for ftmw spectroscopy," *Molecular Physics*, vol. 110, no. 15-16, pp. 1757–1766, 2012.

[97] D. Patterson, J. Rasmussen, and J. M. Doyle, "Intense atomic and molecular beams via neon buffer-gas cooling," *New Journal of Physics*, vol. 11, no. 5, p. 055018, 2009.

[98] N. R. Hutzler, H.-I. Lu, and J. M. Doyle, "The buffer gas beam: an intense, cold, and slow source for atoms and molecules," *Chemical reviews*, vol. 112, no. 9, pp. 4803–4827, 2012.

[99] T. Wall, "Preparation of cold molecules for high-precision measurements," *Journal of Physics B: Atomic, Molecular and Optical Physics*, vol. 49, no. 24, p. 243001, 2016.

[100] M. Herman, R. Georges, M. Hepp, and D. Hurtmans, "High resolution fourier transform spectroscopy of jet-cooled molecules," *International Reviews in Physical Chemistry*, vol. 19, no. 2, pp. 277–325, 2000.

[101] L. Santamaria, V. Di Sarno, I. Ricciardi, M. De Rosa, S. Mosca, G. Santambrogio, P. Maddaloni, and P. De Natale, "Low-temperature spectroscopy of the 12c2h2 ($v1$+ $v3$) band in a helium buffer gas," *The Astrophysical Journal*, vol. 801, no. 1, p. 50, 2015.

[102] J. A. Petricka, *A new cold molecule source: The buffer gas cooled molecular beam*. PhD thesis, Yale University, 12 2007.

[103] N. Harnew, "Classical mechanics, lecture 6 : the centre of mass." https://users.physics.ox.ac.uk/~harnew/lectures/lecture6-mechanics-handout.pdf, 2016. Accessed 22 January 2019.

[104] W. C. Campbell and J. M. Doyle, "Cooling, trap loading, and beam production using a cryogenic helium buffer gas," *Cold molecules: theory, experiment, applications*, pp. 473–508, 2009.

[105] D. Patterson, E. Tsikata, and J. M. Doyle, "Cooling and collisions of large gas phase molecules," *Physical Chemistry Chemical Physics*, vol. 12, no. 33, pp. 9736–9741, 2010.

[106] C. Day, "Basics and applications of cryopumps," 2007.

[107] S. Blake, P. Hackett, R. Clarke, and A. Cox, "Cryogenic pump induced vibration in the tap interaction chamber." https://www.clf.stfc.ac.uk/Pages/ar11-12_full_lsd_instrumentation_engineering_.pdf. Accessed: 2021-21-06.

[108] L. Santamaria, V. Di Sarno, I. Ricciardi, S. Mosca, M. De Rosa, G. Santambrogio, P. Maddaloni, and P. De Natale, "Assessing the time constancy of the proton-to-electron mass ratio by precision ro-vibrational spectroscopy of a cold molecular beam," *Journal of Molecular Spectroscopy*, vol. 300, pp. 116–123, 2014.

[109] J. Piskorski, D. Patterson, S. Eibenberger, and J. M. Doyle, "Cooling, spectroscopy and non-sticking of trans-stilbene and nile red," *ChemPhysChem*, vol. 15, no. 17, pp. 3800–3804, 2014.

[110] Z. Y., *Direct observation of Rydberg-Rydberg transitions via CPmmW spectroscopy*. PhD thesis, MASSACHUSETTS INSTITUTE OF TECHNOLOGY, 2014.

[111] J. P. Porterfield, L. Satterthwaite, S. Eibenberger, D. Patterson, and M. C. McCarthy, "High sensitivity microwave spectroscopy in a cryogenic buffer gas cell," *Review of Scientific Instruments*, vol. 90, no. 5, p. 053104, 2019.

[112] M. Ady and R. Kersevan, "Introduction to the latest version of the test-particle monte carlo code molflow+," in *5th International Particle Accelerator Conference*, 7 2014.

[113] M. Hablanian, *High-Vacuum Technology: A Practical Guide, Second Edition*. Mechanical Engineering, Taylor & Francis, 1997.

[114] J. T. Hodges, H. P. Layer, W. W. Miller, and G. E. Scace, "Frequency-stabilized single-mode cavity ring-down apparatus for high-resolution absorption spectroscopy," *Review of Scientific Instruments*, vol. 75, no. 4, pp. 849–863, 2004.

[115] M. Herman, K. Didriche, D. Hurtmans, B. Kizil, P. Macko, A. Rizopoulos, and P. V. Poucke, "Fantasio: a versatile experimental set-up to investigate jet-cooled molecules," *Molecular Physics*, vol. 105, no. 5-7, pp. 815–823, 2007.

[116] K. Didriche, C. Lauzin, T. Földes, X. de Ghellinck D'Elseghem Vaernewijck, and M. Herman, "The fantasio+ set-up to investigate jet-cooled molecules: focus on overtone bands of the acetylene dimer," *Molecular Physics*, vol. 108, no. 17, pp. 2155–2163, 2010.

[117] R. Toth, "Line list of water vapor parameters from 500 to 8000 cm-1," *see http://mark4sun. jpl. nasa. gov/h2o. html*, 2004.

[118] K. Didriche, T. Földes, C. Lauzin, D. Golebiowski, J. Liévin, and M. Herman, "Experimental 2ch excitation in acetylene-containing van der waals complexes," *Molecular Physics*, vol. 110, no. 21-22, pp. 2781–2796, 2012.

[119] V. Svoboda, V. Horká-Zelenková, J. Rakovskỳ, P. Pracna, and O. Votava, "Oh-stretch overtone of methanol: empirical assignment using a two temperature technique in a supersonic jet," *Physical Chemistry Chemical Physics*, vol. 17, no. 24, pp. 15710–15717, 2015.

[120] L. Xu, C. Spielmann, A. Poppe, T. Brabec, F. Krausz, and T. Hänsch, "Route to phase control of ultrashort light pulses," *Optics letters*, vol. 21, no. 24, pp. 2008–2010, 1996.

[121] R. Drever, J. L. Hall, F. Kowalski, J. Hough, G. Ford, A. Munley, and H. Ward, "Laser phase and frequency stabilization using an optical resonator," *Applied Physics B*, vol. 31, no. 2, pp. 97–105, 1983.

[122] M. Nickerson, "A review of pound-drever-hall laser frequency locking," *JILA, University of Colorado and NIST*, 2019.

[123] R. Barger, M. Sorem, and J. Hall, "Frequency stabilization of a cw dye laser," *Applied Physics Letters*, vol. 22, no. 11, pp. 573–575, 1973.

[124] R. J. Jones, I. Thomann, and J. Ye, "Precision stabilization of femtosecond lasers to high-finesse optical cavities," *Physical Review A*, vol. 69, no. 5, p. 051803, 2004.

[125] K. Huang, H. Le Jeannic, J. Ruaudel, O. Morin, and J. Laurat, "Microcontroller-based locking in optics experiments," *Review of Scientific Instruments*, vol. 85, no. 12, p. 123112, 2014.

[126] M. A. Luda, M. Drechsler, C. T. Schmiegelow, and J. Codnia, "Compact embedded device for lock-in measurements and experiment active control," *Review of Scientific Instruments*, vol. 90, no. 2, p. 023106, 2019.

[127] J. L. Hall, M. S. Taubman, and J. Ye, "Laser stabilization," *OSA Handbook v14*, 1999.

[128] T. C. Briles, D. C. Yost, A. Cingöz, J. Ye, and T. R. Schibli, "Simple piezoelectric-actuated mirror with 180 khz servo bandwidth," *Optics express*, vol. 18, no. 10, pp. 9739–9746, 2010.

[129] A. Chadi, G. Méjean, R. Grilli, and D. Romanini, "Note: Simple and compact piezoelectric mirror actuator with 100 khz bandwidth, using standard components," *Review of Scientific Instruments*, vol. 84, no. 5, p. 056112, 2013.

[130] D. Goldovsky, V. Jouravsky, and A. Pe'er, "Simple and robust phase-locking of optical cavities with> 200 khz servo-bandwidth using a piezo-actuated mirror mounted in soft materials," *Optics express*, vol. 24, no. 25, pp. 28239–28246, 2016.

[131] T. Nakamura, S. Tani, I. Ito, M. Endo, and Y. Kobayashi, "Piezoelectric transducer actuated mirror with a servo bandwidth beyond 500 khz," *Optics express*, vol. 28, no. 11, pp. 16118–16125, 2020.

[132] E. Hecht, *Optics*. Addison-Wesley world student series, Addison-Wesley, 1998.

[133] W. Perkins, "Fourier transform-infrared spectroscopy: Part l. instrumentation," *Journal of Chemical Education*, vol. 63, no. 1, p. A5, 1986.

[134] T. Deleporte, *Quantitative infrared Fourier transform spectroscopy: absolute intensities for 13CO2 and HOBr*. PhD thesis, Université Libre de Bruxelles, 2008.

[135] E. Kretschmer, *Modelling of the instrument spectral response of conventional and imaging fourier transform spectrometers*. Université Laval, 2014.

[136] J. C. Brasunas and G. M. Cushman, "Uniform time-sampling fourier transform spectroscopy," *Applied optics*, vol. 36, no. 10, pp. 2206–2210, 1997.

[137] T. Eom, H. Choi, and S. Lee, "Frequency stabilization of an internal mirror he–ne laser by digital control," *Review of scientific instruments*, vol. 73, no. 1, pp. 221–224, 2002.

[138] L. Luhs, "Hene laser frequency stabilization," *LD didactic*, vol. reference note 4747111, 2012.

[139] Thorlabs, "Pid tutorial." `http://www.thorlabs.de/tutorials.cfm?tabID=5dfca308-d07e-46c9-baa0-4defc5c40c3e`. Accessed 15 june 2016.

[140] A. S. Zachor and S. M. Aaronson, "Delay compensation: its effect in reducing sampling errors in fourier spectroscopy," *Applied Optics*, vol. 18, no. 1, pp. 68–75, 1979.

[141] "How to hitran line-by-line." `http://www.bytran.org/howtolbl.htm`. Accessed: 2021-25-05.

[142] "Definitions and units: Line-by-line parameters." `https://hitran.org/docs/definitions-and-units/`. Accessed: 2021-25-05.

[143] S. E. Fiedler, A. Hese, and A. A. Ruth, "Incoherent broad-band cavity-enhanced absorption spectroscopy of liquids," *Review of scientific instruments*, vol. 76, no. 2, p. 023107, 2005.

[144] S. Kassi, *Spectroscopie laser d'absorption à haute sensibilité de molécules d'intérêt atmosphérique et planétologique*. PhD thesis.

[145] J. Peatross and A. Rundquist, "Temporal decorrelation of short laser pulses," *JOSA B*, vol. 15, no. 1, pp. 216–222, 1998.

[146] P. Wasylczyk, "Ultracompact autocorrelator for femtosecond laser pulses," *Review of scientific instruments*, vol. 72, no. 4, pp. 2221–2223, 2001.

[147] S. Courts, "A review of cryogenic sensors for emerging applications." https://cryogenicsociety.org/26565/news/cryo_sensors_emerging_applications/, 2013. Accessed 19 January 2019.

[148] S. Courts, P. Swinehart, and C. Yeager, "A new cryogenic diode thermometer," *AIP Conference Proceedings*, vol. 613, no. 1, pp. 1620–1627, 2002.

[149] L. S. cryotronics, "Instructions, silicon diode and gaalas diode temperature sensor installation, model dt-470, 471, 670, and 671 cu and di packages, and tg-120-cu package." https://www.lakeshore.com/docs/default-source/product-downloads/installation-instructions/f009-00-00.pdf?sfvrsn=68febeb9_6. Accessed: 2021-21-06.

[150] i. ULVAC, "Instructions, silicon diode and gaalas diode temperature sensor installation, model dt-470, 471, 670, and 671 cu and di packages, and tg-120-cu package." https://showcase.ulvac.co.jp/en/how-to/trouble-shooting/cryo-pump-safety.html. Accessed: 2021-21-06.

[151] E. D. Black, "An introduction to pound–drever–hall laser frequency stabilization," *American journal of physics*, vol. 69, no. 1, pp. 79–87, 2001.

[152] A. Cygan, D. Lisak, P. Masłowski, K. Bielska, S. Wójtewicz, J. Domysławska, R. Trawiński, R. Ciuryło, H. Abe, and J. Hodges, "Pound-drever-hall-locked, frequency-stabilized cavity ring-down spectrometer," *Review of Scientific Instruments*, vol. 82, no. 6, p. 063107, 2011.

[153] G. C. Bjorklund, "Frequency-modulation spectroscopy: a new method for measuring weak absorptions and dispersions," *Optics letters*, vol. 5, no. 1, pp. 15–17, 1980.

[154] P. Du, W. A. Kibbe, and S. M. Lin, "Improved peak detection in mass spectrum by incorporating continuous wavelet transform-based pattern matching," *Bioinformatics*, vol. 22, no. 17, pp. 2059–2065, 2006.

[155] J. M. Gregoire, D. Dale, and R. B. Van Dover, "A wavelet transform algorithm for peak detection and application to powder x-ray diffraction data," *Review of Scientific Instruments*, vol. 82, no. 1, p. 015105, 2011.

[156] Z.-M. Zhang, S. Chen, Y.-Z. Liang, Z.-X. Liu, Q.-M. Zhang, L.-X. Ding, F. Ye, and H. Zhou, "An intelligent background-correction algorithm for highly fluorescent samples in Raman spectroscopy," *Journal of Raman Spectroscopy*, vol. 41, no. 6, pp. 659–669, 2010.

[157] Z. Li, D.-J. Zhan, J.-J. Wang, J. Huang, Q.-S. Xu, Z.-M. Zhang, Y.-B. Zheng, Y.-Z. Liang, and H. Wang, "Morphological weighted penalized least squares for background correction," *Analyst*, vol. 138, no. 16, pp. 4483–4492, 2013.

[158] Q. Bao, J. Feng, F. Chen, W. Mao, Z. Liu, K. Liu, and C. Liu, "A new automatic baseline correction method based on iterative method," *Journal of Magnetic Resonance*, vol. 218, pp. 35–43, 2012.

[159] "Transverse mode." `https://en.wikipedia.org/wiki/Transverse_mode`. Accessed: 2021-09-28.

[160] O. Reich, G. David, K. Esat, and R. Signorell, "Weighing picogram aerosol droplets with an optical balance," *Communications Physics*, vol. 3, no. 1, pp. 1–8, 2020.

[161] C. Schwaferts, R. Niessner, M. Elsner, and N. P. Ivleva, "Methods for the analysis of submicrometer-and nanoplastic particles in the environment," *TrAC Trends in Analytical Chemistry*, vol. 112, pp. 52–65, 2019.

[162] R. Meng, J. Xu, and B. Ge, "Diffraction glare points: principle and application in particle sizing," *Opt. Express*, vol. 26, pp. 22816–22825, Sep 2018.

[163] O. Kliebisch and P. Mahnke, "Real-time laser doppler anemometry for optical air data applications in low aerosol environments," *Review of Scientific Instruments*, vol. 91, p. 095106, Sept. 2020.

[164] G. Castanet, P. Dunand, O. Caballina, and F. Lemoine, "High-speed shadow imagery to characterize the size and velocity of the secondary droplets produced by drop impacts onto a heated surface," *Experiments in Fluids*, vol. 54, p. 1489, Mar 2013.

[165] M. D. Patterson and J. S. Wettlaufer, "Note: Scanned multi-light-emitting-diode illumination for volumetric particle image velocimetry," *Review of Scientific Instruments*, vol. 81, p. 096101, Sept. 2010.

[166] R. Xu, "Light scattering: A review of particle characterization applications," *Particuology*, vol. 18, pp. 11–21, 2015.

[167] S. Sousan, K. Koehler, L. Hallett, and T. M. Peters, "Evaluation of the alphasense optical particle counter (opc-n2) and the grimm portable aerosol spectrometer (pas-1.108)," *Aerosol Science and Technology*, vol. 50, no. 12, pp. 1352–1365, 2016.

[168] L. R. Crilley, M. Shaw, R. Pound, L. J. Kramer, R. Price, S. Young, A. C. Lewis, and F. D. Pope, "Evaluation of a low-cost optical particle counter (alphasense opc-n2) for ambient air monitoring," *Atmospheric Measurement Techniques*, vol. 11, no. 2, pp. 709–720, 2018.

[169] E. P. Fischer, M. C. Fischer, D. Grass, I. Henrion, W. S. Warren, and E. Westman, "Low-cost measurement of face mask efficacy for filtering expelled droplets during speech," *Science Advances*, vol. 6, no. 36, p. eabd3083, 2020.

[170] J. Pribošek and G. Röhrer, "Estimation of the particle sizing error due to particle position in an integrated pm2.5 optical particle counter," in *Multidisciplinary Digital Publishing Institute Proceedings*, vol. 2, p. 850, 2018.

[171] V. Stadnytskyi, C. E. Bax, A. Bax, and P. Anfinrud, "The airborne lifetime of small speech droplets and their potential importance in sars-cov-2 transmission," *Proceedings of the National Academy of Sciences*, vol. 117, no. 22, pp. 11875–11877, 2020.

[172] G. A. Somsen, C. van Rijn, S. Kooij, R. A. Bem, and D. Bonn, "Small droplet aerosols in poorly ventilated spaces and sars-cov-2 transmission," *The Lancet. Respiratory Medicine*, 2020.

[173] B. J. Sumlin, W. R. Heinson, and R. K. Chakrabarty, "Retrieving the aerosol complex refractive index using pymiescatt: A mie computational package with visualization capabilities," *Journal of Quantitative Spectroscopy and Radiative Transfer*, vol. 205, pp. 127–134, 2018.

[174] P. Virtanen, R. Gommers, T. E. Oliphant, M. Haberland, T. Reddy, D. Cournapeau, E. Burovski, P. Peterson, W. Weckesser, J. Bright, S. J. van der Walt, M. Brett, J. Wilson, K. J. Millman, N. Mayorov, A. R. J. Nelson, E. Jones, R. Kern, E. Larson, C. J. Carey, İ. Polat, Y. Feng, E. W. Moore, J. VanderPlas, D. Laxalde, J. Perktold, R. Cimrman, I. Henriksen, E. A. Quintero, C. R. Harris, A. M. Archibald, A. H. Ribeiro, F. Pedregosa, P. van Mulbregt, and SciPy 1.0 Contributors, "SciPy 1.0: Fundamental Algorithms for Scientific Computing in Python," *Nature Methods*, vol. 17, pp. 261–272, 2020.

[175] W. J. Glantschnig and S.-H. Chen, "Light scattering from water droplets in the geometrical optics approximation," *Appl. Opt.*, vol. 20, pp. 2499–2509, Jul 1981.

[176] P. E. Debevec and J. Malik, "Recovering high dynamic range radiance maps from photographs," in *ACM SIGGRAPH 2008 classes*, pp. 1–10, 2008.

[177] S. H. Smith, G. A. Somsen, C. Van Rijn, S. Kooij, L. Van Der Hoek, R. A. Bem, and D. Bonn, "Aerosol persistence in relation to possible transmission of sars-cov-2," *Physics of Fluids*, vol. 32, no. 10, p. 107108, 2020.

[178] C. Y. H. Chao, M. P. Wan, L. Morawska, G. R. Johnson, Z. Ristovski, M. Hargreaves, K. Mengersen, S. Corbett, Y. Li, X. Xie, *et al.*, "Characterization of expiration air jets and droplet size distributions immediately at the mouth opening," *Journal of Aerosol Science*, vol. 40, no. 2, pp. 122–133, 2009.

[179] M. L. Pöhlker, O. O. Krüger, J.-D. Förster, W. Elbert, J. Fröhlich-Nowoisky, U. Pöschl, C. Pöhlker, G. Bagheri, E. Bodenschatz, J. A. Huffman, *et al.*, "Respiratory aerosols and droplets in the transmission of infectious diseases," *arXiv preprint arXiv:2103.01188*, 2021.

[180] N. Gong, K. Tham, A. K. Melikov, D. P. Wyon, S. Sekhar, and K. Cheong, "The acceptable air velocity range for local air movement in the tropics," *Hvac&r Research*, vol. 12, no. 4, pp. 1065–1076, 2006.

[181] G. A. Somsen, C. J. van Rijn, S. Kooij, R. A. Bem, and D. Bonn, "Measurement of small droplet aerosol concentrations in public

spaces using handheld particle counters," *Physics of Fluids*, vol. 32, no. 12, p. 121707, 2020.